Optimisation of Plasma Sprayed Hydroxyapatite Coatings

Tanya. J. Levingstone, BEng

Ph. D **2008**

Optimisation of Plasma Sprayed Hydroxyapatite Coatings

Tanya J. Levingstone, BEng

A thesis submitted in fulfilment of the requirement for the degree

of

Doctor of Philosophy

Supervisors:

Dr. Lisa Looney, Dr. Joseph Stokes

School of Mechanical and Manufacturing Engineering,

Dublin City University, Ireland.

Declaration

I hereby certify that this material, which I now submit for assessment on the programme of study leading to the award of Doctor of Philosophy, is entirely my own work and has not been taken from the work of others save and to the extent that such work has been cited and acknowledged within the text of my work.

Signed: I.D. Number: 99407946

Date:

Acknowledgements

There are many people that I would like to thank for helping me to bring this thesis to completion. Sincere thanks to my project supervisors. Thanks to Dr. Lisa Looney for her supervision and guidance during the course of this work. Her constructive suggestions, comments and advice throughout the project were invaluable. Thanks to Dr. Joseph Stokes for constant assistance and guidance. His dedication during the final months is much appreciated.

The assistance of all the staff in the School of Mechanical and Manufacturing Engineering is greatly appreciated. Particular thanks to Michael Tyrell for the technical support provided. I also greatly appreciate the support provided by the other research students in the department, in particular the numerous scientific discussions with Khaled Benyouis. Thanks also to Niall Barron in the National Institute for Cellular Biotechnology for assistance with the *in vitro* experimental work.

I would like to acknowledge the project funding provided by the Irish Research Council for Science, Engineering and Technology, funded by the National Development Plan. Also, thanks to Stryker Howmedica Osteonics, Cork, for hosting a number of useful industrial visits to their plant.

Finally, I would like to thank my friends and family for their encouragement and understanding. Special thanks to my parents who have provided so much support throughout my studies. Thank you for everything that you have done for me.

Abstract

Optimisation of Plasma Sprayed Hydroxyapatite Coatings

Tanya J. Levingstone

Hydroxyapatite, (HA), is a calcium phosphate bioceramic material which has an almost identical chemical composition to that of the mineral component of bone. Its biocompatibility and osteoconductivity have led to its use in a wide range of applications in both dentistry and orthopaedics. One such application is for the uncemented fixation of implants. The plasma spraying technique, a thermal spray process, is the most commonly used method for the production of HA coatings. This process is a complicated one, affected by a large number of parameters. Due to this complexity, the process – property – structure relationship is poorly understood.

The present work aims to clarify this relationship and use the knowledge gained to develop a novel bi-layer coating. Statistically designed experiments (DOE) were used to determine the effect of five process parameters (factors), Current, Gas Flow Rate, Powder Feed Rate, Spray Distance and Carrier Gas Flow Rate, on the coating properties. A screening design was first carried out to gain an initial understanding of the process. This was followed by a detailed Response Surface Methodology (RSM) experiment. Five properties (responses) were examined, crystallinity, purity, roughness, porosity and thickness.

Models describing the effects of the variables on these coating properties were then developed. The developed models were optimised using two separate optimisation criteria to develop a novel bi-layered coating, designed to provide improved *in vivo* performance over current HA coatings. The performance of this novel coating was evaluated using a cell culture experiment.

Statistically significant models were developed in this work for each of the measured responses. All factors were found to have a significant effect on the measured coating responses. Current, Gas Flow Rate, Spray Distance and the Current * Spray Distance interaction were found to be the parameters with greatest effect on the coating properties. Analysis of the bi-layered coating produced indicates that improved biological performance has been achieved.

Table of Contents

List of Figures

List of Tables

1 Introduction

Hydroxyapatite, (HA), is a calcium phosphate bioceramic material which has an almost identical chemical composition to that of the mineral component of bone. It has excellent biocompatibility and is osteoconductive, allowing bone cells to grow on its surface. For this reason it has been used successfully in dentistry and orthopaedics for many years. One such application is as a coating applied onto hip implants, where it provides enhanced fixation for the implant to human bone.

The plasma spraying technique is the most commonly used method for the application of HA coatings. This is a thermal spray process in which powder particles are melted in a high temperature plasma flame and propelled towards a substrate material to form a coating. The advantages of this process include high coating adhesion strength and also high deposition rate, which allows coatings to be quickly produced.

Although the plasma spray process has been used in industry for many years, it is a process where practice has preceded understanding. The process – property – structure relationships are far from being fully understood. The complexity of the process and the fact that as many as 50 parameters affect the final coating mean that this is quite a significant challenge.

Other challenges with this process relate to the high temperatures which HA particles experience during spraying. These high temperatures cause the decomposition of the HA powder particles within the plasma flame. This leads to the decomposition of HA into new phases, such as α -tri-calcium phosphate (α-TCP) and β-tri-calcium phosphate (β-TCP). The rapid quenching of the particles on the substrate results in a coating with a high content of amorphous calcium phosphate (ACP) phases. These phases are known to dissolve more quickly in the body than HA. Dissolution in vivo is undesirable as it results in a weakened coating which in the long term cannot secure the implant, thus causing implant failure.

There has been a strong research focus on the area of HA coatings in recent years and many improvements have been brought about. Clinical trials indicate that the life of HA coated implants is improving year on year. It is thus clear that patients are benefiting from the improvements that are being brought about. However, the current situation is still far from ideal. Implants failure rates are still high and revision surgeries are still a necessity for a large number of patients. The human cost and economic costs of revision surgeries are high. There are many that believe that HA coated implants have the potential to provide functionality for the life of the patient. Current HA coated implants do not perform to this level. It is clear that in order to make 'life long functionality' a reality, further improvements in plasma sprayed HA coatings are required.

The current focus among the research community is broad, ranging from the production of composite and multi-layer coatings to the investigation of new coating techniques for the production of HA coatings. Even with recent advances in these areas, it is still recognised that there are significant gaps in the understanding of the plasma spray process. Hence, the investigation of this was the primary aim of this research work.

Recent studies of the *in vivo* interaction between bone and calcium phosphates have identified evidence of the occurrence of a dissolution / re-precipitation process within the body, whereby partial dissolution of the coating encourages bone-like material to be deposited. Although this process is advantageous in the initial repair process, excessive dissolution causes a reduction in the mechanical properties of the coating causing premature coating failure.

It was hypothesised that precise control of the spray process parameters during coating deposition would allow the development of a bi-layer coating that would provide a stable base layer, resistant to dissolution (high % crystalline content), and an active top layer, that would encourage bone growth (high % amorphous content). Development of this bi-layer coating, shown in *figure 1.1,* was the second aim of this research.

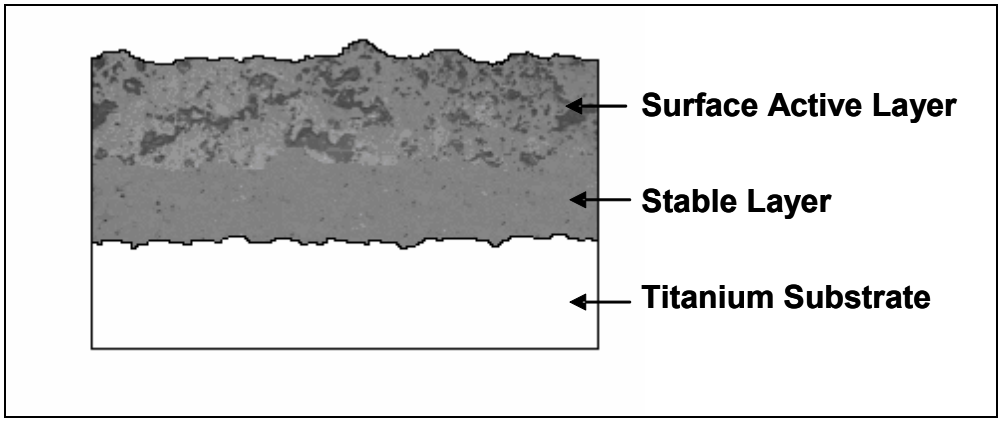

Figure 1.1: Functionally Graded HA Coating

1.1 Objectives of the Research Project

There are two main objectives for this research work:

1) The primary goal is to bring clarity to the relationship between various plasma spray process parameters and the resultant coating properties, through the development of process models (using the Design of Experiment technique) that relate process parameters to various coating properties.

2) The second aim of this thesis is to use the developed process models to optimise the process and to produce a novel bi-layered coating that will demonstrate improved *in vivo* performance.

1.2 Structure of Thesis

The thesis is organised as follows:

Chapter 2 contains a comprehensive literature review. This encompasses an overview of the design and fixation of total hip replacements and a summary of the properties of hydroxyapatite. The plasma spray process is explained along with the theory of coating build-up and a summary of some other techniques that have been used to produce HA coatings. The properties required from HA coatings and also current research in the area of HA coatings are discussed. A

discussion of the Design of Experiment (DOE) methods used in this work is also included.

Further relevant background literature compiled while carrying out the preliminary review of the literature has been published in two Head Start resource publications published through the Materials Processing Research Centre in Dublin City University. Issue 1 entitled "Ceramics for Medical Applications" [1] and Issue 2 entitled "Guide to Hip Replacements for Engineers: Design, Material and Stress Issues" [2].

Chapter 3 details the equipment and experimental methods used in this work. The plasma spray equipment used is explained in detail. The materials used in the study are also detailed. The procedure followed in the post spray heat treatment study of HA coating recrystallisation is presented. The statistical DOE experiments used for the investigation and optimisation of the plasma sprayed coatings are discussed. The various material characterisation and mechanical testing procedures used are outlined. Finally, details of the cell culture experiments, carried out are given.

The results from this work are presented and discussed in Chapter 4. Firstly, the results from characterisation of the materials used are given. Following this, the findings of the post spray heat treatment study are presented. The statistical experimental work is presented in two sections; firstly, the screening test results and secondly, the Response Surface Methodology (RSM) study test results. The optimisation process carried out in the development of the bi-layer coating is presented. Results from the cell culture work carried out are also discussed and analysed.

The conclusions drawn from this investigation are outlined in Chapter 5. Finally, some recommendations for future research are given in Chapter 6.

2 Literature Review

2.1 The Total Hip Replacement

2.1.1 History of the Total Hip Replacement

Disease and injury can impair the normal function of the hip joint leading to pain, muscle weakness and limited movement of the joint. Arthritis is one of the most common causes of hip and knee disorders. In Ireland, arthritis affects approximately 34 % of women and 23 % of men [3]. There are a number of types of arthritis including osteoarthritis and rheumatoid arthritis. Other joint diseases which may lead to joint replacement include avascular necrosis, osteonecrosis and Paget's disease [2]. Most of these degenerative diseases will eventually require surgery to replace one or both of the damaged surfaces of the hip joint using prosthetic components. Replacement of one half of the joint is termed hemiarthroplasty [4], whereas replacement of both components is known as Total Hip Arthroplasty (THA) or Total Hip Replacement (THR).

A total hip replacement has two main components, the acetabular component, which fits into the hip socket and the femoral component, which is inserted into the femur. This is shown in *figure 2.1*.

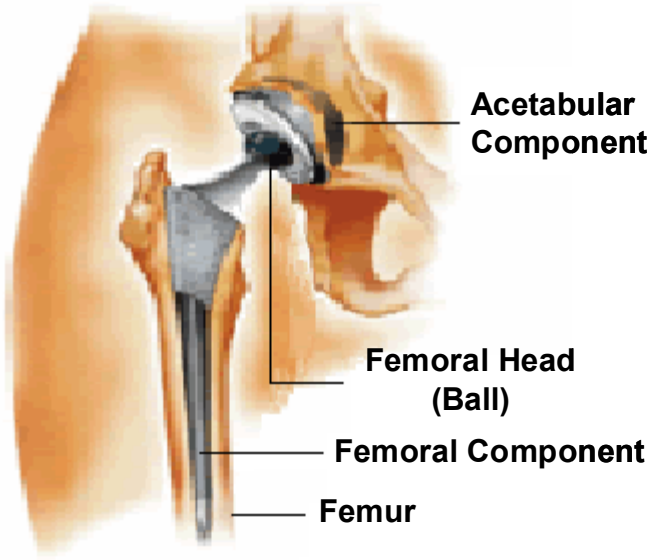

Figure 2.1: Components of a Hip Replacement [5]

The first hip joint replacement procedure was performed by a German physician, Mr. Thomas Gluck, in 1886 [6]. Mr. Gluck's ideas were revolutionary and paved the way for total hip replacement. However, it was not until the introduction of Charnley's 'Low Friction Arthroplasty (LFA)' design in the 1960's that total hip replacement became widely practiced. His design used high density polyethylene for the acetabulum surface and was fixed in place with polymethylmethacrylate (PMMA) acrylic cement [7]. Today, the hip replacement procedure is one of the most commonly performed surgical procedures in the western world. Over 69,000 hip replacement procedures were performed in both public and private hospitals in England and Wales in 2007 [8]. The procedure is widely regarded as one of the most important achievements in orthopaedic surgery in the 20th century [9].

2.1.2 Fixation of Hip Replacements

Joint replacements can be categorised according to the method of fixation used; either cemented or cementless. Cemented fixation uses cement to hold the prosthesis in place whereas cementless fixation relies on the interaction at the prosthesis-bone interface to hold the prosthesis in place.

Cemented implants are fixed in place using the acrylic cement PMMA (polymethylmethacrylate) cement. It has been used in surgery for the fixation of prostheses for about 40 years [10]. Cemented hip replacements have been successful in affording pain relief and improving function. However, the bone-cement interface is not smooth and contains many flaws, such as pores and microcracks. Therefore, under cyclic loading conditions, due to a patient's natural activities, this bone-cement interface may result in fatigue crack nucleation. Cemented fixation also has other disadvantages, such as shrinkage of the cement by up to 7 % during polymerisation [11]. A temperature rise of up to 80 °C also occurs during polymerisation, leading to the death of the immediately surrounding living tissue.

In the 1970's reports of high radiographic failure rates and osteolysis led to a general dissatisfaction with the use of cement for fixation of total joint

replacements [11]. The problems related particularly to young active patients who usually outlived the fixation of a total hip or knee arthroplasty [12]. This dissatisfaction led to major developments in the areas of cementless implants.

There are three main types of cementless implant fixation: mechanical fixation, biological fixation and bioactive fixation. Mechanical fixation methods can be classified as either active or passive. Active fixation methods include the use of screws, bolts, nuts and wires. Passive fixation uses either an interference fit or non-interference fit to hold the implant in place.

Biological fixation involves the porous ingrowth of bone into biocompatible porous biomaterials [13]. The pores must be greater than 100 μm in diameter to allow cells and tissues to form [14]. Biological ingrowth into the porous cavities produces a strong interlocking structure that can withstand more complex stress conditions than mechanical fixation. However, there is no true bonding of the material to the bone and a fibrous layer may form between the bone and implant.

Bioactive fixation or surface active bonding can occur with materials with surface active properties. The definition of a bioactive material is, 'one that elicits a specific biological response at the interface of the material which results in the formation of bond between the tissues and material' [15]. The formation of this intimate bond is called osseointegration. Examples of bioactive materials include bioactive glasses, bioactive glass-ceramics and hydroxyapatite, HA [1]. Of these, HA has been used with the most success. HA-coated prostheses have been used clinically since the mid 1980's [16].

2.1.3 HA-Bone Interface

When a HA coated prosthesis is implanted into bone, it is primarily held in place by press-fit, mechanical fixation. The repair of surrounding bone then begins to occur. The first stage of this repair process involves perfusion of blood into the area, bringing cells generally of mesenchymal origin to the site. These are pluripotential cells; the pathway of their differentiation depends on the local and systemic factors present at the implant site [17]. Hydroxyapatite is bioactive,

allowing bone cells to grow on its surface. It has been shown that bone growth on HA is greater than the amount of bone growth on an uncoated stem [18, 19]. This newly formed bone thus grows around the implant and holds it in place.

For an uncoated implant, bone will grow unilaterally from the bone towards the implant. When the bone trabeculae reach the implant's surface they begin to spread parallel to the surface bridging the gap [20]. For HA coated implants, it is reported by numerous researchers that bone can grow on both surfaces thus closing the gap more rapidly [19-21]. This bi-directional gap filling allows fixation to occur twice as quickly as it would for an uncoated stem. Photomicrographs, taken from a study by Soballe et al. [19], of the growth of bone cells on both an uncoated titanium implant and a HA coated titanium implant are shown in *figure 2.2*. They show the occurrence of bi-directional gap filling on the HA coated implant.

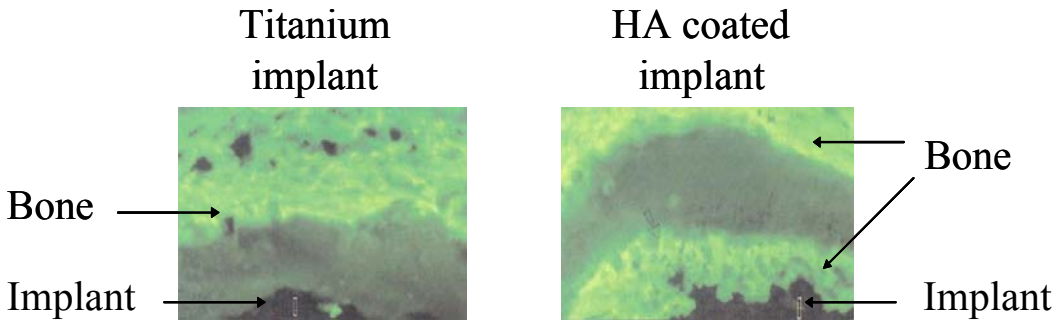

Figure 2.2: Micrographs showing osteointegration into a HA coated implant Adapted from [19]

Another advantage of bioactive coatings is that they protect the body from any metal-ion release from the metallic implant [22, 23]. Release of these ions causes the body to initiate an immune response, forming a fibrous membrane around the implant. This fibrous layer prevents adequate fixation between the bone and the implant and reduces the load that can be applied before failure occurs. The work of Soballe et al. [19] has also demonstrated that as HA has a similar chemical composition to that of bone it does not cause a fibrous membrane to be formed, as shown in *figure 2.3*. This has also been reported by Nagano et al. [24].

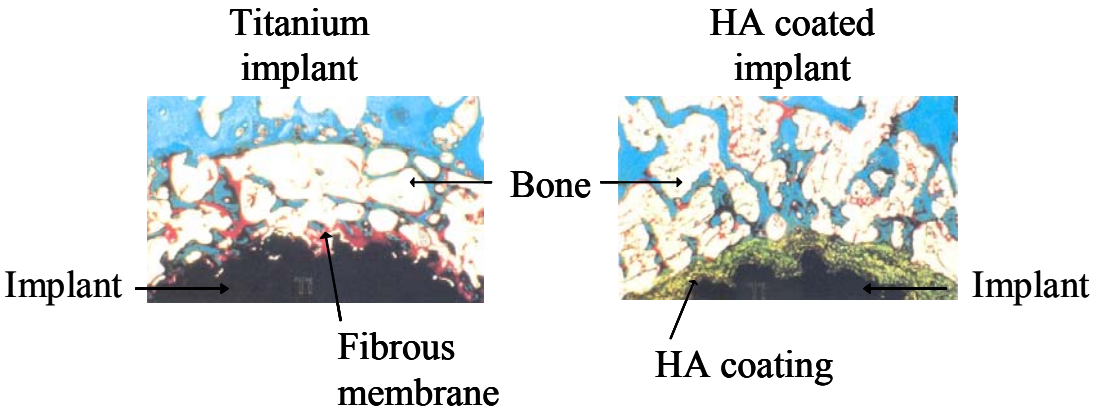

Figure 2.3: Micrographs showing the formation of a fibrous membrane on titanium implants Adapted from [19]

As bone cells have been reported to grow directly onto the HA coating a direct chemical bond between the bone and the implant can be formed. This direct chemical bonding allows the transfer of forces between the two to occur more efficiently. Force transmission and mechanical loading conditions play an important role in bone remodelling [25]. A certain amount of loading is necessary for the adequate remodelling to occur, however, if there is insufficient stress or if too great a stress is applied, resorption of the bone occurs. This remodelling process is controlled by Wolff's law which postulates that "bone continually changes in order to cope with the mechanical loads that it is exposed to" [26]. Other factors that affect the strength of the bone to implant bond include the shape and topography of the implant, surgical factors (relating to the surgical procedure used and the quality of the surgery technique) and the quality of the bone.

The mechanism thought to be responsible for the bone bonding ability of HA coatings is the dissolution / re-precipitation process. In this process, partial dissolution of the coating occurs and calcium and phosphate ions, in the form of Ca^{2+}, $H_2PO_4^-$, HPO_4^{2-}, PO_4^{3-} and $CaH_2PO_4^+$, are released into the fluid surrounding the joint [27]. Proteins and ions activate the surface of the HA coating encouraging the precipitation of calcium and phosphate as HA crystals on the surface of the HA coating [28]. Remodelling of the damaged bone also occurs in conjunction with the coating dissolution. Further remodelling of the implant-

bone interface occurs until a strong bond between the two is formed. This chemical bond will then provide secondary fixation that will prevent loosening. The mechanism is similar to the healing of a fractured bone. Micromotion at the bone/implant interface must be less than 50 μm in order for successful osseointegration and adequate fixation to occur [29].

2.1.4 Clinical Performance of HA-coated Implants

Analysis of the performance of joint replacements can be difficult due to the long follow up times required. Many countries now use 'National Joint Registries' for the collection and reporting of data relating to joint replacement surgery. The first National Joint Registry was the Swedish Total Hip Replacement Register [30]. It was established in 1979 and provides useful data relating to the types of implants and the performance of implants that have been used since then [31].

The use of cementless fixation techniques varies significantly from country to country. Statistics reported in the 1st Annual Report published by the National Joint Registry for England and Wales [32] in September 2004 (*table 2.1*) show that cementless cups and stems are used much more commonly in Australia and Canada than they are in Sweden or England and Wales. 55% of stems implanted in Canada are cementless compared to only 19.30% in England and Wales.

Table 2.1: Implant fixation techniques [32]

National joint registry	*Cemented cups*	*Cementless cups*	*Cemented stems*	*Cementless stems*
Australia	18.50%	81.50%	58.40%	41.60%
Canada	7%	90%	44%	55%
England & Wales *	69.30%	30.70%	80.70%	19.30%

* data only collected between April and December 2003

The main reasons for failure of uncemented implants identified in this report are dislocation (31%), aseptic loosening (19%) and infection (11%) [32]. Loosening of HA coated implants is generally related to dissolution or delamination of the HA coating. When uncemented implants were first introduced, failure rates were high [32]. However, in recent years, the performance of uncemented implant designs have much improved and they now have similar life expectancies to cemented implants [32]. Clinical studies by Oosterbos et al. [33] and Reikeras and Gunderson [34] show survival rates of 100% at 10 years and only one failure out of 245 patients at 8 – 12 years respectively. Clinical results such as these confirm that the initial aspirations of providing increased bone ingrowth and earlier fixation have been achieved.

There are still concerns, however, about the long term performance of HA coatings. These concerns relate mainly to the durability of the coatings in vivo as they are known to dissolve over time leading to weakening of the coating and eventually failure [24, 27, 35]. In order to address these concerns and bring the aspiration of life long functionality to a reality, further investigation into and optimisation of HA coatings is necessary.

2.2 Hydroxyapatite

2.2.1 Calcium Phosphate Bioceramic Materials

Calcium phosphate ceramics have received a lot of research attention in recent years due to their chemical similarity to calcified tissue (bones, teeth). They have been used in dentistry and medicine for about thirty years for applications including dental implants, periodontal treatment, alveolar ridge augmentation, orthopedics, maxillofacial surgery, and otolaryngology [36]. There are various different calcium phosphate compounds. The most important of these are summarised in *table 2.2*. Of the calcium phosphate ceramics outlined in *table 2.2*, Hydroxyapatite (HA) is of most interest as it is the most similar to the calcium phosphate phase present in bone.

Table 2.2: Some Calcium Phosphate Compounds [37, 38]

Symbol	*Phase's Name*	*Chemical Formula*	*Chemical Definition*	*Ca/P*
DCPA	Monetite	$CaHPO_4$	Dicalcium Phosphate Anhydrous	1.00
DCPD	Brushite	$CaHPO.2H_2O$	Dicalcium Phosphate Dihydrate	1.00
OCP		$Ca_8H_2(PO_4)_6.5H_2O$	Octocalcium Phosphate	1.33
α-TCP		α-$Ca_3(PO_4)_2$	α-Tricalcium Phosphate	1.50
β-TCP	Whitlockite	β-$Ca_3(PO_4)_2$	β-Tricalcium Phosphate	1.50
TTCP		$Ca_4(PO_4)_2O$	Tetracalcium phosphate	2.00
OHA		$Ca_{10}(PO_4)_6(OH)_{2-2x}O_x$	Oxyhydroxyapatite	1.67
OA		$Ca_{10}(PO_4)_6O$	Oxyapatite	1.67
HA		$Ca_{10}(PO_4)_6(OH)_2$	Hydroxyapatite	1.67

2.2.2 Chemical Structure

The general chemical formula for HA is $Ca_{10}(PO_4)_6(OH)_2$ and it has Ca/P ratio of 1.67. The structure of calcium HA is reported by Le Geros et al. [39] to have been determined by Beevers and McIntyre [40] and later refined by Kay et al. [41]. The unit cell contains Ca, PO_4 and OH ions closely packed together to represent the apatite structure. Most researchers suggest that hydroxyapatite has a hexagonal crystal structure with a space group, $P6_3/m$ [39, 42]. This structure can be seen in *figure 2.4*. This space group is characterised by a six-fold c-axis perpendicular to three equivalent a-axes (a_1,a_2,a_3) at angles of 120 º to each other. The ten calcium atoms belong to either Ca(I) or Ca(II) subsets depending on their environment. Four calcium atoms occupy the Ca(I) positions: two at levels z = 0 and two at z = 0.5. Six calcium atoms occupy the Ca(II) positions: one group of three calcium atoms describing a triangle located at z = 0.25, the other group of three at z = 0.75, respectively. The six phosphate (PO_4) tetrahedral are in a helical arrangement from levels z = 0.25 to z = 0.75. The network of PO_4 groups provides

the skeletal framework which gives the apatite structure its stability. The oxygens of the phosphate groups are described as one O_1, one O_2 and two O_3 [39]. The dimensions of the unit cell at room temperature are: $a_0 = b_0 = 9.11$Å and $c_0 = 6.86$ Å [43]. *Figure 2.4 (a)* shows the oxygen coordination of columnar Ca(1) ions in apatite. *Figure 2.4 (b)* shows the linking of these columns via the PO_4 tetrahedra. The oxygen atoms in *Figure 2.4 (a)* and in one tetrahedron in *Figure 2.4 (b)* have been numbered, and positions of the horizontal mirror planes at ¼, ¾ *etc.* marked on the *c*-axis.

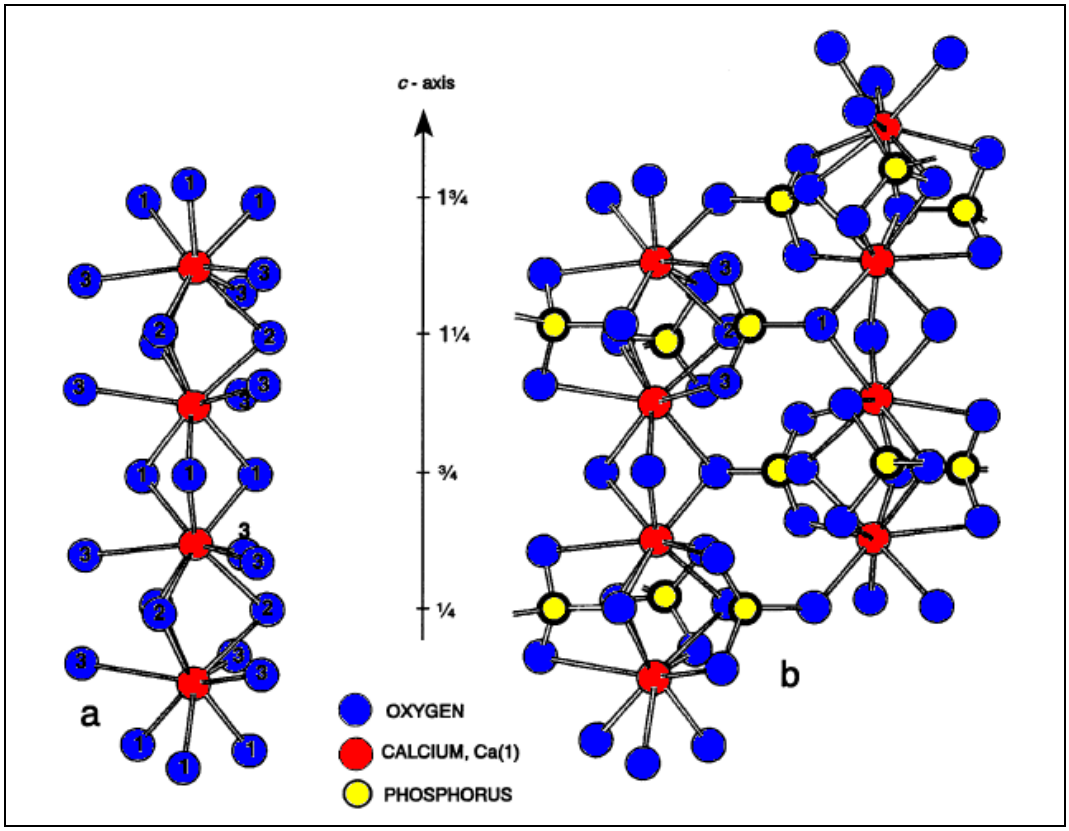

Figure 2.4: Structure of Hydroxyapatite. Adapted from [40]

This commonly accepted $P6_3/m$ structure is usually associated with non-stoichiometric HA containing impurities. A hexagonal $P6_3$ structure has been suggested for stoichiometric HA [44]. This structure gives a poor least squares fit to XRD diffraction and thus its acceptance is limited. Two monoclinic models have also been suggested, P21/b [45] and P21 [46]. These have been found to give a better fit to diffraction patterns and also to be more energetically favourable models of the structure of HA [46].

2.2.3 Biological HA

Biological HA, such as that present in bones and teeth, contains many impurities. This is because the apatite structure is a very hospitable one, allowing the substitutions of many other ions. Biological HA is typically calcium deficient and carbonate substituted. The minor elements associated with biological apatites are magnesium (Mg^{2+}), carbonate (CO_3^{2-}), sodium (Na^+), chloride (Cl^-), potassium (K^+), fluoride (F^-), and acid phosphate (HPO_4). Trace elements include strontium (Sr^{2+}), barium (Ba^{2+}), and lead (Pb^{2+}). The compositions of bone and synthetic HA are compared in *table 2.3*.

Table 2.3: Comparison of bone and hydroxyapatite ceramics (adapted from [47]**)**

Constituents (wt%)	*Bone*	*HA*
Ca	24.5	39.6
P	11.5	18.5
Ca/P ratio	1.65	1.67
Na	0.7	Trace
K	0.03	Trace
Mg	0.55	Trace
CO_3^{2-}	5.8	-

The biocompatibility of synthetic HA is not only suggested by its similar composition to that of biological HA but also by results of in vivo implantation, which has produced no local and systemic toxicity, no inflammation, and no foreign body response [48]. Studies confirming the biocompatibility of HA include those completed by Ducheyne et al. [18], Ducheyne and Qiu [49] and Buma et al. [50].

2.2.4 Dissolution Properties

The rate of in vitro dissolution of HA depends on the composition and crystallinity of the HA. Factors such as the Ca/P ratio, impurities like F^- or Mg^{2+}, the degree of micro- and macro- porosities, defect structure and the amount and type of other phases all have significant effects on biodegradation. The rate of

dissolution is also dependent on the type and concentration of the surrounding solution, the pH of the solution, the degree of saturation of the solution, the solid/solution ratio and the length of suspension in the solution.

Klein et al. [48] report that there are only two calcium phosphate materials that are stable at room temperature when in contact with aqueous solutions, and it is the pH of the solution that determines which one is stable [48]. At a pH lower than 4.2, dicalcium phosphate (DCP) is the most stable, while at higher pH, greater than 4.2, hydroxyapatite (HA) is the stable phase [36, 48]. The solubility of various calcium phosphates in an aqueous solution is shown in *figure 2.5*.

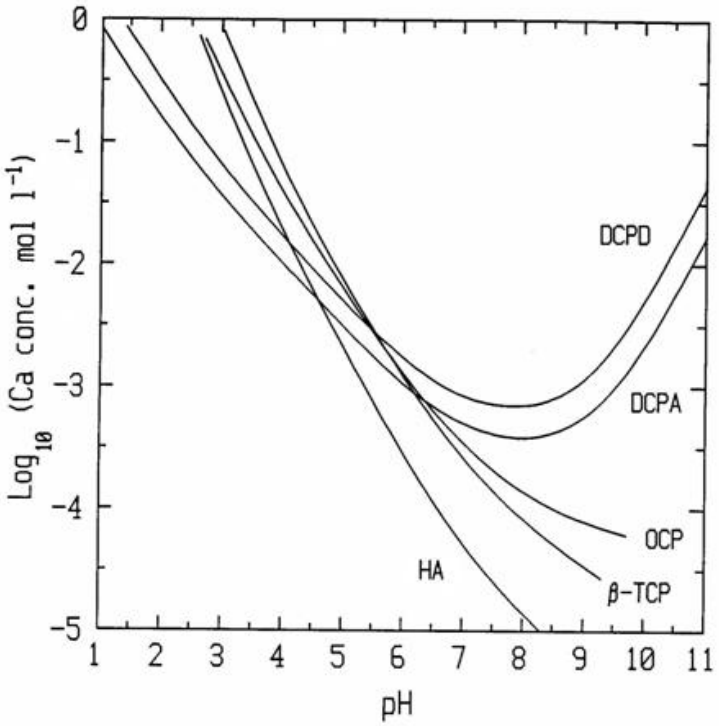

Figure 2.5: Solubility Isotherms of various calcium phosphate phases [51]

The pH of the physiological environment is 7.4. As can be seen from *figure 2.5* that crystalline HA (HA) is stable at these conditions, whereas β-tricalcium phosphate (β-TCP), Octocalcium Phosphate (OCP), Dicalcium Phosphate Anhydrous (DCPA) and Dicalcium Phosphate Dihydrate (DCPD) are less stable. Amorphous calcium phosphate (ACP) is also less stable than crystalline HA at physiological conditions [39]. Decomposition phases, such as calcium oxide (CaO), α-tricalcium phosphate (α-TCP), β-tricalcium phosphate (β-TCP),

oxyhydroxyapatite (OHA) and oxyapatite (OH), are all less stable *in vivo* than HA. The order of dissolution is as follows in the physiological environment is given in *equation 2.1* [39, 52].

$$CaO >> ACP > \alpha\text{-}TCP > \beta\text{-}TCP >> OHA/OA >> HA \qquad \textit{(eqn. 2.1)}$$

The mechanism of degradation of calcium phosphate in the body is unclear. Some researchers, such as Yamada et al. [53], Nagano et al. [24] and de Groot [54], believe that the process is a physio-chemical one, in which particles are ingested by osteoclast-like cells attached to the surface and that intracellular dissolution of these particles occurs. The dissolution process is known to be initiated at dislocations and grain boundary structures [27]. Incoherent grain boundaries, without lattice continuity, are more sensitive to dissolution than semi-coherent grain boundaries [55].

The dissolution of unstable phases in the coating is undesirable because it leads to the reduction in the mechanical strength of the coating. However, these dissolved phases have been shown to enhance bone tissue growth [18, 21]. Studies by both Ducheyne et al. [18] and Porter et al. [21] have reported this affect. Ducheyne et al. [18] compared the performance of three different calcium phosphate coatings (poly(lactic acid)/calcium deficient HA, calcium deficient HA and oxyhydroxyapatite/α-TCP/β-TCP) with an uncoated implant in vivo. The calcium phosphate coated implants were seen to allow a greater degree of bone growth than the uncoated implant. Of the three coatings the oxyhydroxyapatite/α-TCP/β-TCP coating performed better than the other two.

Porter et al. [21] compared the in vivo behaviour of a HA coating with a crystallinity of 70 ± 5 % with an annealed coating with a crystallinity of 92 ± 1 %. The non-annealed coating demonstrated the precipitation of plate-like biological apatite crystallites adjacent to the coating after 3 hours. Similar bone growth type behaviour was not seen in the vicinity of the annealed coating (more crystalline) until a time point of 10 days.

2.2.5 Thermal Behaviour

The plasma spray process involves high temperatures; the plasma flame temperature can be as high as 16,600°C depending on the application involved [56]. When the hydroxyapatite powder particles experience the high flame temperature, thermal decomposition occurs, changing the balance of phases in each particle. This leads to HA coatings with significantly different crystal structure, phase composition and morphology than the original starting powder. The changes occurring within the plasma flame need to be understood in order to ensure that the coating produced has the required composition.

Processes involved in the thermal decomposition of HA

It is widely accepted that the heating of HA leads to three processes, 1) evaporation of water, 2) dehydroxylation and 3) decomposition.

Evaporation of water

Hydroxyapatite easily absorbs water. This water can be present both on the surface of the powder and trapped within pores [57]. When HA is heated at low temperatures the first change to occur is that absorbed water begins to evaporate.

Dehydroxylation

Water is also present as part of the HA lattice structure. At higher temperatures, dehydroxylation occurs where hydroxyapatite gradually looses its hydroxyl (OH^-) group. The dehydroxylation reaction occurs as two steps following the reactions in *equation 2.2* and *equation 2.3* [52, 58, 59].

$$Ca_{10}(PO_4)_6(OH)_2 \rightarrow Ca_{10}(PO_4)_6(OH)_{2-2x}O_x\square_x + xH_2O \qquad \textit{(eqn. 2.2)}$$

(hydroxyapatite) → (oxyhydroxyapatite)

$$Ca_{10}(PO_4)_6(OH)_{2-2x}O_x\square_x \rightarrow Ca_{10}(PO_4)_6O_x\square_x + (1-x)H_2O \qquad \textit{(eqn. 2.3)}$$

(oxyhydroxyapatite) → (oxyapatite)

Where $\square$ is vacancy and $x < 1$

The first step involves the formation of a hydroxyl ion deficient product, known as oxyhydroxyapatite (OHA). OHA has a large number of vacancies in its structure, a bivalent oxygen ion and a vacancy substitute for two monovalent OH^- ions of HA [58]. Further, dehydroxlation leads to the formation of oxyapatite. Oxyhydroxyapatite and Oxyapatite readily retransform to hydroxyapatite in the presence of water [52].

Decomposition

For temperatures below a certain critical point, HA retains its crystal structure during dehydroxylation and rehydrates on cooling. However, once the critical point is exceeded, complete and irreversible dehydroxylation results. This process is called decomposition. Decomposition of HA leads to the formation of other calcium phosphate phases, such as β-tri-calcium phosphate (β-TCP) and tetra-calcium phosphate (TTCP). The reactions involved in decomposition are presented in *equation 2.4*, *equation 2.5* and *equation 2.6* [58, 60, 61]. Firstly, oxyapatite transforms to tri-calcium phosphate, tri-calcium phosphate and tetracalcium phosphate both transform into calcium oxide.

$Ca_{10}(PO_4)_6O_{x}\square_{x} \rightarrow \ 2Ca_3(PO_4)_2\,(\beta) + Ca_4(PO_4)_2O$ *(eqn. 2.4)*

(oxyapatite) $\rightarrow$ (tricalcium phosphate) + (tetracalcium phosphate)

$Ca_3(PO_4)_2 \rightarrow \ 3CaO + P_2O_5$ *(eqn. 2.5)*

(tricalcium phosphate) → (calcium oxide) + (phosphorus pentoxide)

$Ca_4(PO_4)_2O \rightarrow \ 4CaO + P_2O_5$ *(eqn. 2.6)*

(tetracalcium phosphate) → (calcium oxide) + (phosphorus pentoxide)

Effect of crystal structure and atmospheric conditions

The stoichiometry of the HA powder and the partial pressure of water in the surrounding atmosphere have been found to have the greatest effect on the phases formed when HA powder is heated. The consequences of changing these factors have been investigated in a number of studies [58, 62, 63].

The effect of stoichiometry on the thermal stability of HA was shown by Fang et al. [62] from experiments in which HA powder samples with Ca/P ratios of 1.52 to 1.67 or 1.68 were heated to 1100°C. The results show that powder with a Ca/P ratio of 1.52 decomposed to TCP, powder with a Ca/P ratio of 1.67 decomposed to TCP and HA, and no decomposition for powder with a Ca/P ratio of 1.68. This clearly illustrates that the stoichiometry is one of the key factors that controls the thermal stability of HA. Tampieri et al. [64] also showed that stoichiometric HA endures thermal treatments at significantly higher temperatures in respect to non-stoichiometric HA.

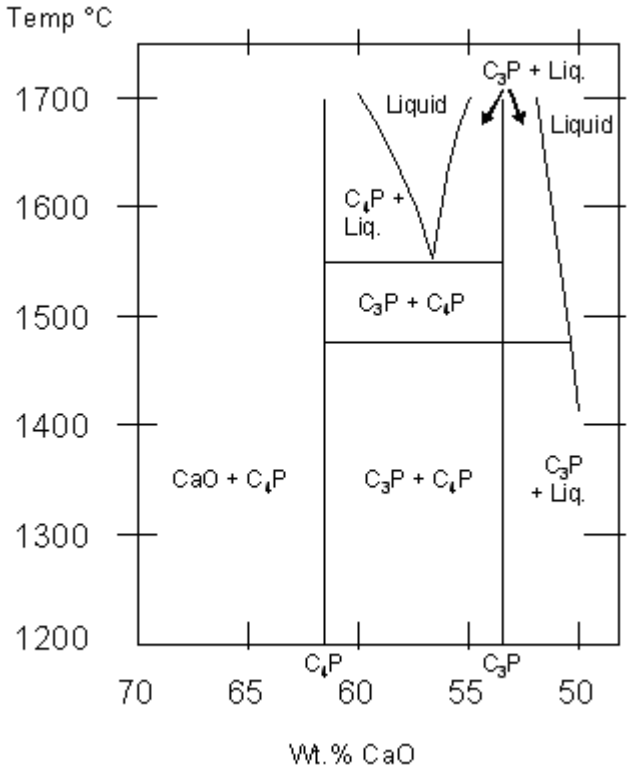

Figure 2.6: Phase diagram of the system $CaO-P_2O_5$ at high temperature. No water present. Adapted from [48]

The phase diagrams shown in *figure 2.6* and *figure 2.7* describe the thermal behaviour of $CaO-P_2O_5$ system at high temperatures in environments both with and without the presence of water vapour. *Figure 2.6* shows the system when no water vapour is present. It can be seen from the diagram that hydroxyapatite is not stable under these conditions but various other calcium phosphates are, including

tetracalcium phosphate (C_4P), tricalcium phosphate (C_3P), monetite (C_2P) and mixtures of calcium oxide (CaO) and C_4P.

Figure 2.7 shows the system at a partial water pressure of 500 mmHg. Under these conditions HA is found to be stable up to a maximum temperature of 1550°C. If the Ca/P ratio is not exactly equal to 10/6, other calcium phosphates are stable at this temperature, such as CaO or C_4P. The diagrams illustrate the importance of both the presence of water and Ca/P ratio in the determination of the stable phases.

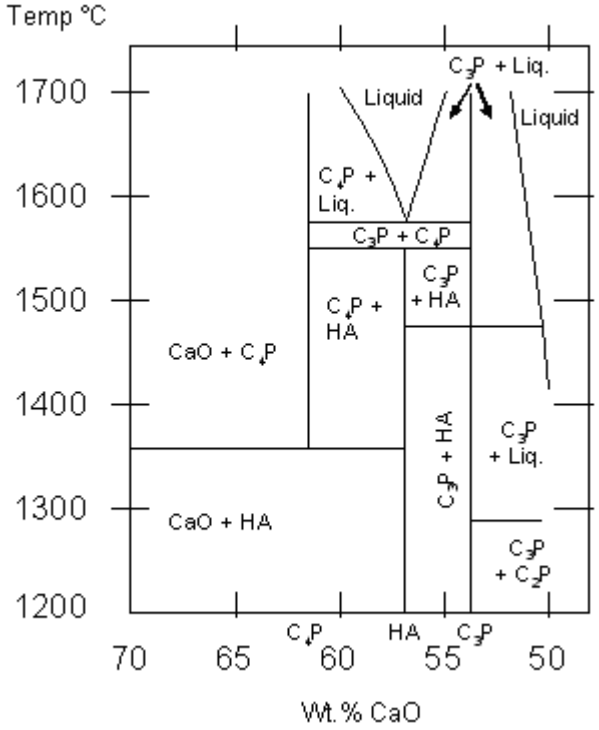

Figure 2.7: Phase diagram of the system CaO-P_2-O_5 at high temperature. Water vapour P H_2O = 500 mmHg. Adapted from [48]

It can be concluded that in order to avoid the dehydroxylation and decomposition of HA during plasma spraying a highly stable, crystalline, stoichiometric HA powder should be used. The environmental conditions can have a large effect on the process and need to be carefully controlled. Spraying in an atmosphere containing water vapour could also be beneficial in controlling the stability of HA during spraying.

Temperature effects on HA

Although there is agreement between researchers about the processes which occur during the thermal decomposition of HA, it is difficult to predict the exact temperatures at which these reactions occur. This is because the reactions do not occur instantly but over a wide temperature range, which depends on a number of factors relating to both the environment and the composition of the HA in question. Researchers have used several techniques, such as Thermogravimetric Analysis (TGA) [60, 64], Differential Thermal Analysis (DTA) [63, 65], X-Ray Diffraction (XRD) [57], and Fourier Transform Infrared Spectroscopy (FTIR) [57], in order to determine the effects of temperature on HA.

The evaporation of water from hydroxyapatite has been reported to occur within a wide temperature range, between about 25°C and 600°C [58, 60, 63, 64]. The total weight loss of absorbed water is reported to be as high as 6.5 wt.% [60]. The temperature ranges in which reactions occur as HA is heated from room temperature to 1730°C are summarised in *table 2.4*.

Table 2.4: Thermal effects on Hydroxyapatite

Temperature	***Reactions***
25 – 600ºC	Evaporation of absorbed water
600 – 800ºC	Decarbonation
800 – 900ºC	Dehydroxylation of HA forming partially dehydroxylated (OHA) or completely dehydroxylated oxyapatite (OA)
1050 – 1400ºC	HA decomposes to form β-TCP and TTCP
< 1120ºC	β-TCP is stable
1120 -1470ºC	β-TCP is converted to α-TCP
1550ºC	Melting temperature of HA
1630ºC	Melting temperature of TTCP, leaving behind CaO
1730ºC	Melting of TCP

2.3 Production of Hydroxyapatite Coatings

2.3.1 Coating Production Techniques

HA has good biocompatibility but poor bending strength and fracture toughness. It is therefore unsuitable for use in load bearing applications, such as the complex physiological loading conditions which occur at the hip joint. It is for this reason that HA is applied as a coating on a stronger substrate, such as a metal, which can provide higher strength and fatigue resistance.

A number of different methods have been used for the production of hydroxyapatite coatings. Thermal spraying techniques, such as plasma spraying, have been used for HA coating production for many years. More recently techniques such as physical vapour deposition (PVD) techniques, chemical vapour deposition (CVD) and electrophoretic deposition (EPD) have been investigated.

Thermal Spraying

The thermal spraying process involves passing the deposition material, in this case HA powder, through a heating zone where it is melted. The molten particles are then propelled towards the substrate where they are deposited to form a coating. The history of thermal spraying dates back to the late 1800's. After filing several patents in 1882 and 1899, in 1911 M.U. Schoop in Switzerland started to apply tin and lead coatings to metal surfaces by flame spraying to enhance corrosion performance [66]. He continued to develop the process with patents in 1911, [67], and 1912, [68]. There are now many different thermal spray processes. Those most important in the production of hydroxyapatite coatings are the plasma spray process, the High Velocity Oxy-Fuel (HVOF) process and Detonation-Gun spraying (D-Gun).

The Plasma Spray Process

Plasma spraying is currently the only FDA approved method for the production of HA coatings. The first industrial plasma spray guns appeared in the 1960's [69]. Advances since then include changes in spray gun and spray nozzle design. High Pressure Plasma Spray and Vacuum Plasma Spray systems have also been

introduced. The introduction of robotisation in the 1980's was another important technological advance.

The thermal energy in the plasma spray process is provided by a high energy plasma that is formed within the plasma gun. The spray gun consists of a cathode (electrode) and an anode (nozzle) separated by a small gap. A DC current is supplied to the cathode. This then arcs across to the anode creating an electric arc. An ionising gas, such as argon, helium, hydrogen or nitrogen, is fed into the arc where it becomes ionised and forms a plasma flame. In some cases a mixture of gases are used. The gas becomes excited to high energy levels and forms a plasma. The plasma that is formed is unstable and it recombines to form a gas again, releasing a large amount of thermal energy. A schematic of the spray gun is shown in *figure 2.8*. The process is discussed in more detail in *Section 2.4*.

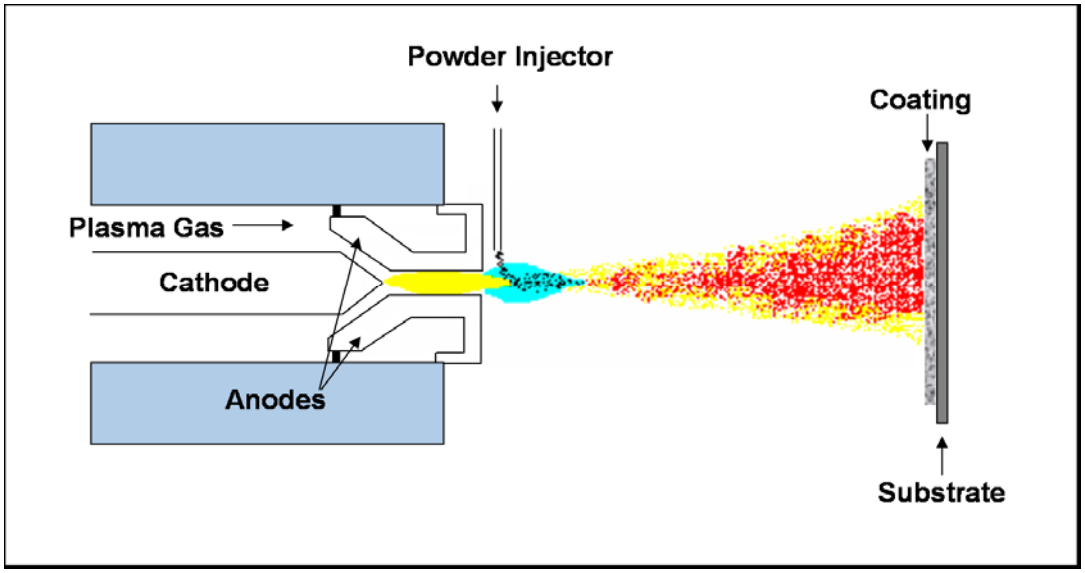

Figure 2.8: Atmospheric Plasma Spraying

Vacuum Plasma Spraying (VPS), also known as low pressure plasma spraying (LPPS), has recently been used for the production of HA coatings [70, 71]. The process consists of a conventional plasma spraying system enclosed in a vacuum tank which provides an inert atmosphere for the gun and work piece. The pressure in the chamber is generally in the range of 50-100 mBar [47]. In a vacuum the plasma jet velocity can be much higher, reaching speeds of up to three times the speed of sound [47].

Other Thermal Spray Processes

Other thermal spray processes that have been recently investigated for the production of HA coatings include High Velocity Oxy-Fuel (HVOF) [72, 73] and Detonation-Gun Spraying (D-gun) [70, 71, 74]. In the HVOF process a high velocity jet is produced by burning a fuel with oxygen at a high pressure. The fuel gases which can be used include acetylene, kerosene, propane, propylene and hydrogen [75]. During spraying the flame can reach temperatures of 3000°C [47], which is lower than the temperatures achievable in other techniques, such as plasma spraying. Further optimisation of this process is necessary before this process would be suitable for commercial use.

The Detonation-Gun process was developed by Poorman et al. in the early 1950's [75]. The term detonation refers to a very rapid combustion in which the flame front moves at supersonic velocities. In operation oxygen mixed with acetylene or propane/butane is fed into the barrel together with the powder. The gas is ignited by a spark and the detonation wave accelerates the powder up to speeds of about 750 m/s. The high kinetic energy of the hot powder particles on impact with the substrate result in a build up of a very dense and strong coating [76].

Studies by Gledhill et al. [70, 71, 74] have investigated the properties of HA coatings produced using the D-Gun process. The in vitro fatigue behaviour and the microstructural properties of HA coatings produced using the D-Gun process was found to compare favourably with coatings produced using other coating techniques. One disadvantage of this technique is that the coating is laid down by a process of rapid bursts of deposition rather than a process of progressive build up of layers, which results in extremely irregular coating thickness.

Other Coating Deposition Techniques

Other techniques that have been investigated for the production of calcium phosphate coatings include the Physical Vapour Deposition (PVD) technique, the Chemical Vapour Deposition process and the electrophoretic deposition technique.

The physical vapour deposition technique involves bombarding a target material with a high energy ion beam within a vacuum. This results in atom sized particles of the material being sputtered onto a metallic substrate, which is also placed in the vacuum chamber, to form a coating. The stages involved in PVD are 1) synthesis of the material to be deposited, 2) transport of the vapour from the source to the substrate, and 3) condensation of the vapour, nucleation and growth of the coating [77].

Many physical vapour deposition techniques have been developed in recent years. These include Radio Frequency Magnetron Sputtering, Ion Beam Assisted Deposition (IBAD), Ion Beam Deposition (IBD), Ion Beam Mixing (IBM) and techniques that are based on plasma-assisted ion implantation such as Plasma Source Ion Implantation (PSII) and Plasma Immersion Ion Implantation (PIII). One disadvantage common to all physical vapour deposition techniques is that the deposition rate is very slow, and for this reason, these systems have been used very little in the preparation of calcium phosphate coatings [47].

The typical HA coatings formed using PVD techniques are amorphous [78]. This is because the sputtered components (Ca, P, O and H) do not possess enough energy to recombine into crystalline HA. It is possible to create coatings with excellent adherence and smoothness [78, 79]. However, as they are so thin, a thickness of 638 nm was reported by Kim et al. [80], their durability in vivo is questionable [81, 82]. Variations in chemical composition of the coatings are brought about in the deposition process, such as distortion of the phosphate lattice, loss of hydroxyl groups, and the incorporation of CO_3^{2-}.

The chemical vapour deposition (CVD) process involves the nucleation and growth of a coating through chemical reactions involved in the gases immediately above the substrate. The process is carried out in a vacuum, at high temperatures, usually about 1000°C. The rate of coating deposition can be maintained by controlling the chemical potential (concentration) of reaction gases. Generally, the rate of deposition and the temperature of deposition determine the reaction kinetics and rates at which the decomposition products can crystallise on the reaction surface [83].

Few researchers have attempted to use the CVD process for the deposition of hydroxyapatite coatings. One of the first studies was carried out by Darr et al. [84], where the metal organic chemical vapour deposition process was used to deposit HA onto Ti6Al4V substrates using volatile monomeric (liquid) complexes.

The Electrophoretic Deposition technique involves the suspension of HA particles in isopropanol or other suitable organic liquid. An electric current is then passed through the suspension causing the migration of charged particles towards the counter charged electrode, resulting in deposition. The particles are deposited with minimal change to their original phase. The size of the particles to be deposited by the electrophoresis is important, particularly since the particles must be fine enough to remain in suspension during the coating process [85]. The rate of particle deposition and the thickness of the coating depend on the electric field strength [47]. The pH, ionic strength and viscosity of the solution also affect the properties of coating formed [86]. Electrophoresis can produce coatings with thicknesses up to 500 μm [85], however, producion of thick coatings takes a long time.

Many researchers, including Wang et al. [86] and Stoch et al. [85], have investigated the use of electrophoretic deposition for the production for HA coatings. Problems encountered include difficulties forming a uniform coating [86] and poor mechanical properties [82]. As the process does not bond the individual particles together, high temperature sintering (850°C – 950°C) of the initial coating at high vacuum (10^{-6} or 10^{-7} Torr), is required [81].

2.3.2 Substrate Preparation for Plasma Spraying

The materials used for hip implants need to be strong under fatigue loading, and must also be biocompatible. Those currently used include titanium and its alloys, particularly Ti-6Al-4V, cobalt chromium, (CoCr) and stainless steel, generally 316L. Ti-6Al-4V is the most commonly used [87]. The use of vanadium as an alloying element in materials use for biomedical applications has been questioned

because of its toxicity. Occasionally such metal ions have been detected in tissues close to the titanium implants [87]. Nevertheless, no evidence of detrimental effects has been traced to the use of Ti-6Al-4V in implants [87].

Substrate surface condition significantly affects bond strength of thermal spray coatings. The surface finish, texture and topography are of particular importance. Impurities or grease on the surface of the substrate will greatly reduce the coating adhesion and may cause cracking or delamination. In most cases an oxide-free substrate surface is also required. The most important step in substrate preparation is surface roughening, as it greatly improves the adhesion of the thermally sprayed coating.

A number of different surface roughening techniques have been used by researchers. These include macro-roughening, chemical etching and grit blasting. Macro-roughening involves making changes on a macro scale to the substrate surface, such as cutting groves or turning screw threads. This technique is sometimes used instead of grit blasting or in some cases it is carried out along with grit blasting. Chemical etching involves immersing the substrate in a chemical prior to spraying. It is not used very often outside research laboratories. Grit blasting is the standard surface roughening technique for spraying applications.

Grit Blasting

The grit blasting process involves propelling irregular grit particles at the surface of the substrate at high velocity. The angularity of the grit physically removes the material from the surface of the substrate [77]. The principal grit blasting parameters are listed in the *table 2.5*. During the blasting process some of the grit particles become embedded in the surface. For this reason, the grit must be of a material which does not have any adverse effects on the quality of the coating, or affect the biocompatibility of the coating. The most commonly used grit for grit blasting titanium implants is pure white alumina, Al_2O_3 [88, 89].

The grit blasting angle used will affect the number of particles embedded in the surface of the material, the profile of the indentation and the surface roughness achieved. The optimal blasting angle (angle between the surface of the substrate and the nozzle axis) was found by Amada and Hirose [88] to be 75°. At this angle both the fractal dimensions and coating adhesion were at a maximum.

Table 2.5: Grit blasting parameters [75]

Process Part	*Parameters*
Grit	Material, grain size, hardness
Blasted Substrate	Elastic modulus, thickness, hardness
Grit Feed Principle	Suction, gravitational
Blasting Atmosphere	Cabinet blasting, open-air blasting
Blasting Technique	Blasting time, blasting angle, blasting distance

After grit blasting it is necessary to remove any remaining grit particles from the substrate. Air blasting is often used to remove embedded particles following grit blasting [90], however, Yankee et al. [91] found that 5 minutes ultrasonic cleaning was more effective at removing residual grit from the substrate material than blasting with high pressure air.

The choice of grit size depends on the thickness of the piece to be sprayed, and also on the desired surface roughness. Fine grit and low blasting pressure is recommended for thinner pieces and coarser grit for a rougher surface. A surface roughness of approximately 3 μm has been found by Yang and Chang [92] to be sufficient to produce high adhesion strengths for HA coatings.

2.3.3 Hydroxyapatite Powder

The composition and crystallinity of HA powder are very important characteristics. The ASTM Standard Specification (ASTM Designation: F1185-88, [93]) states that ceramic HA for surgical implants has to have a minimum HA

content of 95 %, established by a quantitative X-ray diffraction analysis, while the concentration of trace elements should be limited to the values shown in *table 2.6*. The HA phase is required by the International Standards Institute (ISO 13778-1: 2000, Implants for surgery, Hydroxyapatite – Part 1: Ceramic hydroxyapatite [94]) to have a crystallinity of at least 45%. The maximum allowable total limit of all heavy metals is 50 ppm. The Ca/P ratio for HA used for surgical implants must be between 1.65 and 1.82 [93].

Table 2.6: Limits to Concentrations of Trace Elements

Elements	*ppm. max*
Arsenic (As)	3
Cadium (Cd)	5
Mercury (Hg)	5
Lead (Pb)	30

The shape and microstructure of HA powders also affect the quality of coatings. The morphology of the powder particles relates directly to the rate of heating experienced in the plasma flame. Irregularly shaped particles have a greater surface area to volume ratio than spherical particles, which results in a greater degree of particle heating within the plasma flame [77]. Spherical particles also have better flow properties than angular particles.

Powder with a narrow range of particle size will result in a more consistent coating. The particles must also be capable of withstanding the spraying environment. Cheang and Khor [95] observed that weakly agglomerated HA powders fragment within the plasma stream giving a new distribution of smaller particles.

2.4 The Plasma Spray Process

2.4.1 Plasma Arc Formation

Plasma is a complicated phenomenon. It is often referred to as the 'Fourth State of Matter' [96], as it differs from solid, liquid and gaseous states, and does not obey

the classical physical and thermodynamic laws. Plasmas are used in many different processing techniques, for example for the modification and activation of surfaces. There is currently much research being carried out into understanding them and controlling them.

As outlined in *Section 2.3.1*, the heating affect in the plasma spray process is provided by a plasma generated within the plasma gun. Plasmas are formed by adding energy to a gas. In the plasma spray gun, a high current is used to produce an electric arc and the gas is passed through this arc to form the plasma.

The actual processes involved in plasma formation are complicated. All gases at a nonzero absolute temperature contain some charged particles, electrons and ions, along with some neutral gas atoms. The charged particles only substantially affect the properties of the gas at concentrations where the space charge formed by the particles is large enough to restrict their motion. Dissociation and ionisation of the gas leads to the appearance of free electric charge carriers. As the charge concentration increases, the restriction on particle motion becomes more and more stringent and, at sufficiently high concentrations, the interaction of positively and negatively charged particles results in persistent macroscopic neutrality within the whole gas. Any disturbance of the macroscopic neutrality induces strong electric fields, which quickly restore it. The gas is thus termed quasi-neutral. This means the density of electrons plus the density of negative ions will be equal to the density of positively charged ions [96]. An ionised gas at such concentrations is called a plasma. This term was proposed in 1923 by the American physicist Langmuir [97].

Due to the nature of plasmas, when selecting gases for plasma formation, it is necessary to choose gases that are easily ionised and dissociated. It is also necessary to protect the electrodes from oxidation. The four main gases which are used are argon, helium, hydrogen and nitrogen. Both argon and helium are monatomic gases and hydrogen and nitrogen are diatomic gases. Monatomic gases need only to be ionised to enter the plasma state. Diatomic gases must first be dissociated and thus need a larger energy to enter the plasma state, resulting in a plasma flame with higher thermal conductivity than monatomic plasma flame

[98]. Adding small quantities of nitrogen or hydrogen to argon leads to increased plasma enthalpy. This increases the heat transfer rates from the plasma to the powder particles and promotes the melting of the powder particles.

As discussed in *Section 2.3.1*, a plasma spray gun consists of a nozzle, which is the anode, and an electrode, the cathode. The cathode is made of thoriated (2%) tungsten and the anode of high purity copper. A recirculated cooling system prevents the gun components from overheating during spraying and thus increases component life. The plasma flame is produced by passing a plasma gas through an electric arc created between the nozzle and electrode within the plasma gun. The arc is formed between the tip of the cathode and the wall of the anode. The arc continually fluctuates in length and position due to drag forces of gas flowing in the gun and magneto-hydrodynamic forces [69]. This arc fluctuation can lead to a certain degree of voltage fluctuation.

The plasma flame has a very high velocity and can reach temperatures of up to 16,600°C [56]. Particle velocities as high as 2300 m/s have been reported by Fauchais [69]. The high velocity of the plasma flame creates vortex rings that coalesce and result in large scale eddies which entrain cold surrounding gas bubbles [69]. Over time electrical erosion of the nozzle leads to voltage drop drastically affects the heat and momentum transferred to particles [69]. The condition of the nozzle must therefore be monitored.

2.4.2 Coating Build-up

Coating Formation

In the plasma spraying process the powder particles are fed into the plasma flame by the plasma carrier gas. As they travel within the flame, being propelled towards the substrate, the high temperatures cause them to begin to melt. The degree of particle melting that occurs depends on the amount of heat to which the particles are exposed. This depends on the heat content in the plasma flame, the location of the particles within the flame, the velocity of the particles and the particle size. When particles impact on the substrate they may be fully-molten,

semi-molten or solid and thus within the flame they may be solid, liquid, vapour or a combination of all three phases. The possible phase compositions of particles as they pass through the plasma flame are shown in the diagram *figure 2.9*.

During the plasma spraying of HA coatings, it is likely that powder particles exhibiting many of these different states would be present within the flame. Particles are melted to a greater or lesser extent depending on their individual size, shape and density. The greater the variation between the particles within a batch of powder the greater the degree of variability in particle melting.

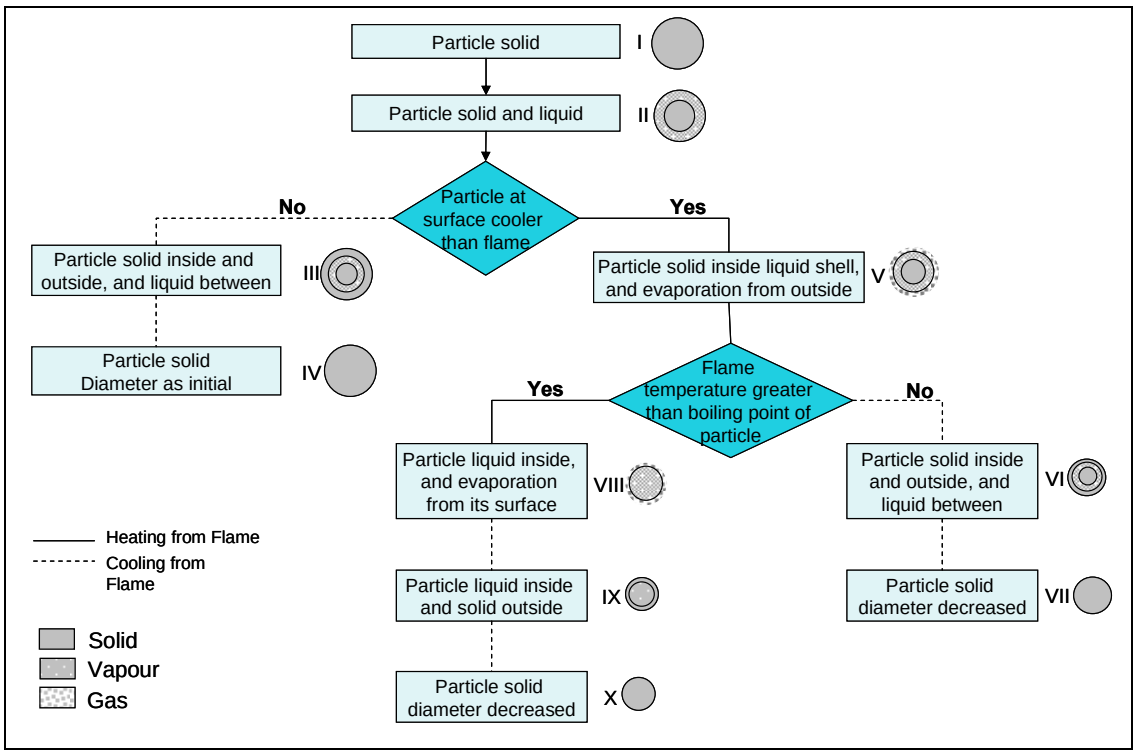

Figure 2.9: Phenomena occurring as particles pass through the plasma flame [Adapted from [75]**]**

From *figure 2.9* it can be seen that when the outer layer of a particle is melted (liquid phase) if the temperature of the flame is cooler than the surface of the particle, the outer layer will begin to solidify again (III). If the flame temperature is greater than that of the surface of the particle, evaporation of the liquid phase will start to occur, causing the diameter of the particle to decrease (V).

As discussed in *Section 2.2.5*, HA powder is readily transformed into other phases when exposed to high temperatures. *Figure 2.10* shows the phases that would be present for particle at stage V in *figure 2.9*.

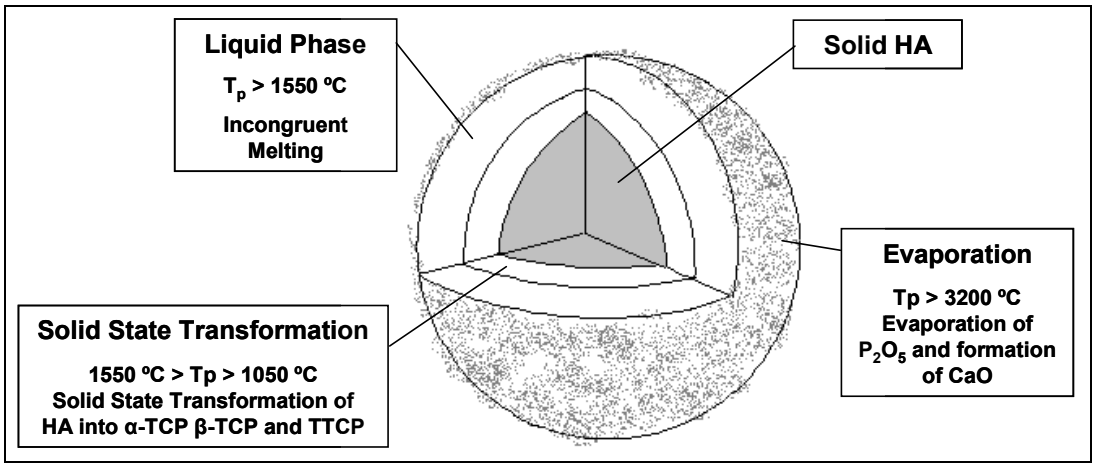

Figure 2.10: Transformations inside a plasma particle prior to Impact [Adapted from Dyshlovenko et al. [99]**]**

Microstructure of the Coating

When a partially-molten particle comes into contact with the substrate two processes occur, deformation and solidification. Deformation is the first process to occur and it is due to the pressures generated when the particles impinges on the substrate. Firstly the particle begins to deform from its initial spherical shape to form a cylinder. The time of deformation from sphere to cylinder was estimated by Kudinov and Houben as 10^{-10} -10^{-9} s [75]. The cylinder then expands in the radial direction.

The degree of deformation, and thus the shape of the particles, is dependent on a number of properties, such as the viscosity and wettability of the molten particles, the condition of the cooling of the particles, the powder granularity and the surface morphology of surface. After deformation is complete, solidification begins. The solidification process typically begins at the interface between the particles and the substrate (or previously deposited layer), as this interface acts as a heat sink.

The solidified particles are called lamella or splats. The particle solidification time for hydroxyapatite has been suggested to be as short as 10^{-7} to 10^{-6} s [100], depending on the thermal conductivity of the materials involved and also the thickness of any previously deposited lamellae on which they impact. The temperature of the substrate is affected by the heat transferred from both the plasma flame and also the droplets impacting on it. It can be in excess of 1000°C, depending on the spray parameters used [33].

The particles flatten, cool down and solidify so rapidly that the next impinging particulates hit already solidified splats or lamellae [101]. Successively impacting particles cause lamella to build-up, forming the coating. One pass of the plasma gun generally produces a coating layer about 5 -15 lamellae thick. Once a layer has been applied to the whole substrate the gun returns to the initial position and another layer is applied. Between the depositions, reactions between the surface of the deposited layer and the surrounding environment may occur, such as absorption of water or oxidation. Cooling of the layer also occurs. The number of layers applied depends on the required coating thickness.

Lamella Morphology

The lamella may exhibit one of two principle morphologies: 1) 'pancake' or 2) 'flower', as shown in *figure 2.11*. Particle size, velocity and temperature have been recognised as the plasma spray conditions that have the greatest influence on splat formation [102]. The properties of the substrate or previously deposited layer also effect lamella formation.

Yankee and Pletka [102] investigated the effect of different plasma gas flow rates, percentage of secondary gas, plasma/particle velocity and plasma/particle temperature on splat characteristics. They used a parameter called the Madejski parameter, ξ_m, to provide a numerical indication of the degree of droplet spreading. The Madejski parameter is defined as the ratio of splat diameter to initial droplet diameter. The results showed that the splat size was inversely proportional to the plasma velocity, with smaller droplets being formed at high plasma velocities. This was thought to be due to the shorter residence time of the

HA particles in the flame leading to less superheating in the droplets. The largest splats observed were produced under conditions of relatively low plasma velocity.

The morphology of the splats in this study was seen to depend on the temperature of the plasma. Hotter plasma conditions produced splats of 'pancake' rather than 'flower' morphology. The formation of the arms of the 'flower' splats was thought to depend on the viscosity of the molten particle. The appearance of splat arms indicates that solidification occurred after the effects of surface tension became dominant over viscous flow forces. The size and mass of the particles were also seen to influence the splat characteristics, larger particles being more likely to create splats of flower morphology. A variety of splats can be obtained within the one spraying operation. This is because the particles, due to their different size and injection velocity distribution, experience different trajectories and thus different thermal and momentum histories [101].

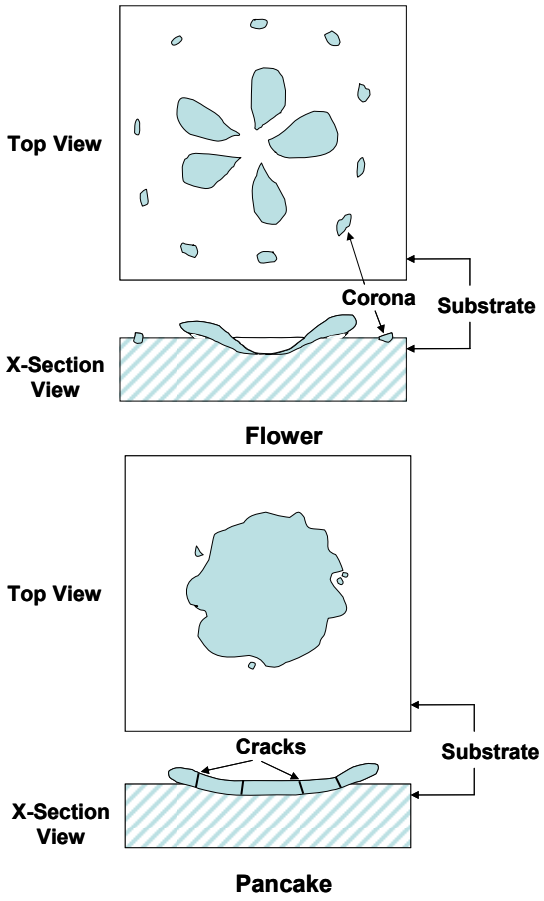

Figure 2.11: Splat Morphologies [Adapted from [75]**]**

Ultrastructure of the Coating

The microstructure of a coating relates to the individual splat level, the ultrastructure, however, relates to a level smaller than this, the grain level. Examination of the ultrastructure of a coating looks at the crystals that are formed during recrystallisation. The size and structure of the crystals formed depends on the phenomena occurring inside each newly generated coating layer. Factors such as spraying technique, powder grain size, sprayed material properties and also the material, roughness and temperature of the substrate all affect the form of the solidified grains. In addition, microstructural features such as pores, cracks and splat boundaries also influence the coating quality.

During solidification the crystals often grow in one preferential direction within the lamellae. In general, two types of lamellae are formed, either columnar or fine-grained equiaxed, (sometimes referred to as brick-wall) [75]. In columnar lamellae the crystals grow perpendicular to the substrate surface. Fine-grained equiaxed crystals grow parallel to the surface. These crystal structures are shown in the *figure 2.12*.

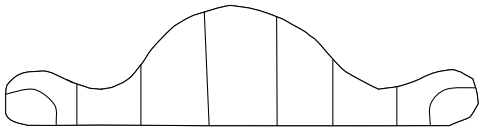

Columnar

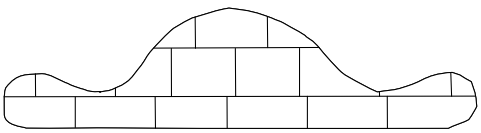

Fine-grained Equiaxed

Figure 2.12: Possible ultrastructures of the lamellae resulting from their solidification [Adapted from [75]**]**

The dimensions of the crystals in the thermally sprayed coatings vary between a few and a few hundred nanometers [75]. The ultrastructure is generally columnar if the coating cools and solidifies rapidly. A fine-grained equiaxed microstructure results when the heat removal rate at the interface is low [75]. If the rate of heat

removal is very high, the coating may solidify before any crystals can be formed. Higher amorphous phase content at high cooling rates has been reported by Wong et al. [100].

Yankee and Pletka [103] found that in HA coatings the grain size and phase stability varied as a function of the deposit thickness. Crystallite size of the initial layers is very small, as fast cooling and rapid solidification restrict crystal growth. The slower cooling rates towards the outer layers allows for the growth of larger crystals. Thus in a "bulk" HA coating gradients (from the lower to the upper surfaces) of several ultrastructural features may be exhibited, including grain size, grain orientation, and phases present.

2.4.3 Process Parameters

Introduction

The quality of plasma coatings is controlled by as many as 50 process parameters [104]. These parameters relate to various parts of the spraying process. The major parts being the powder, the powder injector, the plasma gun, the plasma flame itself and the substrate. The main process parameters of interest are shown in the *figure 2.13*.

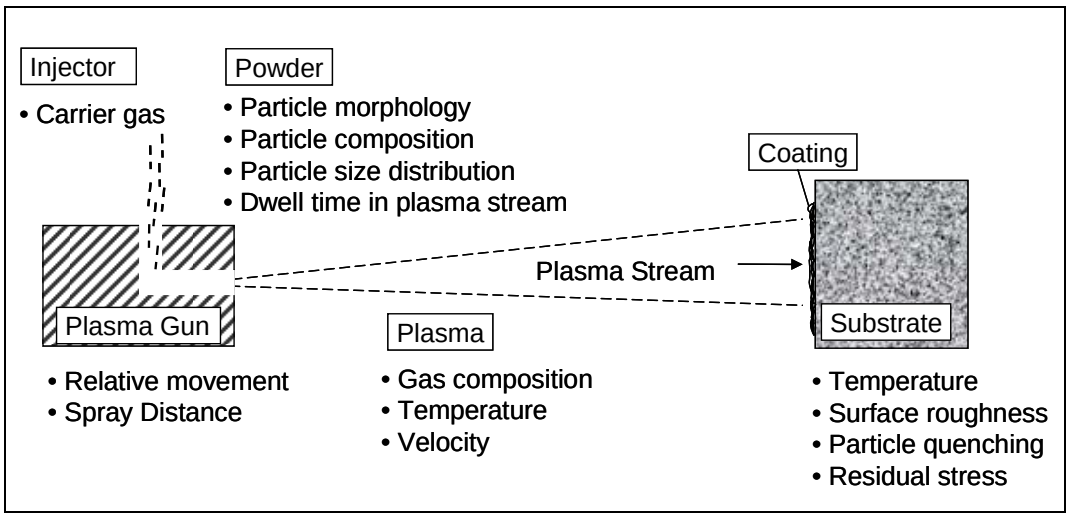

Figure 2.13: Plasma spraying process parameters

Parameters can be split into primary and secondary parameters. Primary parameters are those that can be controlled directly by the user. Secondary parameters cannot be directly controlled and instead depend on the primary parameters. Because of various economic reasons (such as time requirements) and theoretical reasons (such as parameter interdependence), it is not possible to control all possible parameter variations. In fact only eight to twelve parameters are routinely controlled at pre-set levels [66]. The most important primary and secondary parameters are listed in the *table 2.7*.

Table 2.7: Primary and Secondary Parameters

Primary Parameters	***Secondary Parameter***
Powder Particle Morphology	Plasma Flame Temperature
Powder Particle Composition	Plasma Flame Velocity
Powder Injection Angle	Dwell Time in Plasma Flame
Plasma Forming Gas	Particle Velocity
Plasma Forming Gas Flow Rate	Particle Melting
Current	Substrate Temperature
Power	Particle Quench Rate
Carrier Gas	Residual Stress Development
Carrier Gas Flow Rate	Coating Thickness
Spray Distance	
Substrate Material	
Substrate Surface Properties	
Substrate Pre-Heating	
Traverse Velocity	
Number of Passes of the Plasma Gun	

Understanding the effects of the process parameters on these two properties is necessary in order to understand the thermal history of sprayed particles. The key parameters in the plasma spray process are discussed in detail in the following sections.

Plasma Power Level

Depending on the design of the individual spray system, the current, voltage or power level can be adjusted. Studies are thus reported using all three parameters. Power is equal to current multiplied by voltage and so current is proportional to power. Typical Current values that are used for spraying HA coatings range from 350 A [105] to 1000 A [106].

The affect of power on the temperature of the plasma flame has been investigated by Cizek et al. [107] and Guessama et al. [108]. Both studies found that high current or power level caused an increase in particle temperature and velocity. Cizek et al. [107] used the 'SprayWatch' temperature and velocity measurement system to show that high power levels result in an increased flame temperature which causes a greater degree of particle melting. Increasing the power level was also found to cause an increase in the velocity of the plasma flame. A net power increase of 10 kW was seen to cause an increase of 80 ºC in particle temperature and an increase of 60 ms^{-1} in particle velocity.

Guessama et al. [108] used a two-colour pyrometry analyser to measure the in-flight particle characteristics alumina particles during plasma spraying. In the study a particle temperature increase from 230 ± 272 ºC to 263 ± 168 ºC was measured with an increase in current from 350 to 750 A. A velocity increase from 221 ± 34 ms^{-1} to 324 ± 46 ms^{-1} was observed over this range.

The effect of power and current on hydroxyapatite coatings was studied by Tsui et al. [90], Quek et al. [106], Sun et al. [109] and Yang et al. [110]. Increased power or current was found to lead to a decrease in the purity and crystallinity of HA coatings by Tsui et al. [90] and Sun et al. [109]. The findings of Yang et al. [110] contradicted those of Tsui et al. [90] and Sun et al. [109], with crystallinity being found to increase with increasing spray current. Tsui et al. [90] also reported that the porosity level and extent of microcracking decreased with increasing power level. The findings of Quek et al. [106] were in agreement with a well splatted, less porous coating resulting when spraying at high current.

Plasma Forming Gases

The selection of the plasma forming gas affects the properties of the plasma flame. The four main gases which are used are argon, helium, hydrogen and nitrogen. Argon has many advantages as a plasma gas. It is relatively cheap, easily ionised and is inert thus protecting the powder particles and electrodes within the plasma gun from the environment [77]. Argon is used as the primary gas in most plasma-spraying units [77, 82].

Helium is an expensive gas and produces a high temperature plasma and low enthalpy and density, and is only used in special cases. Using hydrogen as the plasma gas leads to the production of a plasma that has a greater thermal content than helium or argon. However, it has been found to be unsuitable for the plasma spraying of niobium, zirconia or titanium as it leads to embrittlement [77]. The hazardous nature of hydrogen requires special handling as it can be explosive in the presence of an ignition source. It is thus necessary to check pipe work for leaks which can lead to a build-up of hydrogen in the working atmosphere.

Nitrogen is a cheap gas but has the potential to react with the sprayed material. For this reason it is not suitable for the spraying of some materials such as some carbides [77]. Nitrogen, even when mixed with argon, greatly reduces the life of the electrodes due to the aggressive environment it produces in the plasma.

Nitrogen or hydrogen are diatomic gases and thus result in a plasma jet with higher thermal conductivity than monatomic plasma jets. Their addition, in small quantities, to argon leads to increased plasma enthalpy. This increases the heat transfer rates from the plasma to the powder particles and promotes the melting of the powder particles [77]. Fauchais [69] reports an increase from 600 m/s to 2200 m/s in the velocity of an argon plasma flame with the addition of H_2.

Leung et al. [98] studied the effects of different gases on the plasma jet and on the resultant coating. It was found that the size and shape of the jet, the momentum that the carrier gas imparts on the powder particles and the trajectory of these particles all vary depending on the gases used. The study found that the length of

the jet with just helium as the carrier gas did not change much compared to when no carrier gas was used, but the jet length when argon and nitrogen carrier gases were used decreased noticeably. Helium was found to contribute to the volume of the plasma and increase the width of the plasma jet. However, as more helium was added, the helium began to quench the plasma.

Guessasma et al. [108] and Cizek et al. [107] report that the increasing the gas flow rate used during spraying leads to an increase in particle velocity. Guessasma et al. [108] reported that increasing the gas flow rate from 30 to 50 standard litres per minute (SLPM) resulted in an increase in the average particle velocity from 186 to 269 ms^{-1} and also a slight increase in particle temperature from 2516 ± 131 ºC to 2526 ± 203 ºC. Cizek et al. [107] report no significant change in particle temperature with an increase in gas flow rate.

Powder Particle Size

The size of the powder particles affects their melting characteristics within the plasma flame. Large particles are reported to undergo a lesser degree of melting in the plasma flame than small particles [95, 111]. Cheang and Khor [95] found that larger particles above 55µm were crystalline and showed little or no melting during plasma spraying. Particles from 55 to 30 µm were partially melted and had mixtures of crystalline and amorphous phases. Particles less than 30 µm were fully melted and contained large amounts of amorphous phases and also traces of CaO.

Kweh et al. [111] found similar results, reporting that coating properties deteriorated with increasing particle size. The study found that SHA (spheroidised feedstock HA) 20 - 45 µm particles produced a much denser lamellar coating than 45 - 75 and 75 - 125 µm SHA coatings [111]. Larger particle sizes, 45 - 75 and 75 - 125 µm, possess numerous unmelted particles, cavities and macropores, whereas in the 20 - 45 µm coating, there is little or no significant indication of the presence of cavities and a flatter smoother surface profile as a result of neatly stacked disc-like splats is observed. Good interlamellar contact and minute amount of unmelted

particles with the absence of macropores in the SHA 20 - 45 μm coating led to an improvement in the mechanical strength and properties of the coating.

The size of particles also affects the velocities as they travel at within the plasma flame [69]. Small particles can reach their maximum velocity quicker than larger particles. On impact with the substrate smaller particles solidify more quickly than larger ones. The choice of particle size is limited because of the momentum that has to be given to particles for their penetration within the plasma jet. When the particle size is decreased, the carrier gas velocity has to be increased drastically (proportional to the negative third power of the particle diameter). For particles below 5-10 μm, the carrier gas flow rate has been found to drastically disturb the plasma jet [69].

In order to have uniform particle melting, it is important that the powder selected has a narrow particle size distribution. A ratio in diameter of 2 can correspond to a ratio of mass of 8 which means that the particles will undergo quite different particle melting in the flame [69].

It has been suggested that in the ideal situation only a thin outer surface layer of a powder particle should become molten during the plasma spraying process [112]. This allows adhesion of the particle to the substrate but prevents the complete phase transformation of the particle that would occur if the particle was fully molten.

Powder Carrier Gas

The carrier gas carries the powder into the plasma gun. When selecting the powder carrier gas it is necessary to consider the chemical reactivity of the powder being used, an inert gas will prevent chemical changes in the powder particles. The velocity of the powder carrier gas is also important, particularly when the powder injector is radial to the plasma flame. In this case the initial momentum that the carrier gas imparts determines where powder particles will enter the plasma jet. The centre of the plasma jet is the hottest part of the plasma, possesses the highest plasma velocity and is the most viscous portion of the

plasma. In a radial injected plasma gun, the powder particles are forced into the plasma flame perpendicular to the direction of the flame Therefore, the particles can only pass through the hottest part of the plasma and attain their maximum velocity by being pushed through to the centre of the jet.

If the carrier gas flow rate is too high, disturbance will be caused to the plasma flame. The ideal carrier gas flow rate would inject particles into the plasma jet at a momentum similar to that of the plasma jet. The path followed by powder particles at different carrier gas flow rates is shown in *figure 2.14.*

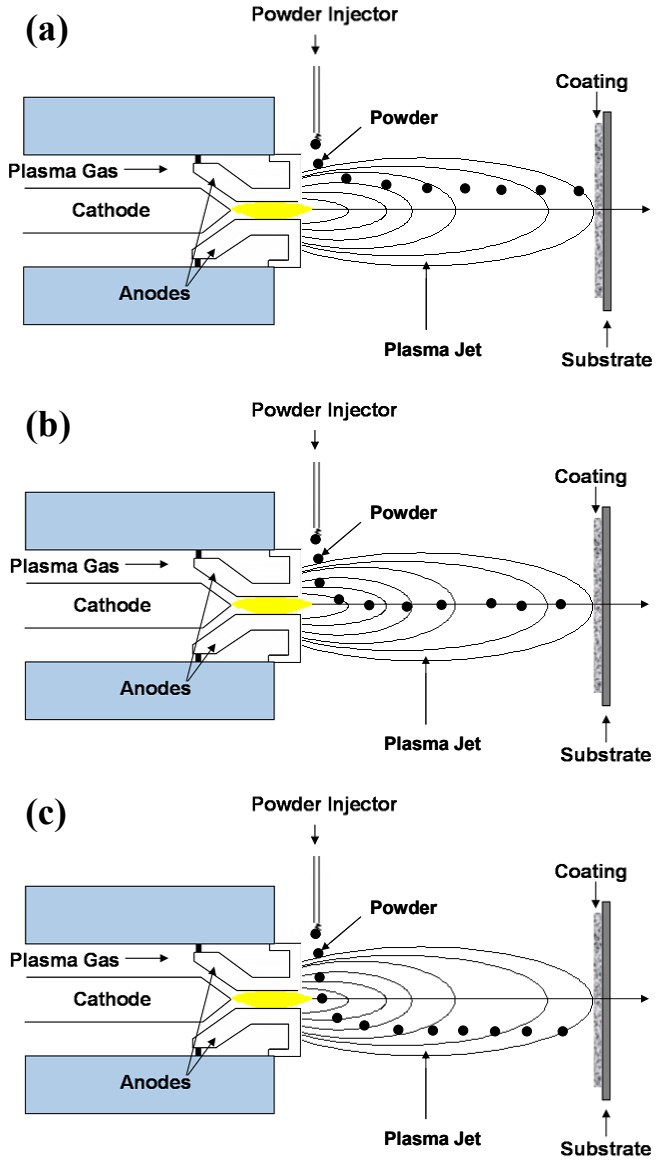

Figure 2.14: Carrier Gas Flow Rate a) too low b) correct c) too high

The choice of powder carrier gas also affects the flow of particles into the plasma jet. Argon is most commonly used as the carrier gas [82]. Leung et al. [98] found that nitrogen has a gas momentum value that is 37% greater than that of argon, and for helium it was 10% less than it was for argon for the flow rates used. The nitrogen carrier gas, which had the highest momentum, achieved the highest radial distance between the particles trajectory centre and the torch axis. It also seemed to be the least influenced by the swirl motion of the plasma jet, whereas particles carried by helium were found to be highly influenced by the vortex flow.

Cizek et al. [107] found that powder feed rate has little affect on the temperature and velocity of the plasma flame. Mawdsley et al. [113] reported that carrier gas flow rate had an effect on the thickness of plasma sprayed coatings, with high carrier gas flow rates found to increase coating thickness.

Powder Feed Rate

The rate at which powder is fed into the plasma flame has two main effects. Firstly, it affects the coating thickness; increasing the quantity of particles increases the thickness of the coating. This then influences the coating cooling characteristics and thus particle solidification and residual stress development. Secondly, the feed rate affects the temperature of the plasma flame; introducing a greater number of particles into the flame reduces its temperature. According to Cizek et al. [107] the effect of powder feed rate on the velocity and temperature of the plasma flame is small.

Spray Distance

The spray distance, also called the stand-off distance (SOD), is the distance between the spray gun and the work piece. The SOD affects the final coating in a number of ways. It affects the length of time that the particles are exposed to the heating effect of the plasma flame and thus the degree of particle melting that occurs. The velocity at which the particles impinge on the substrate is also influenced by the SOD. A longer SOD may cause a reduction in the velocity of the droplets during spraying due to the frictional forces from air molecules [109].

The SOD also affects the temperature of the substrate and the coating that has been deposited there. A shorter SOD will mean that the substrate experiences more of the heating effects of the plasma flame and thus is maintained at a higher temperature. This allows recrystallisation of the sprayed coating to occur. A greater SOD will mean that the substrate experiences less of the heating effects from the flame, thus the sprayed particles will solidify quickly and a more amorphous coating will result.

The effect of spray distance on HA coatings has been investigated by a number of researchers [109, 111, 114]. Kweh et al. [111] found that coating properties deteriorated with increasing spray distance. Coatings sprayed at distances between 10 and 14 cm were investigated and it was found that there was an increasing amount of porosities and unmelted particles with non-uniform deposition in coatings sprayed at larger spray distances (12 and 14 cm). The amount of unmelted particles was greater in coatings sprayed at 12 and 14 cm than in coatings sprayed at 10 cm. The coating with the best mechanical properties resulted at a spray distance of 10 cm.

Sun et al. [109] studied the effects of varying the spray distance from 80 mm to 160 mm. It was found that the crystallinity and hydroxyl contents of HA coatings decreased with increasing spray distance.. Longer spray distances were seen to cause increased particle melting, lower porosity and a greater number of microcracks. The results disagreed with the finding by Kweh et al. that better mechanical properties resulted a high spray distances [111]. This can be explained by the fact that the spray distances used here were greater than those used by Kweh et al.

Lu et al. [114] investigated spray distances of 80, 120, 160 and 200 mm. The findings of this study contradicted those of Sun et al. [109] as crystallinity was found to increase with increasing spray distance. Lu et al. [114] suggest that at longer spray distances the particles begin to cool and resolidify allowing a coating with increased crystallinity to be formed.

The change in the temperature and velocity of the particles themselves within the plasma flame has been investigated by Cizek et al. [107] using the camera based SprayWatch diagnostics system. Cizek et al. measured the change in temperature and velocity as the spray distance is increased from 50 to 150 mm. A decrease in particle temperature of 220 ºC and a decrease in velocity of 90 ms^{-1} was found over this range.

Plasma Gun Relative Movement

Movement of the plasma gun is necessary to deposit the coating over the surface of the substrate. The velocity at which the plasma gun travels determines the time between the deposition of each layer. Traverse speeds used for spraying vary greatly, values ranging from as low as 75 mm/s [115] and as high as 750 mm/s [106] have been reported. Slow speeds allow for more cooling between each layer deposition, whereas greater speeds reduce the level of cooling that occurs between each deposited layer. The speed selected also has an effect on recrystallisation and residual stress development. The velocity also affects the residence time of the plasma jet at a particular location, affecting the heating and thickness of layered splats but also the impact angle of the particles, which according to Fauchais [69] should be as close to 90º as possible in order to allow the best particle adhesion.

Summary

This section has highlighted the effects of various plasma spray process parameters on the resultant HA coatings. Evidence of process effect contradictions that exist within the literature has been highlighted. These contradictions emphasise the necessity for the use of multi factor process modelling, such as that carried out in this work, in order to obtain a better understanding of the process. The following section discusses techniques for the characterisation of HA coatings.

2.5 Properties of Hydroxyapatite Coatings

2.5.1 Coating Purity

The chemical composition of the final coating is dependent on the thermal decomposition occurring during spraying. As discussed in *Section 2.2.5*, the high temperatures experienced by HA powder particles in the plasma spraying process lead to the dehydroxylation and decomposition of the particles. At temperatures of above 800 ºC dehydroxylation of HA occurs, above 1050 ºC HA decomposes to β-TCP and TTCP and above 1120 ºC β-TCP is converted to α-TCP [52, 58, 59]. The phase composition of the final coating is thus dependent on the thermal history of the powder particles. A higher plasma flame temperature and the longer residence time of the particles within the flame leads to a greater degree of phase transformation.

The ISO standard specification (ISO 13779-2:2000) [116] states that the maximum allowable level of other non-HA phases in a HA coating is 5%. Control over the phase purity of HA coatings is important due to the differences in dissolution properties between the different calcium phosphate phases, as discussed in *Section 2.2.4*.

2.5.2 Coating Crystallinity

During plasma spraying, when the particles reach the substrate they are generally partially molten, consisting of a molten portion and an unmelted core. The molten portion may either recrystallise or be converted to the amorphous phase, depending on the cooling rate [109, 117]. The final coating thus contains the crystalline phase from the unmelted core and either recrystallised or amorphous phase from the molten portion of the particle. The crystallinity of a HA coating thus depends on the degree of melting of the powder particles within the plasma flame and on the particle cooling rate.

The coating crystallinity has been reported by Gross et al. [118] to be lower at the interface with the Ti substrate than at the surface of the coating. This is because titanium has a higher rate of thermal diffusivity than HA and thus the cooling rate

of the initial coating layers is faster. The thermal diffusivity of titanium is 8 x 10^{-2} cm^2/s and of HA is 5 x 10^{-3} cm^2/s [118]. A coating thickness of 20μm is reported to be necessary for recrystallisation of amorphous material to occur [117].

The amount of recrystallisation that occurs also depends the decomposition of HA within the plasma flame. As the HA structure is a complicated one, diffusion mobility and reconstruction of atoms is difficult [119]. Dehydroxylation, that is the loss of hydroxyl (OH^-) groups, during plasma spraying leads to lattice distortion and vacancies which makes the diffusion and reconstruction of atoms very difficult [109]. This effect causes the retention of the amorphous phase, with recrystallisation only occurring in hydroxyl rich areas within the coating [118, 119].

As discussed in *Section 2.2.4*, coatings that contain a high degree of crystallinity have lower dissolution rates and are thus more stable in vivo [39, 52]. Highly amorphous coatings dissolve more quickly leading to the rapid weakening and disintegration of the coating. However, it has been recognised that the amorphous HA content promotes beneficial physiological activity [28]. While moderately enhanced levels of Ca^{2+} and HPO_4^{2-} ions in the biofluid space at the implant-tissue interface have been seen to assist bone remodelling, excessive amounts of these ions cause an increase in the local pH and concurrent cytotoxic effects on bone cells [52].

Although, it is recognised that it is desirable for a HA coating to contain both amorphous and crystalline phases, the exact percentage of each phase required to produce the optimal in vivo response is not yet clear. The ISO standard specification (ISO 13779-2:2000) [116] states that in order for a HA coating to have sufficient mechanical properties in vivo the crystalline content should be greater than 45%. The crystallinity of HA coatings reported in literature varies greatly. Tsui et al. [115] report that a coating crystallinity of about 65-70% is common in HA coatings for biomedical use. Dalton and Cook [120] compared 4 different commercially available coatings and found crystallinity to vary between 57 and 61 %.

2.5.3 Coating Adhesion

Although it is well recognised that the coating adhesion is one of the most important parameters affecting the performance of an implant in vivo, the actual mechanisms involved are still not fully understood. Generally, the bottom surfaces of the lamellae are not in full contact with the substrate. The areas that are in contact are called the 'welding points' or 'active zones' [75]. The greater the contact area the better the adhesion of the coating will be. Researchers, such as Lacefield [82], believed that substrate to coating bonding was entirely mechanical. It is now recognised that a mechanical anchorage, physical interaction and chemical interaction are all involved in coating adhesion.

Mechanical anchorage is the main mechanism involved in coating adhesion. The levels achieved depend on the substrate surface roughness. The adhesion strength of a ceramic coating is in many cases a linear function of the average surface roughness [66]. Substrate preparation techniques, such as grit blasting, are used to increase roughness prior to spraying. The amount of mechanical anchorage achieved is reduced if a large amount of shrinkage occurs during solidification of the particles.

If there is close contact between the atoms of the lamella and the substrate forces, known as Van der Waals forces, may occur between the atoms. The surfaces must approach each other to reach the field of attraction of the atoms which is approximately 0.5 nm [75]. These forces contribute to the coating to substrate bonding. In order for them to be present, the surface must be clean and both materials should be in a higher energy state.

Diffusion and chemical reaction between the lamella and substrate also contribute to coating adhesion. Diffusion occurs mainly as a result of the presence of a high concentration of vacancies in rapidly solidified lamella [75]. According to Fick's law, diffusivity increases with increasing contact temperature [66]. Diffusive adhesion generally plays only a minor role in the overall coating adhesion as rapid cooling and solidification of the particles means that the diffusion depth is very small. The amount achieved can be increased by preheating the substrate.

Chemical adhesion results when a chemical compound forms between the coating and substrate.

According to ISO requirements (ISO 13779-2:2000) [116] the adhesion strength should not be less than 15 MPa. Ideally, the coating adhesion strength would be as high as possible. The adhesion strength of plasma sprayed a HA coating on a titanium substrate is generally about 28 MPa [121].

2.5.4 Cohesive Strength

The strength of plasma sprayed HA coatings depends on the cohesion between the individual particles of the coating. Coating strength has been recognised as one of the major areas of weakness within HA coatings. Yang et al. [121] observed that during adhesion testing coating failure tends to be partially cohesive (that is occurring within the coating) rather than just adhesive (that is at the implant coating-interface). The cohesive strength is dependent on a number of factors such as the porosity, the number of defects present and the coating thickness.

2.5.5 Porosity

Porosity is an inherent characteristic of all sprayed coating. Porosity in thermal spray coatings can be in the form of open pores, which are open to the atmosphere, and closed pores, present within the coating itself with no connection to the surface. The porosity required for HA coatings is unspecified by the Food and Drug Association (FDA), it is however an important parameter. According to Sun et al. [35] the porosity of commercially available HA coatings varies greatly and can be as high as 50%.

A porous coating allows greater penetration of bone cells and greater levels of cell attachment [122]. It also allows a greater degree of dissolution of the coating which, as has been discussed can have a positive influence on bone growth. However, increased porosity also negatively affects the mechanical properties of a coating. Denser coatings are reported to be at lower risk of bonding degradation, such as cracking, spalling and delamination, during in vivo contact with aggressive body fluids [52].

Dalton and Cook [120] compared four commercially available HA coated implants. Characterisation of the coatings showed that they all met FDA requirements. The implants were implanted into canines and the reduction in coating thickness was studied at 3, 6 and 12 weeks. Coating porosity varied to a greater extent, from 5 to 14%. This variation in porosity was found to have a large affect on the dissolution of the coatings, with the greatest degradation occurring for the coating with the largest porosity.

Pores can also be formed due to the liberation of oxygen, nitrogen and hydrogen as the temperature of the material decreases and the solubility of these materials reduces accordingly [77]. In some cases these gases can escape to the atmosphere, otherwise, they remain trapped within the coating.

2.5.6 Residual Stress

Residual stresses are the internal stresses existing in a component that is under no external load condition [123]. They are generated from inhomogeneouosly distributed non-elastic changes in dimensions. Residual stresses are inherently induced in any coating deposited by thermal spray methods because of the differences in the thermal properties between the coating and the substrate material. The process is also complicated by the differences between the thermal expansion coefficients of the various phases within the material of the coating and the different temperature ranges experienced by different regions of the component at different times during the process.

The presence of residual stresses leads to crack generation and flaking or peeling of the coating [124]. The parameters that affect residual stress generation include the plasma flame temperature, the sprayed particle properties, the substrate temperature, cooling effects. The coating thickness also affects the residual stress present. Adding a greater number of layers results in higher residual stresses.

Residual stress generation can be reduced by controlling the temperature of the substrate, for example by using a substrate preheat step. The pre-heat temperature

selected must be low enough so as not to adversely affect the substrate. Residual stress levels in plasma sprayed coatings on titanium of 44.2 MPa were reported by Yang et al. [121] and between about 18 and 41MPa by Tsui et al. [90].

2.5.7 Coating Thickness

The thickness of the final coating is dependent on the number of passes of the plasma gun, the amount of powder fed into the plasma flame and the deposition efficiency. Increasing the number of passes of the plasma gun causes the coating thickness to be increased. Higher powder feed rates also result in a thicker coating. Deposition efficiency tends to be decreased at high spray distances as unmelted portions of the particles may be deagglomerated and blown away before they impact on the substrate [109]. The morphology and degree of flattening of splats also affects the coating thickness.

Thick coatings remain in the body for longer times. They also provide better protection for the bone from metal-ion released from the substrate; however, they tend to be brittle and the presence of residual stresses in these thicker coatings leads to cracking. Thin coatings perform better mechanically; however, they provide less protection from metal-ion release and also dissolve quickly in vivo. Generally, HA coatings are between 50 μm and 200 μm in thickness [35].

2.5.8 Coating Roughness

Coating roughness gives a measure of the degree of particle melting within the plasma flame. A smoother coating generally implies that the particles reach a more fluid state within the plasma flame and thus are more viscous and can spread out to a greater degree on impact with the substrate [125]. The roughness of the coating is affected by the size of the particles used for plasma spraying.

Gross and Babovic [126], found that partially melted particles were not able to flatten on the coating surface giving rise to large undulations and thus higher coating roughness. HA powder particles with an average size of 20 to 30 μm were found to give a coating roughness of 4 to 6 μm.

The surface roughness of the HA coating affects osteoblast cell attachment and thus bone growth on the coating once it is implanted into the body. Whereas fibroblasts and epithelial cells prefer smoother surfaces, osteoblasts attach and proliferation better on rough surfaces [17, 127]. High surface roughness values also lead to a greater coating dissolution rate. The optimal value for coating roughness is still unclear.

2.6 Advances in Hydroxyapatite Coatings

A number of different approaches have been taken in order to produce HA coatings with superior characteristics. Techniques investigated include the use of post-spray treatments, bond layers, composite coatings and functionally graded coatings.

2.6.1 Post-Spray Treatments for HA Coatings

Plasma sprayed HA coatings tend to have a high amorphous content and to have high porosity levels. Post spray treatment processes can be used to improve these properties. Various post spray heat treatments have been investigated, including furnace heat treatment; in air [27, 115, 128-130] or vacuum [131], laser treatment [45, 132, 133] and hot isostatic pressing (HIPing) [87, 134]. These treatments can raise the crystallinity and purity of the HA coatings, with removal of the non-HA compounds, under suitable conditions [115, 129].

Tsui et al [115] found that heat treatment of 700 ºC for 1h was effective in increasing the degree of crystallinity, OH- ion content and purity, without promoting significant mechanical degradation. Tetra-calcium phosphate (TTCP), tri-calcium phosphate (TCP) and calcium oxide were still present after 1h at 600 °C, but had disappeared after 1h at 700 °C. Kweh et al report improvement in microhardness [111] and reduction of in vitro dissolution [135] of HA coatings after treatment for 1 hour at 800 °C.

Lu et al. [130] investigated the effect of treatment temperatures of 500 °C to 800 °C and treatment times of 2 to 6 hours. It was found that the post spray heat treatment temperature has a more important effect on the degree of recrystallisation of HA coatings than treatment time.

2.6.2 Bond Layers

Bond layers consist of an additional coating layer applied between the ceramic coating and the metal implant. The addition of a bond layer to the coating/implant system offers a number of advantages, primarily offering an improvement in the adhesion of the coating to the substrate. The coating also plays a role in improving substrate biocompatibility by reducing the release of metal ions. The bond layer can also reduce the thermal gradient at the coating/substrate interface and thus reduce the forces that give rise to cracking and delamination.

A number of different materials have been used as bond layers including, titania (TiO_2) [136, 137], zirconia (ZrO_2) [137, 138] and dicalcium silicate (C_2S) [137]. Kim et al. [136] found that the favourable chemical affinity of titania with respect to both HA and Ti, greatly contributed to the coating adhesion strength. In their study, titania bond layers were found by to improve the adhesion strength by as much as 60%. Kurzweg et al. [137] also confirmed the advantages of using a titania bond coat showing that adhesion strengths with a titania bond layer were twice the value of a HA coat without a bond coat.

Zirconia bond layers have been found by some authors to offer an improvement in bond strengths [137, 138]. Chou and Chang [138] found the bond strength to increase from 28.6 ± 3.2 to 36.2 ± 3.0 MPa. It was suggested however, that the rougher surface of the ZrO_2 bond coat may have been partly responsible for this improvement. Kurzweg et al. [137] investigated CaO-stabilised zirconia, ($CaOZrO_2$), and 73 mol% titania and 27 mol% non-stabilised zirconia (TiO_2+ZrO_2) bond layers. Adhesion test results for these materials showed that the use of the $CaOZrO_2$ bond layer resulted in lower adhesion strengths than the HA coating without a bond layer. The TiO_2+ZrO_2 bond layer improved adhesion

strength. The use of thin (10 – 50μm) dicalcium silicate (C_2S) bond layers was also reported to increase the adhesion strength of hydroxyapatite coatings [137].

2.6.3 Composite Coatings

Various materials have been added to HA to improve the final coating characteristics. These additives aim to enhance various properties of the coating, including bio-activity [55], thermal stability [64] and the mechanical properties of the coating [139].

Silicon is thought to play a critical role in the bone calcification process. Porter et al. [55] investigated the effects of adding silicate ions into HA coating. Ca, P and Si ions were reported to diffuse through the ceramic grains to the bone-HA interface, driven by a concentration gradient. The increased concentration of these ions at the HA-ceramics interface was seen to accelerate the precipitation of biological apatite and induced bone apposition at the surface of the ceramic.

Tampieri et al. [64] added calcium hydroxide ($Ca(OH_2)$) to HA to try to improve thermal stability of HA during firing treatments. The $Ca(OH_2)$ additions, compensated for Ca/P deviations, possibly restoring the correct stoichiometry, producing a positive effect in terms of phase stability up to very high sintering temperatures; practically no decomposition occurred up to 1450°C. The best results were obtained with additions around 2 wt% or 4 wt% depending on powder preparation.

The effects of adding yttria stabilised zirconia (YSZ) to HA coatings was investigated Fu et al. [139]. It was found to decrease the formation of CaO, tricalcium phosphate (TCP) and tetracalcium (TTCP) phosphate in the as-sprayed HA coatings. The dissolution rate of HA/YSZ is slower and bond strength is superior to that of HA coating without zirconia.

2.6.4 Functionally Graded Coatings

A functionally graded coating consists of many coating layers, all of which have different composition and thus functionality. For example a coating consisting of two materials, material A and material B, might have a high ratio of A to B for the initial layer with the amount reducing with each layer so that the final layer has a higher ratio of material B than material A. Functionally graded coatings that have been investigated include HA-glass [53], HA-titanium [140, 141] and fluorine-substituted apatite (FA) and β -tricalcium phosphate (β-TCP) [142].

Functionally graded coatings containing HA and glass were prepared by Yamada et al. [53]. The concentration of glass increased from the innermost to the outermost. The glass phase was found to improve adhesion of the coating to the titanium substrate. Chu et al. [141] designed a functionally graded coating consisting of HA and titanium. The titanium component improved the mechanical properties of the coating and also assisted in reducing the residual stresses in the final coating, as the thermal expansion coefficient was gradually increased from the substrate to the outer layer of the coating. Khor et al. [140] also produced HA-titanium functionally graded coatings. This research used the titanium alloy, Ti-6Al-4V and found improvements in microstructure, density, porosity, microhardness and Young's modulus.

Functionally graded coatings consisting of fluorine-substituted apatite (FA) and beta-tricalcium phosphate (β-TCP) were produced by Wong et al. [142]. The coating produced had four layers, the outermost layer containing FA + 50 wt% TCP, the next FA + 40 wt% TCP, + 30 wt% TCP and finally the innermost FA + 20 wt% TCP. The HA component of the coating is expected to enhance early-stage bone ingrowth and bone bonding, whereas the remaining porous FA component aims achieve long-term fixation of an implant.

2.6.5 Drug Release Coatings

Another area of recent advance is the use of drug releasing layers on HA coatings. These layers are designed to supply drugs, for example antibiotics and antiresorptive drugs, locally to the bone surrounding the implant. Drug releasing

layers have been produced from numerous different polymeric and ceramic materials. The benefits of these drug release coating layers have been shown by a number of researchers [143, 144]. Peter et al. [143] used the antiresorptive drug zoledronate grafted to a HA coated implant. In vivo studies in rats showed an increase in mechanical fixation of the implants. Martins et al. [144] found that their collagen-hydroxyapatite composite paste had potential for use in sustained antibiotic release.

2.7 Analysis of HA Coatings

In order to predict the behaviour of HA coatings in the body, they need to be characterised and the chemical composition and structural properties understood. In this section, the various characterisation techniques that are used for the analysis of HA coatings are introduced and discussed.

2.7.1 Phase Composition

The phase composition of HA coatings can be determined using a number of methods. The most commonly used are X-ray Diffraction and FTIR. Both methods can be used to determine the amorphous content of HA coatings and the quantity of other phases present.

X-Ray Diffraction

X-ray Diffraction (XRD) is one of the most important methods for determining the atomic arrangements in matter. It can be used to identify the phases present in samples and also to provide information on the physical state of the sample, such as grain size, texture and crystal perfection. It is a non-destructive technique and samples are acceptable in many forms, such as powder, single crystal, or flat polished crystalline materials.

In general, the use of X-ray Diffraction is restricted to crystalline materials, although some information may be obtained on amorphous solids and liquids. It is recommended as a technique for the verification of the phase composition of

plasma-sprayed HA coatings by the Food and Drug Administration (FDA) and required by ASTM F1185-88, "Standard Specification for Composition of Ceramic Hydroxyapatite for Surgical Implants" [93].

Diffraction is the change in direction and intensity of a group of waves that occurs after passing by an obstacle or through and aperture whose size is approximately the same as the wavelength of the waves. X-rays are a portion of the electromagnetic spectrum having wavelengths from 10^{-10} to 10^{-8} m, (1 to 100 Å) although only 0.3 to 2.5 Å is used for X-ray Diffraction [145]. They are produced by bombarding a metal with high energy electrons. Copper is typically used as the target because the Kα characteristic radiation is a useful wavelength, 1.5406 Å, and the target is easily cooled for high efficiency [145]. As x-ray wavelengths are in the order of magnitude of atomic dimensions, when a beam of x-rays impinges on a solid material, a portion of the beam will be scattered in all directions by the electrons associated with each atom or ion that lies within the beams path [146].

The specific phase relationships between two or more scattered waves affect the intensity of the resultant peaks. If the path length difference between two scattered waves is an integral number of wavelengths the scattered waves are still in phase and constructive interference occurs. This means that the waves mutually reinforce each other. If the waves are out of phase, interference or partial reinforcement may occur.

The condition required for constructive interference to occur is described by Bragg's law [145, 146]–

$$n\lambda = 2d_{hkl}\sin\theta \qquad \textit{(eqn. 2.7)}$$

where n is the small interger giving the order of reflection, λ is the x-ray wavelength, d_{hkl}, the interplanar spacing, is the magnitude of the distance between two adjacent and parallel planes of atoms, and θ is the grazing angle between the lattice plane and the incident ray. d_{hkl} is a function of the Miller

indices, (h, k and l), as well as the lattice parameters. For example, for a crystal structure having cubic symmetry –

$$d_{hkl} = \frac{a}{\sqrt{h^2 + k^2 + l^2}} \qquad \textit{(eqn. 2.8)}$$

where, a is the lattice parameter or unit cell edge length. If Bragg's law is satisfied high intensity peaks result, if it is not satisfied, then interference will be non-constructive in nature so as to yield a very low-intensity diffracted beam [146].
A crystalline material is a three-dimensionally periodic arrangement of atoms in space. The arrangement can be described by the unit cell, which is the basic repeating unit having all the fundamental properties of the crystal as a whole. The unit cell is always a parallelepiped and has typical edge dimensions of 3 to 20 Å for most inorganic solids [145]. The arrangement of atoms within the unit cell depends on the type of atoms, the nature of their bonds, and their tendency to minimise the free energy by a high degree of organisation.

The size, shape, symmetry and the arrangement of atoms in the unit cell can be determined by examining the diffraction pattern produced by the diffracted beams. The intensities of the beams are related to the types of atoms and their arrangement in the crystal. The sharpness of the diffracted beams is a measure of the crystallinity of the sample.

Phase identification using XRD is based on the unique pattern produced by every crystalline phase. The composition of a sample can therefore be determined by comparing the diffraction pattern with the compilation of standard patterns that have been developed for most known compounds by the Joint Committee of Powder Diffraction Society, (J.C.P.D.S.). The relevant J.C.P.D.S. standards for calcium phosphate materials are listed in *table 2.8*.

The XRD pattern for HA consists of a series of sharp peaks, the diffusion background and some additional peaks. The diffusion background represents the amorphous phase and sharp peaks represent the crystalline HA [117]. The tallest HA (211) peak is located at 31.8 ° 2θ. Amorphous HA can be found as a broad

hump between 28.9 and 34.2 º 2θ. Peak broadening can be caused by the presence of micro-stresses, disorder, stacking faults and dislocations within the sample [78].

Table 2.8: J.C.P.D.S Standards for Calcium Phosphate Materials

Elements	*Symbol*	*Formulae*	*Peak 2θ(º)*	*J.C.P.D.S*
Hydroxyapatite	HA	$Ca_{10}(PO_4)_6(OH)$	31.8	9-432
α-tricalcium phosphate	α-TCP	$\alpha\text{-}Ca_3(PO_4)_2$	30.8	9-348
β-tricalcium phosphate	β-TCP	$\beta\text{-}Ca_3(PO_4)_2$	31.1	9-169
Tetracalcium phosphate	TTCP	$Ca_4(PO_4)_2O$	29.8	25-1137
Calcium oxide	CaO	CaO	37.3	37-1497
Oxyapatite		$Ca_{10}(PO_4)_6O$	31.7	89-6495
Octacalcium phosphate	OCP	Ca_8H_2 (PO4) $6.5H_20$		26-1056
Dicalcium phosphate anhydrous	DCPA	$CaHPO_4$	30.2	9-80
Dicalcium phosphate dihydrate	DCPD	$CaHPO_4.2H_20$	20.9	9-77

Coating Crystallinity

There are three main methods currently used for the determination of the crystallinity of HA coatings using X-ray Diffraction. These are the Rutland Method, the Relative Intensity Method and the Rietveld Method. The Rutland Method is a commonly used accurate method for determining crystallinity [90, 109, 147]. The method involves comparing the total area under the diffraction pattern with the area of the amorphous region of the pattern. The % crystallinity is then determined using *equation 2.9*.

$$Crystallinity(\%) = \frac{\sum A_c}{\sum A_c + \sum A_a} x100 \qquad \textit{(eqn. 2.9)}$$

where $\sum A_c$ is the sum of the areas of all HA crystalline peaks and $\sum A_a$ is the sum of the area under the amorphous peak.

Diffraction scans can be carried out over the 20 to 40 º 2θ range or over the 20 to 60 º 2θ range. Using a range of 20 to 60 º 2θ allows the amorphous and impurity phases to be determined more accurately. Errors using this method can be due to incorrect determination of the amorphous area because of the presence of overlapping peaks in the HA diffraction pattern.

The Relative Intensity Method involves comparing the intensity of the maximum HA peak for the different XRD patterns. This is calculated using *equation 2.10*. A taller peak indicates a more crystalline material. This method has been used by researchers such as Kweh et al. [111] and Yang et al. [110]. The results are not considered to be as reliable as other methods.

$$Crystallinity(\%) = \frac{A_{[221]}}{As_{[221]}} x100 \qquad \textit{(eqn. 2.10)}$$

where $A_{[221]}$ is the integrated area intensity of the (221) peak of the HA coating and $As_{[221]}$ is the integrated area intensity of the (221) peak of a standard HA material.

The Rietveld method has been used by researchers such as Knowles et al. [148] and Rogers et al. [149]. The Rietveld method uses the least squares method to refine a curve profile until it matches that of the diffraction pattern for a particular material. It is especially useful if a pattern contains many over lapping peaks. The Reitveld method is more complex to carry out than the other methods and requires specific software for the analysis of XRD patterns.

Coating Purity

The purity of HA coatings can be compared by calculating the areas of all non-HA peaks that are found in the diffraction pattern. A measurement of this impurity area can be determined by calculating the area in the region where the tallest

peaks of impurity phases are present. The impurity peaks that would be expected to be present in HA coatings are those of TTCP, α-TCP and β-TCP. The tallest peaks of these phases fall between 29.8º 2θ and 31.1º 2θ. The % purity of a coating can then be calculated using *equation 2.11*.

$$Purity(\%) = \frac{\sum A_c - \sum A_i}{\sum A_c} x100 \qquad \textit{(eqn. 2.11)}$$

where $\sum A_c$ is the sum of the areas of all HA crystalline peaks and $\sum A_i$ is the sum of the area of the impurity peaks.

The Rietveld method can also be used to quantitatively determine the percentage of various impurity phases in HA coatings. Curve profiles can be fitted to the phases present and a quantitative measure of these phases can then be determined. This method is useful when large percentages of impurity phases are present.

There is still a considerable amount of disagreement among the research community about the best practice for determining the crystallinity and purity of HA coatings. There is little standardisation in testing methods and thus comparing crystallinity across the board is difficult. This problem is currently under review by the International Organization for Standardisation, who is drawing up an *International standard, ISO 13779-3, Implants for Surgery - Hydroxyapatite - Part 3: Chemical analysis and characterisation of crystallinity and phase*. The final version of this standard is not yet available.

2.7.2 Coating Porosity

The porosity of HA coatings is most commonly calculated from microscope images of the cross-section of the coated sample. The pore area fraction can be calculated manually by drawing a calibrated grid on the microscope image. *Equation 2.12* is then used to calculate the pore area fraction.

$$A = \frac{(x + x^1)}{y} \qquad \textit{(eqn. 2.12)}$$

where, A is the area fraction, x is the number of intersections of the grid that fall within a pore, x^1 is half the number of intersections of the grid that fall on a pore boundary, y is the total number of grid intersections in the field of view.

Image analysis software can be used to calculate the pore area fraction. This software allows pores in the coating to be highlighted and the pore fraction of the coating can then be calculated by the software. The BSI standard testing method for the determination of the porosity of ceramics coatings is outlined in DD ENV 1071-5:1995 [150].

2.7.3 Coating Microstructure

The microstructure of a coating can be examined using optical microscopy. An electron microscope can be used where magnifications higher than that of an optical microscope are required. In an electron microscope an image of a structure is formed using beams of electrons instead of light radiation. This beam of electrons travels in a wave-like manner, with its wavelength being inversely proportional to its velocity. Thus accelerating the beam to very high velocities can give very small wavelengths, in the order of 0.003 nm [146]. The smaller the wavelength used the better the resolution that can be achieved, however the resolution that is practically achievable is dependant on the sample type and profile of its surface. The most common electron microscopy techniques are scanning electron microscopy (SEM) and transmission electron microscopy (TEM).

An SEM image is created by scanning the surface of the sample with a beam of electrons. The beam excites the material of the specimen causing it to undergo a number of different interaction events with either the electrons or nuclei of the atoms of the sample. These interactions result in the emission of a variety of radiations, including secondary electrons, backscattered electrons and Auger electrons. These electron beams can be collected and then displayed on a screen.

The types of radiation of most interest are secondary electrons and backscattered electrons as they provide information about the surface topography of the sample.

The SEM is one of the most versatile instruments for investigating the morphology of materials, allowing a large range of magnification. One disadvantage, however, is that the surface of specimens to be viewed using the SEM must be electrically conducting. Unfortunately, HA is electrically non-conducting and may require the use of electrically conducting copper tape or may need to be coated with an electrically conducting material; carbon if chemical analysis is required or gold to enhance topographical contrast.

2.7.4 Surface Roughness

The surface profile of the substrate is an important parameter when producing plasma sprayed coatings. The roughness of the surface can be described using a number of different measures, for example R_a, R_q and R_{max}. In engineering applications, roughness is most often described by the parameter R_a (absolute roughness), defined occurring to *equation 2.13* [75]:

$$R_a = \frac{\int_0^l |y| dx}{l} \qquad \textit{(eqn. 2.13)}$$

The R_a parameter is the average distance between the surface of the coating and the mean line, as shown in the *figure 2.15*.

Surface profilometry methods can be contact, which for example may measure the surface roughness by running a needle over the surface, or non-contact methods, such as laser profilometry.

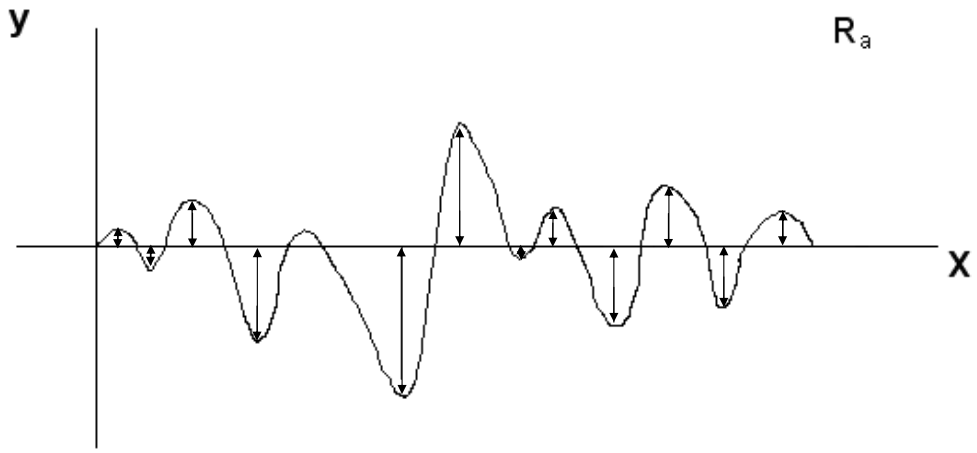

Figure 2.15: The R_a Parameter

2.7.5 In Vitro Analysis

In vitro studies are useful for predicting how well the coating will perform in vivo. Studies that have been carried out on bioceramic coatings range from monitoring the behaviour of a material when submersed in saline solution [74] or simulated body fluid [22, 135, 151], to evaluation using cell culture techniques [122, 152-155]. Cell culturing involves growing bone cells on the surface of the coating and evaluating changes in the cells over a specific period of time. Changes that can be monitored include changes in shape of the cells (cell morphology), the quantity of cells present (cell proliferation), and the number of cells that are living and dead (cell viability). Biochemical changes, such as the expression of different genes, within the cell can also be measured. These changes indicate the level of cell differentiation occurring, that is, how quickly the cells are becoming bone tissue.

Measuring the proliferation of cells gives us important information about how well these cells can grow on the coating in question. Differences in cell number do not directly indicate a change in cell growth, but can also indicate a difference in cell attachment, apoptosis or necrosis [122]. Cellular behaviour can be influenced by characteristics of the material, including chemistry, composition and topography and the absorption and release of compounds into the cell culture media (phosphate, calcium, magnesium, albumin)[122].

Measuring cell viability gives an indication as to how well the cells can survive on the material, indicating the cytotoxicity of the material. Examining changes in cell morphology indicates how well the cells interact with the material, different cells have different morphologies. For a coating to be successful it is necessary for the cells to not only grow but also differentiate into bone tissue. The differentiation of bone cells is marked by the expression of different genes. To get a true understanding as to the performance of a material these gene expression levels need to be measured.

Differential gene expression can be defined into three biological periods; cellular proliferation, cellular maturation and focal mineralisation [156]. There are a number of different genes expressed during these stages of differentiation. Three commonly examined genes examined are: type 1 collagen, alkaline phosphatase and osteocalcin. Type 1 collagen is the most abundant extracellular protein in bones [157]. It is expressed earliest, in the cellular proliferation stage. Alkaline phosphatase is a protein which is attached to the extracellular surface of the cell membrane [158]. It is expressed during in the osteoblast maturation stage. Osteocalcin is expressed latest, during the mineralisation stage.

Various different cells types are available for experimental work. These can be derived from numerous different sources most commonly mouse, rat or human bone. Examples of some of the most commonly used cell lines include the human osteoblast-like cells Saos-2 [122] and MG-63 [155] and rat osteoblast-like cells ROS and RCT-3. The patterns of behaviour of these bone cells have been found to correlate well to that of cells in bone tissue in vivo [159].

Cell culture studies have been used to evaluate numerous different biomaterials [122, 152, 154, 155]. Rouahi et al. [122] examined the growth of Saos-2 cells on discs of microporous and non-porous HA in comparison to titanium. The surface morphology was found to have an effect on the behaviour of the cells. Richard et al. [155] cultured cells on calcium-deficient hydroxyapatite thin films produced using electrodeposition. Areas of the coating with two different morphologies and compositions were examined and the results were compared to those for cells

cultured on cell culture plastic. In this study cell morphology, cell viability, cell proliferation and gene expression were examined over 28 days. The differentiation of osteoblast cells was found to be enhanced on the calcium phosphate coating compared to the titanium plate.

Yang et al. [152] reported that cell proliferation and type I collagen synthesis were higher on porous surfaces than on dense ones. This is related to greater protein absorption and to the increased surface area available for cell attachment.

Wang et al. [154] carried out a study to determine the effect of the phase composition of calcium phosphate ceramics on osteoblast behaviour. The compositions studied were pure HA, a 70/30 mixture of HA and TCP and a 35/65 mixture of HA and TCP and pure TCP. In this study, the phase composition of the ceramics did not have a significant affect on the expression of the osteocalcin, osteonectin and production of bone sialoprotein and osteocalcin in SaOS-2 cells.

2.8 Optimisation of Hydroxyapatite Coatings

2.8.1 Introduction

Demands for superior quality HA coatings have led to the need for a greater understanding of the scientific phenomena involved in their production. Studies of HA coatings have mainly followed the classical experiment model, varying one spray parameter at a time in order to gain a greater understanding of the process [77, 95, 106, 114]. Using this approach can give some information about the process; however, the understanding that can be gained is limited. Complicated process relationships, such as quadratic relationships and interaction effects can not be identified using the classical experimental approach. There is therefore a clear need for the use of more sophisticated and powerful statistical experimental methods. The benefits of this type of statistical experimentation have been demonstrated by other researchers in studies of plasma sprayed coatings of various other materials, such as zirconia [160], titanium nitride [161], alumina [113, 162, 163] and alumina-titania [104, 164]. Recently, researchers such as Dyshlovenko et al. [165, 166] and Cizek et al. [107] have begun to use statistical

experiments to investigate the complex relationships in plasma sprayed hydroxyapatite coatings. Clear relationships between the spray process parameters and resultant HA coatings have not yet been developed.

2.8.2 DOE Experiments

Statistical experiments vary factors simultaneously to obtain a maximum of information with a minimum number of experiments [66]. The statistical experiment approach is usually called Design of Experiment (DOE). This method is advantageous from an economic perspective as a large amount of information can be obtained from a minimal number of experiments. In the DOE technique, the parameters to be changed in the experiment are termed "factors" or "variables". The different possibilities for a factor are called the levels. Levels can be either qualitative or quantitative. The measured output from the experiment is termed the response. Once the experiment has been run, the effect of each factor can be evaluated by contrasting the average response when the factor was not changed with the average result when it was changed. Responses can then be represented as a polynomial regression equation of the following form:

$$Y = b_0 + \sum b_j X_j + \sum b_{ij} X_i X_j + \sum b_{ijk} X_i X_j X_k \qquad \textit{(eqn. 2.14)}$$

where i, j and k vary from 1 to the number of variables; coefficient b_0 is the mean of the responses of all the experiment; b_i coefficient represents the effect of the variable X_i and b_{ij} and b_{ijk} are the coefficients of regression which represent the effects of interactions of the variable X_iX_j and $X_iX_jX_k$ respectively.

The Design of Experiment method was introduced by Sir R. A. Fisher in the early 1920's [167]. Fisher developed a method to carry out agricultural experiments in which the effects of properties, such as fertiliser, sunshine and rain on a crop were determined. Further improvements in the DOE technique were brought about by Dr. Genechi Taguchi in the 1940's [167]. A number of special orthogonal arrays were introduced which made the implementation of DOE easier. The DOE method has been applied across a wide range of disciplines since the 1920's. A

number of different DOE methods have since been developed, including factorial experiments and Response Surface Methodology techniques, such as the Central Composite Design and the Box-Behnken Design. The method selected for a particular experiment depends on considerations such as the objectives of the experiment, the number of factors being investigated and the resources available.

2.8.3 Factorial Experiments

A factorial experiment is an experiment in which several factors are controlled and their effects at each of two or more levels investigated [168]. Analysis of a factorial experiment allows identification of the main effects and also interaction effects between the factors. In a full factorial experiment all possible combinations of the levels of the factors are investigated. Two-level full factorial experiments are the most common. In this type of experiment factors are set at a low level (coded -1) and a high level (coded +1). A two level experiment with k factors is called a 2^k experiment. For example, a 2^3 experiment is used to study three factors at two levels and will consist of 8 experiments. The design for this experiment is shown in *table 2.9*.

Table 2.9: 3-factor, 2-level Factorial Experiment

Run	***X1***	***X2***	***X3***
1	-1	-1	-1
2	1	-1	-1
3	-1	1	-1
4	1	1	-1
5	-1	-1	1
6	1	-1	1
7	-1	1	1
8	1	1	1

When carrying out experiments, factors may exist that are not of primary interest but still affect the results. Examples of such factors include specific operators, different batches of materials and so on. It is necessary to eliminate the affect of these factors from the overall results experiments. This can be achieved by organising the experiment into blocks. Experiments should also be run in random order to eliminate the effects of any factors that cannot be controlled and cannot be blocked.

Centrepoints are also usually added to factorial designs. These points are the centre value between the high (+1) and low (-1) values selected for each factor and are coded 0. The purpose of centre points is to allow process stability to be determined. Generally between 3 and 6 centrepoints are added to an experiment design.

Fractional Factorial Designs

If a large number of factors are being investigated, full factorial experiments are not very efficient and thus a fractional factorial experiment can be used. Fractional factorial experiments involve fewer than the full 2^k run of experiments [169]. Generally, a fraction of the number of runs required for a full factorial experiment, such as ½ or ¼ and so on is used. The general term used for a fractional factorial design is 2^{k-m}, where a ½ fractional factorial experiment is termed a 2^{k-1} experiment and so on. A graphical representation of a 2^3 full factorial matrix and a 2^{3-1} ½ fractional factorial matrix is given in *figure 2.16*.

The aim of a fractional factorial experiment is to reduce the number of experimental runs required by extracting the part of a full factorial experiment which enables the main factors and some first order interactions to be obtained [170]. This is achieved by confounding of the effects of some of the factors and as a result, high order interactions between factors cannot be estimated. This type of experiment can be used to obtain information on the main effects and low-order interactions and is often used for screening designs.

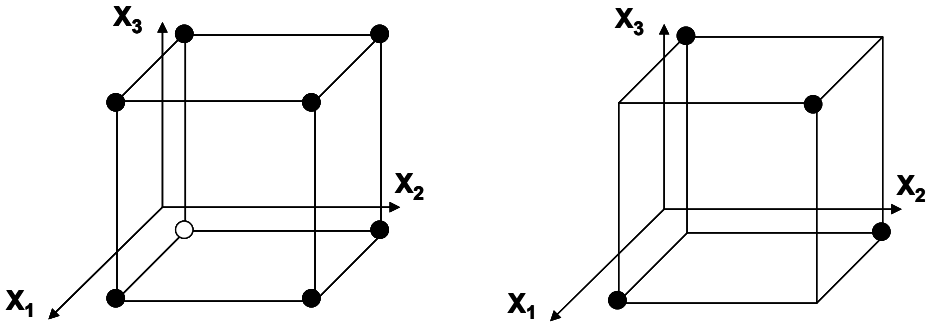

a) 2^3 matrix b) 2^{3-1} matrix

Figure 2.16: Graphical representation of the matrices a) 2^3 and b) 2^{3-1} with the simplification $X_3 = X_1X_2$

The construction of a 2^{5-2} matrix is shown in *table 2.10*. A full 2^3 matrix is used for columns $X_1X_2X_3$ and the following columns are obtained by multiplication $X_4 = X_1X_2$ and $X_5 = X_1X_3$.

Table 2.10: 3-factor, 2-level Factorial Experiment

Run	*X1*	*X2*	*X3*	X_4 (X_1X_2)	X_5 (X_1X_3)
1	-1	-1	-1	1	1
2	1	-1	-1	-1	-1
3	-1	1	-1	-1	1
4	1	1	-1	1	-1
5	-1	-1	1	1	-1
6	1	-1	1	-1	1
7	-1	1	1	-1	-1
8	1	1	1	1	1

2.8.4 Screening Designs

Screening designs are used in the early stages of investigations to allow more information to be obtained about a process. They are generally carried out prior to

carrying out a Response Surface Methodology experiment. Screening designs usually have a small number of experimental runs. These studies can identify the factors which have the greatest affect on the process and thus allow the factors under investigation to be reduced. Information can also be obtained about the parameter space under investigation and allow the correct range to be selected for each parameter. This preliminary information can be used to develop a Response Surface Methodology experiment.

2.8.5 Response Surface Methodology (RSM)

Response surface methodology (RSM) can be used to maximise or minimise a response, reduce variation by locating a region where the process is easier to manage or to optimise a response. The two most popular Response Surface Methodology techniques are the Central Composite Design (CCD) and the Box-Behnken Design (BBD).

Central Composite Design

A Central Composite Design (CCD) consists of a factorial or fractional factorial design with centre points, augmented with a group of star points. The design matrix (d) can be described according to *equation 2.15*.

$$d = \begin{bmatrix} F \\ E \\ C \end{bmatrix} \qquad \textit{(eqn. 2.15)}$$

F is either a 2^k factorial or fractional factorial experiment. E is a matrix with 2k rows, where all of the factors are set to 0, the midpoint, except one factor, which is placed at the star point or axial point. The distance from the centre of the design space to the star point is ± α. The value of α depends on the type of centre composite design being used and also on the number of factors under investigation.

The value of α can be calculated from the *equation 2.16*.

$$\alpha = (2K)^{1/4} \qquad \textit{(eqn. 2.16)}$$

The correct choice of the axial spacing, α, can be used to make the design rotatable. In a rotatable design, the variance of the predicted values of y is a function of the distance of a point from the centre of the design and is not a function of the direction that point lies from the centre. These values can be set outside the parameter space to allow for curvature considerations in the regression analysis.

There are three types of CCD, depending on where the star points are placed. The three designs are compared in *table 2.11* and *figure 2.17*.

Table 2.11: Types of Central Composite Design [171]

Central Composite Design Type		***Description***
Circumscribed	CCC	These are the original form of the central composite design. The star points establish new extremes for the low and high settings for all factors.
Face Centered	CCF	In this design the star points are at the centre of each face of the factorial space.
Inscribed	CCI	These are used when the star points need to be set within the limits of the original design.

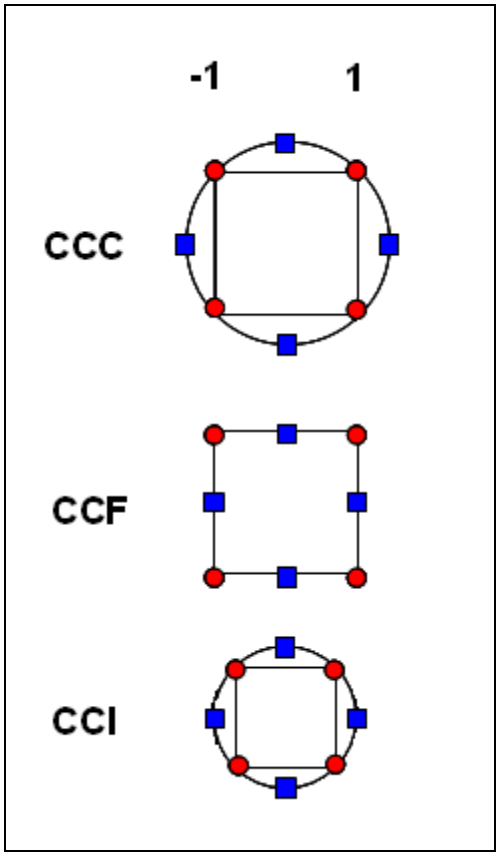

Figure 2.17: Comparison of the Three Types of Central Composite Designs

Box Behnken Design

The Box-Behnken design is an independent quadratic design which does not contain an embedded factorial design. The design treatment combinations are at the midpoints of edges of the process space and at the centre [171]. This type of design requires three levels for each factor.

2.8.6 Comparison of Response Surface Designs

CCDs are rather insensitive to missing data which makes them more robust than other designs. CCC designs provide high quality predictions over the entire design space, but require factor settings outside the range of the factors in the factorial part of the experimental design. CCI experiments only use points within the factor ranges originally specified, but do not provide the same high quality prediction over the entire space compared to CCC. CCF designs provide relatively high quality predictions over the entire design space and do not require using points

outside the original factor range. However, the CCF designs give poor precision for prediction of pure quadratic coefficients. Box-Behnken designs require fewer treatment combinations than Central Composite Designs in cases where there are 3 or 4 factors. As the number of factors are increased the numbers of experiments required increases also; for 5 factors, 41 experiments are necessary. Box-Behnken designs are sensitive to missing data, they are rotatable but contain regions of poor prediction quality.

2.8.7 Analysis of Variance (ANOVA)

Analysis of Variance (ANOVA) can be used to evaluate DOE models. There are a number of adequacy measures that can be used to determine the statistical significance of the models developed. The most important of these are the R^2, Adjusted R^2, Predicted R^2 and Adequate Precision. The formulae used to calculate these values and an explanation of what these represent are given in *Appendix A*.

2.8.8 Studies of Plasma Sprayed HA Coatings

Currently, very little information exists in the literature relating to the use of the Design of Experiment method for the analysis of plasma spraying of HA. Some of the first studies in this area have been carried out by Cizek et al. [122] and Dyshlovenko et al. [107, 166]. Cizek et al. [107] used as the Spray Watch camera system to determine the effect of plasma spray parameters on the thermal and velocity properties of plasma sprayed HA coatings. Although useful models are developed, the information is not related to the properties of the coating produced.

Dyshlovenko et al. [165] used the DOE technique to examine the plasma spraying of HA followed by a laser post spray treatment process. The models produced had a low significance, poor reconstructive ability and poor predictive ability. In a separate study, Dyshlovenko et al. [166] used a factorial experimental design to investigate the relationship between plasma spray parameters and the microstructure of HA coatings. In the study three responses were examined, the fraction of HA, the fraction of decomposition phases and the amorphous content of the coatings.

In these studies by Dyshlovenko et al. [165, 166], the number of factors investigated and responses modelled was small. It is clear that further, more in depth studies are required in order to gain a greater understanding of the process. A summary of the experimental type, factors and responses investigated in these studies is given in *table 2.12*.

Table 2.12: Summary of DOE studies of Plasma Sprayed HA Coatings

Exp Type	*Description*	*Factors*	*Responses*	*Reference*
Taguchi	6 factors; 3 levels; 2 responses; 18 experiments	Power Input; Main gas flow rate; Secondary gas flow rate; Carrier gas flow rate; Powder feed rate; Spray distance	Particle temperature; Particle velocity	Cizek et al. [107]
2^4 Factorial Design	3 factors; 2 levels; 3 responses; 16 experiments	H_2 content of plasma gas; Electric arc power; Spray distance	Fraction HA phase; Fraction decomposition phase; Fraction amorphous phase	Dyshlovenko et al. [166]
2^4 Factorial Design	4 factors; 2 levels; 4 responses; 16 experiments	Electric arc power; Ar content of plasma gas; Carrier gas flow rate; Laser power density	% HA; % TTCP; % α - TCP; Depth of laser melt zone	Dyshlovenko et al. [165]

2.9 Chapter Summary

This chapter has discussed background information relating to plasma sprayed hydroxyapatite coatings. The properties of hydroxyapatite have been described, and the spraying process explained. The current understanding of the effect of plasma spray parameters on the properties of HA coatings have been outlined. The properties required from the ideal plasma sprayed hydroxyapatite coating have been discussed, along with the techniques used for coating analysis. Finally, the methods involved in process optimisation using the Design of Experiment technique have been discussed. In the following chapter, the experimental procedures and equipment used in this work are detailed.

3 Experimental Procedures and Equipment

3.1 Introduction

This chapter describes the experimental equipment used in this research work and the experimental procedures that were followed. The plasma spray system is firstly discussed, with each of the components of the system being explained in detail. Following this, details of the powder and substrate material used in this work are given. The experimental work that was carried out as part of this research work is then explained. This work consisted of three parts: 1) a post spray heat treatment study which examined the recrystallisation of plasma sprayed HA coatings, 2) a two-part Design of Experiment study (Screening and Response Surface Methodology) used to develop process models and design an optimised bi-layer HA coating, and 3) an cell culture study in which the two layer of the optimised bi-layer coating were evaluated. The procedures used for characterisation of the substrate material and HA powder and analysis of HA coatings produced in this work are also described in this section.

3.2 The Plasma Spraying System

3.2.1 Plasma Spray Equipment

The plasma spray equipment used for this experimental work was an atmospheric plasma spray rig supplied by Sulzer Metco, UK. The equipment was installed in a purpose built, sound-proofed room in the National Centre for Plasma Science and Technology in Dublin City University by Sulzer Metco. The plasma room set-up is shown in *figure 3.1*. The plasma spray system consists of the three main components: the plasma gun, the powder feeder and the control unit. These components are identified in *figure 3.1*. Each component of the system is described individually in the following sections.

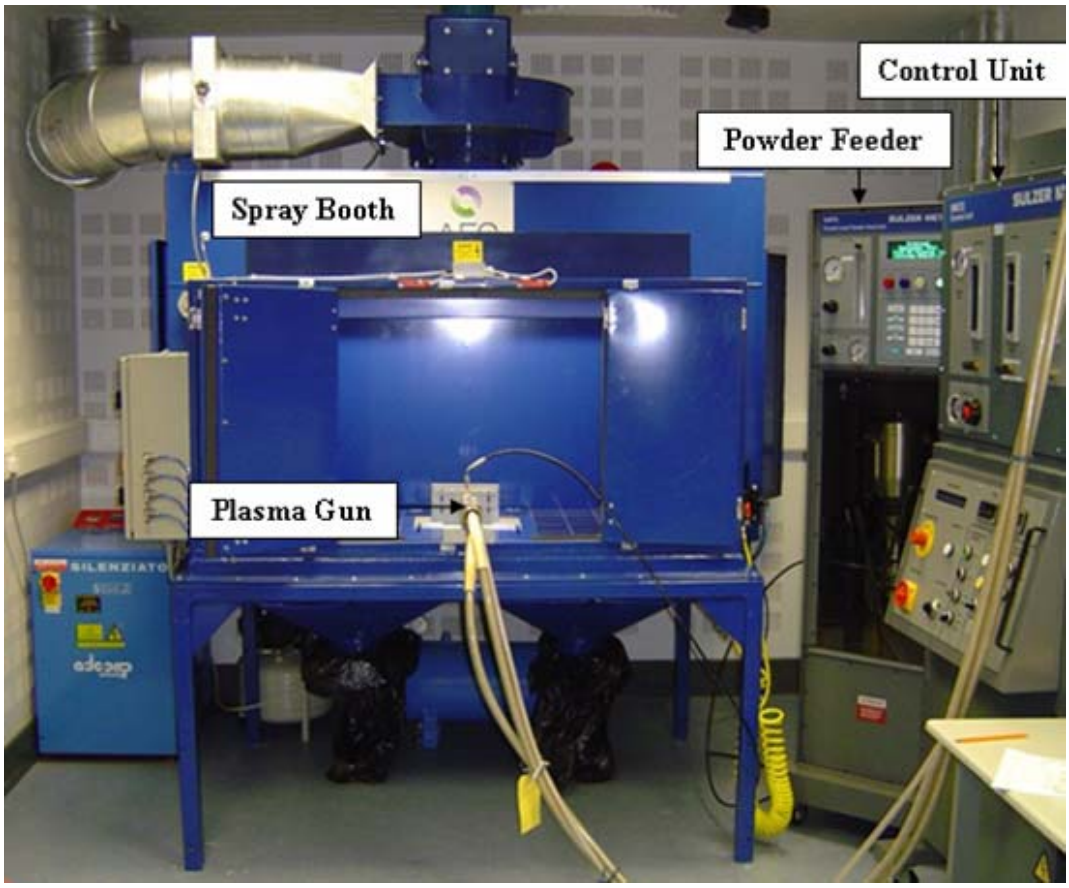

Figure 3.1: Plasma Spray System

The Plasma Gun

The plasma gun used in the current research was the Sulzer Metco 9MB-Dual Plasma Spray Gun. The gun has a machine mountable base assembly which allows the gun to be mounted directly onto the spray booth or onto a traverse unit. It was fitted with a Sulzer Metco 9MB63 electrode and a Sulzer Metco 3M7-GH nozzle. The spray gun has radial powder injection which means that powder is introduced into the spray stream outside of the nozzle at right angles to it (see *figure 3.2*). This is beneficial as it reduces build-up on the nozzle, reduces the risk of contamination and eliminates cleaning problems. The spray gun is shown in *figure 3.2*.

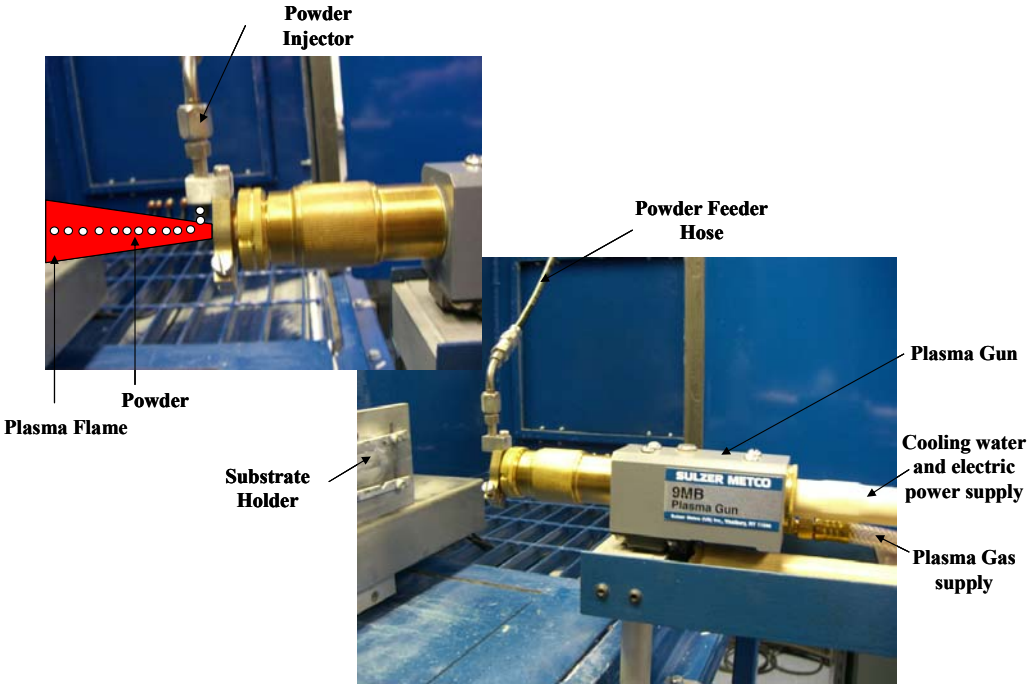

Figure 3.2: Sulzer Metco 9MB-Dual Plasma Spray Gun

Cooling System

Due to the high temperatures involved in the system, a closed loop heat exchanger is used to cool the components of the plasma gun thus preventing component damage. Water is stored in a header tank on the roof of the building above the plasma room. The water is then circulated through the distribution unit. The distribution unit installed is the 1010/E JAM (Junction and Monitoring) – Box. A flow rate of approximately 12 l/min is necessary to provide adequate cooling. The 3M7-GH nozzle used incorporates a 'TAP', (Thin Annular Passage) cooling design. This consists of a series of passages which channel the water to provide uniform flow around the surface of the nozzle and thus provides more efficient cooling.

Control Unit

The control unit installed is the Sulzer Metco 9MCE plasma control unit, shown in *figure 3.3*. The purpose of the control unit is to regulate the arc current, plasma gas ratios, and flow rates. Power is supplied to the system by a high voltage D.C. electrical energy supply. The 9MCE control unit allows spraying to be carried out

using two plasma forming gases, a primary gas and secondary gas. Two gases are supplied directly to the plasma room, argon and hydrogen. The primary plasma forming gas flow rates are calibrated for a pressure of 75 psi (5.17 Bar). Argon was the primary plasma forming gas used in this work. The secondary gas flow rates are calibrated for a pressure of 50 psi (3.45 Bar). No secondary gas was used in this work. It is necessary to ensure that the pressure is adjusted to the required level before spraying otherwise the gas flow rates displayed will not be accurate.

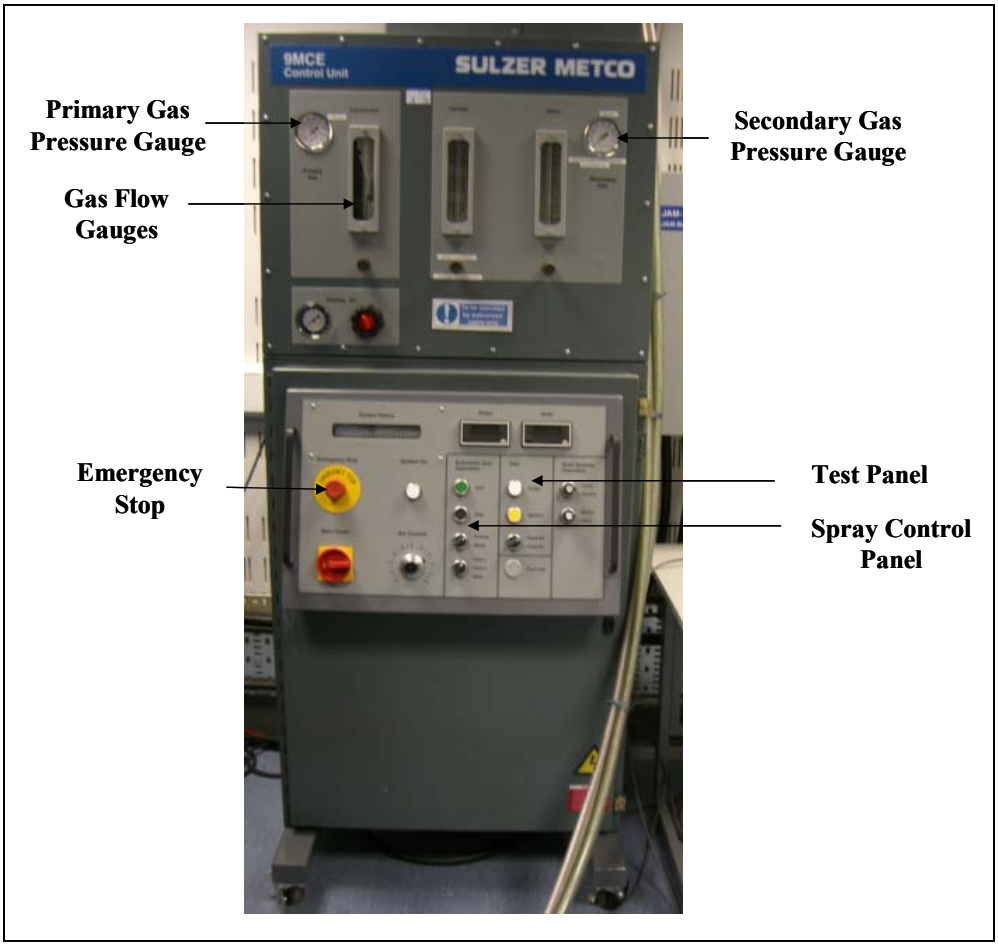

Figure 3.3: Sulzer Metco 9MCE Control Unit

Powder Feeder

The powder feeder used was the Sulzer Metco 9MPE closed-loop powder feeder, shown in *figure 3.4*. This unit controls the powder feed rate and also the carrier gas flow rate. The powder for spraying is stored in a hopper in the powder feeder. The powder is carried from here to the plasma gun by a fluidised bed system. This

uses a carrier gas (argon) to entrain the powder particles and carry them to the desired location. A weight loss metering system provides continuous closed-loop adjustment of powder feed rate. The powder carrier gas flow rate is also calibrated for a pressure of 75 psi (5.17 Bar).

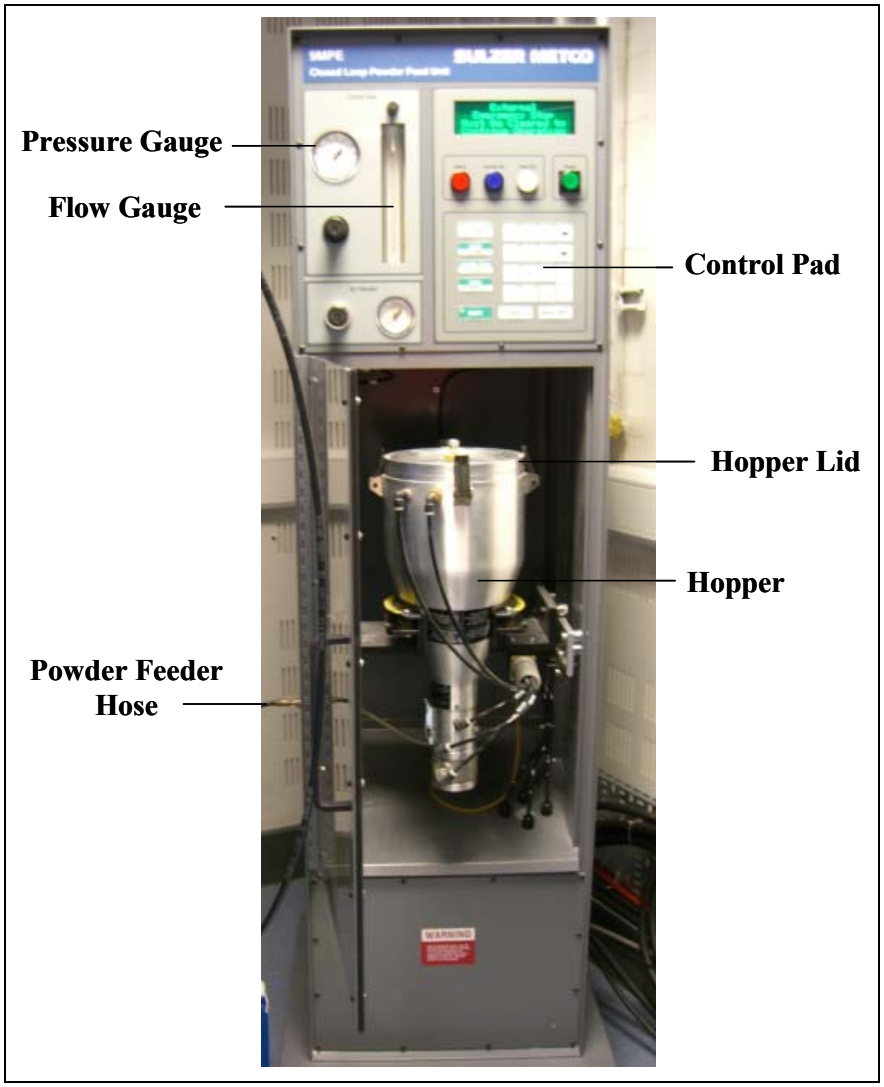

Figure 3.4: Sulzer Metco 9MPE Closed-Loop Powder Feeder

Spray Booth and Extraction System

The plasma gun and substrate material are housed within a spray booth. The spray booth is fitted with a dry extraction system that removes hazardous gases and powder particles from the plasma spray room. This extraction system consists of a supply system, to supply air, and an exhaust system, containing filters, to remove the contaminants generated by the spray process. Powder particles present in the

air are collected in a dry collector in the system. The spray booth and extraction system for this rig was supplied by Air Filtration Services Ltd. (AFS).

3.2.2 Equipment Development

Substrate Holder

A holder to secure the substrate during plasma spraying was designed during the study. This is shown in *figure 3.5*. The design consisted of an aluminium L-shaped plate with two stainless steel clamping bars attached to the front of it. The clamping bars could be moved up and down by adjusting the screws at the back of the holder. Notches were cut into the clamping bars to allow secure fixation of the titanium alloy discs.

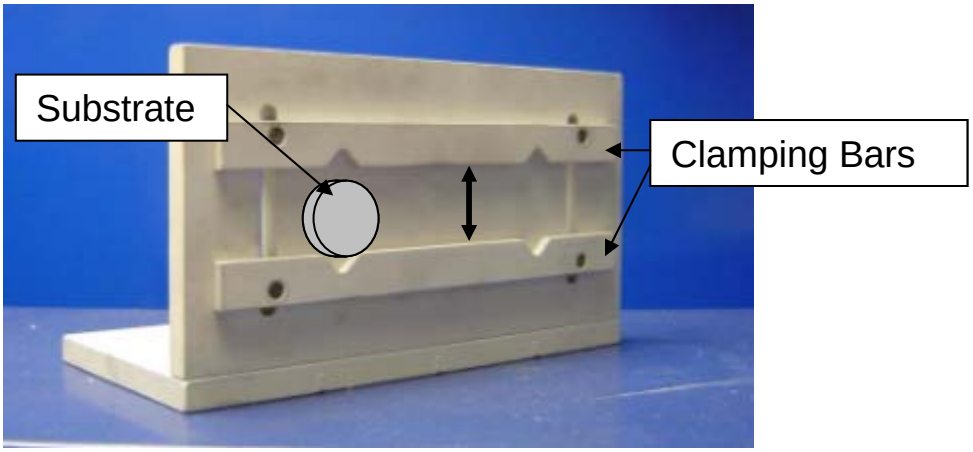

Figure 3.5: Sample Holder

Substrate Movement

Movement of either the plasma gun or the sample to be sprayed is necessary in order for a coating to be produced. It was decided that movement of the sample would be the most appropriate as it is a lower mass than the plasma gun. The sample mover designed during the study used a pneumatic cylinder as the basis for the design. The cylinder is run from the compressed air supply in the plasma room. This allows movement in the x-direction (across the face of the gun), the speed of which can be adjusted by adjusting variable restrictors on the cylinder. The pneumatic diagram for the sample movement device is presented in *Appendix*

B. Movement in the y-direction (in and outwards from the gun, that is the spray distance) is achieved by sliding the sample holder forward or backwards on sliding rods to the required stand-off distance.

3.3 Materials

3.3.1 Substrate

Two types of substrate were used for the plasma spraying of HA. Preliminary tests involved spraying on rectangular aluminium coupons 50 mm x 20 mm x 2 mm in size. The titanium alloy Ti6Al4V was then used for the remainder of the experimental work. This was used as it is a biocompatible material and is the most commonly used material for HA coated hip replacements. The Ti6Al4V substrate material was in the form of discs, 10 mm in diameter x 2 mm in thickness, cut from a 10 mm diameter rod of Ti6Al4V. Prior to spraying the discs were prepared following the procedure outlined in *Section 3.5*, and analysed following the procedures in *Section 3. 9*. The results are presented in *Section 4.2*.

3.3.2 Hydroxyapatite Powder

The powder used for hydroxyapatite coating production is Captal 60-1 Thermal Spraying Hydroxyapatite Powder, supplied by Plasma Biotal Ltd., UK (*figure 3.6*). This HA powder is produced specifically for thermal spray applications. It has a typical particle size of 45 μm.

This powder particle size was selected based on the findings of Kweh et al. [111] who reported that HA coatings produced using powder with small particle sizes (20-45 μm) result in denser coatings than when using powders with a larger particle size. The powder was initially characterised as per the procedures outlined in *Section 3.8*. The results of which are presented in *Chapter 4.2.1*.

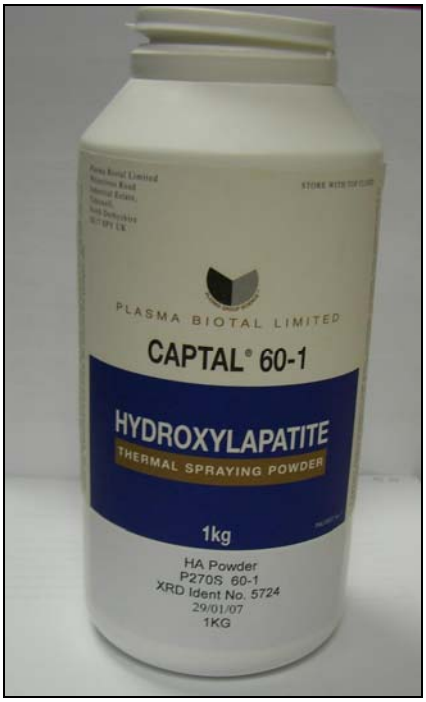

Figure 3.6: Captal 60-1 Hydroxyapatite Powder

3.3.3 Post Spray Heat Treatment Study Coupons

The post spray heat treatment study was carried out prior to the installation of the DCU plasma rig. The plasma sprayed HA coupons used in the post spray heat treatment study were supplied by Plasma Biotal Ltd., UK. These consisted of 50mm x 20mm x 2mm stainless steel coupons. The stainless steel coupons were prepared by grit blasting and ultrasonic cleaning before the HA coating was applied. The as-received coating is shown in *figure 3.7*.

Figure 3.7: Plasma Biotal HA coating

3.4 Post Spray Heat Treatment of HA Coatings Procedure

Post spray heat treatment of the HA coatings was carried out by heating the coatings in a furnace in air at three treatment temperatures, 600 ºC, 700 ºC, and 800 ºC. 600 ºC was chosen as the lowest value in the post spray heat treatment study, selected based on the results of a study by Lu et al. [130] in which 500ºC was found by to be insufficient to allow recrystallisation of HA. The high value of 800 ºC was selected based on knowledge relating to the thermal behaviour of HA, as discussed in *Section 2.2.5*, where temperatures above 800 ºC have been found to cause dehydroxylation of HA which would prevent recrystallisation [58]. Two treatment times were investigated in this study, 1 hour and 2 hours. The samples were placed in the furnace, and heated at a rate of 4 ºC per min to the designated temperatures. They were kept at this temperature for a treatment time of either 1 or 2 hours and then left in the furnace to cool down slowly overnight. The coatings were characterised using XRD, SEM and surface roughness measurement as per the procedures outlined in *Section 3.10*.

3.5 Substrate Preparation

3.5.1 Grit Blasting Procedure

The substrate material was grit blasted prior to plasma spraying. Pure white alumina oxide, 500 μm (mesh 36) in size, was used for grit blasting the titanium discs. This is commonly used for medical applications as it is biocompatible [91, 137, 172]. Grit blasting was carried out using a blasting pressure of 5 Bar and a blasting angle of 75º, following recommendations from the research of Amada and Hirose [88]. The samples were grit blasted for 2 minutes, ensuring that the full surface was roughened.

3.5.2 Substrate Cleaning Procedure

Following grit blasting the samples were cleaned to remove any traces of the alumina oxide grit, grease and other contamination. The post grit blasting cleaning procedure was based on the findings of a study by Yankee et al. [91]. Samples were firstly blown with high pressure air to remove any surface alumina particles.

Samples were then placed in a beaker of dilute acetone solution which was placed in an ultrasonic cleaner for 5 minutes. The samples were then removed, carefully rinsed in water, dried and then stored carefully in a sealed bag to avoid recontamination.

3.6 Plasma Spray Procedure

3.6.1 Spraying Procedure

Preliminary work using the plasma spray rig involved development of the spraying procedure for use in further experimental work. Initial repeatability problems were encountered due to powder feed rate instability. A powder feed rate set-up procedure was found to be necessary each time the spray parameters were changed. In order to reduce powder waste during the powder feed rate set-up, a powder collection pot was used to collect the powder. This powder could then be reused for spraying. The spraying procedure that was followed for all experimental work is documented in *Appendix C*.

3.6.2 Safety Equipment

The plasma spray process is a hazardous one, involving high temperatures, high noise levels, UV light and harmful gases and air-borne particulates. The items of personal protection required when spraying are outlined in *table 3.1*.

Table 3.1: Personal Protection Equipment Required for Plasma Spraying

Hazard	***Protective Equipment***
UV light from Plasma Arc	Eye Protection (shade 11)
Fumes, Gases and Powders	Face mask with appropriate filters
High dB noise (~ 130 dB)	Ear plugs and Hearing Protectors
High temperature of sprayed components	Flame resistance coveralls and gloves
Irritation from HA powder	Powder handling gloves

3.7 Process Modelling

Following development of a suitable spraying procedure and completion of initial trials, the Design of Experiment technique was utilised to determine the effects of various spray parameters on the HA coatings produced. This experimental work was carried out in two stages, as is recommended for Design of Experiment studies. The first step involved completion of a screening experiment and following this a more detailed Response Surface Methodology (RSM) experiment was carried out. Details of this experimental work are given in the following sections.

3.7.1 Software Selection

A number of Design of Experiment software packages are currently available. Three packages were evaluated for use in this research. These were Qualitek-4, supplied by Nutek Inc., Modde 7 supplied by Umetrics, and Design Expert 7 supplied by Stat-Ease Inc. The software package selected was Design Expert 7. This was selected as it was found to have to best user interface and the statistical information of interest was clearly displayed making developed models easier to analyse.

3.7.2 Screening Design

Parameter Selection

As discussed in the literature review (*Section 2.4.3*), a large number of parameters affect the plasma spray process. When running a screening experiment as many of the process parameters as possible should be selected for investigation. Parameters that are found not to influence the coating properties can be excluded from further experimental investigations.

The parameters included in the screening experiment were identified from primarily from literature. The parameters that have been found to be important in other studies of plasma spray coatings include primary gas flow rate, power level or current, spray distance, traverse velocity, powder feed rate, carrier gas flow rate

and primary gas / secondary gas ratio [122, 166]. Other possible parameters identified in the literature review include the size, shape and composition of the HA powder, the roughness and pre-heat temperature of the substrate material, the plasma gun nozzle and the deposition time. Including all of these parameters in the experiment design would have resulted in a very large experimental programme that would not have been economically plausible.

The focus of this work was based on the main plasma parameters, therefore, no powder or substrate parameters were varied within the study. The powder used for all experimental work was Captal 60-1 Thermal Spray HA Powder, supplied by Plasma Biotal. The titanium substrates were all grit blasted using the same procedure (detailed in *Section 3.5.1*). No substrate preheating was carried out during spraying.

Argon was selected as both the primary plasma forming gas and the powder carrier gas. This was selected as it is an inert gas that does not react with HA and because of this it reduces the likelihood of impurity phase formation in HA coatings. No secondary plasma forming gas was used. Using argon as the only plasma forming gas is in line with current industrial practice.

Although the traverse velocity has been found by some authors to affect the coating it was not included as a factor in this study. This was not included because it was not possible to accurately adjust the velocity of the sample mover system. Inclusion of this parameter would have introduced error. The velocity was therefore set at a constant velocity of 38 mm/s and maintained at this velocity for all experiments. A deposition time of 35 seconds was used for all experimental work. The nozzle used in the plasma gun was also kept constant during the experiments. The 3M7-GH nozzle, recommended by Sulzer Metco, was used for all experimental work.

After consideration of all possible parameters, those selected for the study were the Current, Gas Flow Rate, Carrier Gas Flow Rate, Powder Feed Rate and Spray Distance. Each of these parameters had been identified in literature as having an affect on the properties of plasma sprayed coatings. These were all easily

adjustable and easily controllable. The Current and Gas Flow Rate are controlled directly through the control unit. Current is measured in Amps (A) and Gas Flow Rate in standard cubic feet per hour (SCFH), the conversion is 1 SCFH = 0.4721 standard litres per minute (SLPM).

The Carrier Gas Flow Rate and Powder Feed Rate are controlled through the powder feed unit. The Carrier Gas Flow Rate is measured on the powder feed unit in standard cubic feet per hour (SCFH). Powder Feed Rate is measured in grams per minute (g/min). The Spray Distance is controlled by moving the substrate holder back and forth on a sliding rail. The distance is measured in millimetres (mm). All parameters that were not investigated in the study were kept constant during the experiments. The values at which they were set are summarised in *table 3.2*.

Table 3.2: Values of Parameters not varied in the Study

Parameter	***Setting***
HA Powder	Plasma Biotal Captal 60-1
Primary Gas	Argon
Powder Carrier Gas	Argon
Gun Nozzle	Sulzer Metco 3M7-GH
Traverse Velocity (mm/s)	38
Deposition Time (s)	35
Substrate Roughness (Ra) (μm)	3.12
Substrate Pre-heat Temperature (ºC)	None
Post-spray heat Temperature (ºC)	None

Parameter Level Selection

In order to determine the levels at which the parameters should be set in the screening design a design space investigation was carried out. The first consideration was the equipment limits which determine the maximum and minimum possible settings for each parameter. These are given in *table 3.3*.

Table 3.3: Equipment Limits for the Selected Spray Parameters

Parameter	*Min*	*Max*
Current *(A)*	0	1000
Gas Flow Rate *(SCFH)* *[SLPM]*	30 [14.2]	300 [141.6]
Powder Feed Rate *(g/min)*	0	99.9
Spray Distance *(mm)*	0	170
Carrier Gas Flow Rate *(SCFH)* *[SLPM]*	0 [0]	25 [11.8]

A design space investigation was then carried out, based on knowledge of the equipment limits and on parameter levels reported in literature [107, 110, 165, 166]. The study involved varying each of the parameters to identify the range within which viable coatings are produced. A visual inspection was used to determine whether a viable coating has been produced. In order for a coating to be deemed viable, it was required that the substrate material should not be visible through the coating following spraying.

Information from the literature was used to identify the starting values for each parameter. Each parameter was then varied separately while setting the remaining parameters at set central values. The investigation for each parameter was started at the central value, identified from literature, and increased and decreased from this point until either the equipment limit was reached or until a viable coating was not produced. The values investigated for each parameter are given in *table 3.4* to *3.8*. The other spray parameters were set as per the values in *table 3.2*. The results from this investigation are given in *Section 4.4.1*.

Table 3.4: Current Range Investigation

Parameter	*Variables*					
	1	***2***	***3***	***4***	***5***	***6***
Current *(A)*	**350**	**450**	**600**	**750**	**850**	**950**
Gas Flow Rate *(SCFH)*	100	100	100	100	100	100
Powder Feed Rate *(g/min)*	15	15	15	15	15	15
Spray Distance *(mm)*	100	100	100	100	100	100
Carrier Gas Flow Rate *(SCFH)*	15	15	15	15	15	15

Table 3.5: Gas Flow Rate Range Investigation

Parameter	*Variables*					
	1	***2***	***3***	***4***	***5***	***6***
Current *(A)*	600	600	600	600	600	600
Gas Flow Rate *(SCFH)*	**50**	**70**	**100**	**130**	**170**	**190**
Powder Feed Rate *(g/min)*	15	15	15	15	15	15
Spray Distance *(mm)*	100	100	100	100	100	100
Carrier Gas Flow Rate *(SCFH)*	15	15	15	15	15	15

Table 3.6: Powder Feed Rate Range Investigation

Parameter	*Variables*					
	1	***2***	***3***	***4***	***5***	***6***
Current *(A)*	600	600	600	600	600	600
Gas Flow Rate *(SCFH)*	100	100	100	100	100	100
Powder Feed Rate *(g/min)*	**5**	**10**	**15**	**20**	**25**	**30**
Spray Distance *(mm)*	100	100	100	100	100	100
Carrier Gas Flow Rate *(SCFH)*	15	15	15	15	15	15

Table 3.7: Spray Distance Range Investigation

Parameter	*Variables*					
	1	***2***	***3***	***4***	***5***	***6***
Current *(A)*	600	600	600	600	600	600
Gas Flow Rate *(SCFH)*	100	100	100	100	100	100
Powder Feed Rate *(g/min)*	15	15	15	15	15	15
Spray Distance *(mm)*	**40**	**60**	**80**	**100**	**120**	**130**
Carrier Gas Flow Rate *(SCFH)*	15	15	15	15	15	15

Table 3.8: Carrier Gas Flow Rate Range Investigation

Parameter	*Variables*				
	1	***2***	***3***	***4***	***5***
Current *(A)*	600	600	600	600	600
Gas Flow Rate *(SCFH)*	100	100	100	100	100
Powder Feed Rate *(g/min)*	15	15	15	15	15
Spray Distance *(mm)*	100	100	100	100	100
Carrier Gas Flow Rate *(SCFH)*	**5**	**10**	**15**	**20**	**25**

The coating sprayed at the central values in this preliminary investigation (Current – 600 A, Carrier Gas Flow Rate – 100 SCFH, Powder Feed Rate – 15 g/min, Spray Distance – 100 mm, Carrier Gas Flow Rate – 15 SCFH) was compared against the starting HA powder. The results are presented in *Section 4.4.2*.

The information gained about the parameter settings from the design space investigation was used to select the parameter ranges for the screening experiment. The low and high levels for the screening experiment were set within the acceptable process limits identified. The selected values for each parameter are presented in *table 3.9*.

Table 3.9: Screening Design Parameters and Levels

	Low Level	*High Level*
Current (A) *A*	450	750
Gas Flow Rate (B) *SCFH* *[SLPM]*	70 [33]	130 [61.4]
Powder Feed Rate (C) *g/min*	10	20
Spray Distance(D) *mm*	80	120
Carrier Gas Flow Rate (E) *SCFH* *[SLPM]*	10 [4.7]	20 [9.4]

Experimental Design

A two level fractional factorial design was selected for the screening design. A ¼ fraction (2^{5-2}) factorial design was used. The experiment was designed using the Design Expert software. The fractional factorial experiment required eight experimental runs (N1 – N8). Three centre point experiments were also carried out (N9 - N11). As discussed in *Section 2.8*, centre points allow the process stability to be determined. The screening design is shown in *table 3.10*. The experiment was run in random order to eliminate the effects of any uncontrolled factors. One coating was sprayed for each experimental run.

Three responses were examined in the screening study, coating roughness measured using the surface profilometer (as per the procedure in *Section 3.10.6*), and coating crystallinity and purity calculated from the XRD patterns of each coating (as per the procedure outlined in *Section 3.10.3*). The surface of the coatings was also examined using SEM.

The roughness and surface properties were examined in order to understand the degree of melting of the particles during the coating process. The crystallinity and purity were measured as these are known to be two of the most important properties affecting the dissolution rate of HA coatings and are strictly controlled by the FDA.

Table 3.10: Screening Design Experimental Design

Exp Name	*Run Order*	*Variables*				
		Current (A) *A*	**Gas Flow Rate (B)** *SCFH*	**Powder Feed Rate (C)** *g/min*	**Spray Distance (D)** *mm*	**Carrier Gas flow rate (E)** *SCFH*
N1	4	450	70	10	120	20
N2	11	750	70	10	80	10
N3	8	450	130	10	80	20
N4	10	750	130	10	120	10
N5	7	450	70	20	120	10
N6	3	750	70	20	80	20
N7	5	450	130	20	80	10
N8	1	750	130	20	120	20
N9	6	600	100	15	100	15
N10	2	600	100	15	100	15
N11	9	600	100	15	100	15

Key
Fractional Facorial Experiment Runs
Centre Point Experiment Runs

3.7.3 Response Surface Methodology (RSM) Study

Design Expert was again used for the design of the Response Surface Methodology (RSM) study. The parameters and levels used for the RSM were selected based on the results of the screening study (discussed in Chapter 4). It was identified from the screening design that all five parameters had a significant affect on the coating, based on the three responses (roughness, crystallinity and purity) studied. All five parameters were thus included in the RSM study. A Central Composite Design (CCD) was selected for this study, based on analysis of the options recommended by the software. The CCD consisted of a 5^{-1} Fractional Factorial Design (16 experiments), ten star point experiments and five centre point experiments. This gave a total of 31 experimental runs for the design.

Two levels were used for each factor; the parameters and levels used are shown in *table 3.11*. The experiments were run in random order. The full experimental design is shown in *table 3.12*. As some of the characterisation methods used were destructive, two coatings were required for each experimental run. These were produced by mounting two titanium discs in the sample holder and spraying them simultaneously.

Table 3.11: RSM Study Parameters and Levels

	Low Level	***High Level***
Current (A) *A*	550	750
Gas Flow Rate (B) *SCFH* *[SLPM]*	90 [42.5]	150 [70.8]
Powder Feed Rate (C) *g/min*	10	20
Spray Distance(D) *mm*	70	100
Carrier Gas flow rate (E) *SCFH* *[SLPM]*	10 [4.7]	20 [9.4]

Crystallinity, purity and roughness were again selected as responses for the optimisation study. Two further responses, porosity and thickness, were added in order to further characterise the coatings. The results are presented in Section 4.6. Following development of the response surface models, model validation was determined using three point prediction tests.

Table 3.12: RSM Study Design

Exp Name	*Run Order*	*Variables*				
		Current (A) *A*	**Gas Flow Rate (B)** *SCFH*	**Powder Feed Rate (C)** *g/min*	**Spray Distance (D)** *mm*	**Carrier Gas flow rate (E)** *SCFH*
N1	22	550	90	10	70	20
N2	20	750	90	10	70	10
N3	17	550	150	10	70	10
N4	24	750	150	10	70	20
N5	14	550	90	20	70	10
N6	7	750	90	20	70	20
N7	10	550	150	20	70	20
N8	11	750	150	20	70	10
N9	19	550	90	10	100	20
N10	21	750	90	10	100	20
N11	23	550	150	10	100	20
N12	18	750	150	10	100	10
N13	8	550	90	20	100	20
N14	13	750	90	20	100	10
N15	12	550	150	20	100	10
N16	9	750	150	20	100	20
N17	6	550	120	15	85	15
N18	4	750	120	15	85	15
N19	29	650	90	15	85	15
N20	28	650	150	15	85	15
N21	25	650	120	10	85	15
N22	15	650	120	20	85	15
N23	3	650	120	15	70	15
N24	2	650	120	15	100	15
N25	27	650	120	15	85	10
N26	30	650	120	15	85	20
N27	16	650	120	15	85	15
N28	31	650	120	15	85	15
N29	5	650	120	15	85	15
N30	26	650	120	15	85	15
N31	1	650	120	15	85	15

Key
Fractional Factorial Experiment Runs
Star Point Runs
Centre Point Experiment Runs

Determination of Model Validity

Analysis of the validity of the Response Surface Models developed for each response, was carried out was carried out using point prediction tests. This involved carrying out three validation experiments, at parameter settings selected randomly using the Design Expert software. The test conditions used for each of these experiments are given in *table 3.13*. The response values measured for each test condition were compared to the values predicted by the surface response models.

Table 3.13: Model Validity Factor Levels

	Current (A) *A*	***Gas Flow Rate (B)*** *SCFH*	***Powder Feed Rate (C)*** *g/min*	***Spray Distance (D)*** *mm*	***Carrier Gas flow rate (E)*** *SCFH*
1	600	120	10	80	17
2	700	100	15	90	12
3	600	110	20	85	15

3.7.4 Coating Optimisation

Optimisation of the RSM models developed in this work was also carried out using the Design Expert Software. The process required the selection of a goal, for example to maximise or minimise a response, and an importance level, based on selection of the most critical parameters, for each response. The response surface models were then optimised for these goals and importance levels in order to determine the required settings for each parameter. The optimisation of the developed models is discussed further in *Section 4.7*.

3.8 Characterisation of HA Powder

3.8.1 Powder Morphology

The morphology of the HA powder was examined using both the Reichert "MeF2" Universal Camera Optical Microscope and the LEO 440 Stereo Scan

Scanning Electron Microscope. The parameters used for SEM analysis are given in *table 3.14*. The Reichert "MeF2" Universal Camera Optical Microscope was used to obtain images up to a magnification of 80 x. The Beuhler Omnimet Enterprise image analysis software was used to manually measure the particle size using the feature measurement tool available in the software. The SEM was used to obtain higher magnification images.

Table 3.14: Parameters used for SEM Analysis of HA Powder

Parameter	*Value*
Probe Current *(pA)*	150
Accelerating Voltage *(KeV)*	15
Magnificaiton *(x)*	50 - 200

3.8.2 Phase Identification

The phases present in the HA powders were identified using X-ray Diffraction (XRD). Scans were carried out using the Bruker D8-Advance Diffractometer. The parameters used are given in *table 3.15*.

Table 3.15: Parameters used for XRD Scan of HA Powder

Parameter	*Value*
Scan Type	Locked couple
Range *(º2θ)*	20 – 60
Increment *(º)*	0.02
Scan Speed *(sec/step)*	5
Incident beam diverence *(º2θ)*	1.0
Receiving Slit *(º)*	0.2

In order to carry out the scan a sample of powder was mounted on a glass slide using double sided tape. The slide was then attached to the XRD plate. Diffraction scans of the HA powder were carried out in accordance with ASTM F 2024-00,

the ‘Standard Practice for X-ray determination of phase content of plasma-sprayed hydroxyapatite coatings’ [173].

The phases present in the powder was then determined from the resultant diffraction pattern using the Bruker Diffract Plus EVA software. This software allows the XRD pattern to be matched to standard diffraction patterns in a library of J.C.P.D.S. files. The tallest peaks of impurity phases of interest in the material are found between 29º 2θ and the start of the tallest HA peak. The impurity area was taken to be between 29º 2θ and the start of the tallest HA peak. The purity was determined using *equation 2.11*. Bruker Diffract Plus EVA software was used to calculate the impurity and crystalline areas.

3.8.3 Crystallinity Determination

X-ray diffraction patterns were also used to determine the % crystallinity of the HA powder. This was calculated using the area of crystalline peaks in the region 20 to 40 º 2θ and the area of the amorphous diffuse background in this region. The areas of interest were determined using the area calculation tool in the Bruker Diffract Plus EVA software. The crystallinity was then calculated using *equation 2.9*.

The XRD technique is known to be a very repeatable one with very little error. This was confirmed by comparing repeated scans of the same sample. Errors in the determination of the coating crystallinity and purity may arise from the determination of the areas used for the crystallinity and purity calculations. Thus, one XRD scan was carried out for each coating and the crystallinity and purity calculations were repeated three times for each sample.

3.8.4 Thermograviometric Analysis

Thermograviometric analysis (TGA) and Differential Thermal Analysis (DTA) of the HA powder was carried out in order to determine its thermal behaviour and expected melting temperature. The analysis was carried out using the Stanton Redcroft Differential Thermal Analyser/ Thermal Gravimetric Analyser. The

DTA technique measures the temperature difference between a sample and an inert reference sample as a function of temperature. The TGA measures the weight change of a sample as a function of temperature. The equipment used in this study was capable of heating the sample up to a temperature of 1500 ºC. In this work, a 20 mg sample of the HA powder was heated in an alumina pan at a rate of 10 ºC/min up to a temperature of 1450 ºC. The powder was then cooled to room temperature also at a rate of 10 ºC/min.

3.8.5 Density Determination

The density of the HA powder was determined using the Micromeritics Helium Pycnometer. The helium pycnometry technique involves forcing helium into the voids in a sample, as the helium can enter even the smallest voids and pores it can be used to measure the volume per unit weight of a sample.

3.8.6 Particle Size Analysis

Particle size analysis was carried out using the Malvern Mastersizer particle size analyser. This is a laser diffraction based system. A sample of the powder particles are passed through a beam of laser light. The laser beam is scattered onto a detector array, an algorithm is used to determine the particle size. Prior to analysis 0.5 g of the HA powder was added to 30 ml of a dispersant solution. The suspension was stirred and then placed in an ultrasonic bath for 5 minutes. The dispersant solution used consisted of 1 g of sodium hexametaphosphate in 1000 ml of de-ionised water. This was prepared according to the standard BS ISO 14887, Sample preparation - Dispersing procedures for powders in liquids [174]. Particle size analysis was then carried out in accordance with BS ISO 13320-1:1999 – Particle size analysis – Laser diffraction methods – Part 1: General principles [175].

3.8.7 Surface Area Determination

The surface area of the powder was determined using the Micromeritics GEMINI BET surface area analyser. BET stands for Brunauer, Emmett and Teller, the three

scientists who optimised the theory for measuring surface area based on gas absorption. In physical gas absorption an inert gas, such as nitrogen, is adsorbed onto the surface of a solid material. Since the area of a molecule of N_2 is known, the area covered by a monolayer of adsorbed N_2 can be calculated.

3.9 Analysis of Substrate

3.9.1 XRD

An XRD scan of the titanium substrate was carried out using the same scanning parameters as for the HA powder, outlined in *table 3.15*. The analysis was carried out following the grit blasting procedure.

3.9.2 Roughness

The surface roughness (Ra) of the grit blasted titanium disks was determined using a Mitutoyo Surftest 402 surface roughness tester. This equipment consists of a stylus that is run over the surface of the coating. Prior to measurement the accuracy of the roughness tester was checked using a calibration block. The sample was held in place using tape to prevent movement during measurement that would lead to inaccuracy. Three measurements were taken for each sample and then the average of these was determined.

3.10 Analysis of HA Coatings

3.10.1 Coating Mounting, Grinding and Polishing

The HA coated samples were sectioned in order to allow their cross-section to be examined. Standard Bakelite mounting resin was found not to be suitable for the HA coated samples as it was difficult to distinguish between the coating and Bakelite under microscope examination. A clear resin was found to given better results. The resin used was Beuhler Epoxide Resin and Epoxide Hardener, mixed at a resin to hardener ratio of 5:1. The samples were placed in moulds which were then filled with the resin taking care to maintain the desired sample orientation. They were cured for at least 12 hours prior to removal from the moulds.

Grinding and polishing was carried out on the Motopol 2000 grinder and polisher. The grinding and polishing of HA coated samples posed problems due to the hardness mismatch between the titanium substrate and the HA coating. HA is also brittle and easily damaged during the grinding process. Conventional polishing procedures have been shown in work by Taylor [77] to have detrimental effects on the hydroxyapatite coatings. The grinding and polishing procedure used were developed based on the work of Taylor [77] and also on advice from Bueler, the supplier of the equipment. The protocol followed is given in *table 3.16*.

Table 3.16: Grinding Procedure used for HA coated samples

Process	*Surface*	*Abrasive*	*Lubricant*	*Time*	*Speed*	*Force*
Planar Grinding	SiC – Paper	P60	Water	Until Planar	250rpm	10N
	SiC – Paper	P240	Water	2 mins	250rpm	10N
Sample Integrity Stage	UltraPol	6μm Diamond Suspension	-	7 mins	150rpm	10N
	MicroCloth	3μm Diamond Suspension	-	7 mins	150rpm	10N
Final Polishing Stage	MicroCloth	Masterprep polishing suspension 0.05μm	-	10 mins	150rpm	10N

Grinding was carried out until damage caused by sectioning of the HA coated sample was removed and the sample was planar. Following polishing, the mounted samples were cleaned in a dilute acetone solution to remove any remaining polishing debris. Beuhler polishing cloths and 3μm and 6μm Beuhler

MetaDi monocrystalline diamond suspensions were used to polish the samples. Masterprep Polishing Suspension 0.05μm was used for the final polishing stage.

3.10.2 Surface Morphology

The surface morphology and polished cross-section of the HA coatings was examined using the SEM. The scanning parameters used were as for the HA powder (see *table 3.14*). HA is a non-conducting material, but as the HA layer is thin, it was possible to obtain good images of the surface of the HA coated titanium discs by ensuring good contact between the titanium substrate and the aluminium sample mounting plate. For the analysis of the mounted, polished sections of HA coated titanium, it was necessary to provide a conducting path between the titanium substrate and the aluminium sample plate using copper tape.

3.10.3 Crystallinity and Purity Measurements

The crystallinity and purity of HA coatings were again determined using XRD. The same scan parameters used were as for the HA powder, outlined in *table 3.13*. The XRD scans were carried out on as sprayed coatings, the coating was not removed from the substrate. The coated HA discs were mounted on the XRD plate using double sided tape. The crystallinity and purity of the coatings were also determined using the procedures set out for HA powder in *Section 3.8.2* and *Section 3.8.3*.

3.10.4 Porosity Measurement

The porosity measurements were carried out in accordance with the BSI standard 1071-5: 1995: Advanced technical ceramics – Methods of test for ceramic coatings - Part 5: Determination of porosity [150]. Porosity measurements through the cross-section of the coated samples were carried out. The samples were first mounted, ground and polished according to the procedure in *Section 3.10.1*.

Micrographs of each of the coating cross-sections were then obtained using the Reichert “MeF2” Universal Camera Optical Microscope. The coating sections to

be measured were selected at random points along the cross section of the sample. A magnification of 20 x was used for each coating.

The Beuhler Omnimet Enterprise image analysis software was used for the analysis of the coatings. A programme, called a routine, was developed in the software to calculate the porosity of the coating. The routine consisted of a number of steps. Firstly the image was sharpened. The grey scale level was adjusted to highlight the pores in the coating in red. Areas within the coating were selected at random for analysis. The percentage of the selected area within the image that was highlighted in red was then determined by the software. Porosity measurements could not be carried out for all coatings as some were too thin for accurate measurements to be obtained. Measurements were repeated four times for each coating.

Use of image analysis software allows accurate porosity determination. Errors in using this method relate to selection of the correct grey level to highlight pores in the coatings. The amorphous content of a HA coating appears as dark regions within the coating using microscope analysis. For coatings containing a high amorphous content it was difficult to accurately select pores. The porosity value measured is the pore area fraction, the area of pores per unit area of coating.

3.10.5 Thickness Measurement

The micrographs of the polished samples taken using the optical microscope were used to determine the thickness of the coatings. The Omnimet Enterprise image analysis software was used for these measurements. A measurement bar was added to the image to determine the thickness of the coating. To reduce measurement error, this measurement was repeated at 6 locations along the length of the coating.

3.10.6 Roughness

The surface roughness (Ra) of the coatings was determined using a Mitutoyo Surftest 402 surface roughness tester using the parameters outlined in *Section 3.9.2*. Four measurements were carried out for each coating.

3.11 Biocompatibility Testing

In order to evaluate the expected in vivo response to the HA coatings produced in this study, a cell culture study was carried out in conjunction with the National Institute for Cellular Biotechnology (NICB). Details of this study are given in this section.

3.11.1 Cells

The cells used for biocompatibility testing were MG-63 human osteoblast bone cells, supplied by LGC Promochem. These cells were cultured in standard growth medium, supplemented with 10% fetal bovine serum. 100ml of the medium consisted of 87 ml of Eagle's minimum essential medium, 10 ml fetal bovine serum, 1 ml non-essential amino acids, 1 ml Glutamine and 1 ml sodium pyruvate. Cells were proliferated at 37ºC in humidified incubator in the presence of 5% CO_2 until there was a sufficient stock for the experimental work.

3.11.2 Cell Culture Study

Four surfaces were compared in this study, cell culture plastic (the control), titanium, a dense HA coating (Coating A) and a porous HA coating (Coating B). The cell seeded coatings were then incubated for 4 different time points, 7 days, 14 days, 21 days and 28 days. Cell content, cell viability and gene expression analysis were carried out at each time point. The expression levels of the following genes were selected for investigation: Type 1 Collagen, Alkaline Phosphatase, Osteocalcin and Glyceraldehyde Phosphate Dehydrogenase (GAPDH). The cell testing work carried out is summarised in *table 3.17*.

Table 3.17: Cell Culture Test Summary

Surface	*Tests*	*Incubation*	*Genes for Analysis*
Contol	Cell Content	7, 14, 21, 28 days	Type 1 Collagen
Uncoated Titanium	Cell Viability		Alkaline Phosphatase
HA Coating A	Gene Expression		Osteocalcin
HA Coating B			GAPDH

Before cell testing was carried out, the Ti and HA-coated discs were sterilised using dry heat at 160 ºC for 3 hours. The discs were placed in four 24-well plates, one plate for each time point. Two sets of samples in triplicate were required for each surface at each time point, one for cell proliferation and cell viability analysis and one for gene expression analysis. The discs were laid out in each of the plates as shown in *table 3.17,* each surface being run in triplicate.

Table 3.18: 24-Well Plate Set-up

	Cell Proliferation and Viability			**Gene Expression Analysis**		
Control	1	2	3	1	2	3
Titanium	1	2	3	1	2	3
Coating A	1	2	3	1	2	3
Coating B	1	2	3	1	2	3

Prior to starting the experiment, Day 0 cell proliferation and viability measurements were made. An RNA sample was also taken for gene expression analysis. Cells were seeded on the surface of the discs at a density of 10,000 cells per well with 0.5ml of the previously prepared culture medium, along with 1% antibiotics (Pen-Strep). The cells were placed in an incubator for 1 hour to allow well attachment to occur. Following this an extra 1ml of cell medium was added to each well. The plates were incubated at 37ºC with 5% CO_2 for 7, 14, 21 and 28 days. Every seven days half the medium was replaced with fresh medium.

3.11.3 Cell Proliferation and Viability

At each time point the cell proliferation and cell viability were determined using a hemacytometer and a phase contrast microscope. Prior to counting, Trypan blue solution was added to cell suspension in order to stain dead cells for the cell viability counts. All counts were carried out in triplicate and an average of the counts was taken.

3.11.4 RNA Extraction and Quantifiation

The expression of extracellular matrix (ECM) mineralization markers in MG-63 cells on the four surfaces was determined by RNA extraction and quantitative real time PCR. Total RNA was isolated at each time point using the RNeasy Mini kit (Qiagen, UK). The cells were lysed and the cell lysate was then homogenised. The purified RNA was stored at -80ºC. The total RNA concentrations were determined spectrophotometrically at a wavelength of 260 nm.

3.11.5 Quantitative Real-Time PCR

Prior to carrying out Real-Time PCR, the cell culture triplicates were pooled. The RNA samples for each condition were carried out in triplicate to account for any pipetting errors. Four genes were measured in this study Glyceraldehyde-3-phosphate Dehydrogenase (GAPDH), Alkaline Phosphatase (ALPL), Type 1 Collagen (COL1A2) and Bone Gamma-Carboxyglutamate Protein (BGLAP), also called osteocalcin. The gene expression assays for each gene were supplied by Taqman.

Relative gene expression was carried out using the Applied Biosystems 7500 Fast Real-Time PCR System. The cycle conditions for RT-PCR were as follows: 95ºC for 20 minutes, 40 cycles of 95 ºC for 3 minutes and 60 ºC for 30 minutes. GAPDH was used as the control on each plate. Water was also used as the non template control (NTC) on each plate. Four PCR plates were run. The set-up of plate 1 is shown in *Appendix D*. All surfaces and genes for Day 14 were run together on the final plate.

3.11.6 Statistical Analysis

Statistical analysis for cell culture work was carried out using StigmaStat 3.0. The One-Way Anova test was used to test for significance. A p-value of < 0.05 represented a significant difference.

4 Results and Discussion

4.1 Introduction

In this chapter, the results of the experimental work carried out as part of this research are presented and discussed. Firstly, the results from characterisation of the powder and substrate materials used are presented. Following this, the results from the heat treatment study of HA coatings are described. Thirdly, the results of the initial coating production investigation experimental work are discussed, with initial DCU HA coatings being compared to HA feedstock powder. The Screening Experiment and the DOE models developed for the screening experiment are then discussed. Following this, the results from the Response Surface Methodology study are presented and discussed in detail along with the DOE models developed for each response. The results from the optimisation process are then given along with the discussion of the bi-layer coating produced. Finally, the results from the cell culturing experimental work are presented and analysed.

4.2 Materials

4.2.1 Hydroxyapatite Powder

Powder Morphology and Size

The results from the scanning electron microscopy conducted on the Plasma Biotal Captal 60-1 HA powder particles are shown in *figure 4.1*. It can be seen in this micrograph that the particles consist of an agglomeration of smaller particles, due to the powder production process utilised by Plasma Biotal. The powder is seen to consist of a mix of the particles with a spherical morphology and particles with a slightly irregular morphology. Powder containing a large amount of highly irregular shaped particles is not suitable for plasma spraying as they are heated unevenly in the plasma flame, leading to the introduction of process variability. Highly irregular particle morphology also leads to poor particle flowability within the hopper, powder feed hose and on injection into the plasma flame and to flow instability during the spray process. The fraction of irregular shaped particles present in the powder appears (from SEM analysis) to be low and the degree of

irregularity is small and thus this powder was deemed suitable for use in this work.

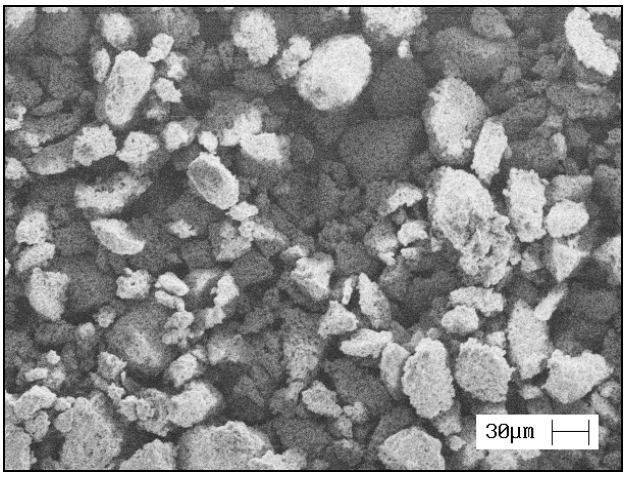

Figure 4.1: Plasma Biotal Captal 60-1 HA Powder Micrograph

The size, density and surface area of the powder particles were found using the procedures outlined in *Section 3.8*. The particle size distribution within the powder was determined using laser particle size analysis. The resulting relative and cumulative volume % particle size distribution within the coating are shown in *figure 4.2*. The mean particle size of the HA powder was found, from the laser particle size analysis, to be 38.3 µm (D(v,0.1) = 3.56 µm, D(v,0.9) = 70.07µm). This was lower than the 45 µm typical average particle size reported by the supplier. It is possible that some of the agglomerated particles may have broken up during transport of the powder. The dispersion of the powder to create a suspension prior to particle size analysis may also have caused a certain degree of particle break up. The 38.3 µm average particle size meets the requirements for this study as it falls within the 20 – 45 µm average particle size range found by Kweh et al. [111] to produce dense, good quality coatings.

The particle size analysis results indicate that the size of the particles fall within two separate clusters, one between 0.1 and 1.0 µm and the other between 10 and 100 µm. The particles in the 0.1 to 1.0 µm cluster are most likely present as a result of deagglomeration of the larger HA agglomerates. The remainder of the particles fall within a narrow range (10 to 100 µm) which fits this application, as a

narrow particle size distribution results in less variation in the degree of melting of particles within the plasma flame.

The average density of the powder sample was found using helium pycnometry to be 3.28 g/cm^3. The surface area of the powder was found using BET surface area analysis to be 0.4640 m^2/g. These powder properties are similar to those of other commercial HA thermal spray powders [176] and thus deemed suitable for this application.

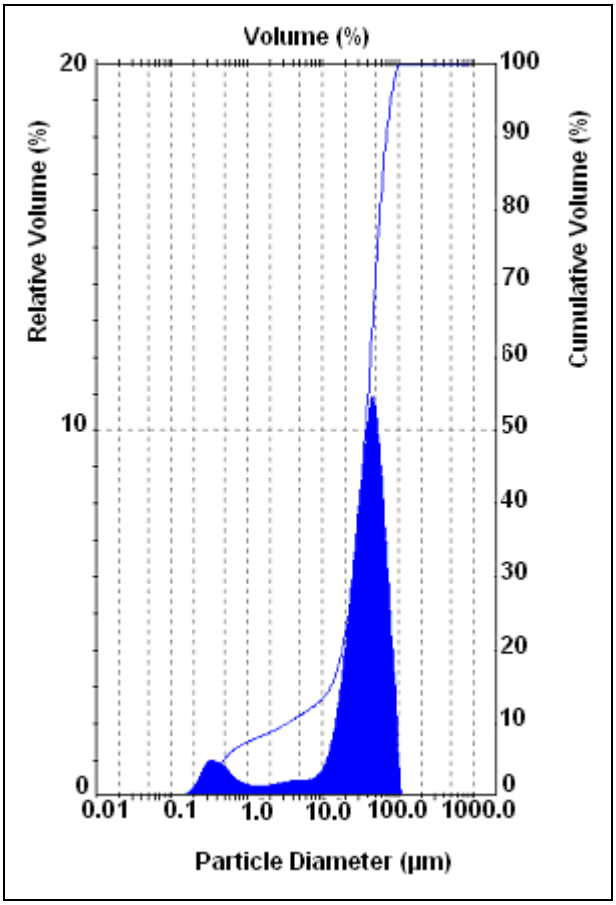

Figure 4.2: Particle Size Distribution of Plasma Biotal Captal 60-1 HA Powder

Crystallinity and Phase Composition

The XRD pattern for the HA powder is shown in *figure 4.3*. The crystallinity and purity of the HA powder was calculated from this diffraction pattern using the *equation 2.9* and *equation 2.11* in *Section 2.7.1*. The crystallinity was found to be 99.96%, which meets the > 95 % crystallinity requirement for HA powder for

medical applications as outlined in ISO 13779-:2000 [94]. The purity was 99 %, which meets the > 95% purity requirement set out in the ASTM standard F1185-88 [93]. Analysis of the peaks in the pattern shows that the main phase present is HA (JCPDS 9-0432) and a minor trace of tetracalcium phosphate (JCPDS 25-1137) is also present.

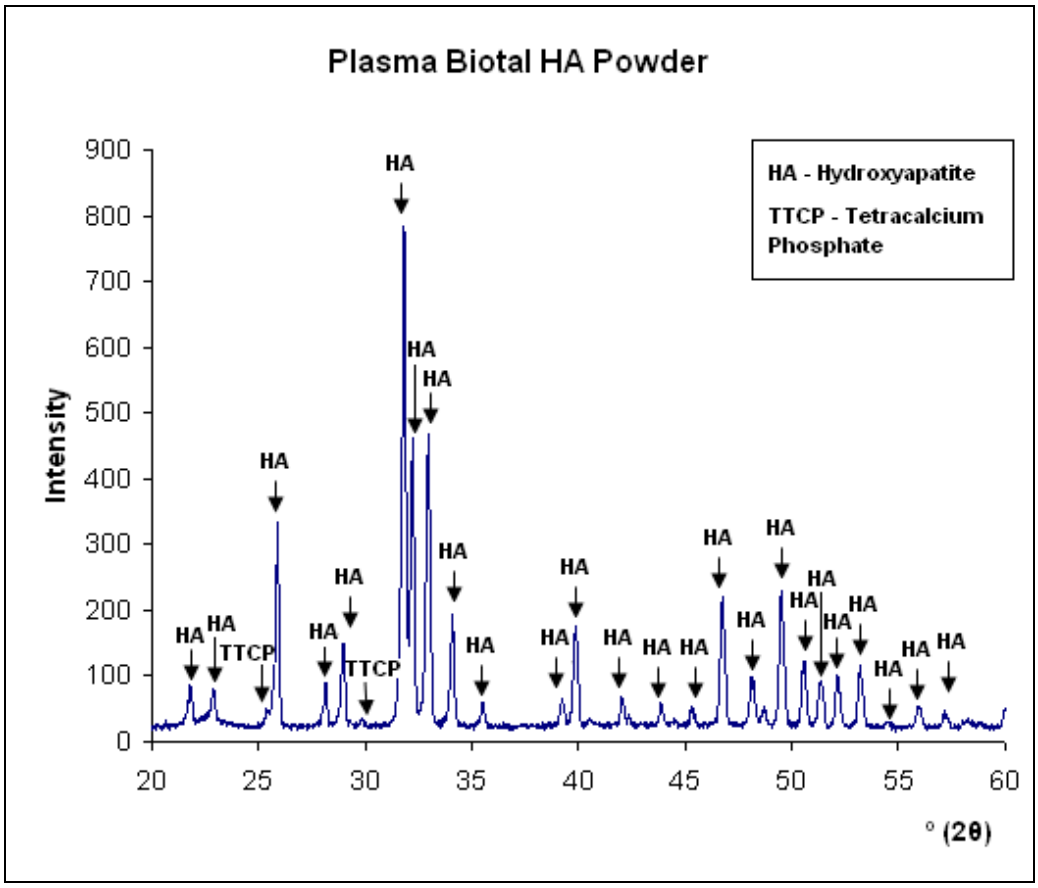

Figure 4.3: Plasma Biotal Captal 60-1 HA Powder XRD Pattern

Thermal Properties

The graph in *figure 4.4* shows the results for the thermogravimetric analysis (TGA) of the HA powder. The TGA curve shows the % weight loss of the powder while being heated from 20 ºC to 1400 ºC. From *figure 4.4* it can be seen that no weight loss occurs between ~100 ºC and ~ 900 ºC indicating the absence of absorbed water in the sample. Weight loss is observed to occur from ~ 900 ºC to ~1350 ºC, relating to dehydroxylation of HA followed by the formation of β-TCP. Similar results for thermogravimetric analysis of HA powder have been reported by Gross et al. [177] and Tampieri et al. [64]. The Differential Thermal Analysis

(Diff T) plot does not provide any useful information as a very small degree of weight loss occurs for HA.

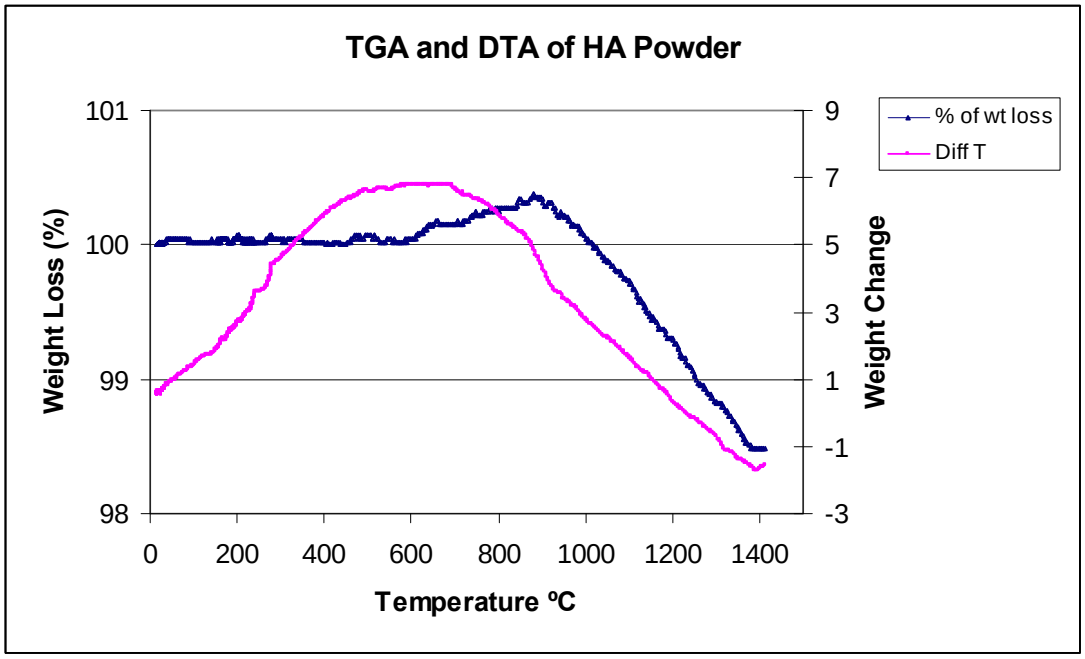

Figure 4.4: TGA and DTA results for the HA powder

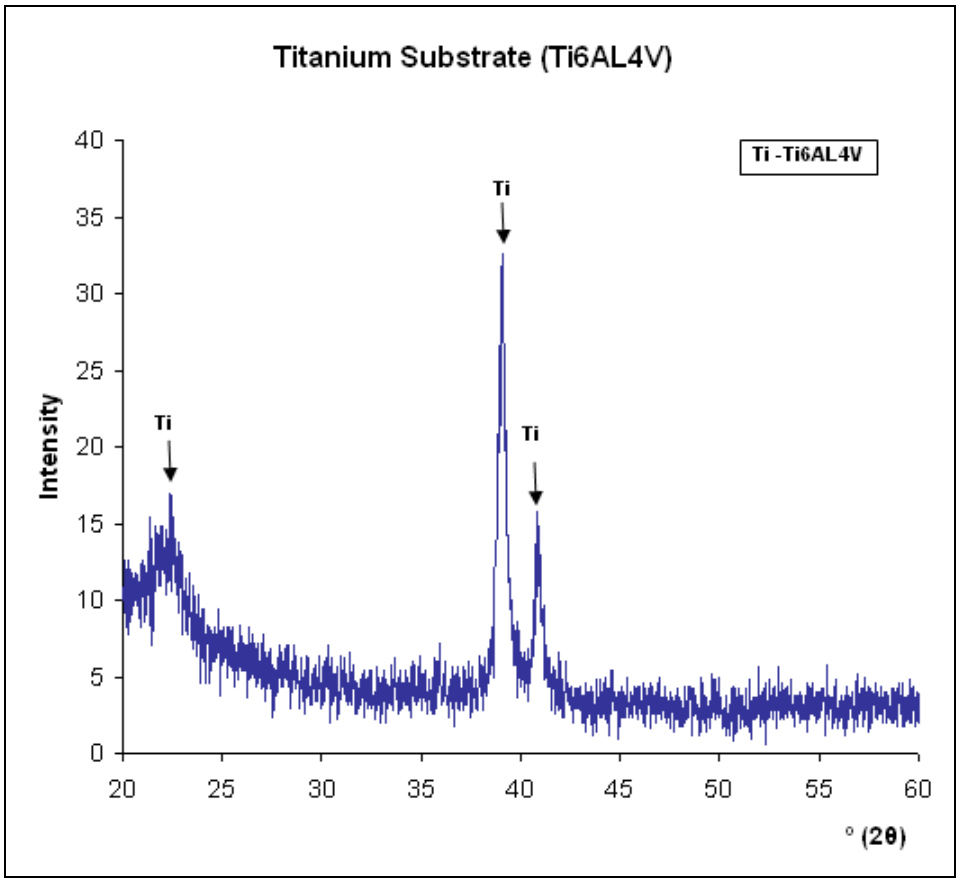

Figure 4.5: XRD pattern of Ti6Al4V substrate material

4.2.2 Substrate Material

XRD

The XRD pattern for the titanium (Ti6Al4V) substrate material is shown in *figure 4.5*. The main peaks for the substrate material are found at 23.1 º 2θ, 39.8 º 2θ and 40.8 º 2θ. It is necessary to know the position of these peaks so that they can be identified if found to be present in the XRD patterns of very thin HA coatings.

Surface Roughness

Prior to spraying, the roughness of ten grit blasted titanium discs, selected randomly, was measured using the surface profilometer following the procedure outlined in *Section 3.9*. An image of a grit blasted titanium disc is shown in *figure 4.6*.

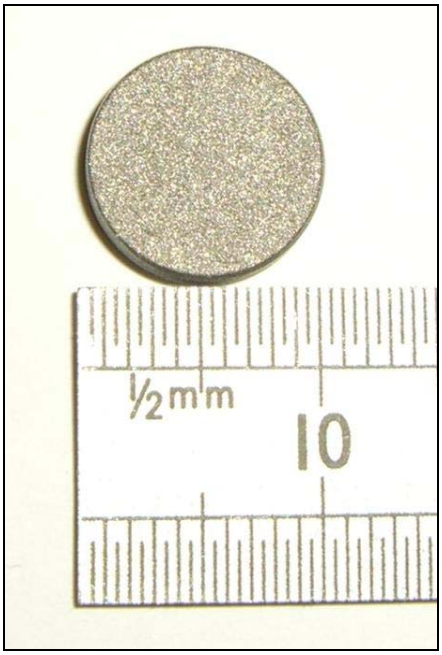

Figure 4.6: Grit blasted substrate

The roughness results are given in *table 4.1*. As is discussed is *Section 3.5.1*, to ensure consistent results, great care was taken to ensure that the grit blasting procedure and subsequent cleaning were carried out in the same manner for each titanium disc. The average surface roughness was 3.12 µm. This value matches the roughness values suggested by Yang and Chang [92] to provide the

requirements for high coating adhesion without generating excessive oxidation of the microsurface of the Ti-alloy during grit blasting. The standard deviation recorded is less than the 1.0 μm standard deviation reported in a study of grit blasting for plasma spray applications by Bahbou et al. [178]. This indicates that the procedure followed is repeatable and results in a roughness suitable for this application.

Table 4.1: Substrate Surface Roughness

Sample	*R_a value (μm)*				
	1	*2*	*3*	*Average*	*SD*
1	3.0	3.2	3.4	3.2	0.2
2	3.5	3.4	3.1	3.3	0.2
3	3.4	2.7	3.0	3.0	0.4
4	3.1	3.2	3.2	3.2	0.1
5	2.8	3.4	3.1	3.1	0.3
6	3.3	3.5	2.9	3.2	0.3
7	3.0	2.6	3.2	2.9	0.3
8	2.8	2.9	2.8	2.8	0.1
9	2.9	2.8	3.0	2.9	0.1
10	3.0	3.3	2.9	3.1	0.2
			Average	3.1	0.2

4.3 Post Spray Heat Treatment Results

Post spray heat treatment of plasma sprayed HA coatings was carried out to investigate the potential for recrystallisation of the amorphous phases of the plasma sprayed coating. As discussed in the literature review, a high coating crystallinity is required in order to improve coating stability *in vivo*. The coatings used in this study were supplied by Plasma Biotal (detailed in *Section 3.3.2*) as the work was carried out prior to installation of the DCU plasma spray rig. The study was carried out following the procedure outlined in *Section 3.4*. Post spray heat treatment temperatures of 600 °C, 700 °C and 800 °C and treatment times of 1 hour and 2 hours were examined in this study. Changes in coating crystallinity, purity, morphology and physical appearance were analysed and are presented here.

4.3.1 Coating Crystallinity and Purity

The crystallinity and purity of the Plasma Biotal HA coated discs were determined using XRD. The XRD patterns for an as-sprayed HA coating and a HA coating treated at 800 °C for 1 hour, are shown in *figure 4.7*. The as-sprayed coating pattern contains crystalline peaks with evidence of an amorphous diffusion background between 30.5° 2θ and 33.5° 2θ. The peaks present in the diffraction patterns were found to match the standard diffraction pattern for HA (JCPDS 9-432), indicating that the coating analysed is HA. A very high intensity peak was identified at 26° 2θ. A HA peak would be expected at this position; however, it would not be expected to have such a high intensity. It is possible that residual stresses in the sample could have caused this deviation from the expected intensity level. The presence of residual stresses in the coating is also indicated by the fact that the as-sprayed samples were visibly warped. This relates to the spray procedure used by Plasma Biotal in production of the coatings. This peak could also be due to the presence of a contaminant in the coating, possible from residue of a previously sprayed powder in the hopper. Information regarding potential contaminants could not be obtained from Plasma Biotal.

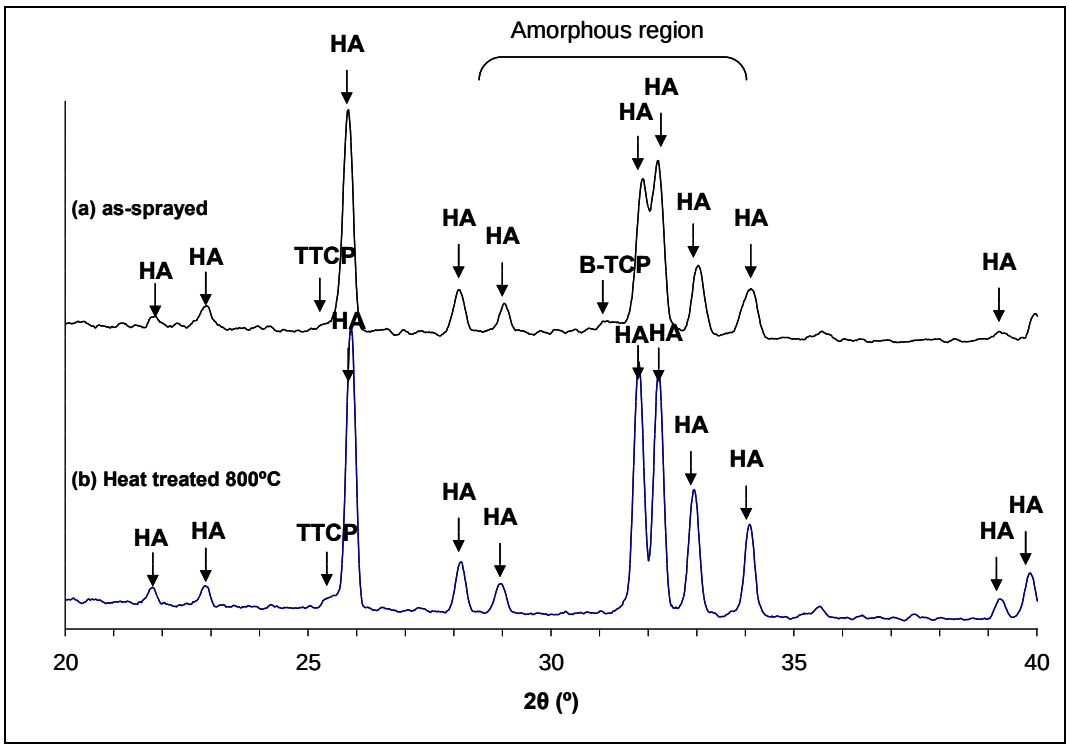

Figure 4.7: XRD patterns for (a) as-sprayed HA coating and (b) HA coating after heat treatment at 800°C for 1 hour

The impurity phase, β-tricalcium phosphate, was identified in the pattern with a peak of 31.5° 2θ. The intensity of these peaks was very low indicating that these phases were present in small amounts. The XRD pattern for the HA coating treated at 800 °C shows that after treatment the HA peaks were sharper and the amorphous diffuse background was reduced. This indicates that the coating crystallinity was increased compared to the as-sprayed coating.

The % crystallinity of each sample was determined from the XRD patterns using *equation 2.9* as per the procedure outlined in *Section 3.10.3*. The results after treatment at 600 °C, 700 °C or 800 °C for periods of 1 and 2 hours are shown in *figure 4.8*. As indicated by examination of the XRD patterns, the % crystallinity of the coatings was found to increase with increasing heat treatment temperature, the as-sprayed coating having a crystallinity of 77% ± 2% and the samples treated at 800°C having a crystallinity of between 85% ± 2% and 88% ± 2%. It is clear from this that the post spray heat treatment procedure has allowed the amorphous content of the coating to recrystallise. The β-TCP peak is seen to disappear after heat treatment indicating that transformation to HA has occurred. This finding is consistent with the findings of Tsui et al. [115] and Lu et al. [130].

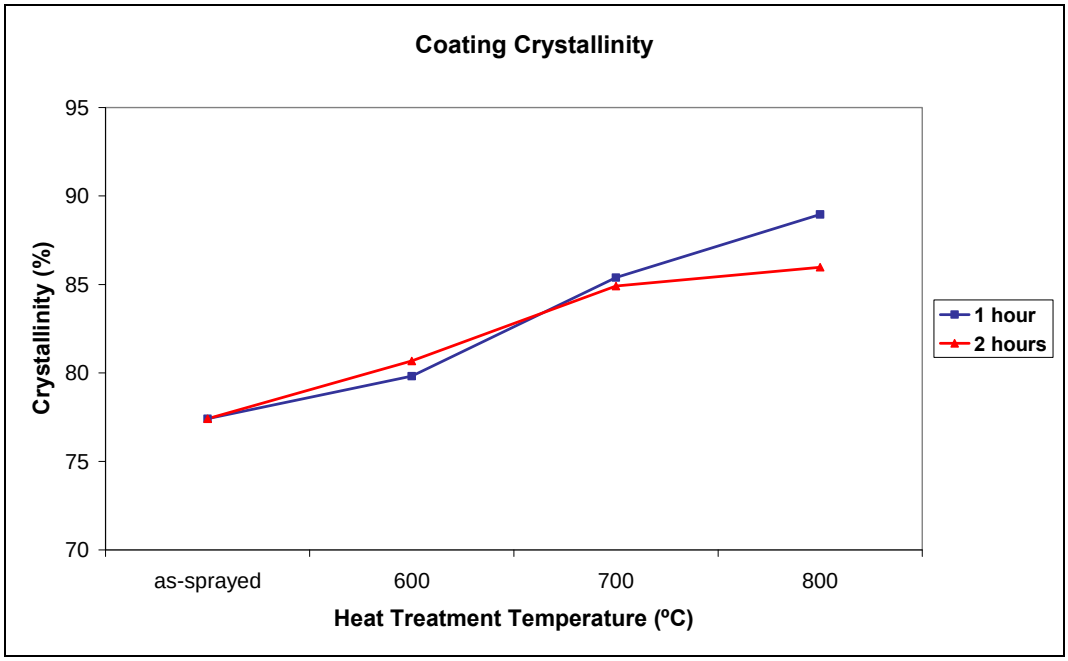

Figure 4.8: Coating crystallinity after 1 and 2 hours heat treatment

From *figure 4.8,* it can be seen that the treatment times investigated had little effect on the crystallinity at temperatures of 600 ºC and 700 ºC. This has also been reported by Lu et al. [130]. At 800 ºC recrystallisation appeared to decrease with increased holding time. This is, in all probability, due to the beginning of the dehydroxylation process which is reported to have a negative affect on recrystallisation in HA coatings recystallisation [109, 118, 119, 130]. The onset of dehydroxylation between about 800 ºC and 900 ºC has been reported by Sridhar et al. [58].

From examination of these results, the optimal settings in order to obtain maximum recrystallisation are a treatment temperature of 800 ºC and a holding time of 1 hour. Similar effects of heat treatment time and temperature on HA coatings have been observed by Espanol et al. [129], Lu et al. [130] and Fazan and Marquis [27].

4.3.2 Surface Roughness

Surface roughness measurement was carried out following the procedure in *Section 3.10.6*. The results, given in *figure 4.9*, indicate that increasing the heat treatment temperature led to an reduction in the surface roughness of the coating. The average Ra value for the un-treated coating was 11.50 ± 1.13 μm and for the coating treated at 800 °C was 10.68 ± 0.97 μm. Although this change in roughness was found to be almost insignificant (smaller than the limits of experimental error), it gives an indication that the temperatures used have allowed sections of the coating to become mobile and susceptible to deformation forces leading to a change in the coating surface morphology.

As discussed in the literature review, high surface roughness is required for HA coated implants to provide an increased surface area for cell attachment, as shown by Boyde et al. [127] and Boyan et al. [17]. The reduction in surface roughness caused by heat treatment is small and unlikely to have any significant effect *in vivo*. The microstructure of the un-treated coatings and coatings following post spray heat treatment was examined more closely using the SEM.

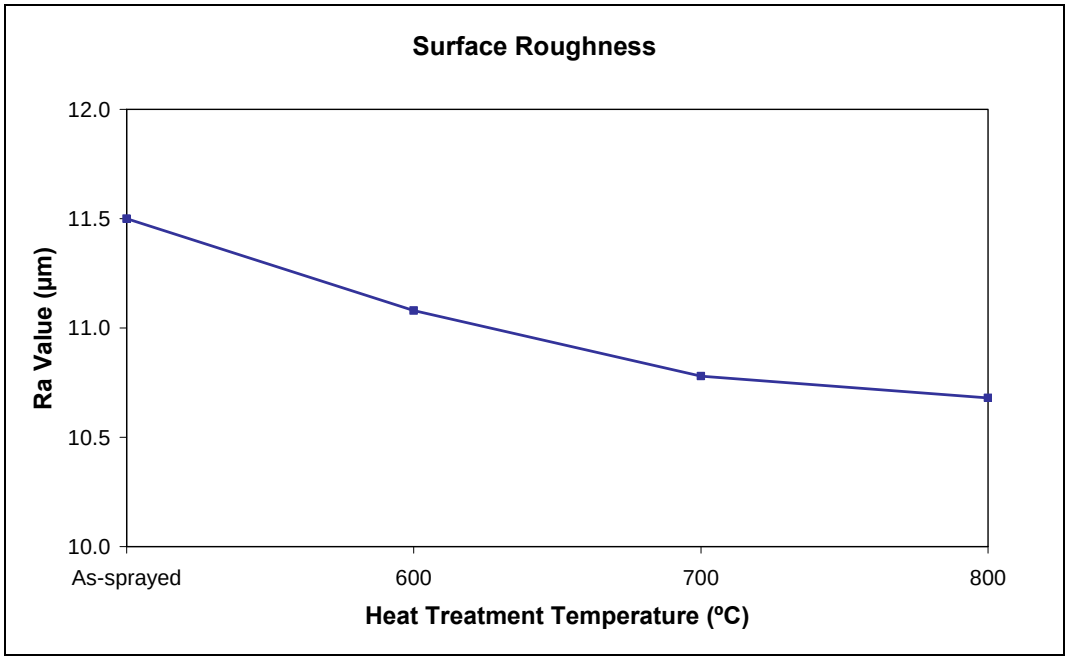

Figure 4.9: Effect of heat treatment temperature on surface roughness

4.3.3 Coating Morphology

SEM micrographs showing the surface morphology of the as-sprayed HA coating and a HA coating after heat treatment at 800 °C are shown in *figure 4.10*. The as-sprayed coating, (*figure 4.10a*), is seen to consist mainly of partially melted particles. The spherical shape of these particles can be observed. Some flattened splats, which are generally formed by fully molten particles, can also be seen. Pores can also be identified in the coating.

After heat treatment, the HA splats had a more flattened/melted morphology as seen in the micrograph in *figure 4.10b*. The surface porosity also appears reduced. These micrographs confirm, that as found from measurement of the surface roughness of the coating, the heat treatment process has allowed parts of the HA coating to become mobile and susceptible to deformation forces and thus a change in the surface morphology of the coatings can be observed.

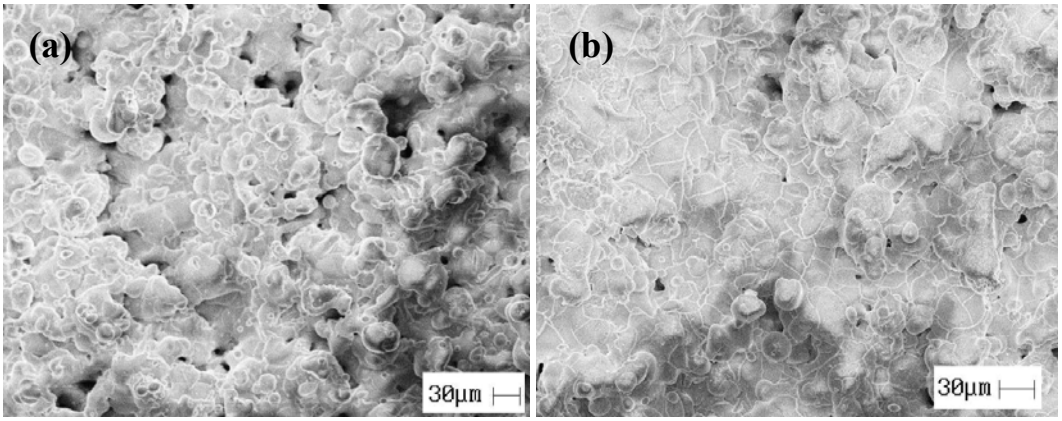

Figure 4.10: SEM micrographs of (a) as-sprayed HA coating and (b) HA coating after heat treatment at 800°C for 1 hour

Closer examination of the samples revealed that numerous microcracks were present in the coatings treated at 800 ºC, shown in *figure 4.11*. The cracks were seen to follow the splat boundaries and are caused by the shrinkage of the amorphous phase. Crack formation is detrimental to the coating as it leads to a decrease in the mechanical strength of the coating [115] and increased coating dissolution which is known to be initiated at microcrack sites [27]. These dissolution initiation sites counteract the improvements in coating stability brought about by the increase in crystallinity following the heat treatment process. The formation of microcracks following post spray heat treatment has also been reported by Fazan and Marquis [27] and Lu et al. [130].

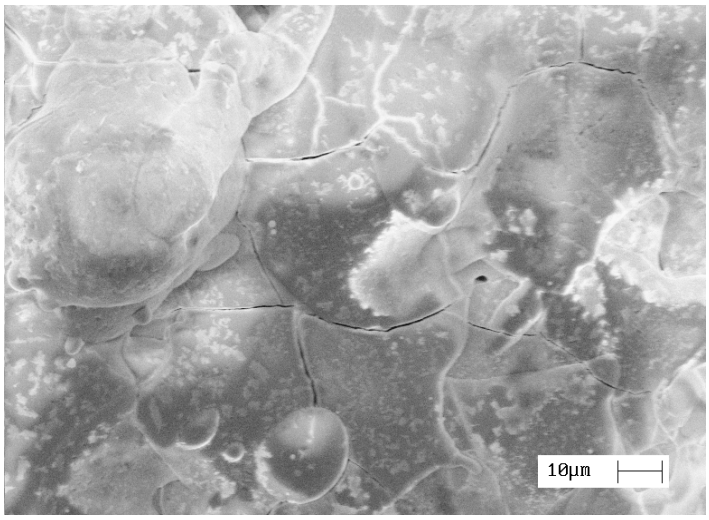

Figure 4.11: Microcrack formation after treatment at 800ºC for 2 hours

SEM examination of coatings treated at 700 ºC indicated that the degree of microcracking at this temperature was significantly less than at 800 ºC. A heat treatment temperature of 700 ºC thus appears more favourable. A further advantage of using a temperature of 700 ºC rather than 800 ºC is that it is less likely to have an adverse effect on the titanium substrate [115].

The post heat treatment process was found to cause a change in the colour of the coatings. The as-sprayed coatings were a greyish-white colour. After heat treatment the samples were green in colour, with the sample treated at 800 °C undergoing the biggest colour change. A change in the colour of the HA coating is undesirable from an aesthetic point of view. The end user of HA coated implants, the surgeon, would expect the HA coating to be white in colour. *Figure 4.12* shows a HA coating following treatment at 800 °C for 2 hours.

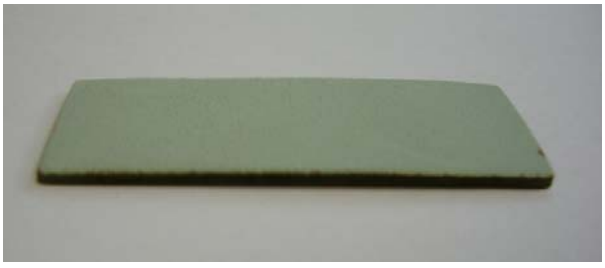

Figure 4.12: Green appearance of coating after heat treatment at 800 °C for 2 hours

Other researchers, such as Fazan and Marquis [27] and Sridhar et al. [58], have also observed a colour change in HA coatings following post spray heat treatment at similar temperatures. This colour change is due to the presence of coating impurities [27]. It is unclear as to the exact nature of the impurities present. Energy Dispersive X-ray Analysis (EDX) was performed to investigate the elemental composition of as-sprayed and heat treated samples. No difference could be observed between the two. Colour change of the HA coatings has been found not to occur when the post spray heat treatment was carried out in a vacuum [58].

The findings of this study indicate that post spray treatment can allow recrystallisation of the amorphous component of HA coatings. Taking into

account the requirement for high crystallinity and the necessity to maintain the structural integrity of the coating a treatment temperature of 700 °C and treatment temperature of 1 hour were selected as being most appropriate. Although improvements in crystallinity can be achieved, the process also has disadvantages. Both colour change and crack formation that occur during heat treatment are undesirable. It is hypothesised that control of coating crystallinity through optimisation of plasma spray process parameters would avoid the necessity for post spray heat treatment and thus avoid the associated detrimental affect of heat treatment on the coating structure.

4.4 Preliminary Process Investigation

Before beginning the Design of Experiment study, a preliminary process investigation was carried out. The parameter space, were first investigated in order to select suitable ranges for the production of HA coatings. The preliminary coatings produced in this study were compared to the original HA feedstock powder.

4.4.1 Parameter Space Investigation

The parameter design space investigation was carried out prior to the screening experiment, as per the procedure outlined in *Section 3.7.2*. The aim of this preliminary investigation was to determine suitable ranges for each of the parameters investigated. The results are shown in *table 4.2.*

In the study, the current was varied from 350 A to 950 A. A current of 350 A was found not to be suitable as it did not produce enough heat to sufficiently melt the powder particles. The coating in this case was very thin and was poorly adhered to the substrate. A current of 950 A was found to be too high as it approached the maximum equipment limit for current and caused an equipment power supply fault. Such high current values are rarely used for plasma spraying as they cause excessive damage to the electrode within the plasma gun. A low gas flow rate of 50 SCFH was found to be too low to produce an adequate coating, resulting in a very thin layer even at long spray times. Using powder flow rates of less than 10

g/min and greater than 20 g/min led to powder flow stabilisation problems within the powder feeder unit. A spray distance of 40 mm resulted in cracking and peeling of the resultant coating due to deformation of the substrate material from the high temperature plasma flame, whereas a spray distance of 130 mm was found to be too long and did not produce an adequate coating due to the reduction in deposition efficiency. Finally, using a carrier gas flow rate of 5 SCFH was too low to allow powder particles to enter the plasma stream and thus the resultant coating was very thin and unmelted powder was found in the vicinity of the plasma gun. A carrier gas flow rate of 25 SCFH caused powder flow stabilisation problems. The parameter levels that were found to produce adequate coatings are highlighted in blue in *table 4.2*.

Table 4.2: Results of the Parameter Range Investigation

Parameter	***Variables***					
	1	***2***	***3***	***4***	***5***	***6***
Current *(A)*	**350**	**450**	**600**	**750**	**850**	**950**
Gas Flow Rate *(SCFH)*	**50**	**70**	**100**	**130**	**170**	**190**
Powder Feed Rate *(g/min)*	**5**	**10**	**15**	**20**	**25**	**30**
Spray Distance *(mm)*	**40**	**60**	**80**	**100**	**120**	**130**
Carrier Gas Flow Rate *(SCFH)*	**5**	**10**	**15**	**20**	**25**	-

* The parameters that can be used to produce an acceptable HA coatings are identified in blue.

The understanding of the parameter ranges that was gained from this preliminary analysis was used for the selection of the parameter ranges suitable for further investigation in the screening design. In order to understand the effects of the plasma spray process, a coating sprayed using the central plasma spray parameter settings was selected from those produced in the preliminary parameter range investigation and was compared to the feedstock powder. The results from this comparison are discussed in the following section.

4.4.2 Initial HA Coating Investigation

In order to determine the effects of the spraying process on the HA powder feedstock, a comparison was made between the original feedstock material and an initial HA coated substrate selected from the parameter space investigation study. The selected coating was sprayed using the parameters outlined in *Section 3.7.2.* Examples of the initial DCU coatings are shown in the photographs in *figure 4.13.* The XRD patterns of the starting powder and a DCU produced coating are compared in *figure 4.14*.

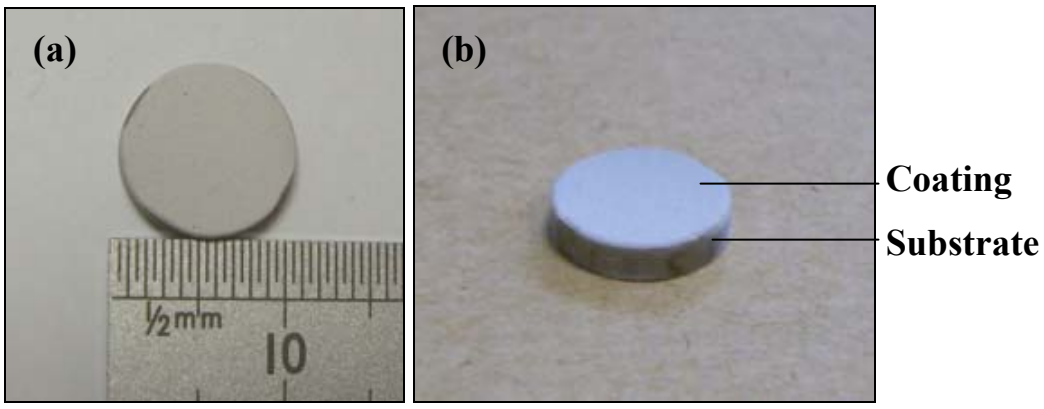

Figure 4.13: DCU Plasma Sprayed HA coated samples. a) DCU coated samples b) side profile

From the analysis of *figure 4.14*, it is clear that transformation of the HA feedstock powder into other calcium phosphate phases has occurred during the spraying process. The main peaks of α-TCP and β-TCP can be identified in the XRD pattern of the plasma sprayed powder. The transformation of HA to β-TCP indicates that, according to the phase transformation temperatures outlined in *table 2.4,* the powder particles have experienced temperatures of greater than 1050 ºC within the flame. The presence of α-TCP indicates that the temperature range in which β-TCP is stable has also been exceeded; particle heating of greater than 1120 ºC has occurred. The reduction in crystallinity of the HA coating is evident from the presence of the amorphous diffusion background in the plasma sprayed coating. The appearance of a calcium oxide peak (CaO) is also observed in the sprayed coating. As reported in *Section 4.2.1*, the crystallinity of the powder was found to be 99.96% and the purity was found to be 99%. The crystallinity of this initial DCU HA coating was 75.8% and the purity was found to be 97.7%.

Following investigation of the process parameter space and initial DCU HA coating investigation, the first step of the design of experiment study, the screening design, was carried out.

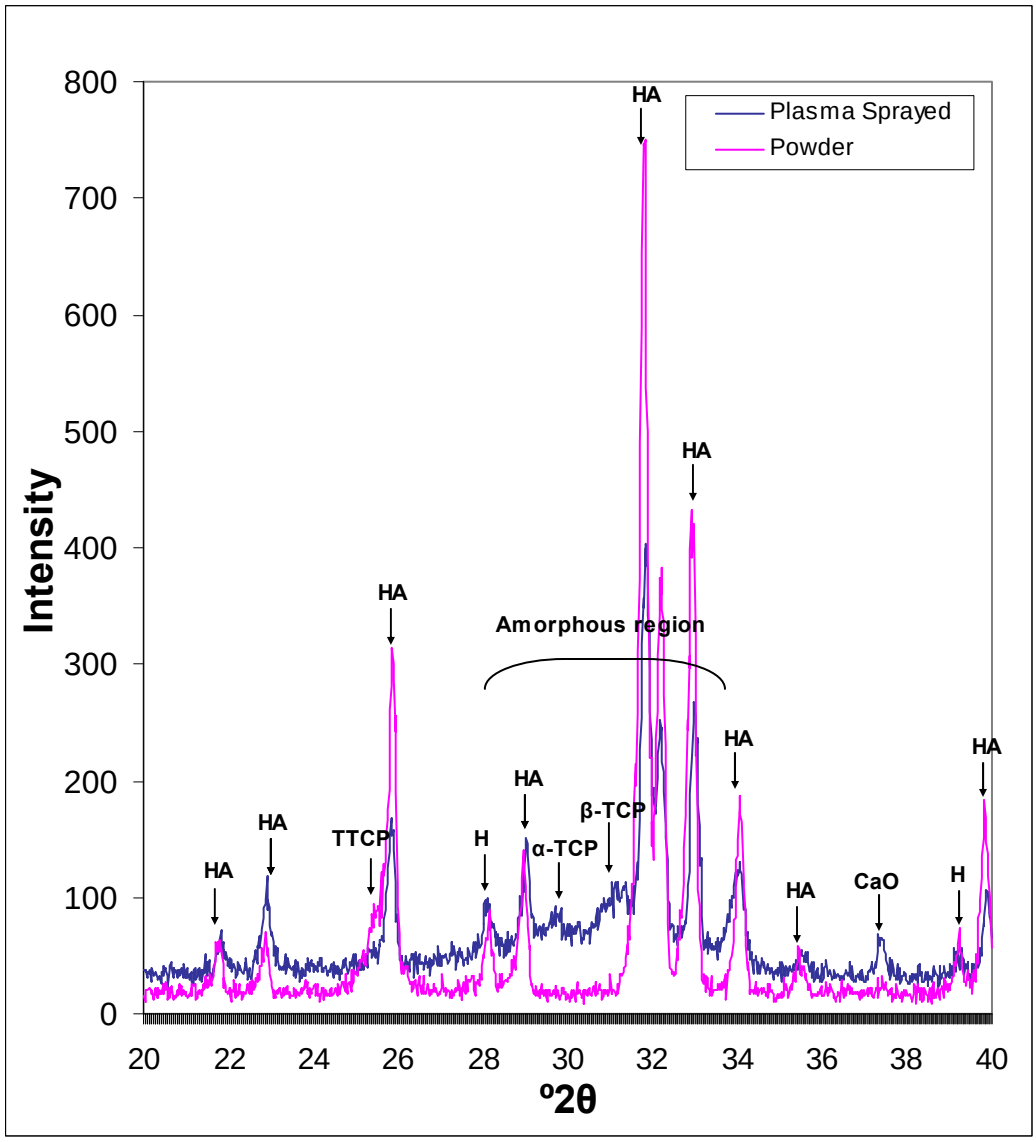

Figure 4.14: Comparison of Plasma Biotal HA powder and DCU Plasma Sprayed HA coating

4.5 Screening Test

4.5.1 Introduction

The coatings for the screening experiment were sprayed according to *table 3.9* in *Section 3.7.2*. In this section the results are presented and discussed. The experimental data is first analysed and following this, the models developed using the Design Expert software are discussed. The models are discussed based on the factor levels required to give high response values. The desirability of a high or low value for each response is discussed in detail in the model optimisation section (*Section 4.7)*.

4.5.2 Initial Analysis of Screening Test Coatings

Following spraying, the 11 coatings produced were analysed. Three responses were measured: coating roughness, coating crystallinity and coating purity. Visual examination of each coated sample was carried out prior to response measurement. It was seen that a viable coating was not produced for experiment N1. The criterion for viability was evidence that the substrate was fully coated based on visual inspection. Low deposition efficiency results for this set of plasma spray parameters and the coating was seen to be extremely thin and patchy with the titanium substrate being visible through it.

Coating N1 was sprayed using the low level for Current (450 A), Gas Flow Rate (70 SCFH) and Powder Feed Rate (10 g/min) and the high level for Spray Distance (120 mm) and Carrier Gas Flow Rate (20 SCFH). Based on current knowledge of the process it is known at that the set of parameters would have fed a low volume of powder through a relatively cool plasma flame at a high speed. This condition results in a low degree of powder melting. Spraying using a larger spray distance generally results in reduced deposition efficiency. It is clear that these conditions are not suitable for the production of HA coatings. Further characterisation of coating N1 was not carried out. The surface roughness, crystallinity and purity of each of the remaining screening test samples were determined and the results for each response are presented in the following sections.

4.5.3 Coating Roughness

The surface roughness (Ra) of the coatings was carried out according to the procedure outlined in *Section 3.10.6*. Four measurements were taken for each sample and then the average of these determined. The average roughness was found to vary between 6.15 µm and 13.4 µm. The results are given in *table 4.3.* The coating with the lowest roughness was that produced for experiment N3. The highest roughness was found for experiment N6. The results are represented graphically in *figure 4.15*.

Table 4.3: Surface Roughness Results

Exp Name	*R_a value (µm)*					
	1	*2*	*3*	*4*	*Average*	*SD*
N1	-	-	-	-		
N2	10.5	9.5	10.5	11.7	10.6	0.90
N3	5.0	6.2	5.7	7.7	**6.2**	1.14
N4	8.0	9.2	8.7	8.7	8.7	0.49
N5	12.0	10.7	9.7	9.5	10.5	1.14
N6	15.7	11.5	12.2	14.2	**13.4**	1.91
N7	7.2	7.0	7.2	7.7	7.3	0.30
N8	10.2	11.2	11.7	11.0	11.0	0.62
N9	12.7	10.7	8.7	10.5	10.7	1.64
N10	9.2	9.0	9.2	10.5	9.5	0.69
N11	11.0	11.2	10.5	9.7	10.6	0.67

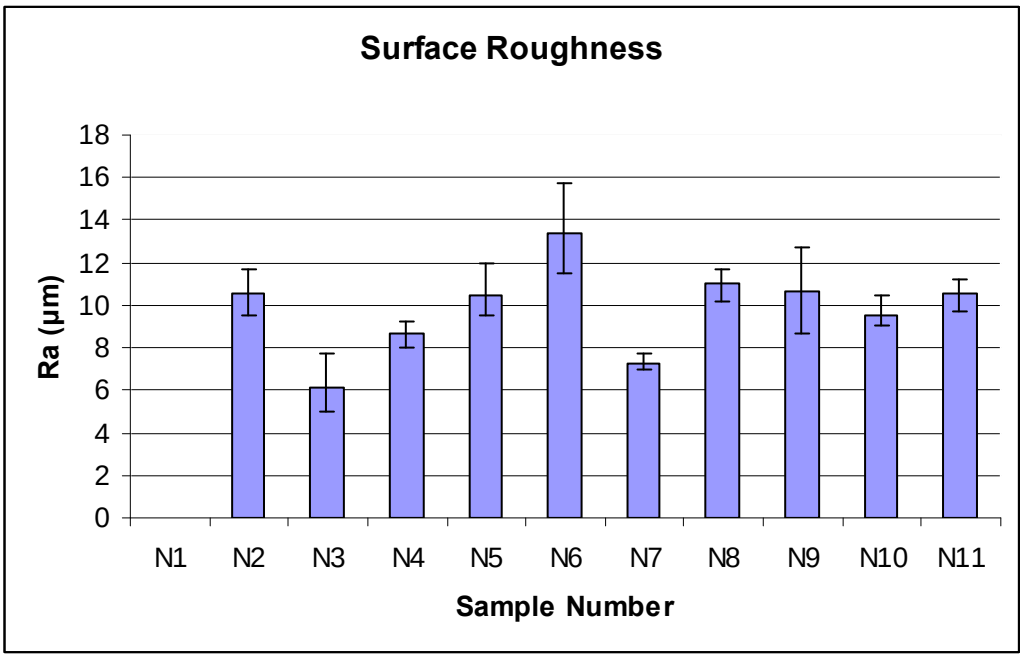

Figure 4.15: Graphical Representation of Surface Roughness Results

It can be seen from *table 4.3* and *figure 4.15* that the standard deviation between repeated measurements is low and thus the measurement error is low. Experiments N9, N10 and N11 were the repeated centre point experiments, added to determine process repeatability. As expected the roughness values of each of these coatings were similar.

4.5.4 Coating Crystallinity

XRD was carried out on each coating. The % crystallinity was determined from the XRD pattern following the procedure outlined in *Section 3.10.3*. The % crystallinity was found to vary between 54.9 % and 87.6 %. The % crystallinity of all coatings exceeds the 45% required by ISO 13779-2:2000 [116] as discussed in *Section 2.5.2*. The values for each coating are given in *table 4.4*. The results are shown graphically in *figure 4.16*. The measurement error in determining crystallinity is low, indicating that the measurement technique is repeatable.

Table 4.4: Crystallinity Results

Exp Name	*Crystallinity (%)*				
	1	*2*	*3*	*Average*	*SD*
N1					
N2	87.8	86.7	88.2	**87.6**	0.78
N3	66.8	63.2	65.6	65.2	1.84
N4	82.3	82.9	78.3	81.3	2.49
N5	65.5	65.4	64.4	**65.2**	0.61
N6	77.0	78.2	77.1	77.4	0.68
N7	77.8	78.7	76.9	77.8	0.90
N8	66.7	64.5	66.3	65.8	1.17
N9	79.6	81.3	78.9	79.9	1.24
N10	55.1	55.9	53.7	**54.9**	1.11
N11	76.2	78.2	73.7	76.1	2.25

The deviation between the two of the three centre point experiments measurements (N9 and N11) was found to be low. The crystallinity of coating N10 was expected to be similar to coatings N9 and N11, however, it was much lower. It is possible that the cooling rate of the sample may have been affected by early removal of the sample from the sample holder thus leading to a lower than

expected % crystallinity. This coating was considered to be an outlier and was not included in the data used for the development of the crystallinity model.

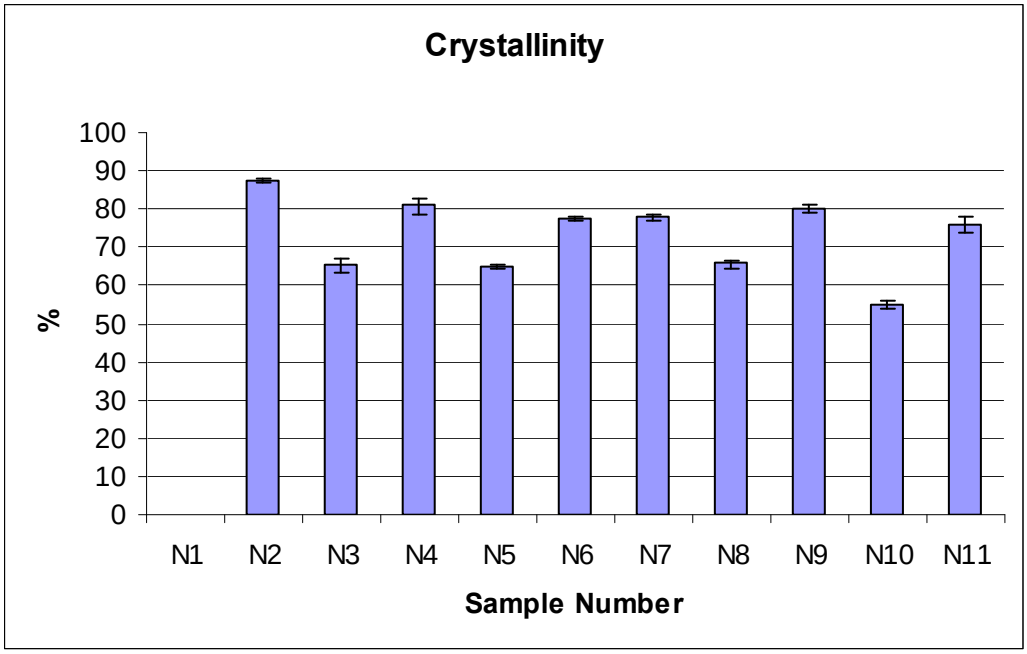

Figure 4.16: Graphical Representation of Crystallinity Results

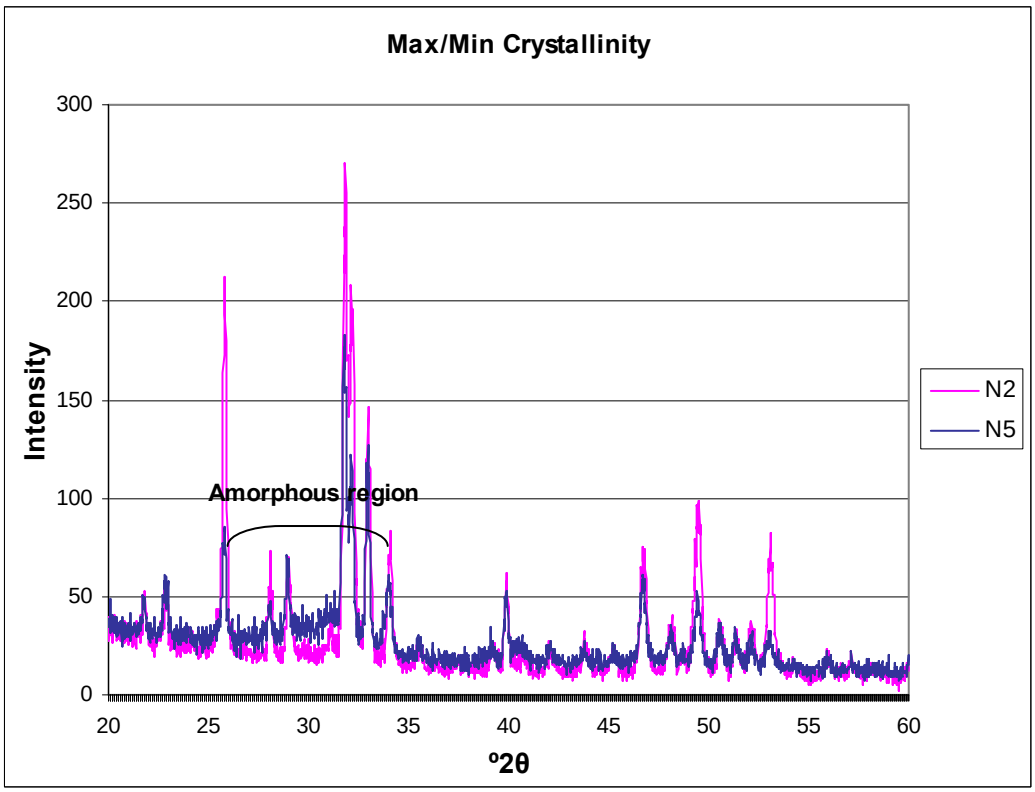

Figure 4.17: XRD patterns for coatings with max and min crystallinity

The coating with the maximum crystallinity was found to be sample N2. The coating with the minimum crystallinity, after exclusion of N10, was found to be sample N5. The XRD patterns for both of these samples are shown in *figure 4.17*. The XRD peaks for coating N2 can be seen to be much higher than the peaks for coating N5. The height of XRD peaks is an indication of the crystallinity of the material, with taller peaks being more crystalline.

4.5.5 Coating Purity

The coating purity was determined using the procedure outlined in *Section 3.10.3*. The XRD patterns were utilised to determine the coating purity. Three purity measurements were carried out for each of the XRD patterns. The purity was found to vary between 95.5 % and 99.4 %. The % purity of all coatings exceeds the 95 % required by *ISO 13779-2:2000* [116]. The results are given in *table 4.5* and presented graphically in *figure 4.18*. Again, measurement error was seen to be small.

Table 4.5: Purity Results

Exp Name	*Purity (%)*				
	1	*2*	*3*	*Average*	*SD*
N1					
N2	99.3	99.4	99.4	**99.4**	0.06
N3	97.8	97.8	97.8	97.8	0.00
N4	98.9	98.9	99.0	98.9	0.06
N5	97.6	97.6	97.5	97.6	0.06
N6	97.8	97.7	97.8	97.7	0.06
N7	98.2	98.3	98.2	98.2	0.06
N8	96.4	96.3	96.4	**96.4**	0.06
N9	97.4	97.4	97.5	97.4	0.06
N10	95.4	95.5	95.5	**95.5**	0.06
N11	97.2	97.3	97.1	97.2	0.10

The purity of coating N9 and N11 was found to be similar indicating process repeatability. Again, the purity of coating N10 was seen to be much less than coating N9 and N11. It was again considered an outlier and not included for the development of the purity model. The highest purity was found for sample N2 and the lowest purity, after elimination of coating N10, was found for sample N8. The

increase in intensity of the peaks of the impurity phases α-TCP and β-TCP, for coating N8 over those in coating N2, can be seen in the XRD scan in *figure 4.19*.

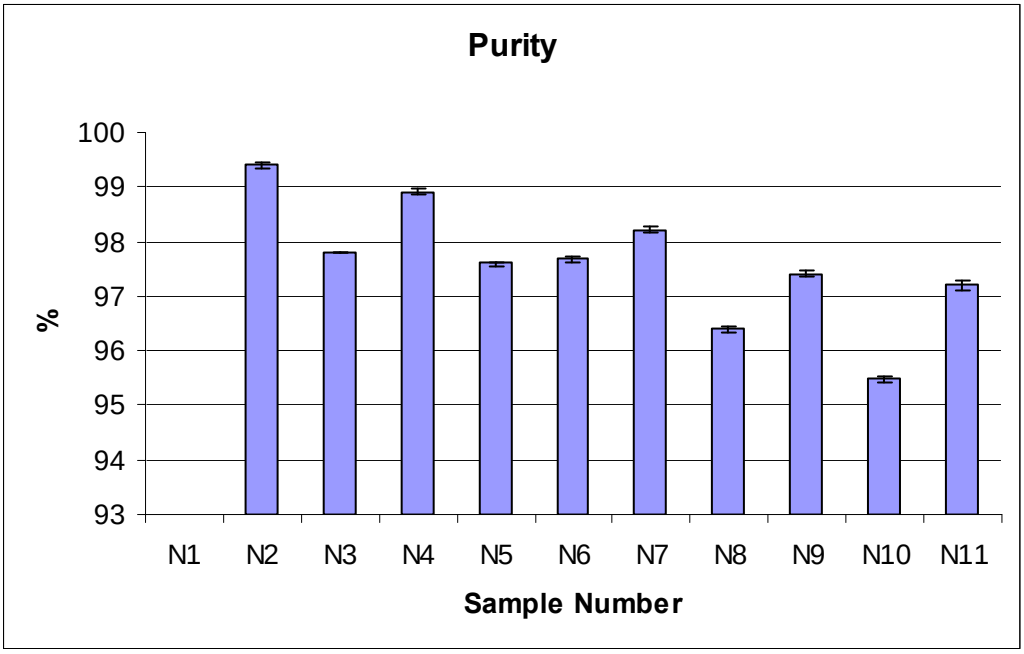

Figure 4.18: Graphical Representation of Coating Purity Results

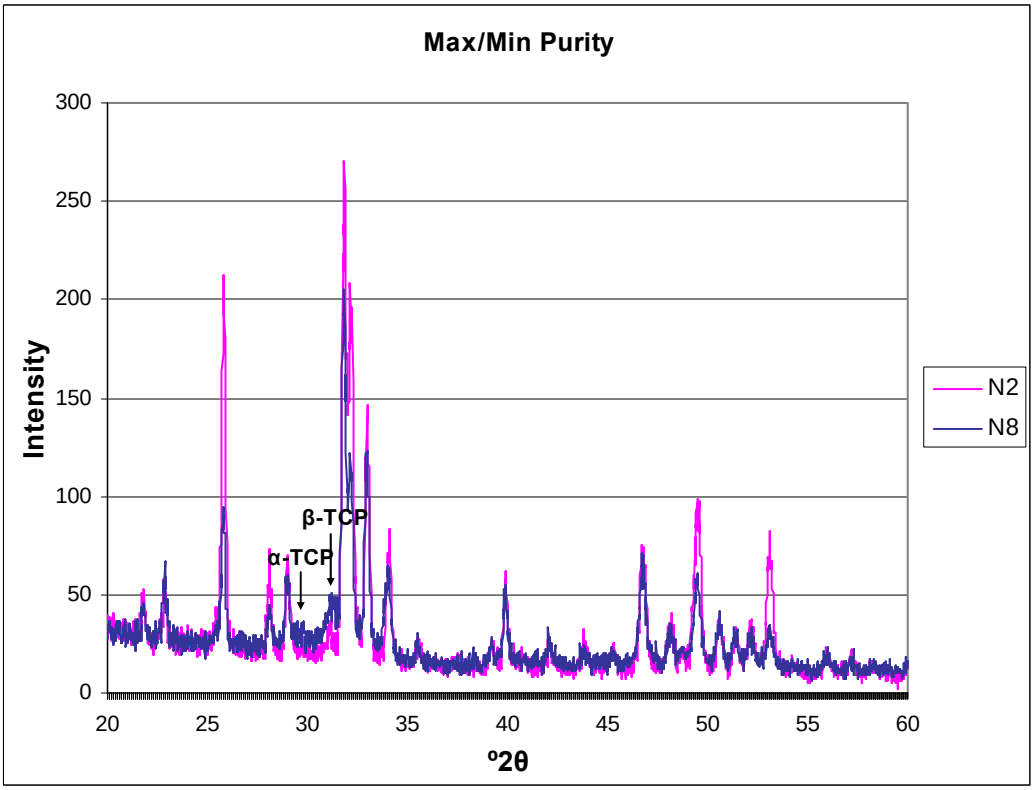

Figure 4.19: XRD patterns for coatings with max and min purity

4.5.6 Model Development

The average roughness, crystallinity and purity values for each experiment are shown in *table 4.6*. The highest and lowest values for each response are listed in bold print in the table. From *table 4.6* it can be seen that the Roughness, Crystallinity and Purity of the coatings vary substantially, within the parameter space under investigation in the screening design. This emphasizes the requirement for optimisation of the process. These average responses were analysed using the Design Expert software in order to determine the main effects on the process. In the model, Current is termed A, Gas Flow Rate is termed B, Powder Feed Rate is termed C, Spray Distance is termed D and Carrier Gas Flow Rate is termed E.

Table 4.6: Screening Results Summary

Exp Name	*Variables*					*Average Response*		
	Current A	**Gas Flow Rate** B	**Powder Feed Rate** C	**Spray Distance** D	**Carrier Gas Flow Rate** E	**Roughness** *(μm)*	**Crystallinity** *(%)*	**Purity** *(%)*
N1	450	70	10	120	20	-	-	-
N2	750	70	10	80	10	10.6	**87.6**	**99.4**
N3	450	130	10	80	20	**6.2**	65.2	97.8
N4	750	130	10	120	10	8.7	81.3	98.9
N5	450	70	20	120	10	10.5	**65.2**	97.6
N6	750	70	20	80	20	**13.4**	77.4	97.7
N7	450	130	20	80	10	7.3	77.8	98.2
N8	750	130	20	120	20	11.0	65.8	**96.4**
N9	600	100	15	100	15	10.7	79.9	97.4
N10	600	100	15	100	15	9.5		
N11	600	100	15	100	15	10.6	76.1	97.2

Roughness Model

The main effects on Roughness were modelled using the backward selection method to automatically eliminate insignificant model terms. Factors that had p-values of less than 0.1 (90% confidence interval) were included in the model and

factors with p-values greater than this were eliminated. The elimination of insignificant model terms allows a more accurate model to be built. In this case, Current (A), Gas Flow Rate (B) and Powder Feed Rate (C) were found to affect the coating roughness, whereas, Spray Distance (D) and the Carrier Gas Flow Rate (E) were found not to significantly affect the roughness and were not included in the model. The ANOVA table and model statistics are shown in *table 4.7*.

Table 4.7: ANOVA table for the Roughness Model

Source	*Sum of Squares*	*Mean Square*	*F-Value*	*p-value Prob >F*	*Significance*
Model Significance	34.88	11.63	33.08	0.0010	*significant*
A-Current	13.56	13.56	38.59	0.0016	
B-Gas Flow Rate	8.83	8.83	25.12	0.0041	
C-Powder Feed Rate	7.68	7.68	21.86	0.0055	
Curvature	1.30	1.30	3.70	0.1123	*Not significant*
Lack of fit	0.91	0.30	0.72	0.6260	*Not significant*
R^2	0.95				
Adj R^2	0.92				
Pred R^2	0.82				
Adeq Precision	17.776				

From the ANOVA table it can be seen that the model (given in *equation 4.1* and *equation 4.2*) has a p-value of 0.0010, which indicates that the model is significant at a confidence level of 99%. The curvature is not significant, indicating the factor range is adequate. A strong curvature is undesirable as it can mask the effect of the factors. If curvature is found to be significant it indicates the requirement for reduction of the factor ranges. The lack of fit is also not significant, indicating that the model adequately fits the data.

As discussed in the *Section 2.8* and *Appendix A*, a number of different statistical measures can be examined to determine the adequacy of a model, the most important of these being the R^2 value. For an adequate model this should be above 0.6, the closer the value to 1 the better the model. The R^2 value in this case was 0.95. The Adjusted R^2 and Predicted R^2 values also give a better indication of model adequacy. They should both be as close to 1 as possible. Values of greater than 0.7 are preferred. The values for this model were 0.92 and 0.82 respectively

(see *table 4.7*). The Adjusted R^2 and Predicted R^2 should also be within 0.2 of each other. The difference between the two values for this model is 0.1. The Adequate Precision value should be greater than 4. The Adequate Precision value for this model is 17.776. As the R^2, Adjusted R^2, Predicted R^2 and Adequate Precision values all exceed the required values, it can be concluded that a satisfactory model has been developed.

From the ANOVA table (*table 4.7*), it can be seen that the roughness of the coating is affected by three factors, Current (A), Gas Flow Rate (B) and Powder Feed Rate (C). The F-value in the ANOVA table indicates the extent of the effect of each factor on the roughness, the higher the F-value the greater the effect. Current (A) is found to have the greatest effect, followed by Gas Flow Rate (B) and then Powder Feed Rate (C).

The final mathematical model developed based on the results can be given in terms of coded factors (*equation. 4.1)* or actual factors *(equation 4.2)*. The coded factors model uses the coded low and high levels (-1 and 1) from the experimental design and can be used to quickly calculate the roughness value at one of the experimental points. The actual factors model takes in account the differences between the levels of the factors and the difference in effects. It can be used to determine the roughness when using any Current, Gas Flow Rate and Powder Feed Rate values, within the range of the experiment.

Roughness =	+ 9.45			*(eqn. 4.1)*
	+ 1.4	* A	(Current)	
	– 1.17	* B	(Gas Flow Rate)	
	+ 1.10	* C	(Powder Feed Rate)	

Roughness =	+4.257		*(eqn. 4.2)*
	+ 9.70417 E-003	* Current	
	– 0.039146	* Gas Flow Rate	
	+ 0.21912	* Powder Feed Rate	

The Predicted vs. Actual graph is shown in *figure 4.20*. In this graph the values predicted by the model are plotted against the actual measured response values. It shows how accurately the actual values are predicted by the model. If there is a good fit between the model and the data, the experimental data points in this graph closely follow the straight line of the model.

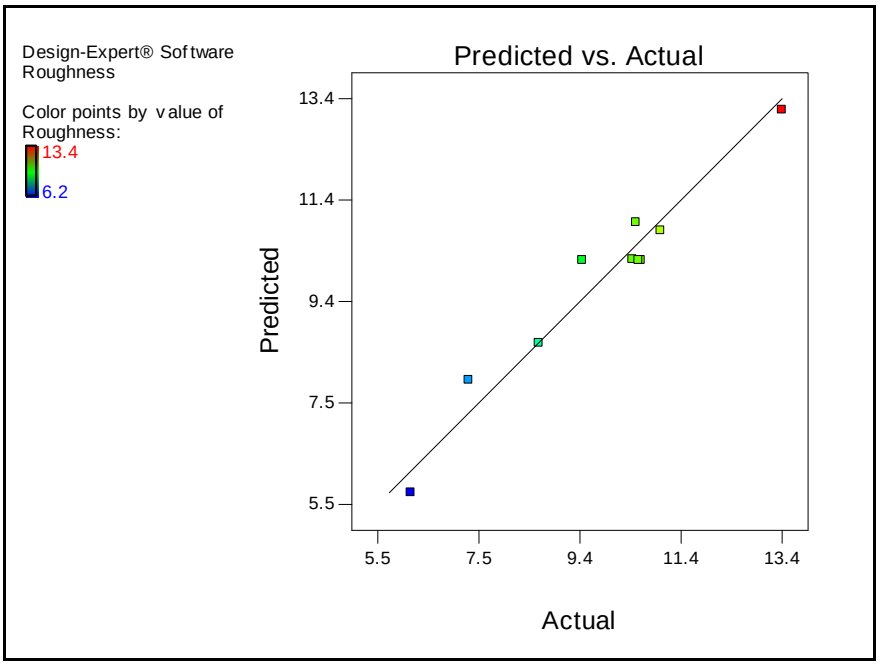

Figure 4.20: Predicted vs Actual Values for Roughness

From the model (*equation 4.1*), Current is seen to have the dominant effect, followed by Gas Flow Rate and then Powder Feed Rate. The effects of Current (A), Gas Flow Rate (B) and Powder Feed Rate (C) on the coating surface roughness are shown graphically in the response effects graphs, *figure 4.21 – figure 4.23*. *Figure 4.21* shows that increasing the Current results in an increase in surface roughness. *Figure 4.22* shows that increasing the Gas Flow Rate causes the coating roughness to decrease. *Figure 4.23* shows that increasing the Powder Feed Rate causes the coating roughness to increase. A coating with the greatest roughness will thus result when the Current is at its higher value, the Gas Flow Rate is at its lower value, and the Powder Feed Rate is at its higher value.

These response effects graphs (*figure 4.21* to *figure 4.23*) indicate the overall effect of each factor. The point at the lower response level on the graph is the

average of the all values of the response for coatings sprayed using the lower level. The point at the higher response level on the graph is the average of all values of the response for coatings sprayed using the higher level. The deviation of the actual values from the average is shown by the error bars.

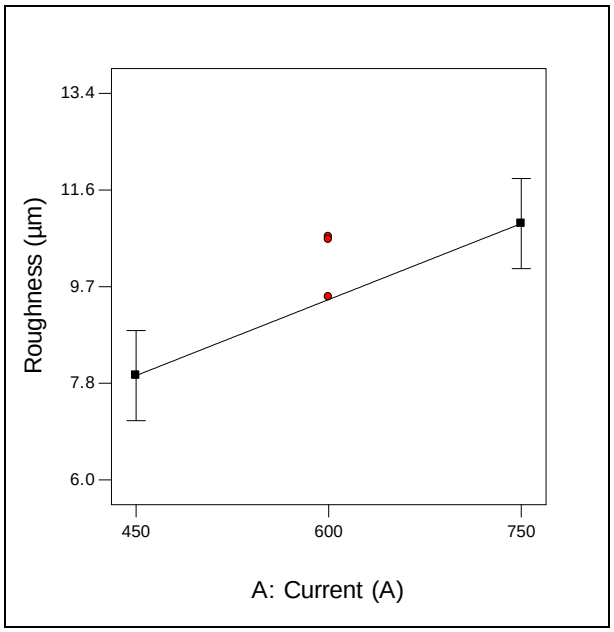

Figure 4.21: Effect of Current on Roughness

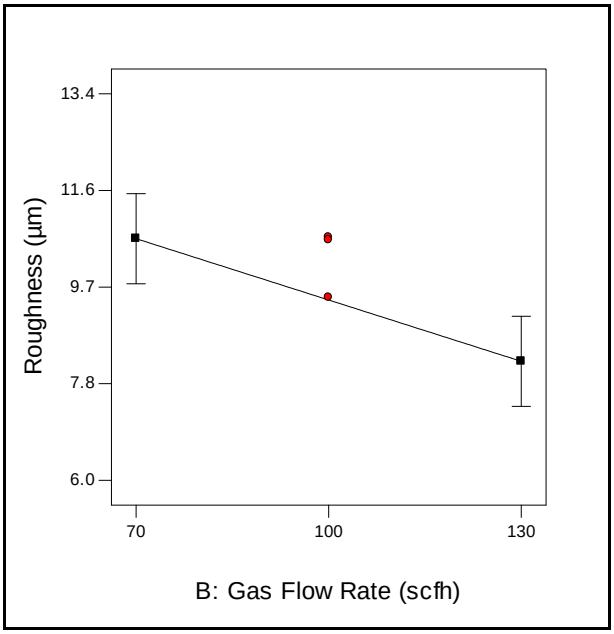

Figure 4.22: Effect of Gas Flow Rate on Roughness

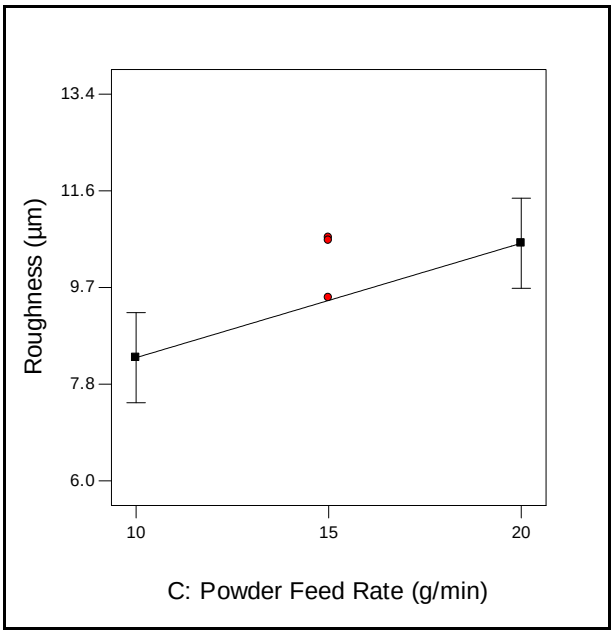

Figure 4.23: Effect of Powder Feed Rate on Roughness

The coating with the highest roughness value was found for experiment N6 and the coating with the lowest roughness was found for experiment N3. In order to help explain the model, the spraying parameters used for each of these experimental runs are summarised in *table 4.8*.

Table 4.8: Spraying Conditions used for Coatings N3 and N6

	Variables					
Exp Name	**Current (A)**	**Gas Flow Rate (B)**	**Powder Feed Rate (C)**	**Spray Distance (D)**	**Carrier Gas Flow Rate (E)**	***Roughness*** *(µm)*
N3	450	130	10	80	20	**6.2**
N6	750	70	20	80	20	**13.4**

As indicated by the model, coating N6 (highest roughness) was produced using a high Current, a low Gas Flow Rate and a high Powder Feed Rate, whereas, coating N3 (lowest roughness) was produced using a low Current, a high Gas Flow Rate and a low Powder Feed Rate. The Spray Distance and Carrier Gas Flow Rate were the same for N3 and N6. They were found not to significantly affect the roughness and thus are not included in the model.

According to literature, the roughness of plasma sprayed hydroxyapatite coatings, relates to the degree of melting of the particles; particles that have experienced a greater amount of melting in the plasma flame spread out to a greater extent on impact with the surface [109, 126]. The individual and overall effects of the process parameters for the high Roughness condition (N6) on the particle temperature and velocity (based on knowledge from literature) are summarised in *table 4.9*. The overall effects are a high particle temperature and low particle velocity.

Table 4.9: Overall effect on particle temperature and velocity for high roughness spray conditions

Factor		*Particle Temperature*	*Particle Velocity*
Current	↑	↑	↑
Gas Flow Rate	↓	↑	↓
Powder Feed Rate	↑	↓	
Overall Effect		↑	↓

In this study, the coating roughness was found to increase with increasing Current. The increase in roughness with increasing Current is contrary to the results of Gross and Babovic [126] who report decreased roughness with increased particle temperature, due to fact that greater particle melting allowed greater particle spreading and flattening on impact with the substrate.

At the low Roughness condition, particle temperature is low and as a result melting of all powder particles does not occur. Only the smaller powder particles are melted, larger particles remain unmelted and bounce off the surface of the substrate rather than being deposited onto it. At the high Roughness condition all particles are melted and thus the larger particles are incorporated into the coating rather than bouncing off it, resulting in a greater degree of coating roughness.

Although the range for current used in this study is similar to that used by others [28, 105, 106, 179], the plasma forming gas used is different. Generally, when spraying HA coatings, argon is used as the primary, plasma forming gas and small quantities of helium or hydrogen are added as a secondary gas to increase the

plasma flame temperature. In this study, argon was used as the plasma forming gas without the addition of a secondary gas. The temperature of the plasma flame will thus be lower than in many other studies, which explains why melting of the full range of particles is not observed.

At the high roughness condition, particle velocity is low and the lower impact force leads to a lesser degree of splat flattening and thus to a rougher coating. The Powder Feed Rate has a lesser affect than Current and Gas Flow Rate on coating roughness. Increasing the Powder Feed Rate causes an increase in the coating roughness. The effect of Powder Feed Rate on the temperature and velocity of the plasma flame is known to be small [107]. At higher Powder Feed Rates the number of powder particles impacting on the substrate at any time is greater, leading to a greater number of overlapping particles and reduced particle spreading and thus higher roughness. High Powder Feed Rates are known to result in thicker coatings [113]. It is possible that coating thickness may have an affect on the Roughness.

Micrographs for the lowest roughness coating (N3) and highest roughness coating (N6), are given in *figure 4.24* and *figure 4.25* respectively.

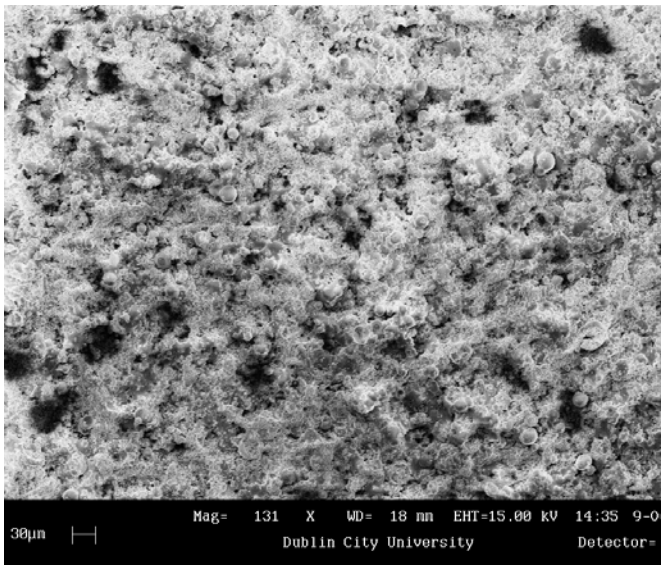

Figure 4.24: Micrograph of the surface morphology of coating N3 (low roughness)

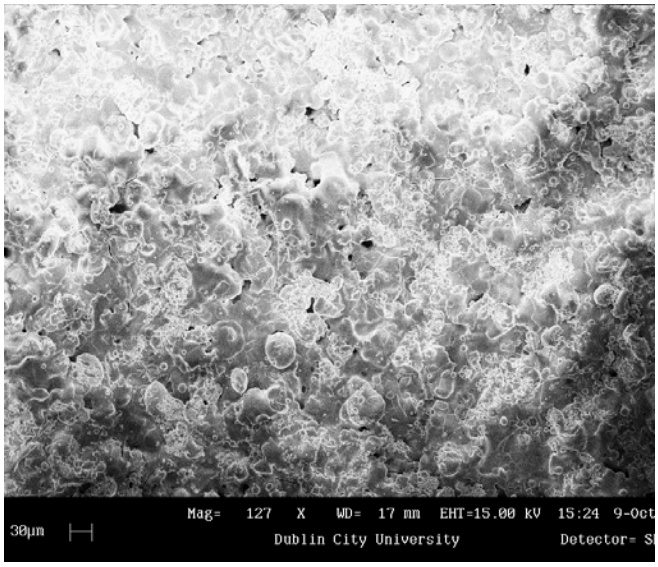

Figure 4.25: Micrograph of the surface morphology of coating N6 (high roughness)

Comparing the micrographs for the lowest roughness coating (N3) and the highest roughness coating (N6), it is clear from the appearance of the coating surface that the particles in the coating sprayed at higher current (N6) has undergone a greater degree of melting. There is also a visible difference in the size of the particles visible within the two coating. For coating N3 (*figure 4.24*) the particles are much smaller than the 30 µm scale bar, whereas for coating N6 (*figure 4.25*), many of the particles appear to be approximately 30 µm.

Crystallinity Model

The main effects on the coating crystallinity were modelled using the backward elimination method to eliminate insignificant terms. Gas Flow Rate (B) and Powder Feed Rate (C) did not significantly affect the crystallinity and were eliminated from the model. The ANOVA table and model statistics for the crystallinity model are shown in *table 4.10*.

From the ANOVA table it can be seen that the model has a p-value of 0.0035. This means that the model is significant at a confidence level of 99%. The curvature and lack of fit were both not significant. The R^2, Adjusted R^2, Predicted R^2 and Adequate Precision values all indicate that the model adequately fits the experimental data.

Table 4.10: ANOVA table for the Crystallinity Model

Source	*Sum of Squares*	*Mean Square*	*F-Value*	*p-value Prob >F*	*Significance*
Model Significance	435.22	145.07	29.38	0.0035	*significant*
A-Current	245.97	245.97	49.81	0.0021	
D-Spray Distance	170.36	170.36	34.50	0.0042	
E-Carrier Gas Flow Rate	241.42	241.42	48.89	0.0022	
Curvature	57.72	57.72	11.69	0.0268	*not significant*
Lack of fit	12.30	4.10	0.55	0.7295	*not significant*
R^2	0.96				
Adj R^2	0.92				
Pred R^2	0.81				
Adeq Precision	14.902				

Current (A), Spray Distance (D) and Carrier Gas Flow Rate (E) were all found to significantly affect the coating crystallinity. Current is found to have the greatest effect, followed by Carrier Gas Flow Rate and then Spray Distance. The final mathematical model for crystallinity is given in terms of coded factors in *equation 4.3* and in terms of actual factors in *equation 4.4*.

Crystallinity = 71.83 *(eqn. 4.3)*
+ 6.20 * A (Current)
– 5.16 * D (Spray Distance)
– 6.14 * E (Carrier Gas Flow Rate)

Crystallinity = + 91.25062 *(eqn. 4.4)*
+ 0.041329 * Current
– 0.25797 * Spray Distance
– 1.22839 * Carrier Gas Flow Rate

The Predicted vs Actual Plot is shown in *figure 4.26*. The data points can be seen to lie close to the diagonal line indicating a good fit.

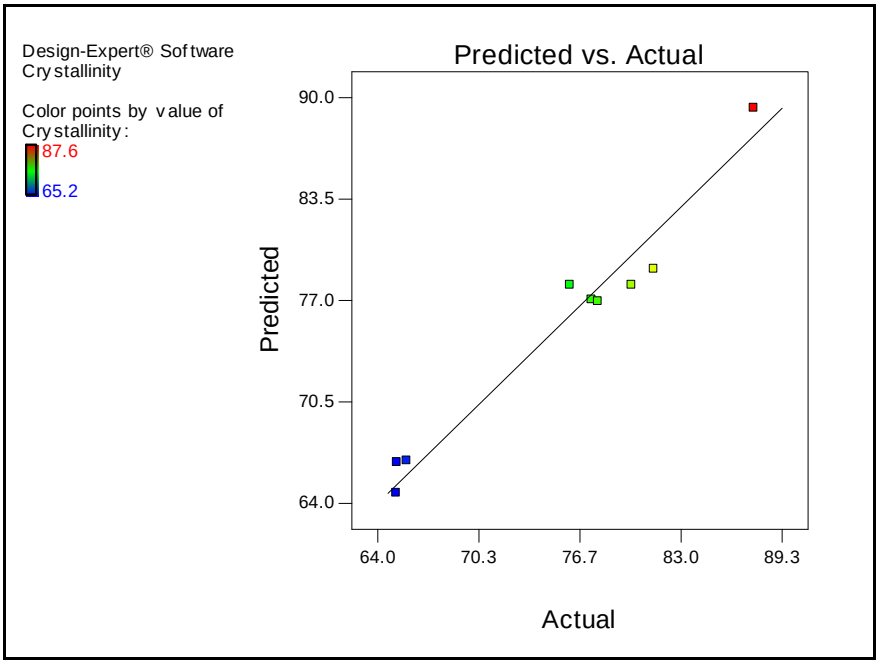

Figure 4.26: Predicted vs. Actual Plot for Crystallinity

Current was found to be the primary factor influencing Crystallinity, followed by Carrier Gas Flow Rate and then by Spray Distance. The effects of Current, Spray Distance and Carrier Gas Flow Rate on the coating crystallinity are shown in *figure 4.27* to *figure 4.29*.

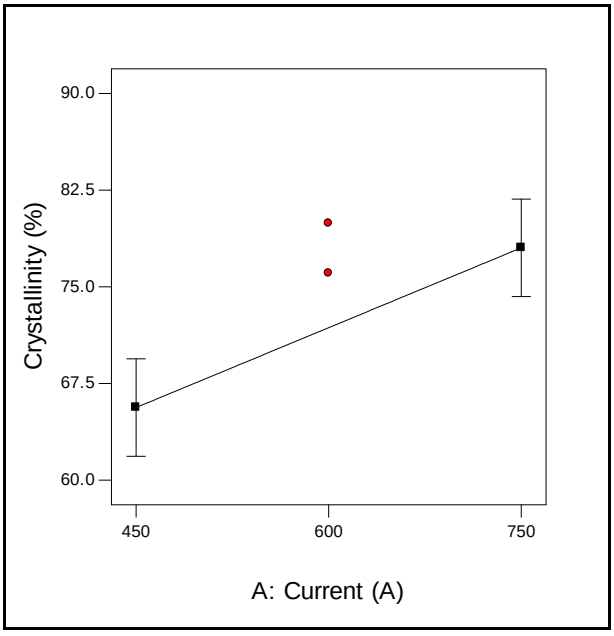

Figure 4.27: Effect of Current on Crystallinity

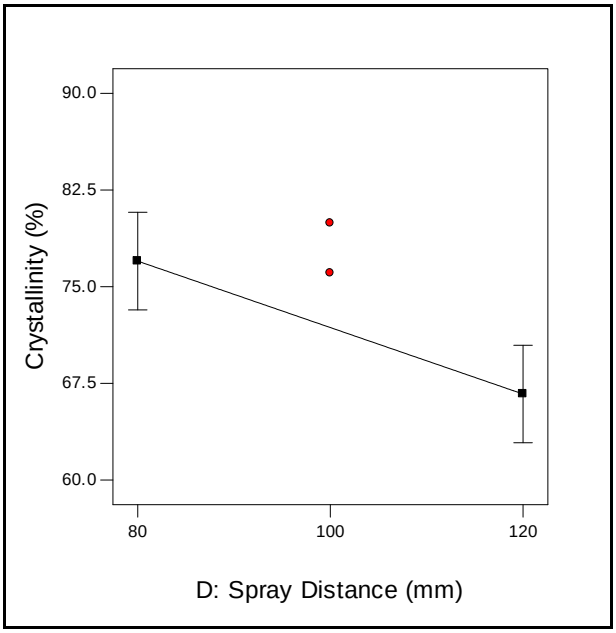

Figure 4.28: Effect of Spray Distance on Crystallinity

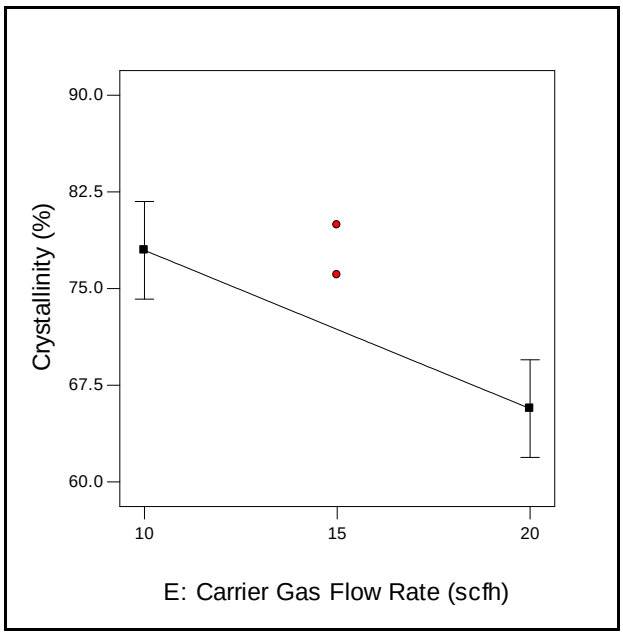

Figure 4.29: Effect of Carrier Gas Flow Rate on Crystallinity

Figure 4.27 shows that increasing the Current causes an increase in the coating crystallinity. *Figure 4.28* shows that increasing the Spray Distance causes a decrease in the coating crystallinity. *Figure 4.29* shows that increasing the Carrier Gas Flow Rate causes a decrease in the coating crystallinity.

The coating with the highest % crystallinity was found for experiment N2 and the coating with the lowest % crystallinity was found for experiment N5. The spraying parameters used for each of these are summarised in *table 4.11*.

Table 4.11: Spraying Conditions used for Coatings N2 and N5

Exp Name	*Variables*					*Crystallinity (%)*
	Current (A)	**Gas Flow Rate (B)**	**Powder Feed Rate (C)**	**Spray Distance (D)**	**Carrier Gas Flow Rate (E)**	
N2	750	70	10	80	10	**87.6**
N5	450	70	20	120	10	**65.2**

As indicated by the model, coating N2 (highest % crystallinity) was produced using a high Current and a low Spray Distance, whereas, coating N5 (lowest % crystallinity) was produced using a low Current and a high Spray Distance. The Carrier Gas Flow Rate was low for both coatings. Looking at the other crystallinity values it can be seen that the majority of coatings with high crystallinity were produced using a low Carrier Gas Flow Rate and the majority of coatings with low crystallinity were produced using a high Carrier Gas Flow Rate. It is probable that Carrier Gas Flow Rate is involved in an interaction with another factor. Interactions cannot be determined from this model as it is a low order screening model but may be identified from the Response Surface Modeling experiment. The Gas Flow Rate was the same for N2 and N5, and found not to significantly affect the % crystallinity. A low Powder Feed Rate was used for spraying coating N2 and a high Powder Feed Rate was used for coating N5. Although these values were different, the overall affect was not found to be significant in this study.

The finding in this study that Crystallinity is high at high Current is in agreement with the findings of Yang et al. [110]. Other studies [90, 106, 109], however, have found the opposite effect. It was found here that Crystallinity increased with decreased Spray Distance. This was in agreement with the findings of Sun et al. [109]. Lu et al. [114] report the opposite effect.

From literature it is known that the crystalline fraction of a HA coating consists of bulk crystalline material and material that has recrystallised following spraying [109]. The bulk crystalline material results from the unmelted central cores of the HA particles, while the recrystallised material results from recrystallisation of amorphous material [117]. The degree of particle melting and the particle cooling rate will thus determine the coating crystallinity. The overall expected effects of the high coating crystallinity spraying conditions (N2) are a high coating temperature and low particle cooling rate, as summarised in *table 4.12*.

Table 4.12: Overall effect on flame temperature and velocity for high crystallinity spray conditions

Factor		*Particle Melting*	*Particle Cooling Rate*
Current	↑	↑	↓
Spray Distance	↓	↓	↓
Carrier Gas Flow Rate	↓	↓	
Overall Effect		↑	↓

For the high coating Crystallinity condition (N2), the high Current value causes an increase in particle melting and an increase in substrate temperature, leading to a low particle cooling rate. The quantity of larger particles deposited at high Current is greater, leading to the presence of a greater amount of bulk crystalline material within the coating, leading to a high % Crystallinity. The low Spray Distance causes particle melting to be low due to reduced residence time in the plasma flame. At low Spray Distance the substrate temperature will be high as it is closer to the plasma flame and thus cooling rate will be low. The Carrier Gas Flow Rate determines the entry positions of particles into the flame. At a low Carrier Gas Feed Rate particles do not enter the center of the plasma flame, and as a result undergo less melting. Carrier Gas Flow Rate has little effect on substrate temperature.

Micrographs of the coating morphology of the highest crystallinity coating (N2), *figure 4.30,* and the lowest crystallinity coating (N5), *figure 4.31,* show visible differences in splat morphology. The particles visible in coating N2 (high crystallinity) appear to have undergone a high degree of melting and those in

coating N5 (low crystallinity), a lesser degree of melting. The powder particles visible in coating N5, retain their spherical shape, indicating that only partial melting of the particles occurred. This indicates that Coating N2 has indeed experienced higher temperatures than Coating N5 during the spraying process.

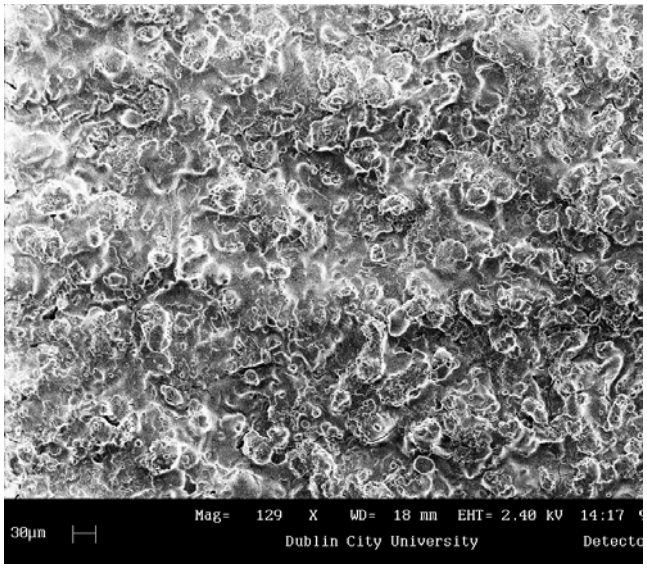

Figure 4.30: Coating N2 (high crystallinity) showing a high degree of melting

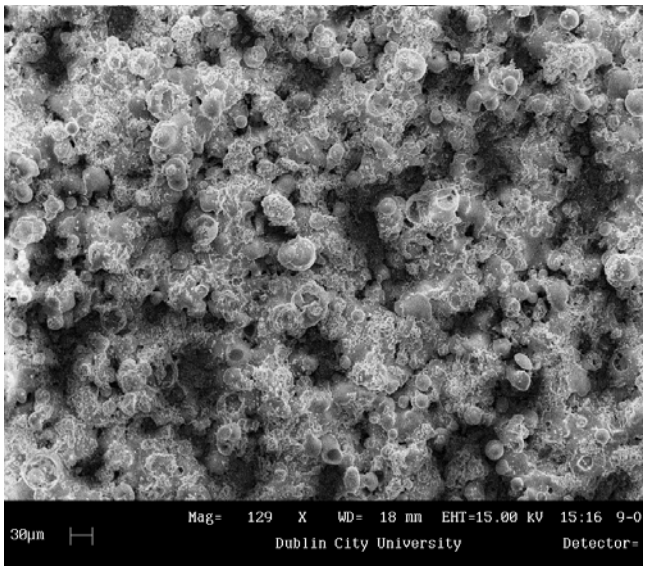

Figure 4.31: Coating N5 (low crystallinity) showing a low degree of melting

The effect of coating thickness on crystallinity has been reported by Gross et al. [118], with higher crystallinity resulting for thicker coatings. The high Crystallinity conditions of high Current and low Spray Distance would be expected to result in a thicker coating due to a greater number of particles being

melted in the flame (based on findings from the roughness model) and increased deposition efficiency at the Spray Distance. The effect of the plasma parameters on coating Thickness is investigated further in the Response Surface Methodology experiment.

Purity Model

The main effects on the coating purity were modelled using the backward elimination method to eliminate insignificant terms. Current (A) and Gas Flow Rate (B) did not significantly affect the purity and were eliminated from the model. The ANOVA table and model statistics for the purity model is shown in *table 4.13*.

Table 4.13: ANOVA table for the Purity Model

Source	*Sum of Squares*	*Mean Square*	*F-Value*	*p-value Prob >F*	*Significance*
Model Significance	5.32	1.77	13.81	0.0141	*significant*
C-Powder Feed Rate	1.33	1.33	10.37	0.0323	
D-Spray Distance	0.76	0.76	5.89	0.0723	
E-Carrier Gas Flow Rate	2.26	2.26	17.57	0.0138	
Lack of fit	0.49	0.16	8.23	0.2496	*not significant*
R^2	0.91				
Adj R^2	0.85				
Pred R^2	0.56				
Adeq Precision	10.44				

From the ANOVA table it can be seen that the model has a p-value of 0.0141. This means that the model is significant at a confidence level of 99%. The lack of fit was not significant. The R^2, Adjusted R^2 and Adequate Precision meet the required values for an adequate model. However, the Predicted R^2 value is less than the required 0.6 and does not meet the requirement to be within 0.2 of the Adjusted R^2. This suggests that the model may contain some inaccuracy. The range of purity values is small, from 95 % to 99%, which makes modelling it accurately more difficult. The model is deemed acceptable for the purposes of this screening experiment.

Powder Feed Rate (C), Spray Distance (D) and Carrier Gas Flow Rate (E) were found to significantly affect the coating purity. Carrier Gas Flow Rate (E) is found to have the greatest affect, followed by Powder Feed Rate. The model for purity is given in terms of coded factors in *equation 4.5* and actual factors in *equation 4.6*.

Purity =	+97.93			(*eqn. 4.5*)
	-0.46	* C	(Powder Feed Rate)	
	-0.34	* D	(Spray Distance)	
	-0.59	* E	(Carrier Gas Flow Rate)	

Purity =	+102.8		(*eqn. 4.6*)
	-0.09125	* Powder Feed Rate	
	-0.017187	* Spray Distance	
	-0.11875	* Carrier Gas Flow Rate	

The Predicted vs Actual Plot is given in *figure 4.32*. Some of the experimental data points lie further from the predicted values line than desired, reflecting the low value of Predicted R^2 highlighted in the ANOVA table.

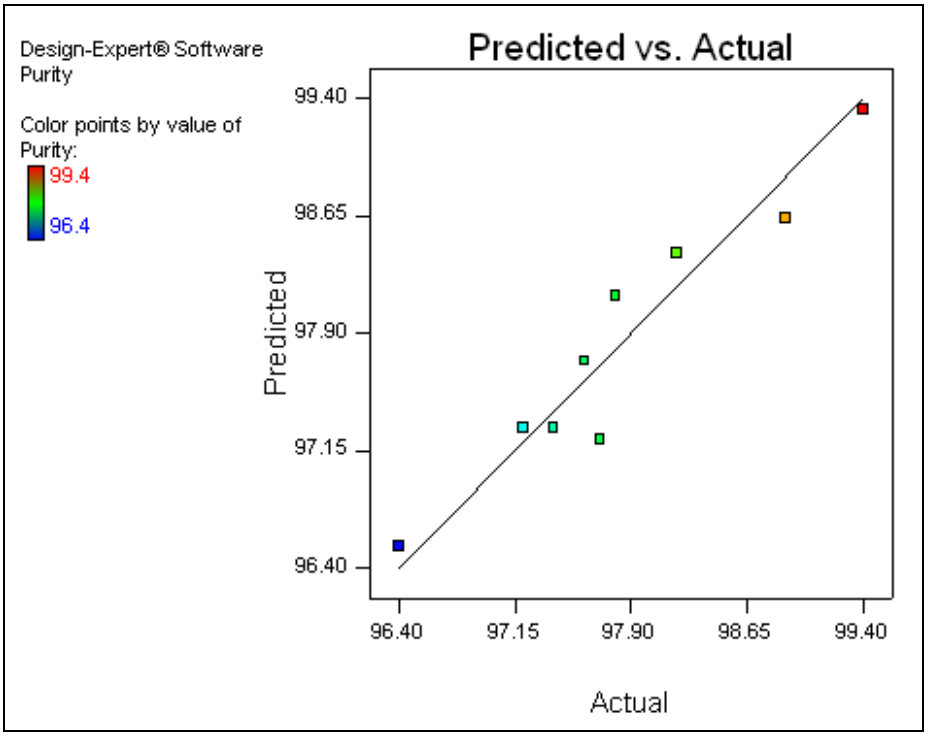

Figure 4.32: Predicted vs. Actual Plot for Purity

Carrier Gas Flow Rate has the greatest effect, followed by Powder Feed Rate and then Spray Distance. The effects of Powder Feed Rate, Spray Distance and Carrier Gas Flow Rate on the Purity are shown in *figure 4.33*, *figure 4.34* and *figure 4.35*.

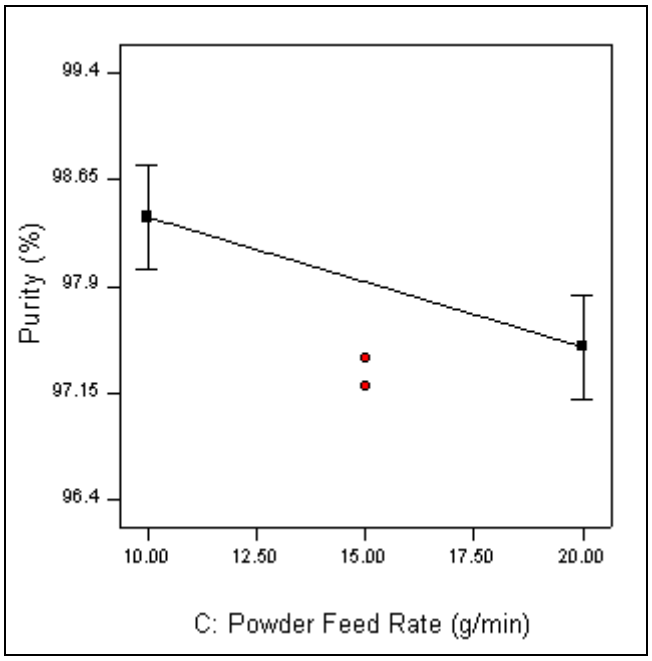

Figure 4.33: Effect of Powder Feed Rate on Purity

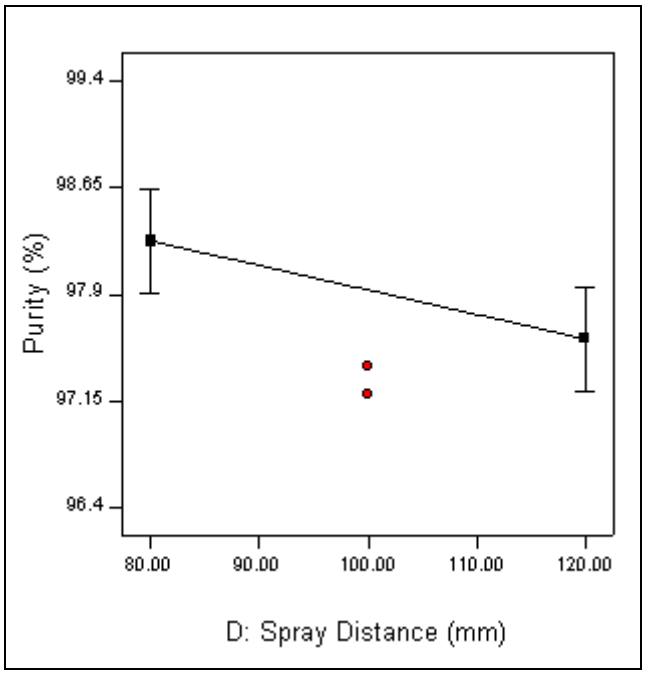

Figure 4.34: Effect of Spray Distance on Purity

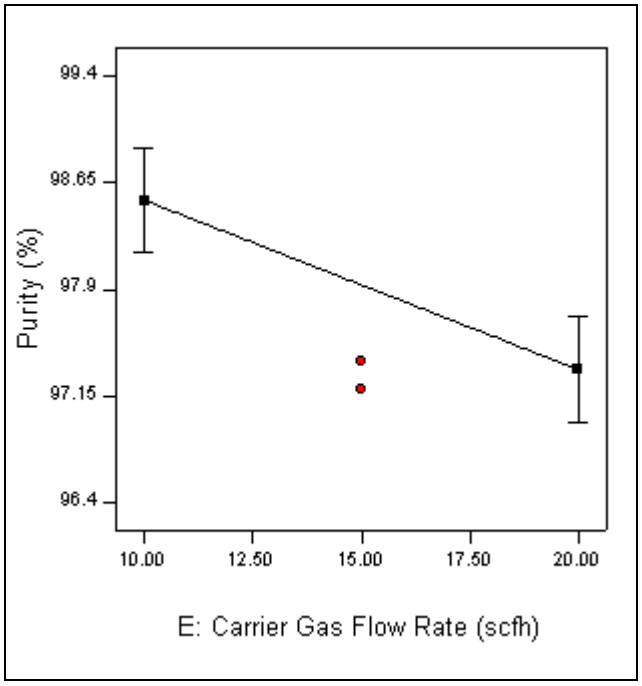

Figure 4.35: Effect of Carrier Gas Flow Rate on Purity

Figure 4.33 shows that increasing the Powder Feed Rate causes a decrease in the coating purity. *Figure 4.34* shows that increasing the Spray Distance causes a decrease in the coating purity. *Figure 4.35* shows that increasing the Carrier Gas Flow Rate causes a decrease in Purity.

The coating with the highest % purity was found for experiment N2 and the coating with the lowest % Purity was found for experiment N8. The spraying parameters used for each of these are summarised in *table 4.14*.

Table 4.14: Spraying Conditions used for Coatings N2 and N8

	Variables					
Exp Name	**Current (A)**	**Gas Flow Rate (B)**	**Powder Feed Rate (C)**	**Spray Distance (D)**	**Carrier Gas Flow Rate (E)**	***Purity (%)***
N2	750	70	10	80	10	**99.4**
N8	750	130	20	120	20	**96.4**

Coating N2 was produced using a low Powder Feed Rate, low Spray Distance and low Carrier Gas Flow Rate. Coating N8 was produced using a high Powder Feed

Rate, high Spray Distance and high Carrier Gas Flow Rate. Current was the same for both coatings. Although Gas Flow Rate was different for coating N2 and N8 its overall affect on coating Purity was not found to be significant in this study.

The purity of a HA coating relates the temperature experienced by the HA particles during spraying. If the particle temperature exceeds 800 °C, HA decomposes to oxyhydroxyapatite (OHA) and oxyapatite (OA), followed by tetracalcium phosphate (TTCP), β-tricalcium phosphate (β-TCP) and α-tricalcium phosphate (α-TCP) (as discussed in *Section 2.2.5*). The literature indicates that the purity of a HA coating is reduced as the temperature of the plasma flame is increased and the as spray distance is increased [109].

The effects of the significant parameters on the particle temperature for the high purity condition (N2) are summarised in *table 4.15*. At low Powder Feed Rate, the flame temperature would be slightly higher than at high Powder Feed Rate, as less cooling of the flame occurs when few particles are injected into it. At low Spray Distance, the particles only remain in the plasma flame for a short time and thus experience less heating. A low Carrier Gas Flow Rate the particles do not penetrate the central, hottest part of the plasma flame and thus remain at a lower temperature. The overall effect at these conditions is a reduction in particle temperature (as shown in *table 4.15*).

Table 4.15: Overall effect on particle temperature for high purity spray conditions

Factor		***Particle Temperature***
Powder Feed Rate	↓	↑
Spray Distance	↓	↓
Carrier Gas Flow Rate	↓	↓
Overall Effect		↓

A high Purity Coating results when the spray conditions lead to a low particle temperature. This agreed with the finding of Sun et al. [109] and is due to the reduced temperature of the powder particles as the particles spend less time in the plasma flame at low spray distances and there is less time for decomposition to occur.

Current and Gas Flow Rate are not found to have a significant affect on the coating Purity in this study. Both parameters are known to affect the plasma flame temperature and so would have been expected to show significant effects here. It is possible that they are involved in interaction effects that can not be detected by the screening study but may be identified by the more powerful RSM study.

Overall Findings of the Screening Experiment

The models developed in the screening experiment highlight some important findings. Firstly, all five parameters were found to have a significant effect on the properties of the coating produced. Not all factors significantly affected each response. It was found that, within the design space investigated in the screening design, Gas Flow Rate has the greatest affect on coating Roughness, Current has the greatest effect on Crystallinity and Carrier Gas Flow Rate has the greatest effect on Purity.

The effects of the five factors on the three responses are summarised in *table 4.16*. The table shows the effect of increasing each of the factors on the response. For example, increasing the Current causes an increase in both the Roughness and Crystallinity. Increasing Spray Distance causes a decrease in both the Crystallinity and Purity. Some of the parameters were found to have similar effects on different responses and some to have opposing effects on difference responses. For example, increasing the Spray Distance causes both the Crystallinity and Purity to decrease, whereas, increasing the Powder Feed Rate causes the Roughness to increase but the Purity to decrease.

Table 4.16: Summary of the effect of increasing factors on the response

Factor	*Roughness*	*Crystallinity*	*Purity*
A-Current	↑	↑	
B-Gas Flow Rate	↓		
C-Powder Feed Rate	↑		↓
D-Spray Distance		↓	↓
E-Carrier Gas Flow Rate		↓	↓

Analysis of the results in the screening experiment indicate that at conditions where the lowest amount of particle melting occurs (low Current and high Gas Flow Rate), all particles are not melted sufficiently to be deposited on the substrate and only smaller particles are deposited. The results from the screening design also highlight that the factor levels used for experimental run N1 did not produce an adequate coating (low particle deposition). The factor levels thus needed to be re-examined before conducting the RSM experiment. As all factors in the screening design influenced the measured responses, they were all included in the Response Surface Methodology experiment. The results of the RSM experiment are discussed in the next section.

4.6 Response Surface Methodology Study

The Response Surface Methodology study was carried out as per the procedure in *Section 3.7.3*. The experimental design used was a Central Composite Design. The design consisted of 31 experiments and the coatings were sprayed according to *table 3.11*. In this section, the parameter and level selection for the study is considered, the measured values for each response are given and the models developed for each response are presented and discussed. The models are described in terms of the resulting high and low response levels. The desirable level for each response is discussed in relation to optimisation of the models in *Section 4.7*.

4.6.1 Parameter and Level Selection

The results from the screening study indicate that each of the five parameters investigated have a significant affect on one or more of the investigated responses. Therefore, they must all be included in the optimisation study. The screening design also indicated that, because an adequate coating was not produced for experimental run N1, adjustment of the parameter ranges used was necessary. The settings used for N1 were: Current – 450 A, Gas Flow Rate – 70 SCFH, Powder Feed Rate – 10 g/min, Spray Distance – 120 mm, Carrier Gas Flow Rate – 20 SCFH. This set of parameters was considered to result in insufficient particle melting.

In order to select the parameter ranges for the RSM experiment, the changes necessary to the screening experiment parameter ranges in order to ensure melting of all particles within the plasma flame were considered. The indications from the screening design (highlighted in *table 4.16*) as to the effect of the parameter levels on the coating properties were also taken into account.

In order to increase the proportion of particles that are melted in the plasma flame the lower level for Current was increased from 450 A to 550 A. The Gas Flow Rate levels were increased from a range of 70 – 130 SCFH to 90 to 150 SCFH. These values were increased to allow increased particle deposition. Both the low and high Spray Distance levels were decreased to increase particle deposition rate. Lower Spray Distances were seen in the screening experiment to result in higher coating Crystallinity and Purity, which is a desirable affect. No range changes were made to the Powder Feed Rate or Carrier Gas Flow Rate. The parameter level changes made for the RSM experiment are summarised in *table 4.17*.

Table 4.17: Changes to Parameter Levels for RSM Experiment

	Old Range	***New Range***
Current *(A)*	450 – 750	550 – 750
Gas Flow Rate *(SCFH)*	70 – 130	90 – 150
Powder Feed Rate *(g/min)*	10 – 20	10 – 20
Spray Distance *(mm)*	80 – 120	70 – 100
Carrier Gas flow rate *(SCFH)*	10 – 20	10 – 20

The responses investigated in the RSM experiment included Roughness, Crystallinity and Purity, as in the screening experiment. Crystallinity and Roughness both appear to have some relation to the coating Thickness and so this was also added as a response for the RSM experiment. Porosity was also included as a response in order to give a better understanding of the mechanical properties of the coating. The RSM experiment was carried out according to *table 3.11* presented in *Section 3.7.3*. The results were analysed using the Design Expert software and models were developed for each response.

4.6.2 Coating Roughness

The roughness of the coatings was calculated following the procedure outlined in *Section 3.10.6*. Four values were measured for each coating and the average roughness calculated. The average roughness ranged between 3.1 μm and 9.5 μm. The results are presented in *table 4.18*. These roughness values are lower than those found for the screening study which ranged from 6.2 μm to 13.4 μm. This is as a result of the changes made to the parameter levels between the two studies.

Table 4.18: Roughness Results for RSM Study

Exp	R_a *value (μm)*				
Name	*1*	*2*	*3*	*Average*	*SD*
N1	8.5	8.7	7.0	8.1	0.93
N2	8.7	9.0	8.5	8.7	0.25
N3	3.2	3.2	5.7	4.0	1.44
N4	7.2	8.0	7.5	7.6	0.40
N5	9.0	9.2	8.2	8.8	0.53
N6	9.0	8.0	9.5	8.8	0.76
N7	6.0	5.2	6.0	5.7	0.46
N8	8.5	7.5	7.2	7.7	0.68
N9	7.7	8.0	8.7	8.1	0.51
N10	8.0	7.5	8.5	8.0	0.50
N11	3.0	3.2	3.0	**3.1**	0.12
N12	5.7	5.2	5.5	5.5	0.25
N13	8.0	9.2	8.0	8.4	0.69
N14	9.7	8.5	7.2	8.5	1.25
N15	4.7	3.5	4.5	4.2	0.64
N16	8.5	7.5	8.2	8.1	0.51
N17	5.7	4.5	7.2	5.8	1.35
N18	8.5	8.5	9.5	8.8	0.58
N19	8.7	9.2	8.7	8.9	0.29
N20	7.0	8.2	7.7	7.6	0.60
N21	9.2	9.0	10.2	**9.5**	0.64
N22	6.7	7.0	9.2	7.6	1.37
N23	7.5	8.7	8.0	8.1	0.60
N24	7.0	7.0	6.5	6.8	0.29
N25	10.2	9.2	9.0	9.5	0.64
N26	7.5	7.2	7.0	7.2	0.25
N27	6.5	9.0	5.0	6.8	2.02
N28	7.7	7.5	8.5	7.9	0.53
N29	7.2	7.2	8.0	7.5	0.46
N30	9.0	8.7	7.7	8.5	0.68
N31	6.5	7.0	8.5	7.3	1.04

4.6.3 Coating Crystallinity

The crystallinity was calculated according to the procedure in *Section 3.10.3*. The results are given in *table 4.19*. The average crystallinity ranged between 71.8 % and 85.2 %. The crystallinity values for the screening design ranged between 65.8 % and 87.6 %. The parameter level changes are seen to have caused an increase in the lower range of the resultant crystallinity values.

Table 4.19: Crystallinity Results for RSM Study

Exp	*Crystallinity (%)*				
Name	*1*	*2*	*3*	*Average*	*SD*
N1	73.0	74.1	73.0	73.3	0.64
N2	81.3	83.0	83.9	82.7	1.32
N3	72.6	71.5	73.5	72.5	1.00
N4	81.7	79.4	82.5	81.2	1.61
N5	81.1	80.1	80.1	80.4	0.58
N6	80.7	80.0	79.3	80.0	0.70
N7	73.1	72.0	72.0	72.4	0.64
N8	85.1	85.9	84.5	**85.2**	0.70
N9	82.5	82.5	81.7	82.2	0.46
N10	75.2	73.8	72.7	73.9	1.25
N11	74.7	73.3	74.7	74.2	0.81
N12	71.2	71.7	72.4	**71.8**	0.60
N13	76.5	76.5	76.5	76.5	0.00
N14	80.4	79.8	79.8	80.0	0.35
N15	71.1	71.1	73.2	71.8	1.21
N16	78.3	79.2	79.2	78.9	0.52
N17	81.6	80.4	80.4	80.8	0.69
N18	75.3	75.7	75.3	75.4	0.23
N19	77.7	77.7	76.8	77.4	0.52
N20	74.4	73.5	74.4	74.1	0.52
N21	81.3	77.2	76.1	78.2	2.74
N22	82.9	76.9	76.0	78.6	3.75
N23	79.4	78.5	78.5	78.8	0.52
N24	74.6	74.8	74.6	74.7	0.12
N25	78.4	81.6	78.4	79.4	1.85
N26	76.8	75.7	75.7	76.0	0.64
N27	78.2	77.6	79.6	78.5	1.03
N28	80.2	79.3	80.2	79.9	0.52
N29	80.2	79.2	81.0	80.1	0.90
N30	79.9	78.9	77.8	78.9	1.05
N31	81.4	80.4	81.0	80.9	0.50

4.6.4 Coating Purity

The purity was calculated according to the procedure outlined in *Section 3.10.3*. The results are given in *table 4.20*. The average purity ranged between 96.1 % and 99.7 %. The Purity range observed for the screening study was from 95.5 % to 99.4 %. Little change in Purity has occurred as a result of the parameter level changes between the screening study and RSM study.

Table 4.20: Purity Results for RSM Study

Exp	***Purity (%)***				
Name	*1*	*2*	*3*	*Average*	*SD*
N1	97.6	97.6	97.5	97.6	0.06
N2	99.3	99.4	99.3	99.3	0.06
N3	99.4	99.4	99.4	99.4	0.00
N4	98.6	98.7	98.7	98.7	0.06
N5	98.7	98.7	98.7	98.7	0.00
N6	98.5	98.6	98.6	98.6	0.06
N7	98.4	98.4	98.3	98.4	0.06
N8	99.0	99.1	99.1	99.1	0.06
N9	97.9	97.9	97.9	97.9	0.00
N10	96.1	96.1	96.2	**96.1**	0.06
N11	98.4	98.4	98.4	98.4	0.00
N12	99.7	99.6	99.7	**99.7**	0.06
N13	96.2	96.3	96.3	96.3	0.06
N14	97.9	97.9	97.9	97.9	0.00
N15	99.3	99.3	99.2	99.3	0.06
N16	97.8	97.8	97.9	97.8	0.06
N17	98.3	98.3	98.3	98.3	0.00
N18	99.1	99.1	99.1	99.1	0.00
N19	97.8	97.8	97.8	97.8	0.00
N20	98.8	98.7	98.8	98.8	0.06
N21	98.3	98.4	98.4	98.4	0.06
N22	98.1	98.1	98.1	98.1	0.00
N23	98.9	98.8	98.8	98.9	0.06
N24	98.3	98.3	98.3	98.3	0.00
N25	98.7	98.8	98.8	98.8	0.06
N26	98.4	98.4	98.4	98.4	0.00
N27	98.2	98.2	98.2	98.2	0.00
N28	98.3	98.3	98.3	98.3	0.00
N29	98.3	98.2	98.3	98.3	0.06
N30	98.3	98.3	98.5	98.4	0.12
N31	98.6	98.6	98.5	98.6	0.06

4.6.5 Coating Porosity

The porosity was measured according to the procedure in *Section 3.10.4*. The results are given in *table 4.21*. The average coating porosity ranged between 6.8 % and 59.1 %. Porosity measurements could not be carried out for all coatings as some were too thin for accurate measurements to be obtained.

Table 4.21: Porosity Results for RSM Study

Exp	***Porosity (%)***					
Name	*1*	*2*	*3*	*4*	*Average*	*SD*
N1	19.45	19.01	21.28	17.09	19.2	1.72
N2	26.51	27.49	22.72	19.07	24.0	3.85
N3						
N4	19.47	12.16	17.64	16.08	16.3	3.11
N5	12.52	7.99	11.61	18.59	12.7	4.40
N6	5.69	5.93	9.34	6.68	6.9	1.67
N7	33.32	33.27	22.86	28.7	29.5	4.95
N8	8.65	6.66	6.89	5.11	**6.8**	1.45
N9	31.34	37.47	32.2	36.70	34.4	3.10
N10	61.94	58.14	57.33	58.9	**59.1**	2.01
N11						
N12	6.70	6.84	7.8	6	6.8	0.74
N13	19.81	16.73	12.34	17.8	16.7	3.16
N14	39.38	38.49	33.15	33.64	36.2	3.23
N15						
N16	12.05	11.24	10.27	11.4	11.2	0.74
N17	12.30	11.55	10.7	11.72	11.6	0.66
N18	13.60	10.19	13.08	12.19	12.3	1.50
N19	31.16	25.36	29.63	34.7	30.2	3.87
N20	18.26	15.7	13.53	15.4	15.7	1.95
N21	24.00	21.17	24.23	24.43	23.5	1.54
N22	10.00	9.54	9.46	9.8	9.7	0.25
N23	29.92	28.09	33.64	26.97	29.7	2.92
N24	10.72	12.46	11.99	10.08	11.3	1.10
N25	6.55	8.24	9.24	7.9	8.0	1.11
N26	36.86	35.14	36.9	37.9	36.7	1.15
N27	29.24	28.74	30.2	28.6	29.2	0.72
N28	14.64	11.56	12.08	12.81	12.8	1.35
N29	13.86	14.60	17.1	15.4	15.2	1.39
N30	14.14	9.38	9.1	11.1	10.9	2.32
N31	18.76	29.64	22.7	25.6	24.2	4.60

4.6.6 Coating Thickness

The coating thickness was measured according to the procedure in *Section 3.10.5*. The results are shown in *table 4.22*. The average coating thickness ranged between 17.2 μm and 543.5 μm. The highest and lowest average thickness values recorded are highlighted in bold print in *table 4.22*. The standard deviation for the coating thickness measurement is higher than for the other responses measured. This is due to the uneven surface profile produced as a result of the spraying process.

Table 4.22: Thickness Results for RSM Study

Exp	*Thickness (μm)*					
Name	*1*	*2*	*3*	*4*	*Average*	*SD*
N1	95.1	91.3	84.3	105.4	94.0	8.80
N2	366.7	366.0	377.1	391.9	375.4	12.10
N3	14.1	21.5	12.6	20.7	**17.2**	4.53
N4	263.0	260.0	260.7	277.8	265.4	8.38
N5	303.0	281.5	271.6	288.2	286.1	13.18
N6	535.4	542.8	545.7	550.2	**543.5**	6.21
N7	77.0	86.7	89.6	88.2	85.4	5.71
N8	191.1	187.4	175.6	177.0	182.8	7.65
N9	119.3	120.0	111.9	138.5	122.4	11.33
N10	147.4	125.9	140.0	200.7	153.5	32.71
N11	26.7	29.6	28.9	35.6	30.2	3.81
N12	41.5	51.9	45.9	52.6	48.0	5.26
N13	146.7	136.3	146.7	119.3	137.3	12.93
N14	340.9	340.8	349.7	353.4	346.2	6.36
N15	13.4	21.5	15.6	19.3	17.4	3.64
N16	215.6	231.1	232.7	167.4	211.7	30.52
N17	37.9	35.6	51.9	45.2	42.6	7.40
N18	312.6	339.3	315.6	313.3	320.2	12.80
N19	283.2	272.9	284.7	264.0	276.2	9.68
N20	51.3	53.7	60.7	44.3	52.5	6.77
N21	205.2	180.0	194.1	194.1	193.4	10.32
N22	277.0	286.0	261.5	261.5	271.5	12.12
N23	320.0	289.0	300.1	294.0	300.8	13.6
N24	110.6	97.9	104.0	104.5	104.2	5.19
N25	108.1	117.1	116.3	117.8	114.8	4.53
N26	237.2	244.5	254.1	248.9	246.2	7.16
N27	208.2	211.9	230.4	204.0	213.6	11.64
N28	207.5	163.8	195.0	209.6	194.0	21.12
N29	214.8	214.9	220.8	196.3	211.7	10.64

N30	307.4	309.7	297.8	323.7	309.7	10.69
N31	190.5	189.6	205.2	187.4	193.2	8.12

A micrograph of the cross-section coating N6 (highest thickness) is shown in *figure 4.36*. The thickness of the coating was measured following the procedure outlined in *Section 3.10.5*. Prior to thickness measurement, coatings were sectioned, mounted in resin, ground and polished according to the procedure set out in *Section 3.10.1*.

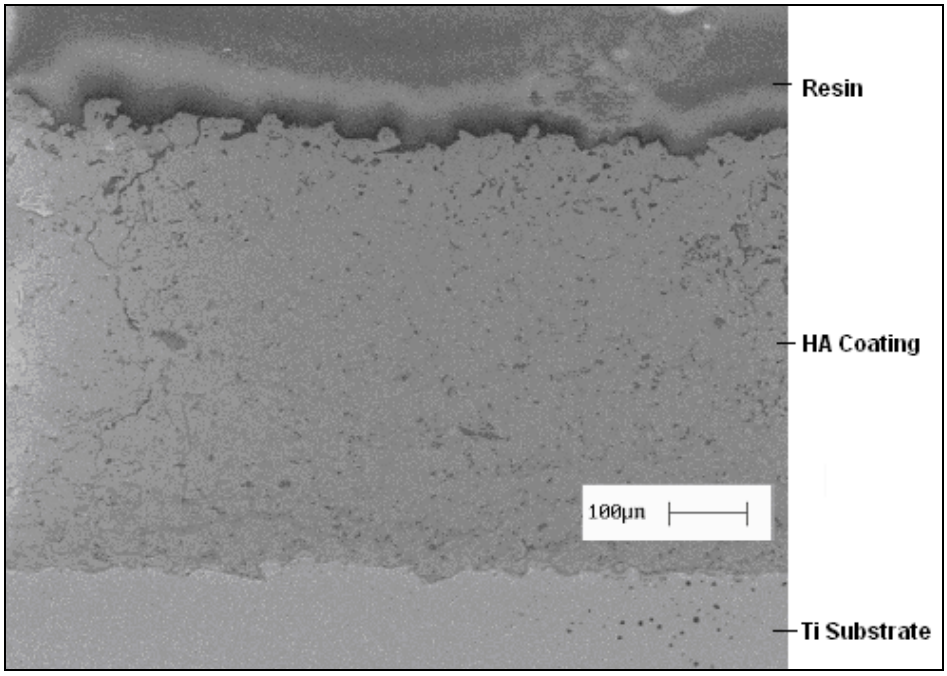

Figure 4.36: SEM of coating N6 (highest thickness)

RSM Study Results Summary

The spray parameters levels used for each experimental run and the average measured response values for each are summarised in *table 4.23*. The Design Expert software was used to develop models for each of these responses. The response models developed for each response are discussed and analysed in the following section.

Table 4.23: RSM Study Summary

Exp Name	*Variable*					*Response (Average Values)*				
	A	**B**	**C**	**D**	**E**	**Roughness**	**Crystallinity**	**Purity**	**Porosity**	**Thickness**
	A	*SCFH*	*g/min*	*mm*	*SCFH*	*µm*	*%*	*%*	*%*	*µm*
N1	550	90	10	70	20	8.1	73.3	96.4	19.2	94.0
N2	750	90	10	70	10	8.7	82.7	99.0	24.0	375.4
N3	550	150	10	70	10	4	72.5	99.1		**17.2**
N4	750	150	10	70	20	7.6	81	98.5	16.3	265.4
N5	550	90	20	70	10	8.8	80.4	97.6	12.7	286.1
N6	750	90	20	70	20	8.8	79.7	97.8	6.9	**543.5**
N7	550	150	20	70	20	5.7	72.4	98.3	29.5	85.4
N8	750	150	20	70	10	7.7	**85**	98.6	**6.8**	182.8
N9	550	90	10	100	20	8.1	82.3	96.8	34.4	122.4
N10	750	90	10	100	20	8	73.8	95.4	**59.1**	153.5
N11	550	150	10	100	20	**3.1**	74.2	97.1		30.2
N12	750	150	10	100	10	5.5	**71.2**	99.3	6.8	48.0
N13	550	90	20	100	20	8.4	76.5	93.8	16.7	137.3
N14	750	90	20	100	10	8.5	80.1	97.1	36.2	346.2
N15	550	150	20	100	10	4.2	73.2	98.8		17.4
N16	750	150	20	100	20	8.1	79.6	97.3	11.2	211.7
N17	550	120	15	85	15	6.8	78.3	97.8	11.6	42.6
N18	750	120	15	85	15	7.9	80.3	98.9	12.3	320.2
N19	650	90	15	85	15	7.5	80.4	97.1	30.2	276.2
N20	650	150	15	85	15	8.5	79.4	97.9	15.7	52.5
N21	650	120	10	85	15	7.3	81.1	97.9	23.5	193.4
N22	650	120	20	85	15	5.8	81.8	97.0	9.7	271.5
N23	650	120	15	70	15	8.8	76.9	98.3	29.7	300.8
N24	650	120	15	100	15	8.9	77.4	97.3	11.3	104.2
N25	650	120	15	85	10	7.6	74.1	98.4	8.0	114.8
N26	650	120	15	85	20	9.5	76.7	98.3	36.7	246.2
N27	650	120	15	85	15	7.6	76.5	97.8	29.2	213.6
N28	650	120	15	85	15	8.1	78.9	97.5	12.8	194.0
N29	650	120	15	85	15	6.8	74.7	97.4	15.2	211.7
N30	650	120	15	85	15	**9.6**	80	97.8	10.9	309.7
N31	650	120	15	85	15	7.2	76.2	97.8	24.2	193.2

4.6.7 Response Models

Coating Roughness

A quadratic model was found to have the best fit for the roughness data. The model was fitted using the stepwise automatic reduction algorithm to remove insignificant terms (95 % significance). The ANOVA table for coating roughness is given in *table 4.24*.

Table 4.24: ANOVA Table for Roughness

Source	*Sum of Squares*	*Mean Square*	*F-Value*	*p-value Prob >F*	*Significance*
Model Significance	55.54	13.89	18.28	< 0.0001	*Significant*
A-Current	13.35	13.35	17.57	0.0003	
B-Gas Flow Rate	28.88	28.88	38.01	< 0.0001	
AB	7.98	7.98	10.50	0.0033	
A^2	5.33	5.33	7.02	0.0135	
Lack of fit	18.11	0.82	2.01	0.2626	*not significant*
R^2	0.74				
Adj R^2	0.70				
Pred R^2	0.63				
Adeq Precision	14.116				

This model has a significance of < 0.0001. The lack of fit is not significant. The R^2 value is 0.74, which is above the recommended value of 0.6. There is less than 0.2 of a difference between the Adjusted R^2 value and the Predicted R^2 value. The adequate precision value is well above 4. It can be concluded that this is a good model.

Two parameters and one interaction are found to significantly affect the coating roughness. These are Current and Gas Flow Rate and the interaction of Current and Gas Flow Rate. Current is a quadratic factor. The model for roughness is given in terms of coded factors in *equation 4.6* and in terms of actual factors in *equation 4.7*.

Roughness =	+7.95			(*eqn. 4.6*)
	+ 0.86	* A	(Current)	
	- 1.27	* B	(Gas Flow Rate)	
	+ 0.71	* A * B	(Current * Gas Flow Rate)	
	- 0.84	* A^2	(Current^2)	

Roughness =	- 9.73718		(*eqn. 4.7*)
	+ 0.089639	* Current	
	- 0.19524	* Gas Flow Rate	
	+ 2.35417E-004	* Current * Gas Flow Rate	
	- 8.40598E-005	* Current^2	

The Predicted vs Actual plot is shown in *figure 4.37.* The experimental data points lie close to the straight line indicating a good fit.

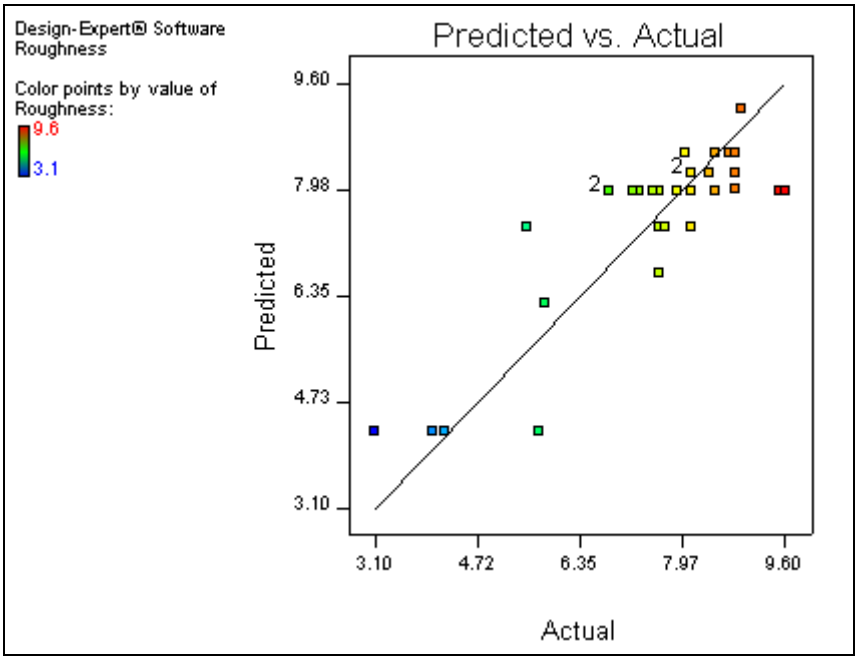

Figure 4.37: Predicted vs Actual Plot for the Roughness Model

The perturbation plot for the roughness model is given in *figure 4.38.* A perturbation plot is useful for comparing the sensitivity of a response to the significant factors; where the greater the slope the greater the sensitivity of the

response to it. The plot shows that, as found in the screening experiment, Roughness is highest at high Current and low Gas Flow Rate. The effect of Gas Flow Rate (B) can be seen from *figure 4.38* and *equation 4.6* to have a greater effect than Current (A) on the coating Roughness. The relationship between roughness and Current is curvilinear, hence the squared term in the model and the curved line on the perturbation plot. The relationship between the roughness and Gas Flow Rate is linear.

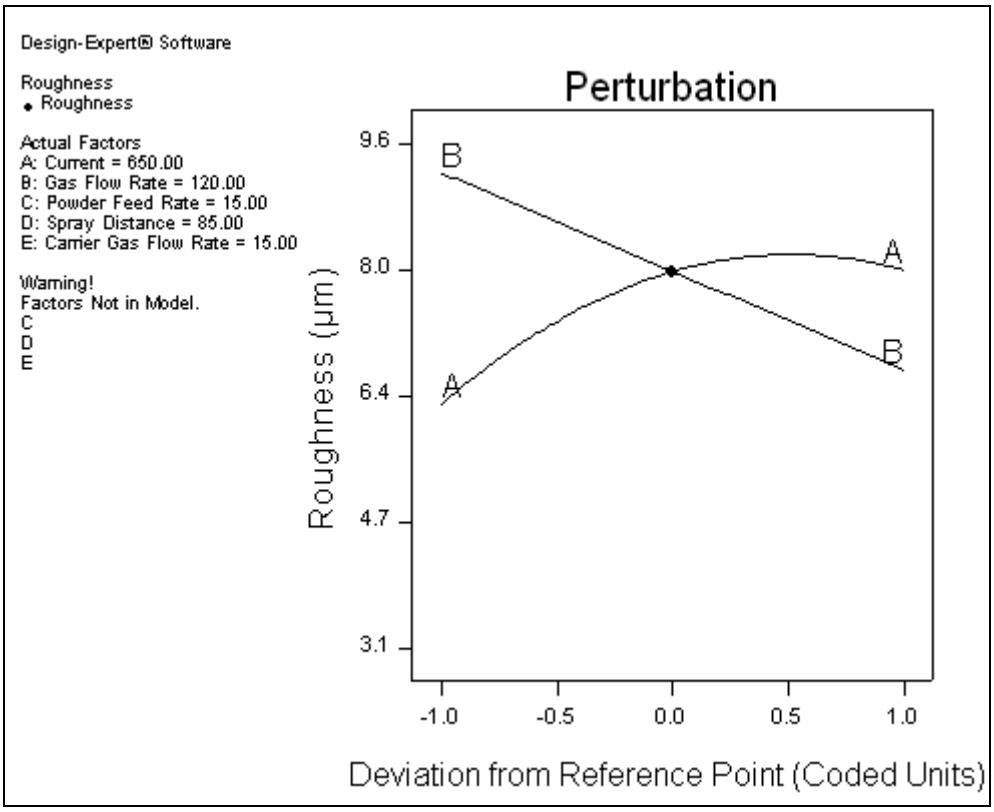

Figure 4.38: Roughness Perturbation Plot

The screening experiment identified Current, Gas Flow Rate and Powder Feed Rate as being the factors affecting the crystallinity of a coating. It was found that the coating roughness could be increased by increasing the Current, decreasing the Gas Flow Rate and increasing the Powder Feed Rate. In the RSM experiment Current and Gas Flow Rate were the only factors found to have a significant affect on the coating roughness. The effects for the RSM study were the same as for the screening study; coating roughness being found to increase with increasing Current and decreasing Gas Flow Rate. Powder Feed Rate was not found to be

significant in this study. This is due to the changes made to the parameters ranges in the RSM study.

The RSM model also showed that there was an interaction effect between the Current and Gas Flow Rate. This interaction is displayed more clearly in *figure 4.39*. The areas of highest roughness are shaded in red and the areas of lowest roughness are shaded in blue.

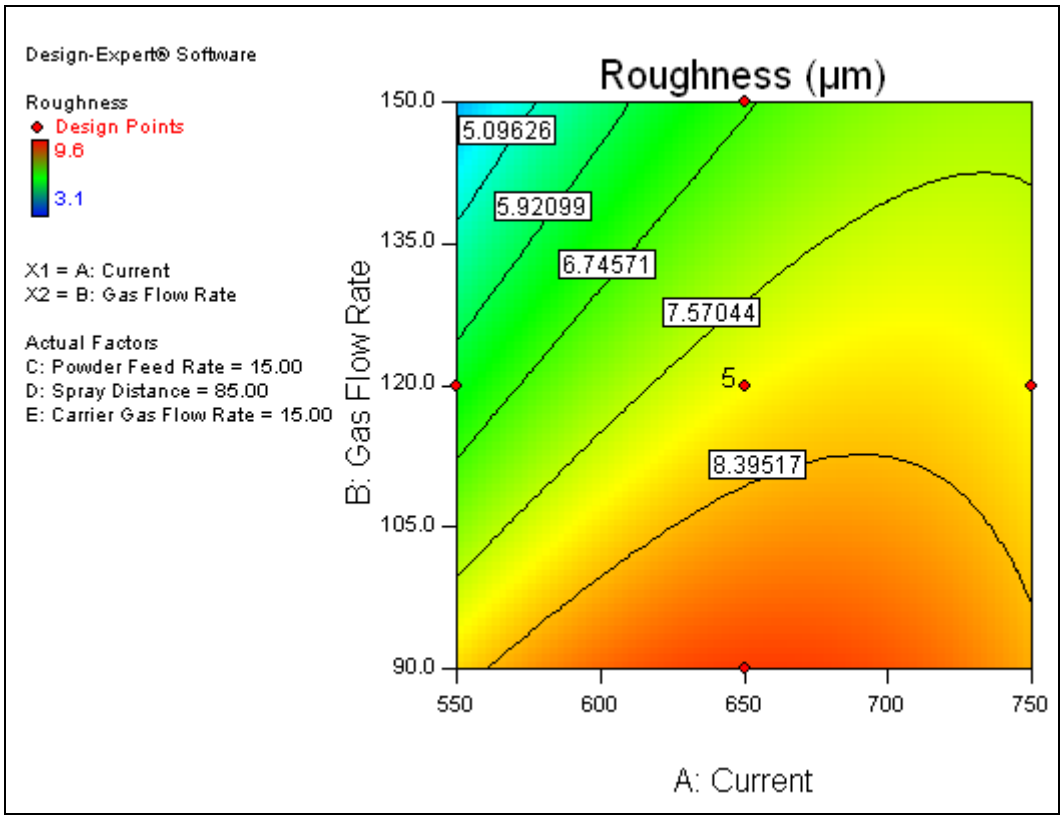

Figure 4.39: Effect of Current * Gas Flow Rate on Roughness

In *figure 4.39*, it can be seen that the greatest roughness results at low Gas Flow Rates. The curvature of the Current and Roughness relationship indicates the roughness increases with increasing Current up to a Current of about 650 A, after which the roughness decreases again. These findings relate well to those of the screening study. At low Current, only smaller particles are melted in the flame and thus the coating roughness is lower. Up to about 650 A the number of larger particles being melted increases and thus the roughness increases. After 650 A the degree of melting of the particles being deposited increases and the particles are

more molten and thus undergo a greater degree of flattening on impact with the substrate.

The effect of Gas Flow Rate is also as found for the screening study, coating Roughness being lower at high Gas Flow Rates. This is due to the high impact velocity at high Gas Flow Rates leading to greater splat flattening and thus lower roughness. The lower degree of particle melting at high Gas Flow Rates also results in only smaller particles being melted in the flame, and thus only smaller particles being deposited on the substrate.

It was observed from the screening experiment that the thickness of the coating may affect its roughness. In order to investigate the relationship between roughness and thickness, roughness was plotted against thickness, as shown in *figure 4.40*. The graph indicates that there is a relationship between roughness and thickness, with coating surface roughness increasing with increasing coating thickness. This confirms the indications of the screening experiment.

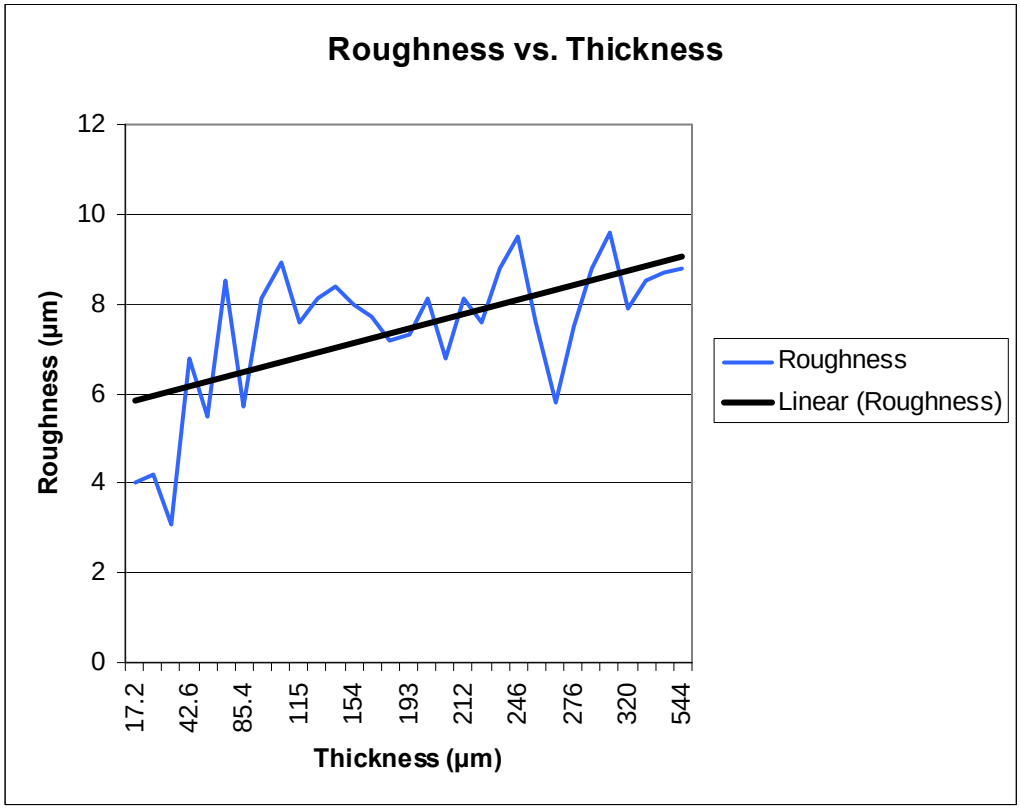

Figure 4.40: Roughness vs. Thickness

Coating Crystallinity

A two factor interaction model (2FI) was found to have the best fit for the crystallinity data. The model was fitted using the stepwise automatic reduction algorithm to remove insignificant terms The ANOVA table for this model is shown in *table 4.25.*

Table 4.25: ANOVA Table for Crystallinity

Source	***Sum of Squares***	***Mean Square***	***F-Value***	***p-value Prob >F***	***Significance***
Model Significance	272.32	38.90	9.64	< 0.0001	*significant*
A-Current	21.78	21.78	5.40	0.0293	
B-Gas Flow Rate	44.49	44.49	11.03	0.0030	
D-Spray Distance	43.56	43.56	10.80	0.0032	
E-Carrier Gas Flow Rate	26.40	26.40	6.54	0.0176	
AB	23.52	23.52	5.83	0.0241	
AD	76.56	76.56	18.98	0.0002	
BE	36.00	36.00	8.92	0.0066	
Lack of fit	90.10	4.74	7.08	0.0353	*not significant*
R^2	0.75				
Adj R^2	0.67				
Pred R^2	0.54				
Adeq Precision	12.65				

This model has a significance of < 0.0001. The lack of fit is not significant at a significance level of 0.01. The R^2 value is high and there is less than 0.2 of a difference between the Adjusted R^2 value and the Predicted R^2 value. The adequate precision value is well above 4. It can be concluded that this is a good model. Four parameters and three interactions are found to significantly affect the coating crystallinity. These are Current (A), Gas Flow Rate (B), Spray Distance (D) and Carrier Gas Flow Rate (E), the interaction of Current and Gas Flow Rate (A * B), Current and Spray Distance (A * D), and Gas Flow Rate and Carrier Gas Flow Rate (B * E). The model is given in terms of coded factors in *equation 4.8* and in terms of actual factors in *equation 4.9*.

Crystallinity = + 77.69 (*eqn. 4.8*)

+ 1.10	* A	(Current)
- 1.57	* B	(Gas Flow Rate)
- 1.56	* D	(Spray Distance)
- 1.21	* E	(Carrier Gas Flow Rate)
+ 1.21	* A * B	(Current*Gas Flow Rate)
- 2.19	* A * D	(Current*Spray Distance)
+ 1.50	* B * E	(Gas Flow Rate*Carrier Gas Flow Rate)

Crystallinity = + 58.23267 (*eqn. 4.9*)

+ 0.086458	* Current
- 0.46512	* Gas Flow Rate
+ 0.84421	* Spray Distance
-1.44222	* Carrier Gas Flow Rate
+ 4.04167E-004	* Current * Gas Flow Rate
- 1.45833E-003	* Current * Spray Distance
+ 0.01	* Gas Flow Rate * Carrier Gas Flow Rate

Figure 4.41 shows the Predicted vs Actual plot for the model.

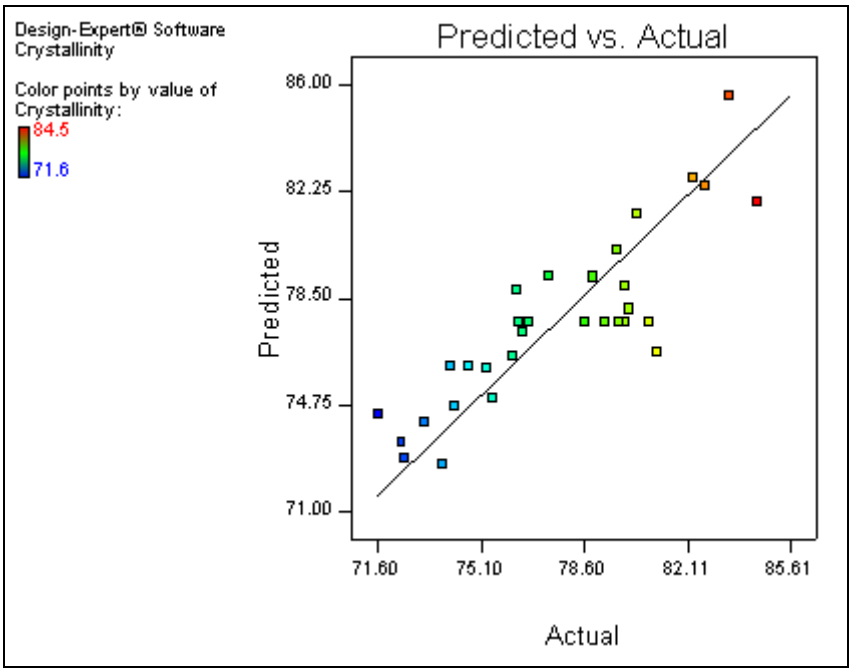

Figure 4.41: Predicted vs. Actual Plot for the Crystallinity Model

The experimental data points lie close to the straight line indicating a good fit. The perturbation plot for the model is shown in *figure 4.42*. This shows that the crystallinity can be increased by increasing the Current (A) and by decreasing the Gas Flow Rate (B), Spray Distance (D) and the Carrier Gas Flow Rate (E).

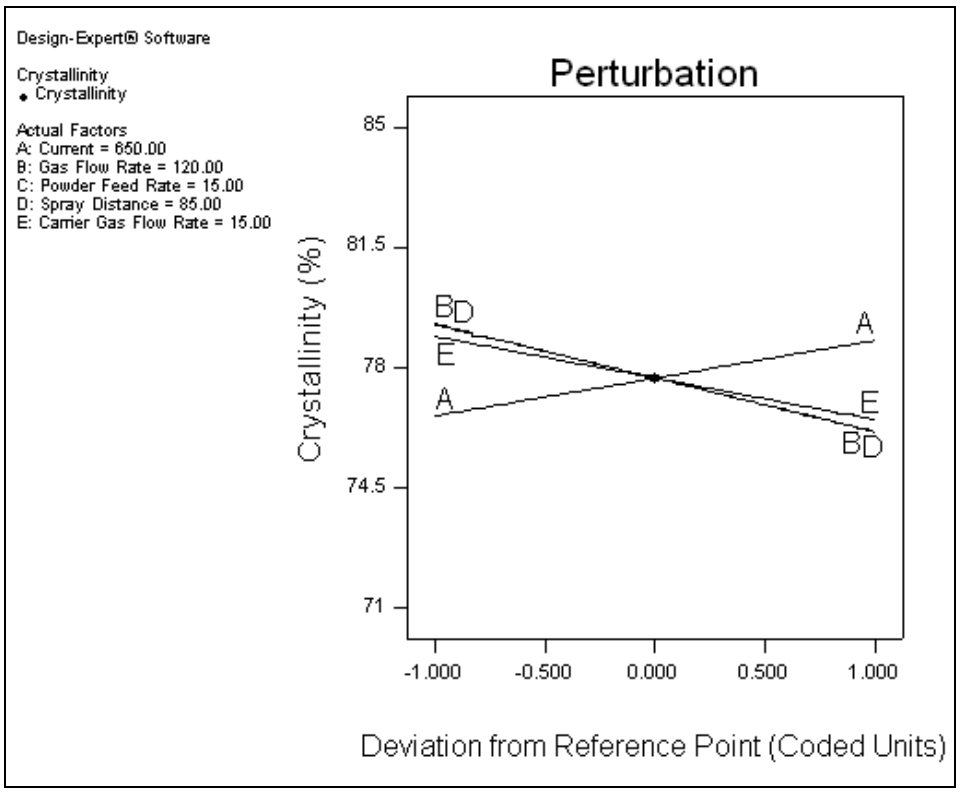

Figure 4.42: Perturbation Plot for Crystallinity

It was identified in the screening experiment that Current, Carrier Gas Flow Rate and Spray Distance affect the crystallinity of the coating. Increasing Current was observed to cause an increase in Crystallinity, increasing Spray Distance caused a decrease in Crystallinity and decreasing Carrier Gas Flow Rate caused an increase in Crystallinity. These effects were also found in the screening experiment. Gas Flow Rate was also found to be significant, with increasing Gas Flow Rate found to decrease Crystallinity. Interactions were found between Current and Gas Flow Rate, Current and Spray Distance, and Gas Flow Rate and Carrier Gas Flow Rate. The contour plots for each of the interactions are shown in *figure 4.43* to *figure 4.46*.

As discussed for the screening study, the crystallinity of a coating depends on the degree of melting that a particle undergoes and amount of recrystallisation that occurs following deposition on the substrate. It was found in the screening model that the spray conditions for production of a high crystallinity coating led to a high degree of particle melting and high substrate temperature. When sprayed at these conditions, a greater number of large particles are deposited leading to an increase in bulk crystallinity and the high substrate temperature allows a high degree of recrystallisation following deposition.

Figure 4.43 shows the interaction between Current and Gas Flow Rate. The highest Crystallinity results at a high Current and low Gas Flow Rate.

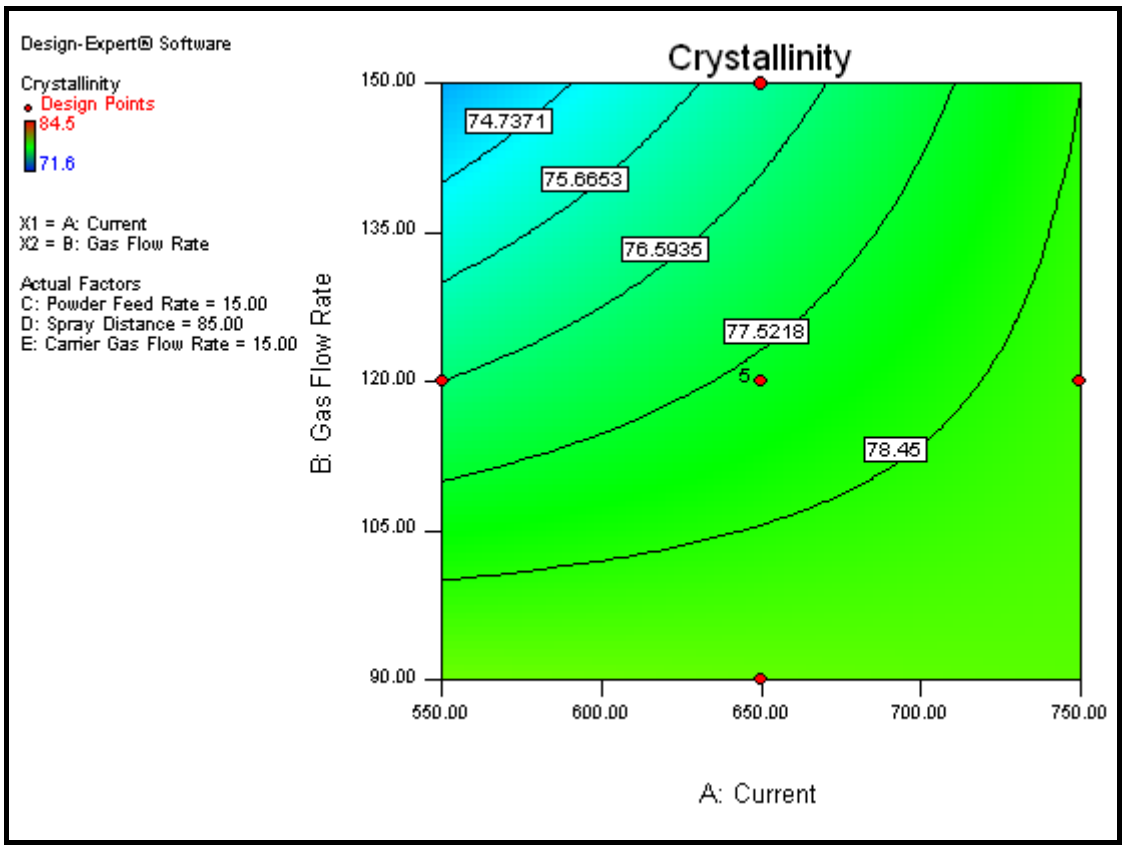

Figure 4.43: Effect of Current * Gas Flow Rate on Crystallinity

At these conditions a greater number of larger particles are deposited and the high Current value leads to high substrate temperature and thus high recrystallisation. There is little change in crystallinity with increasing Current at low Gas Flow Rates. This affect is only found at high Gas Flow Rates (above 130 SCFH) which

explains why Gas Flow Rate was not detected as a significant factor in the screening experiment (the range for Gas Flow Rate in the screening experiment was 70 to 130 SCFH).

The Current * Spray Distance interaction in *figure 4.44*, shows that at a high Current and low Spray Distance the crystallinity of the coating is greatest. At these spray settings the substrate temperature will be high, thus leading to low particle cooling rate and a high degree of particle recrystallisation. At high Current and high Spray Distance, coating crystallinity is low as particle melting is high and the substrate temperature is low leading to less recrystallisation.

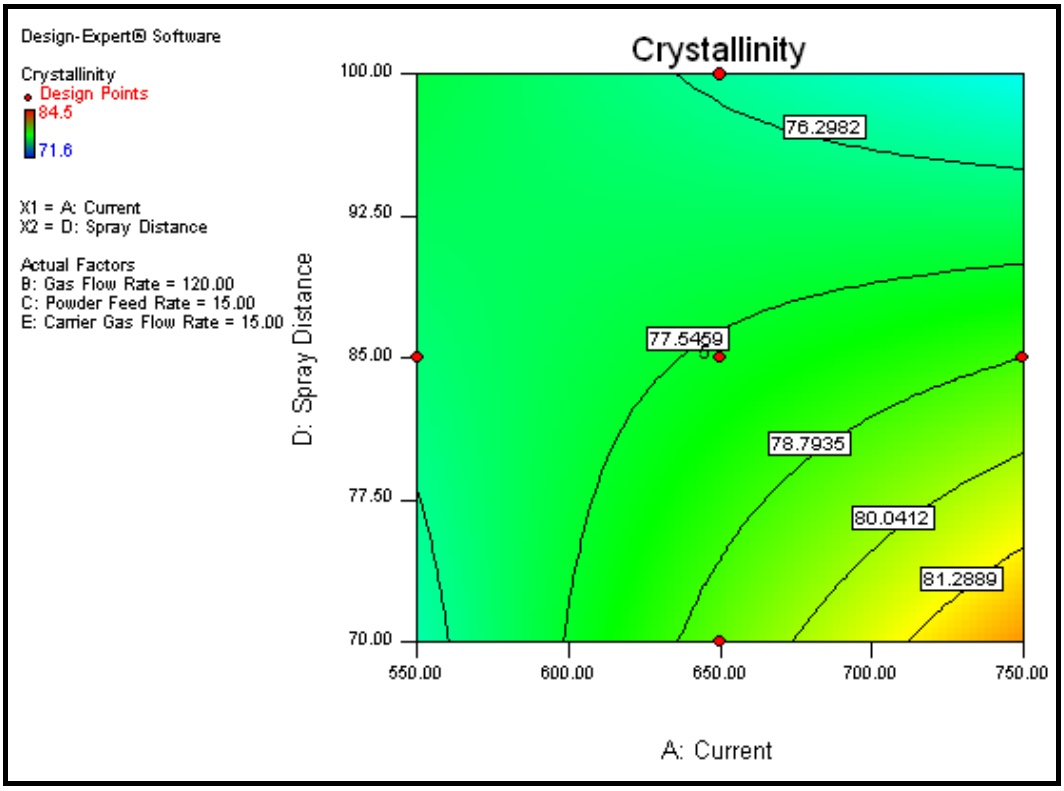

Figure 4.44: Effect of Current * Spray Distance on Crystallinity

Figure 4.45 shows the Gas Flow Rate * Carrier Gas Flow Rate interaction. At a low Gas Flow Rate and low Carrier Gas Flow Rate the particles remain in the outer portion of the plasma flame and so retain more of their bulk crystallinity, leading to a higher overall crystallinity. At high Gas Flow Rates, less of the larger particles are melted and thus the resultant crystallinity is lower.

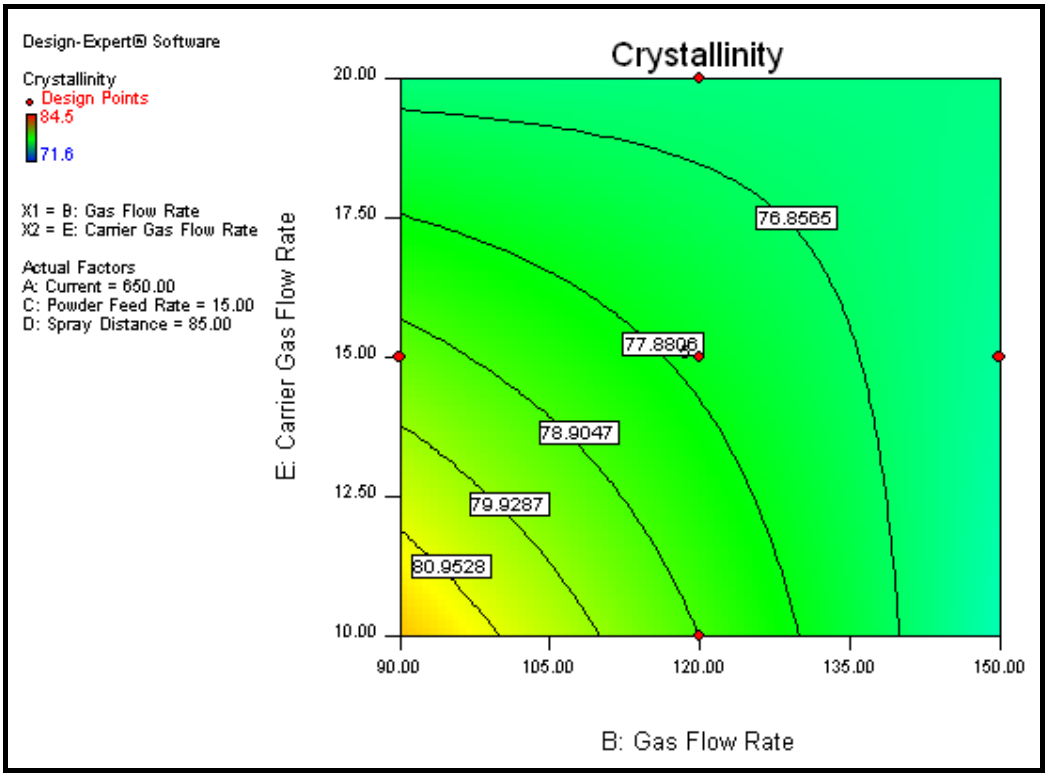

Figure 4.45: Effect of Gas Flow Rate * Carrier Gas Flow Rate on Crystallinity

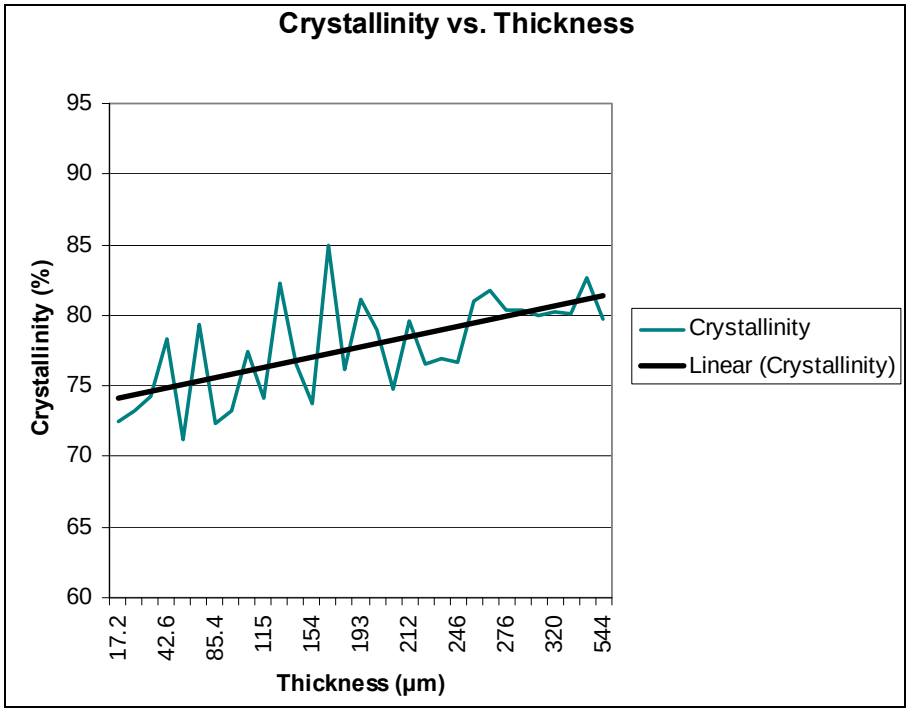

Figure 4.46: Effect of Coating Thickness on Crystallinity

It was suggested in the screening experiment that the crystallinity of a coating is related to its thickness. This was investigated by plotting crystallinity against

thickness. A relationship was found between the two responses, with crystallinity increasing with increasing thickness (*figure 4.46*). This agrees with the findings of Gross et al. [118].

Coating Purity

A quadratic model was found to have the best fit for the purity data. The model was fit using the stepwise automatic reduction algorithm to remove insignificant terms. A significance level of 0.05 was used to eliminate insignificant terms. The ANOVA table for this model is shown in *table 4.26.*

Table 4.26: ANOVA Table for Purity

Source	*Sum of Squares*	*Mean Square*	*F-Value*	*p-value Prob >F*	*Significance*
Model Significance	16.36	1.82	25.72	< 0.0001	*Significant*
A-Current	0.22	0.22	3.14	0.0907	
B-Gas Flow Rate	4.81	4.81	65.27	< 0.0001	
C-Powder Feed Rate	0.12	0.12	1.61	0.2620	
D-Spray Distance	2.47	2.47	33.58	< 0.0001	
E-Carrier Gas Flow Rate	5.42	5.42	73.67	< 0.0001	
AD	0.23	0.23	3.16	0.0739	
BC	0.28	0.28	3.85	0.0511	
BD	2.01	2.01	27.30	< 0.0001	
DE	0.49	0.49	6.61	0.0102	
Lack of fit	1.46	0.09	4.04	0.0929	*not significant*
R2	0.91				
Adj R2	0.87				
Pred R2	0.77				
Adeq Precision	22.42				

A large number of interaction effects were found to be significant for this model. In order to maintain model hierarchy all of the factors involved in interactions were included in the model even if they were not significant as a main effect. The model has a significance of < 0.0001. The lack of fit is not significant. The R^2 value is high and there is less than 0.2 of a difference between the Adjusted R^2

value and the Predicted R^2 value. The adequate precision value is well above 4. It can be concluded that this is a good model. The model is given in terms of coded factors in *equation 4.10* and in terms of actual factors in *equation 4.11*.

Purity =	+98.37			(e*qn. 4.10*)
	+0.12	* A	(Current)	
	+0.52	* B	(Gas Flow Rate)	
	-0.081	* C	(Powder Feed Rate)	
	-0.37	* D	(Spray Distance)	
	-0.55	* E	(Carrier Gas Flow Rate)	
	-0.12	* A * D	(Current * Spray Distance)	
	-0.13	* B * C	(Gas Flow Rate * Powder Feed Rate)	
	+0.35	* B * D	(Gas Flow Rate*Spray Distance)	
	-0.17	* D * E	(Spray Distance*Carrier Gas Flow Rate)	

Purity =	+97.68237		(e*qn. 4.11*)
	+6.00833E-003	* Current	
	-0.014327	* Gas Flow Rate	
	+0.086474	* Powder Feed Rate	
	-0.021512	* Spray Distance	
	+0.029722	* Carrier Gas Flow Rate	
	-6.03125E-005	* Current * Spray Distance	
	-7.60714E-004	* Gas Flow Rate * Powder Feed Rate	
	+5.06250E-004	* Gas Flow Rate * Spray Distance	
	-1.74375E-003	* Spray Distance * Carrier Gas Flow Rate	

Figure 4.47 gives the Predicted vs. Actual plot for the model. The experimental data points lie close to the straight line indicating a good fit. The perturbation plot is shown in *figure 4.48*. This figure shows the main effect of each factor on the Purity. It can be seen from *figure 4.48* and *equation 4.10*, that the factors that have the greatest effect on Purity are Gas Flow Rate (B), Carrier Gas Flow Rate (E) and Spray Distance (D). In the screening model, Purity increased with decreasing Powder Feed Rate, decreasing the Spray Distance and decreasing the Carrier Gas Flow Rate. These effects are also seen here. The RSM model shows that Current

and Gas Flow Rate also significantly affected the coating Purity. The Purity was seen to increase with increasing Current and increasing Gas Flow Rate.

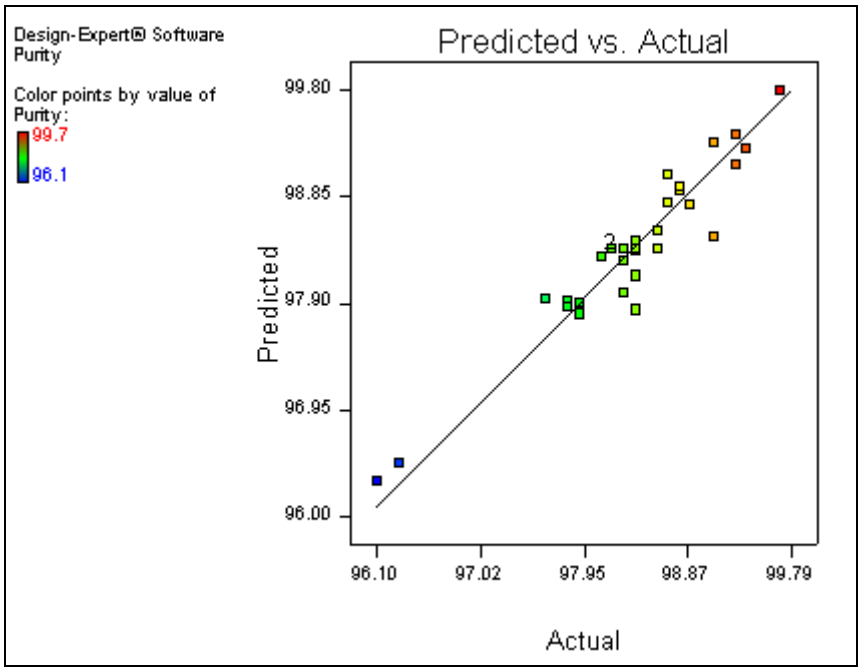

Figure 4.47: Predicted vs Actual Plot for the Purity Model

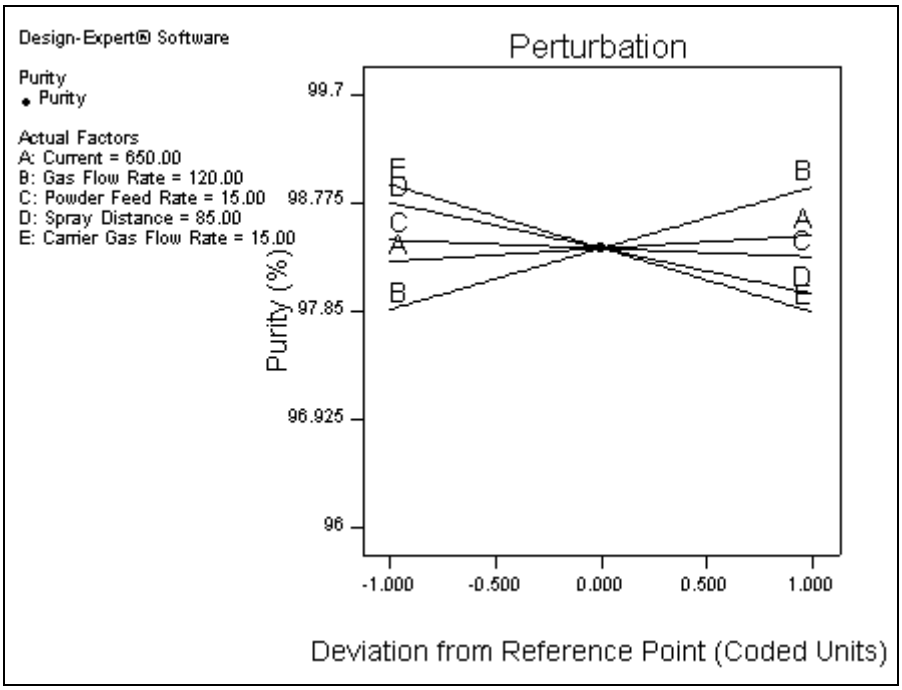

Figure 4.48: Perturbation Plot for Purity

The 2D contour plots for the interactions found to significantly affect the Purity are discussed in figure 4.49 to figure 4.52. The effect of the Gas Flow Rate * Spray Distance interaction on Purity is shown in figure 4.49. Purity is highest at high Gas Flow Rate and low Spray Distance. At higher Gas Flow Rates, there is little change in Purity with changing Spray Distance. A high Gas Flow Rate leads to lower particle heating as particles are propelled rapidly though the plasma flame. The Purity of the particles thus remains high. At low Spray Distances particles also spend less time in the plasma flame, being quickly deposited on the substrate and thus undergo less heating and result in a higher Purity coating.

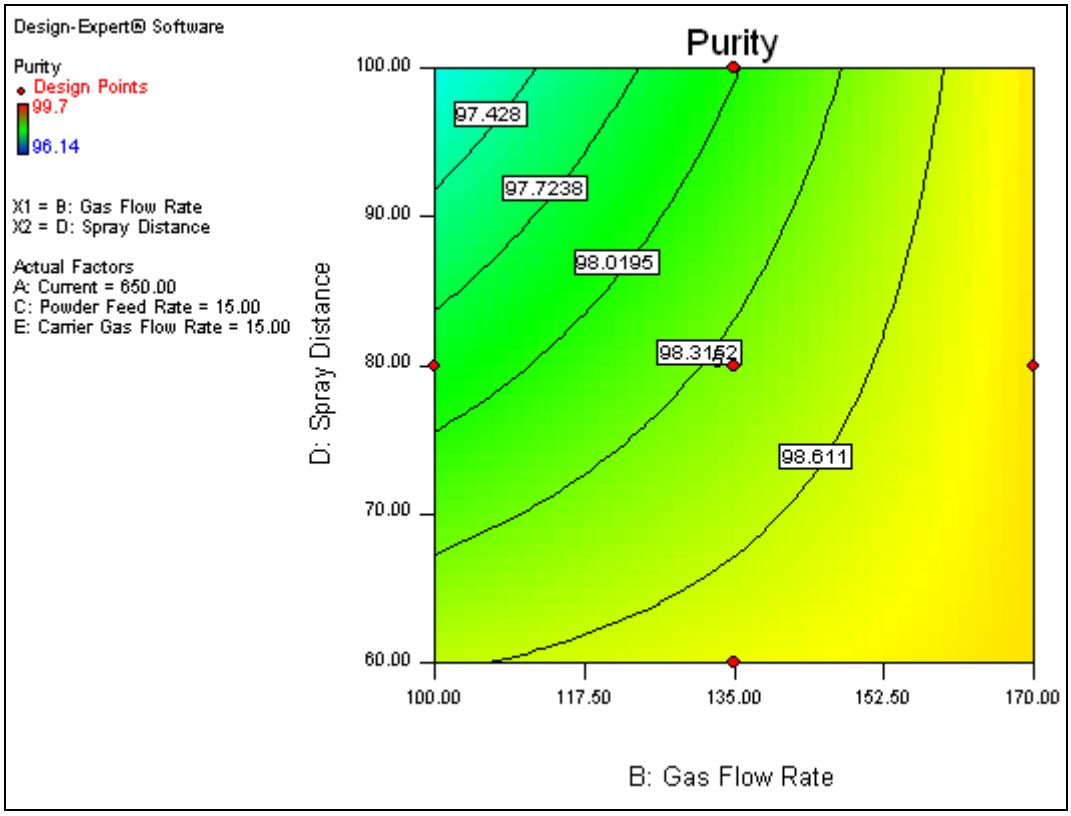

Figure 4.49: Effect of Gas Flow Rate * Spray Distance on Purity

Figure 4.50 shows the effect of the Spray Distance * Carrier Gas Flow Rate interaction on the Purity of the coating. Purity is highest at low Spray Distance and low Carrier Gas Flow Rate. Under these conditions the particles enter only the cooler regions of the plasma flame and spend only a short time in the flame, thus undergoing little decomposition, leading to higher Purity.

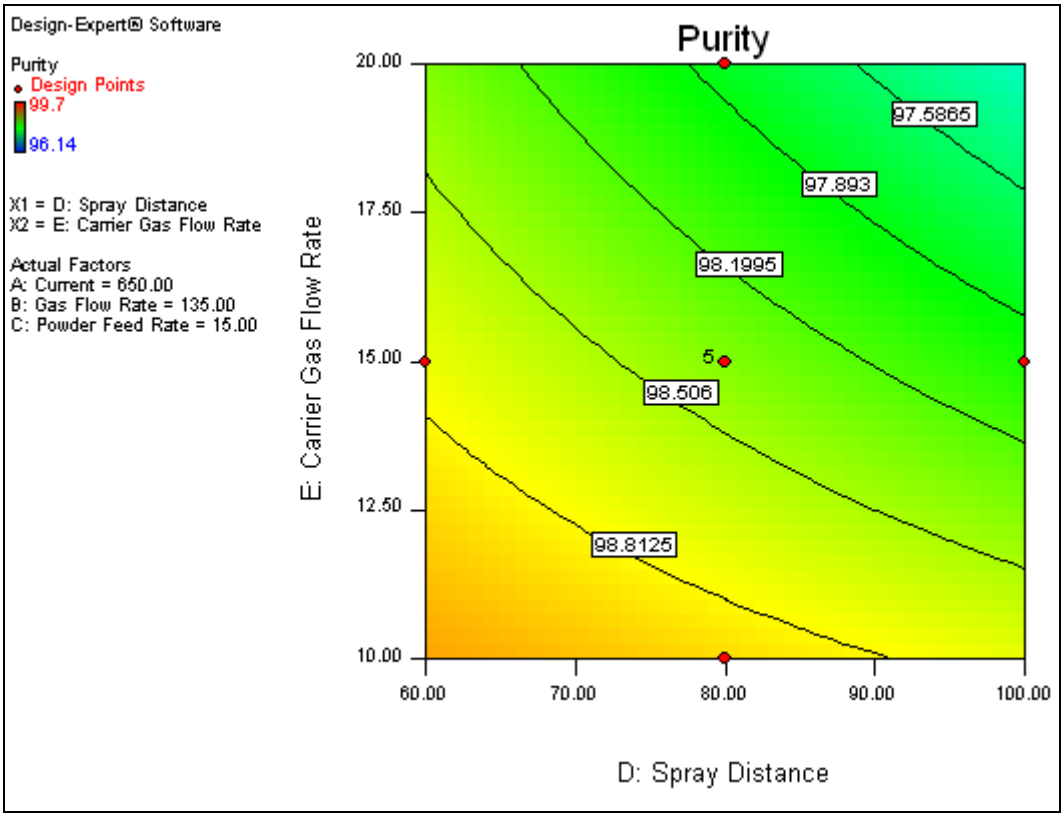

Figure 4.50: Effect of Spray Distance * Carrier Gas Flow Rate on Purity

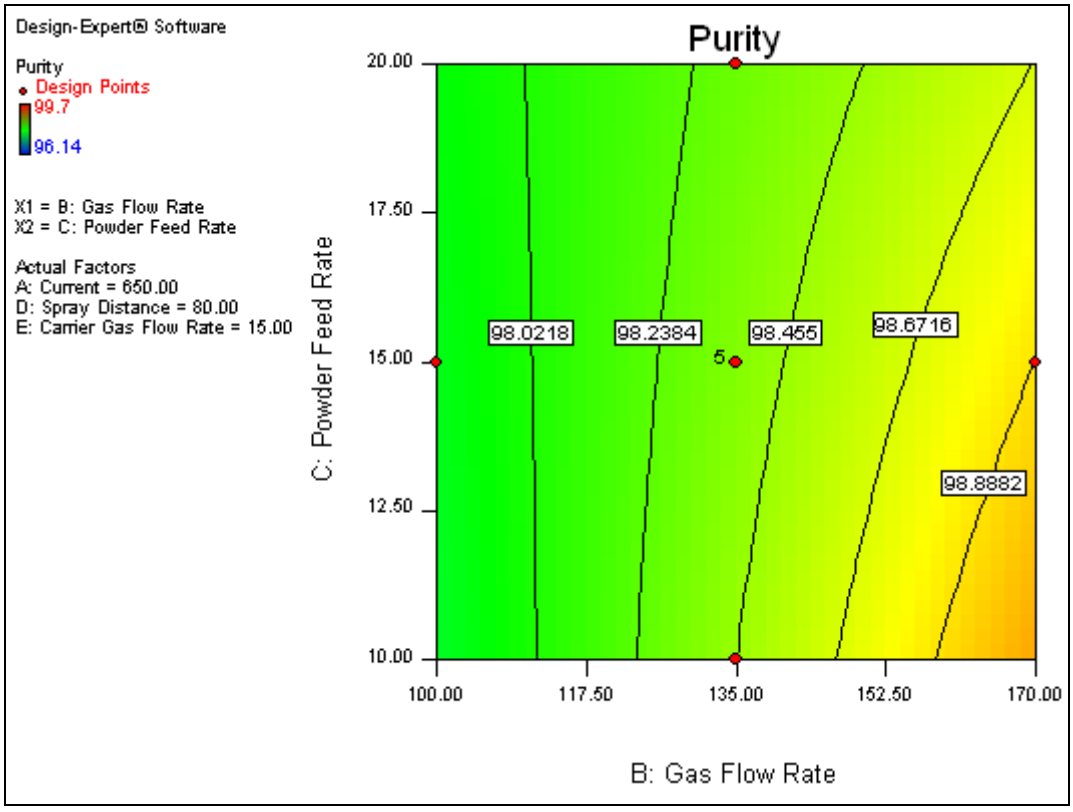

Figure 4.51: Effect of Gas Flow Rate * Powder Feed Rate on Purity

Figure 4.51 shows the effect of the Gas Flow Rate * Powder Feed Rate interaction on Purity. As found in *figure 4.51,* Purity is highest at high Gas Flow Rate. The Powder Feed Rate has little effect on Purity at low Gas Flow Rates, whereas, at high Gas Flow Rates, Purity is higher at low Powder Feed Rates. This may relate to the rate of coating build up, where retransformation of calcium phosphate phases to HA can occur when the coating is open to the atmosphere during cooling, such as is the case at low Powder Feed Rates. *Figure 4.52* shows the effect of the Current * Spray Distance on the Purity. This interaction has the smallest effect on the coating Purity. It is more difficult to explain than the other effects. *Figure 4.52* shows that highest Purity results at high Current and low Spray Distance. This is because at high Current, greater numbers of particles are deposited on the substrate, and as explained above, the centres of the larger particles will tend to not lose their purity as easily as the smaller particles. Particles impact quickly on the substrate at low Spray Distances, and there is insufficient time for the particles to heat up and for other phases to develop. There are smaller changes in Purity with Spray Distance at low Current. There are even smaller changes in Purity with Current at high Spray Distance.

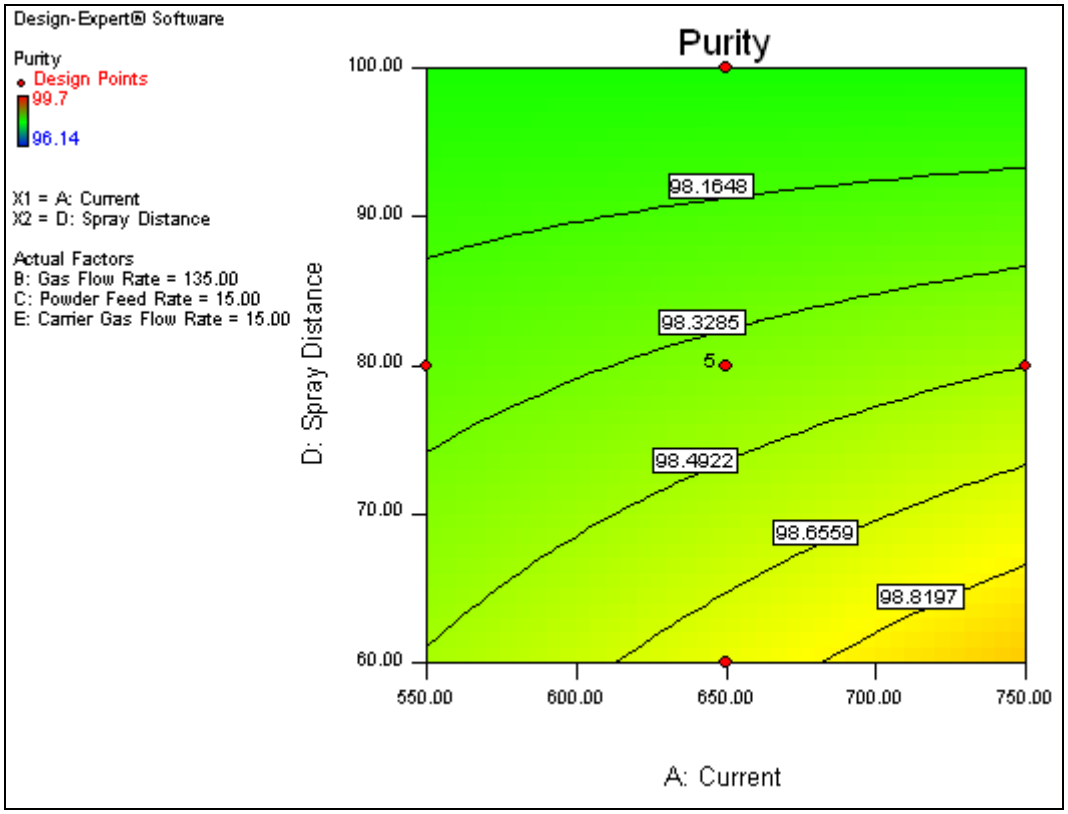

Figure 4.52: Effect of Current * Spray Distance on Purity

Coating Porosity

A two factor interaction model (2FI) was found to have the best fit for the porosity data. The model was fit using the stepwise automatic reduction algorithm to remove insignificant terms. The ANOVA table for this model is shown in *table 4.27.*

Table 4.27: ANOVA Table for Porosity

Source	*Sum of Squares*	*Mean Square*	*F-Value*	*p-value Prob >F*	*Significance*
Model Significance	2724.03	389.147	6.076305	0.0007	*significant*
A-Current	15.16	15.1582	0.236687	0.6319	
B-Gas Flow Rate	474.72	474.7223	7.412514	0.0131	
C-Powder Feed Rate	485.15	485.1488	7.575317	0.0123	
D-Spray Distance	6.73	6.727953	0.105053	0.7492	
AB	157.45	157.4484	2.458466	0.1326	
AD	501.49	501.4888	7.830456	0.0111	
BD	1022.26	1022.26	15.962	0.0007	
Lack of fit	1031.68	64.4798	1.035028	0.5472	*not significant*
R^2	0.68				
Adj R^2	0.57				
Pred R^2	0.42				
Adeq Precision	12.47				

This model has a significance of 0.0007. The lack of fit is not significant. The R^2 value is above the required 0.6 value and there is less than 0.2 of a difference between the Adjusted R^2 value and the Predicted R^2 value. Both Adjusted R^2 and Predicted R^2 lower than the desired 0.6 value. The adequate precision value is well above 4. It can be concluded that although a significant model has been achieved the predictive ability of the model may not be as high as for the other models developed. The reason why this model is not as good as the other models developed related to the missing experimental data (N3, N11 and N15), where some porosity measurements could not be obtained due to low coating thickness.

The model is given in terms of coded factors in *equation 4.12 an*d in terms of actual factors in *equation 4.13.*

Porosity =	+19.20		(*eqn. 4.12*)
	+1.18	* A	(Current)
	-6.58	* B	(Gas Flow Rate)
	-5.81	* C	(Powder Feed Rate)
	-0.76	* D	(Spray Distance)
	-4.12	* A * B	(Current * Gas Flow Rate)
	+7.12	* A * D	(Current * Spray Distance)
	-10.17	* B * D	(Gas Flow Rate * Spray Distance)

Porosity =	-15.52858		(*eqn. 4.13*)
	-0.22733	* Current	
	+2.59389	* Gas Flow Rate	
	-1.16269	* Powder Feed Rate	
	-0.42552	* Spray Distance	
	-1.37202E-003	* Current * Gas Flow Rate	
	+4.74974E-003	* Current * Spray Distance	
	-0.022605	* Gas Flow Rate * Spray Distance	

Figure 4.53 gives the Predicted vs. Actual plot for the model. The experimental data points lie close to the straight line indicating a good fit.

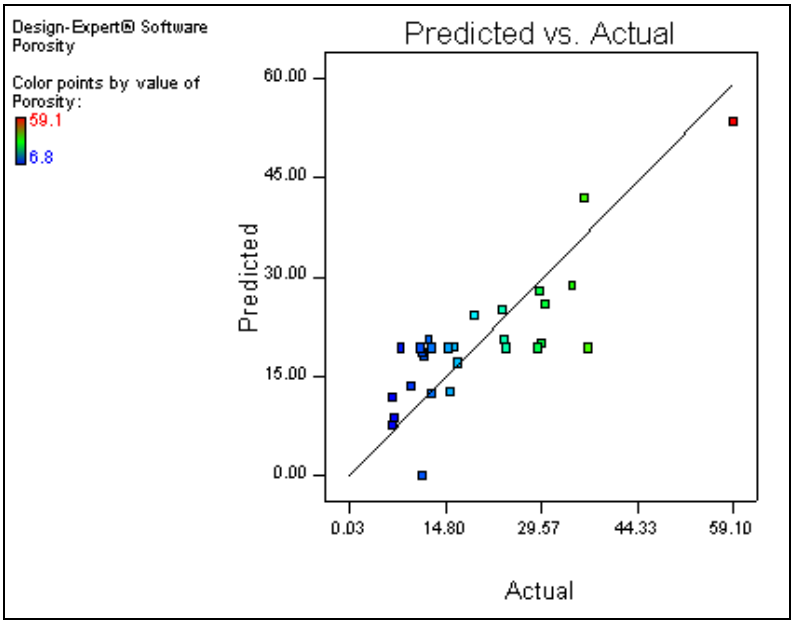

Figure 4.53: Predicted vs Actual for the Porosity Model

The perturbation plot for porosity is shown in *figure 4.54*. The perturbation plot and *equation 4.12* indicate that Gas Flow Rate (B) and Powder Feed Rate (C) have the greatest affect on the Porosity, followed by Current (A) and Spray Distance (D). The Porosity is increased by increasing the Current and Spray Distance and decreasing the Gas Flow Rate and Powder Feed Rate. There were also interaction affects between the Current and Gas Flow Rate, between the Current and Spray Distance, and between the Gas Flow Rate and the Spray Distance. The contour plots for each of the interactions are given in *figure 4.57* to *figure 4.59*.

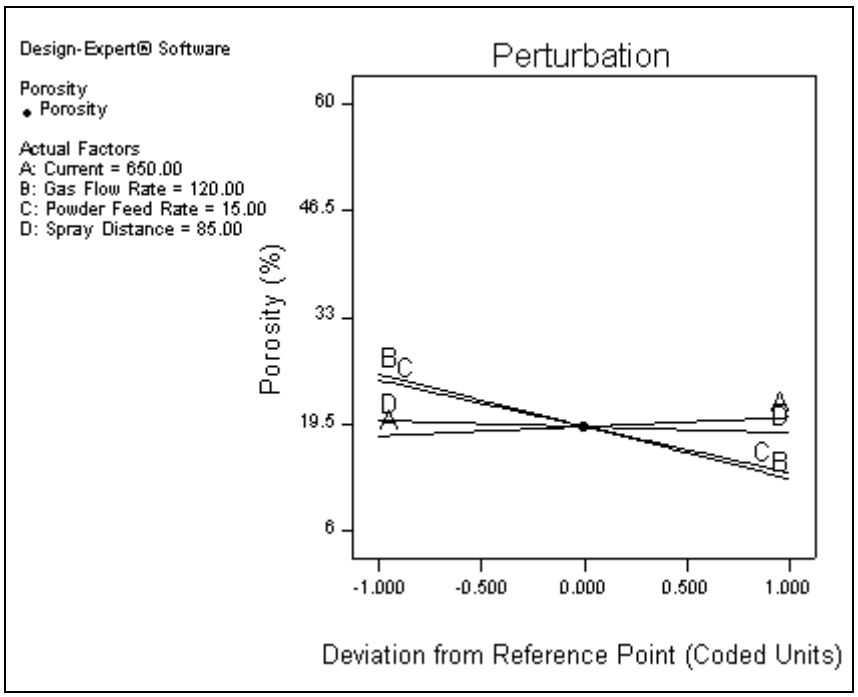

Figure 4.54: Perturbation Plot for the Porosity Model

The porosity of a coating depends on the degree of particle melting within the plasma flame and the amount of spreading on impact with the substrate. If particles are only partially melted they will not flatten out to a large degree and gaps will remain between them, resulting in a more porous coating. A highly molten particle that impacts the substrate at high speed will spread to a greater degree on the substrate thus reducing porosity [106].

The effect of significant factors on the particle temperature and velocity at high porosity spray conditions are summarised in *table 4.28*. The overall effect at these conditions is found to be a high particle temperature and low particle velocity.

Table 4.28: Overall effect on particle temperature and velocity for high porosity spray conditions

Factor		*Particle Temperature*	*Particle Velocity*
Current	↑	↑	↑
Gas Flow Rate	↓	↓	↓
Powder Feed Rate	↓	↑	
Spray Distance	↑	↑	↓
Overall Effect		↑	↓

The model for Porosity (*equation 4.12*) indicates that Gas Flow Rate has the greatest effect on Porosity, with highest Porosity resulting at low Gas Flow Rates. This is due to the lower impact velocity at this condition leading to low particle spreading. This agrees with the findings of Quek et al. [106].

Powder Feed Rate has the second largest effect, with higher porosity resulting at lower Powder Feed Rate. This is due to the lower numbers of particles being deposited with each pass of the spray gun. For this situation, particles cool and solidify separately leading to the formation of gaps and pores.

A number of interaction effects have also been identified for Porosity. The Gas Flow Rate * Spray Distance interaction is found to have the greatest effect. This is shown in *Figure 4.55*. This interaction shows that high Porosity results at low Gas Flow Rate and high Spray Distance and at high Gas Flow Rate and low Spray Distance. At low Gas Flow Rate and high Spray Distance particles will be experience a high degree of melting, resulting in the deposition of larger particles. The low Gas Flow Rate will lead to a low impact velocity and thus, low particle spreading and high porosity.

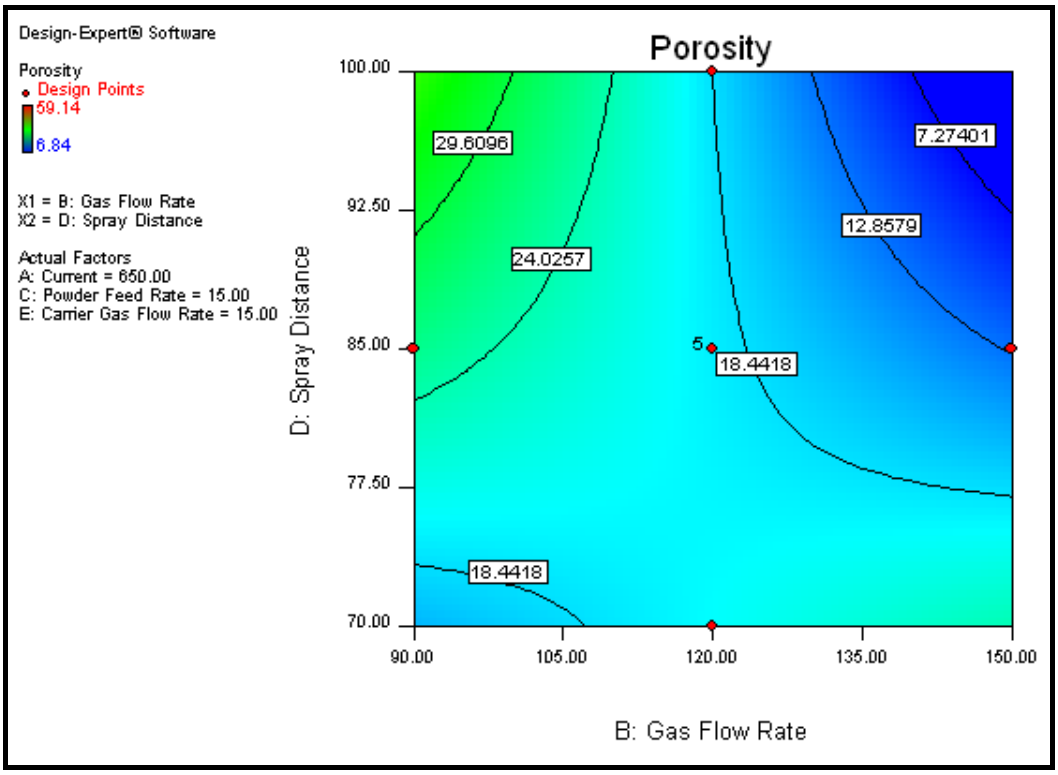

Figure 4.55: Effect of Gas Flow Rate * Spray Distance on Porosity

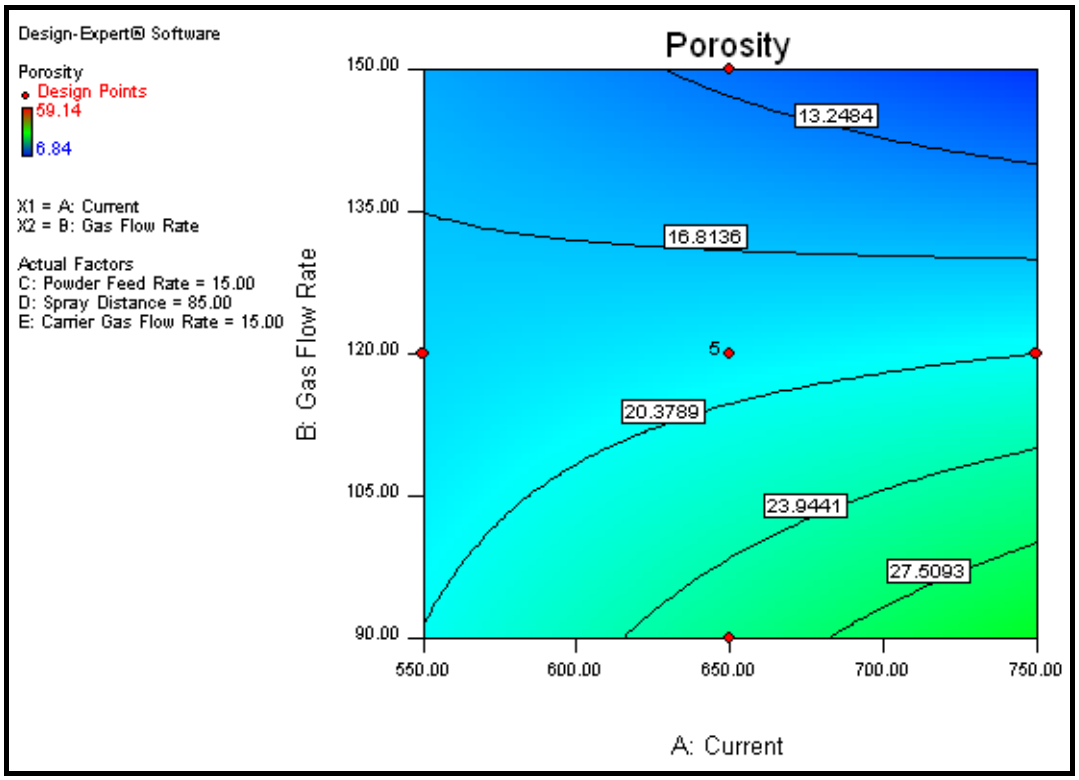

Figure 4.56: Effect of Current * Gas Flow Rate on Porosity

Figure 4.56 shows the effect of the Current * Gas Flow Rate interaction on Porosity. The highest Porosity results at a high Current and low Gas Flow Rate. Again at these conditions, particles experience a high degree of heating and thus melting of the full range of particle sizes occurs. The low Gas Flow Rate causes particles to impact on the substrate at a lower force and thus less spreading of particles occurs. This leads to a greater number of spaces and gaps between particles and thus high porosity.

Figure 4.57 shows the effect of the Current * Spray Distance interaction on Porosity. The highest porosity results for two conditions, low Current and low Spray Distance and high Current and High Spray Distance. At low Current and low Spray Distance particles are less melted due to the lower temperature flame and lower residence time in the flame. This leads to less particle spreading and thus a higher percentage of pores in the coating. At high Current and high Spray Distance, a large amount of particle heating occurs leading to deposition of large particles and thus a greater porosity

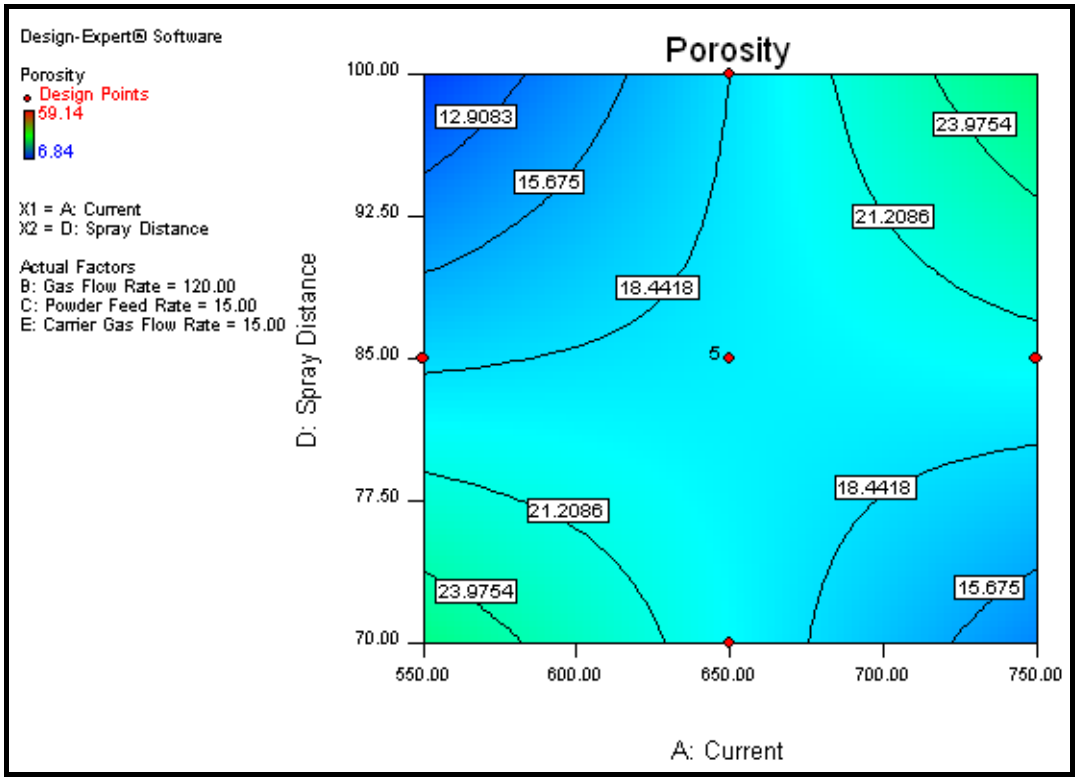

Figure 4.57: Effect of Current * Spray Distance on Porosity

Coating Thickness

A two factor interaction model (2FI) was found to have the best fit for the coating thickness data. The model was fit using the stepwise automatic reduction algorithm to remove insignificant terms (p = 0.05). The ANOVA table for this model is shown in *table 4.29.*

Table 4.29: ANOVA Table for Thickness

Source	*Sum of Squares*	*Mean Square*	*F-Value*	*p-value Prob >F*	*Significance*
Model Significance	382329	47791.13	18.66499	< 0.0001	*significant*
A-Current	144731.9	144731.9	56.52553	< 0.0001	
B-Gas Flow Rate	112663.3	112663.3	44.00105	< 0.0001	
C-Powder Feed Rate	34003.97	34003.97	13.28037	0.0014	
D-Spray Distance	46473.37	46473.37	18.15033	0.0003	
E-Carrier Gas Flow Rate	3661.683	3661.683	1.430083	0.2445	
AD	11681.02	11681.02	4.562061	0.0441	
BC	11619.76	11619.76	4.538138	0.0446	
BE	17494.03	17494.03	6.832354	0.0159	
Lack of fit	46884.68	2604.705	1.10303	0.5190	*not significant*
R^2	0.871585				
Adj R^2	0.824889				
Pred R^2	0.710566				
Adeq Precision	19.13154				

This model has a significance of < 0.0001. The lack of fit is not significant. The Carrier Gas Flow Rate (E) was not significant as a main effect but was included in the model as it forms part of a significant interaction effect. The R^2 value is high and there is less than 0.2 of a difference between the Adjusted R^2 value and the Predicted R^2 value. The adequate precision value is well above 4. It can be concluded that this is a good model.

The model is given in terms of coded factors in *equation 4.13* of actual factors in *equation 4.14.*

Thickness =	+190.19			(*eqn. 4.13*)
	+89.67	* A	(Current)	
	-79.11	* B	(Gas Flow Rate)	
	+43.46	* C	(Powder Feed Rate)	
	-50.81	* D	(Spray Distance)	
	+14.26	* E	(Carrier Gas Flow Rate)	
	-27.02	* A * D	(Current * Spray Distance)	
	-26.95	* B * C	(Gas Flow Rate * Powder Feed Rate)	
	+33.07	* B * E	(Gas Flow Rate * Carrier Gas Flow Rate)	

Thickness =	-883.26428		(*eqn. 4.14*)
	+2.42781	* Current	
	-3.24889	* Gas Flow Rate	
	+30.25178	* Powder Feed Rate	
	+8.32107	* Spray Distance	
	-23.60044	* Carrier Gas Flow Rate	
	-0.018013	* Current * Spray Distance	
	-0.17966	* Gas Flow Rate * Powder Feed Rate	
	+0.22044	* Gas Flow Rate * Carrier Gas Flow Rate	

Figure 4.58 gives the Predicted vs. Actual plot for the model. The experimental data points lie close to the straight line indicating a good fit.

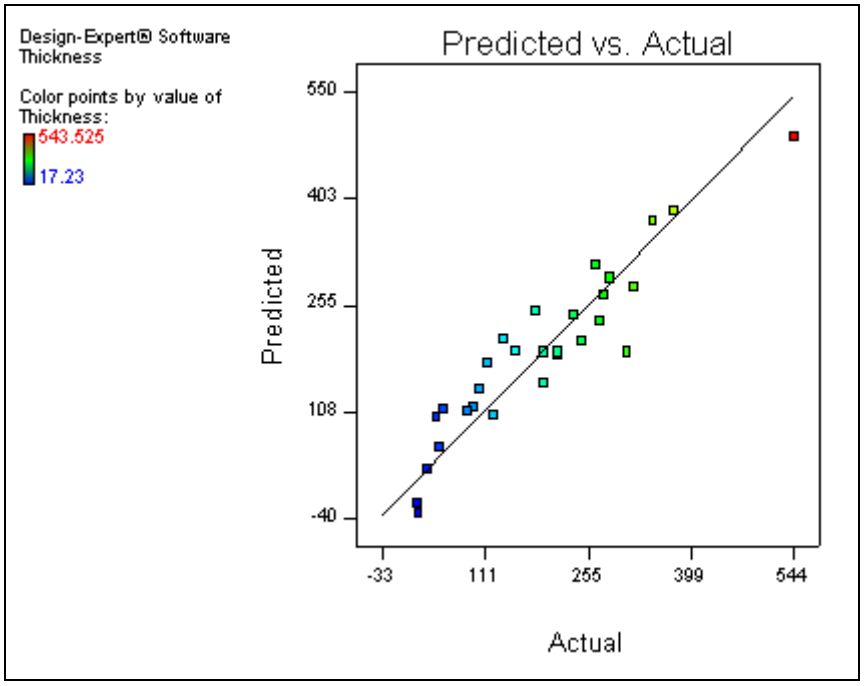

Figure 4.58: Predicted vs Actual for the Thickness Model

The perturbation plot for thickness is shown in *figure 4.59*. The thickness of the coating was found to be affected by all five parameters; Current (A), Gas Flow Rate (B), Powder Feed Rate (C), Spray Distance (D) and Carrier Gas Flow Rate (E). There were also interactions between the Current and the Spray Distance, between the Gas Flow Rate and the Powder Feed Rate and between the Gas Flow Rate and the Carrier Gas Flow Rate. It can be seen from *equation 4.13* and *figure 4.59* that Current (A) has the greatest effect on thickness, followed by Gas Flow Rate (B), Spray Distance (D), Powder Feed Rate (C) and Carrier Gas Flow Rate (E). The thickness increases with increasing Current, Powder Feed Rate and Carrier Gas Flow Rate and decreasing Gas Flow Rate and Spray Distance. The contour plots for each of the interactions are given in *figure 4.60* to *figure 4.62*.

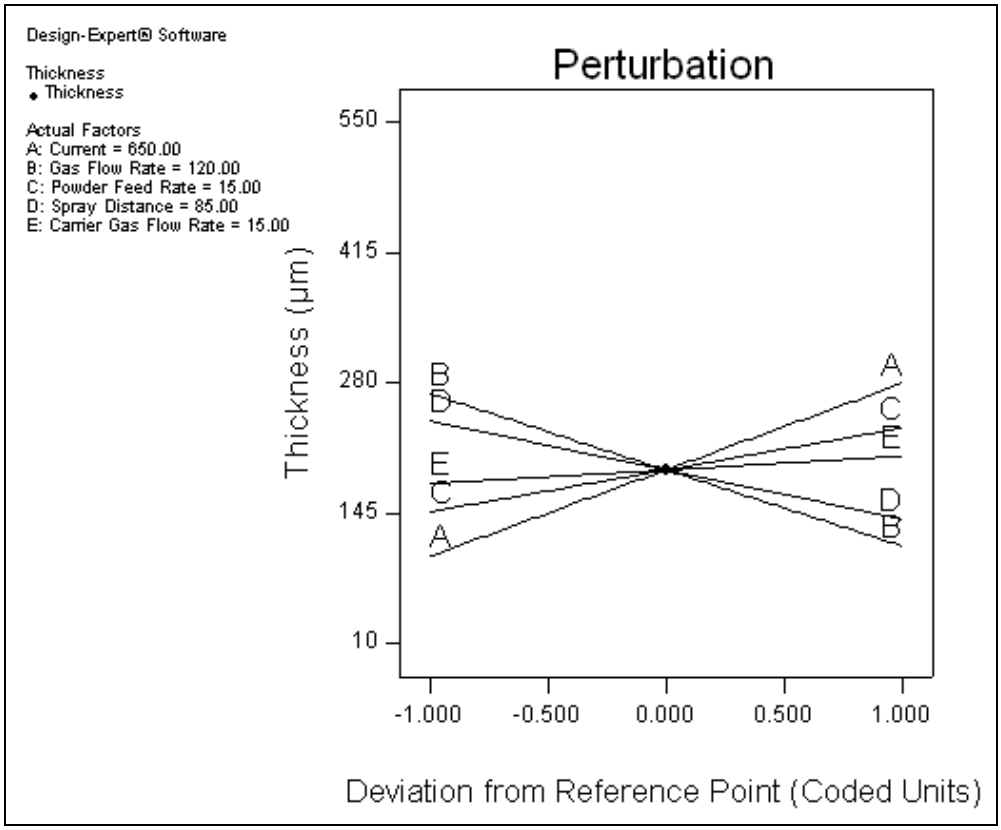

Figure 4.59: Perturbation Plot for the Thickness Model

From the literature, coating thickness is known to relate to the number of particles that are deposited on the substrate surface and also the degree of flattening of the particles on impact. The number of particles that are deposited on the substrate relates to the amount of particles that are fed into the plasma flame, the number of particles that are sufficiently melted within the flame to adhere to the substrate on impact and the number of particles that maintain sufficient velocity to remain in the plasma flame until the point of impact.

Table 4.30: Overall effects on number of particles deposited and degree of particle flattening for high thickness spray conditions

Factor		*Number of Deposited Particles*	*Degree of Particle Flattening*
Current	↑	↑	↑
Gas Flow Rate	↓		↓
Powder Feed Rate	↑	↑	
Spray Distance	↓	↑	↑
Carrier Gas Flow Rate	↑	↑	↑
Overall Effect		↑	↓

Figure 4.60 shows the effect of the interaction between Current and Spray Distance on the coating thickness. It can be seen from this graph that Thickness is greatest at high Current and low Spray Distance. It is known from the findings of the other screening and RSM models that the Current affects the number of particles melted within the plasma flame, with more particles being melted at high Current. At low Current, large particles are not melted and instead bounce off the substrate rather than being deposited onto it. This explains why the coating thickness is low at low Current. Spray Distance affects deposition efficiency and thus thickness, with deposition efficiency being higher at low Spray Distance. At high spray distance, particles begin to cool and loose momentum and fall out of the plasma flame or bounce off the substrate surface.

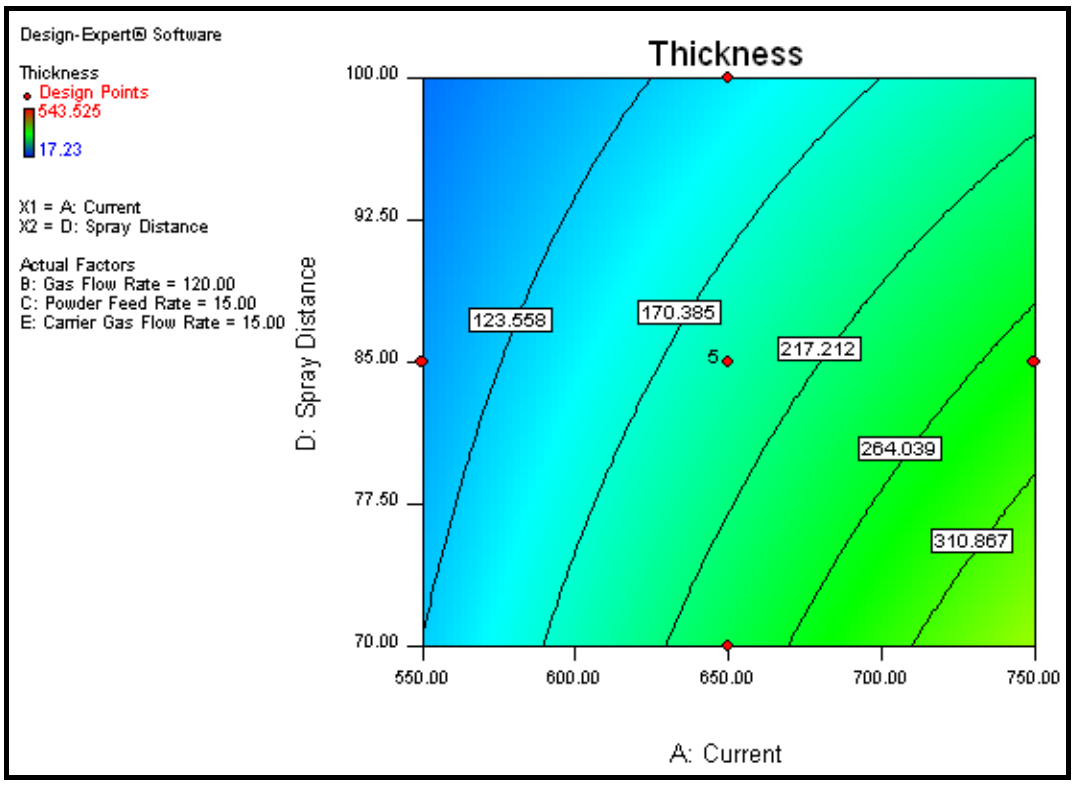

Figure 4.60: Effect of Current * Spray Distance on Thickness

Figure 4.61 shows the effect of the interaction of Gas Flow Rate and Carrier Gas Flow Rate on Thickness. Thickness is highest at low Gas Flow Rate and low Carrier Gas Flow Rate. This is due to the lower degree of splat flattening at low impact velocities. The change in thickness with Carrier Gas Flow Rate is small; Thickness is higher at low Gas Flow Rates up to ~ 105 SCFH. At Gas Flow Rates

greater than this, Thickness is higher at high Carrier Gas Flow Rates. When the Gas Flow Rate is high it is more difficult to force particles into the plasma flame. It is probable that at high Gas Flow Rates and low Carrier Gas Flow Rates fewer particles enter the flame and thus the coating thickness is lower.

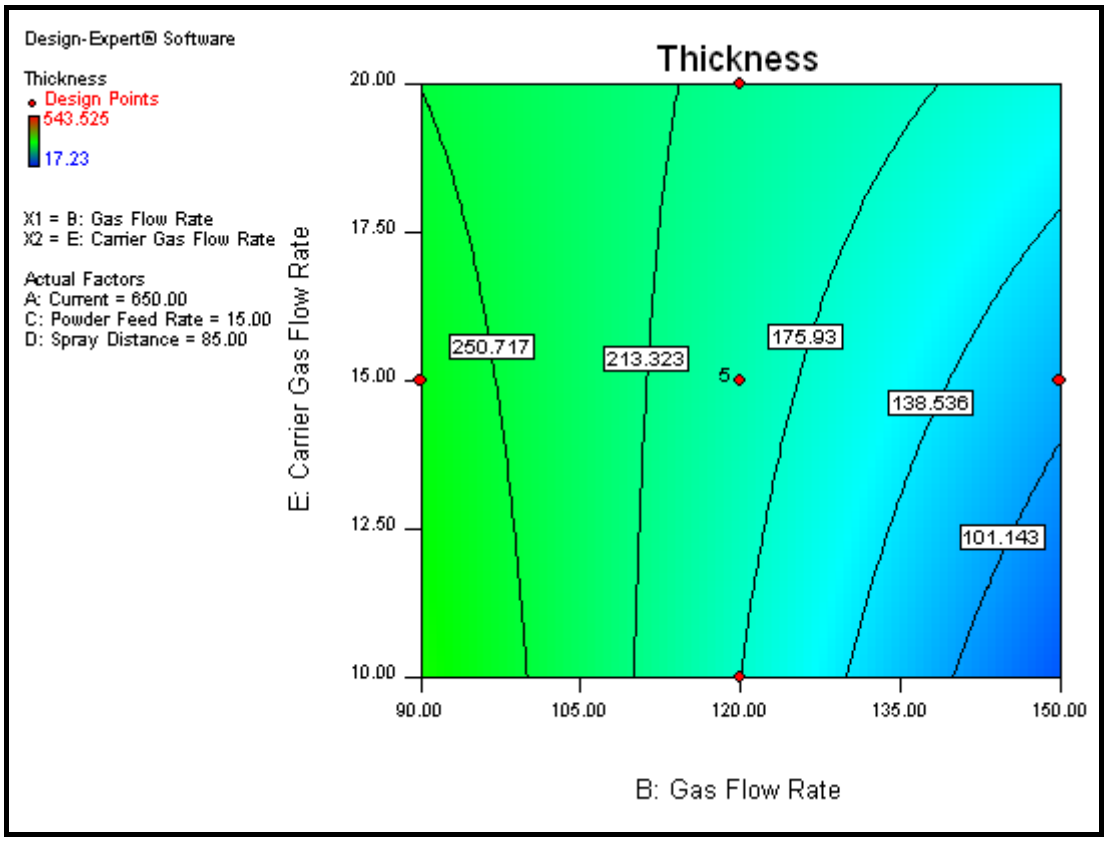

Figure 4.61: Effect of Gas Flow Rate * Carrier Gas Flow Rate on Thickness

The effect of the interaction between Gas Flow Rate and Powder Feed Rate on Thickness is shown in *figure 4.62*. Coating Thickness is highest at low Gas Flow Rate and high Powder Feed Rate. Increasing the Powder Feed Rate increases the number of particles that are fed into the plasma flame and so increases the coating thickness. At low Gas Flow Rate powder particles impact on the substrate at low velocity and thus less flattening occurs, resulting in a thicker coating.

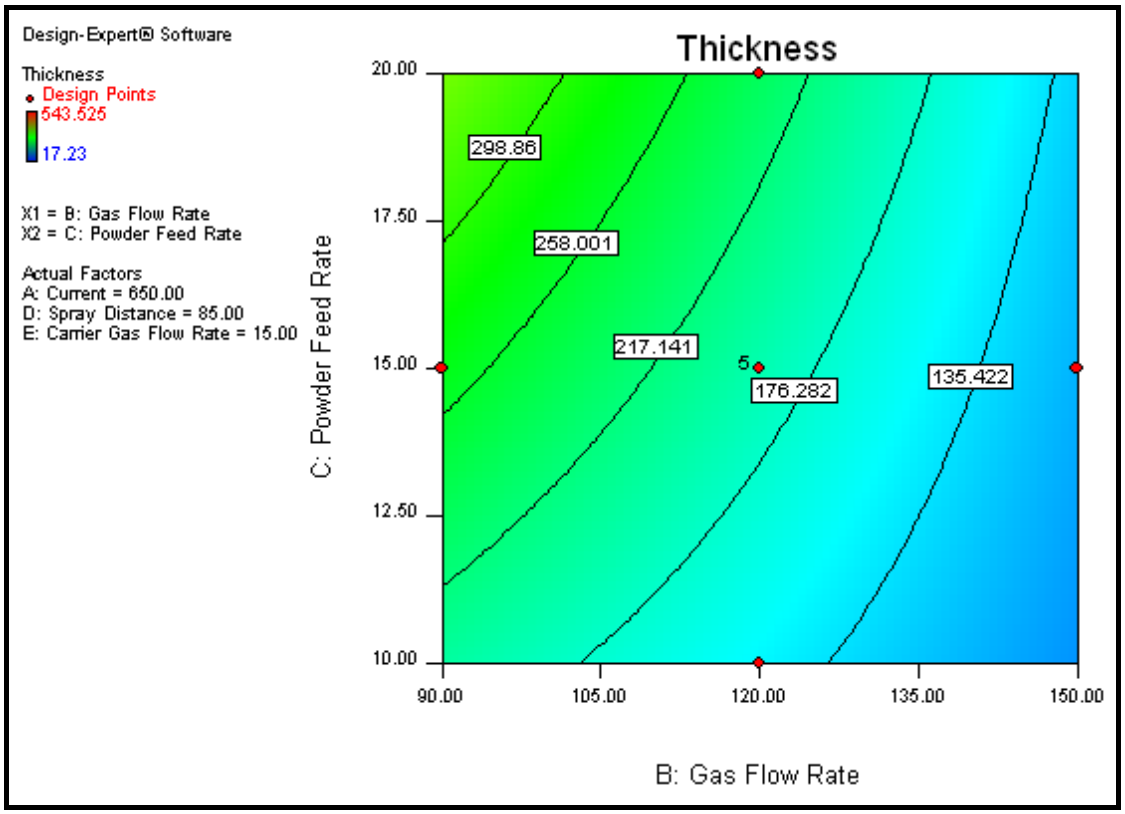

Figure 4.62: Effect of Gas Flow Rate * Powder Feed Rate on Thickness

Summary of RSM Models

The parameters effects observed for the RSM models were found to agree with those found in the screening study. The RSM models have identified that a number of interactions affect each of the responses investigated. These interaction effects give a clearer picture of the affects of parameters on responses. Tradional one-factor-at-a-time experimentation cannot identify interaction effects leading to the types of contradictions in relation in parameters affects identified in the literature. In order to validate the models produced in this RSM study a series of model validation tests were carried out. The results of these tests are detailed in the following section.

4.6.8 Model Validation

The predicted vs actual diagrams presented for each model (*figure 4.37, figure 4.41, figure 4.47, figure 4.53* and *figure 4.*58) show that there is good agreement

between the mathematical models and the measured value for each response. In order to further verify the models three spraying experiments were carried out at new test conditions, called point prediction experiments. The test conditions used for each of these experiments are given in *table 3.13*. The response values measured for each test condition were compared to the values predicted by the developed Response Surface Models. The results are given in *table 4.31*. The % error between the response valve predicted by the model and the actual response value were calculated for each.

Table 4.31: Model Validity Results

		Roughness (*μm*)	*Crystallinity* (*%*)	*Purity* (*%*)	*Porosity* (*%*)	*Thickness* (*mm*)
1	**Predicted Value**	8.0	77.3	97.9	26.4	124.3
	Actual Value	7.6	77.4	98.5	24.1	105.9
	Error %	5	0.13	0.61	8.64	14.8
2	**Predicted Value**	9.1	79.5	97.9	34.9	293.3
	Actual Value	9.4	78.3	98.5	29.9	281.6
	Error %	3.19	1.5	0.61	14.33	3.99
3	**Predicted Value**	8.5	78.6	97.8	16.8	255.3
	Actual Value	8.5	78.8	98.4	15.2	215.2
	Error %	0	0.25	0.61	9.52	15.70
Average Error %		2.73	0.63	0.61	10.85	11.50

It can be seen from *table 4.31* that the models for each response accurately predict the actual measured response values. The percentage error between the predicted and actual responses is very low (< 5 %) for crystallinity, purity and roughness. The average percentage error for the porosity and thickness models was found to be higher (< 11.5 %) than for the other three responses. This is expected as the model statistics indicated that these models have lower predictive power than the other models developed. The percentage error found is still low enough to conclude that the model can predict the response value achieved. The low percentage error found confirms that the models developed in this work are valid and accurate.

4.6.9 RSM Experiment Summary

The RSM study has allowed the development of five response models that relate Roughness, Crystallinity, Purity, Porosity and Thickness to the five factors investigated. The significant factors and interactions found from the process models to affect the five responses are summarised in *table 4.32*. These factor effects are found to agree with the factor effects found for the screening study (*figure 4.16*).

It can be seen that Current and Gas Flow Rate are both very important factors, affecting all of the investigated responses. Both are also involved in a number of interaction effects. High Current is seen to result in a high response for each of the five responses. High Gas Flow Rate results in High Purity and low values for each of the other responses. Spray Distance affects four of the five responses measured, with a high Spray Distance leading to low values for each of the responses. The Current * Gas Flow Rate and Current * Spray Distance interactions are found to influence a high number of responses.

Table 4.32: Summary of the effect of increasing factors on the response

Factor	*Roughness*	*Crystallinity*	*Purity*	*Porosity*	*Thickness*
A-Current	↑	↑	↑	↑	↑
B-Gas Flow Rate	↓	↓	↑	↓	↓
C-Powder Feed Rate			↓	↓	↑
D-Spray Distance		↓	↓	↓	↓
E-Carrier Gas Flow Rate		↓	↓		↑
A*B	↑	↑		↓	
A*D		↓	↓	↑	↓
B*C			↓		↓
B*D			↑	↓	
B*E		↑			↑
D*E			↓		

From this factor response summary, contradictions can be seen to exist between the required factor levels depending on the desired response. For example a compromise must be reached for Gas Flow Rate is aiming to produce a coating with high Crystallinity and high Purity. Design Expert can be used in order to find

the most desirable compromise for a given set of optimisation criteria. This optimisation process is discussed further in *Section 4.7*.

The process models developed in this work provide many benefits, the most important of which being the understanding of the process provided by the models, with a direct relationship between the process parameters and the responses being provided. These process models are extremely powerful tools, both for process control in a manufacturing environment, and also for the development of new coatings (through model optimisation) in the research and development environment.

The models developed in this work provide a significant contribution to the current knowledge relating to the plasma spraying of hydroxyapatite coatings. Although responses such as Crystallinity and Purity relate directly to HA coatings, Roughness, Porosity and Thickness are important parameters when spraying many materials. The process knowledge presented here is thus applicable to other plasma sprayed coatings. Optimisation of the developed process models is presented in the following section.

4.7 Optimisation Process

As outlined in the literature review, there is currently a contradiction in the requirements for HA coatings. On the one hand, for long term coating stability, a dense highly pure, highly crystalline coating is required [52]. On the other hand, the part dissolution of the coating surface has been shown to lead to an improved *in vivo* response, resulting in bone formation [28]. Greater surface roughness and surface porosity have been shown to allow increased bone bonding [122, 180]. The aim for the optimisation of the process models was to produce a bi-layer coating, each layer having different properties. The optimisation process involved in selection of the process parameters for each of these coating layers is discussed in the following sections.

4.7.1 Stable HA Coating

The first process optimisation was that for the stable HA layer. This aims to produce a dense, long lasting coating that will maintain its integrity for long periods in the body. The goal and importance levels for each response are summarised in *table 4.33*.

Table 4.33: Stable HA Layer Optimisation Parameters

	Goal	*Importance*
Roughness (µm)	Maximise	+++
Crystallinity (%)	Maximise	+++++
Purity (%)	Maximise	++++
Porosity (%)	Minimise	++++
Thickness (µm)	Maximise	+

The goal for Roughness was set to be maximised in the optimisation. This was to provide high surface roughness for increased adhesion of the second coating layer. The Crystallinity of the coating was maximised in the optimisation. This is because, as discussed in the literature review, a crystalline coating is more stable in vivo than one containing a high percentage of amorphous material [39, 52]. Dissolution of the amorphous phase would lead to weakening of the coating. The coating purity was also maximised as the other calcium phosphate impurity phases that may be present in the coating dissolve more quickly in vivo [39, 52]. The coating porosity was minimised in order to produce a coating with the highest possible density. Coating thickness was maximised in order to attain the highest possible deposition efficiency.

The Crystallinity was set to an importance level of 5, as this is seen as being the most critical parameter relating to *in vivo* performance. Purity and Porosity were deemed to be of equal importance and set at an importance level of 4. Both also have large influences over coating stability. The Roughness of the coatings is less important so this was set to an importance level of 3. Coating Thickness is also a less critical parameter and given an importance level of 1.

Design Expert can generate hundreds of possible solutions based on the optimisation criteria selected. The desirability of each solution is indicated (1 being the most desirable and 0 the least). The preferred settings can then be selected manually. Five of these results are displayed in *table 4.34*. Solution 1 was selected as the most appropriate as it results in the highest desirability (0.92).

Table 4.34: Dense Optimisation Results

	Solution Number				
	1	**2**	**3**	**4**	**5**
Factor					
Current *(A)*	750	749.95	750	750	750
Gas Flow Rate *(SCFH)*	104.84	102.3	97.04	114.8	107.7
Powder Feed Rate *(g/min)*	19.99	20	20	19.99	18.36
Spray Distance *(mm)*	70.01	70.67	70.43	70	70
Carrier Gas Flow Rate *(SCFH)*	10	10	10	10	10
Response					
Roughness *(µm)*	8.6	8.65	8.75	8.42	8.55
Crystallinity *(%)*	84.69	84.68	85.06	84.07	84.51
Purity *(%)*	98.53	98.44	98.32	98.79	98.61
Porosity *(%)*	6.31	6.64	5.94	7.31	8.63
Thickness *(µm)*	413.96	418.6	433.21	387.71	392.37
Desirability	**0.920**	0.917	0.915	0.914	0.913

The parameter settings selected for spraying the stable HA coating layer were thus, a Current of 750 A, Gas Flow Rate of 104.84 SCFH, Powder Feed Rate of 19.99 g/min, Spray Distance of 70.01 mm and Carrier Gas Flow Rate of 10 SCFH.

4.7.2 Active Surface Layer

The second optimisation process aimed to produce the top, active surface layer of the bi-layer coating. The aim for this optimisation is to produce a porous coating,

high in amorphous content and secondary calcium phosphate phases. This coating will dissolve more quickly in the body providing the calcium and phosphate ions which have been reported to increase bone growth on the coating surface [27]. The optimisation goals and importance level for each response are given in *table 4.35*.

Table 4.35: Porous Coating Optimisation Parameters

	Goal	*Importance*
Roughness (µm)	Maximise	+++
Crystallinity (%)	Minimise	+++++
Purity (%)	Minimise	+++++
Porosity (%)	Maximise	+++++
Thickness (µm)	Maximise	+

In order to produce this coating, Roughness was maximised to give the greatest surface area for cell attachment and coating dissolution. Crystallinity was minimised to give a coating with a high amorphous content which will dissolve more quickly in the body. The purity was minimised to give a coating with the largest amount of secondary calcium phosphate phases which will dissolve more quickly in vivo than HA and increase the biological response. The porosity was maximised to allow the greatest surface area for cell attachment and coating dissolution. The thickness was again maximised to give the coating with the greatest deposition efficiency. The importance levels were set as before. Five of the top optimisation solutions are given in *table 4.36*. Solution 1 was selected as the most desirable (0.793).

Based on the results in *table 4.36*, the spraying parameters used to spray the surface active layer of the bi-layer coating were a Current of 750 A, a Gas Flow Rate of 90.01 SCFH, Powder Feed Rate of 10.2 g/min, Spray Distance of 100 mm and Carrier Gas Flow Rate of 20 SCFH.

Table 4.36: Porous Optimisation Results

	Solution Number				
	1	**2**	**3**	**4**	**5**
Factor					
Current *(A)*	750	750	750	750	750
Gas Flow Rate *(SCFH)*	90.01	90.46	90	90	90.08
Powder Feed Rate *(g/min)*	10.2	10	10.68	12.95	13.63
Spray Distance *(mm)*	100	100	100	99.81	100
Carrier Gas Flow Rate *(SCFH)*	20	19.64	19.62	20	19.99
Response					
Roughness *(µm)*	8.88	8.87	8.88	8.88	8.88
Crystallinity *(%)*	72.7	72.91	72.91	72.75	72.71
Purity *(%)*	95.67	95.73	95.72	95.68	95.68
Porosity *(%)*	53.01	53	52.41	49.35	48.68
Thickness *(µm)*	266.4	263.49	270.64	291.0	296.05
Desirability	**0.793**	0.785	0.785	0.781	0.780

4.8 Bi-layered Coating

The aim of this work was to produce a functionally graded coating consisting of a stable base layer (Coating A) and active surface layer (Coating B). The parameter settings required were determined by optimising the RSM models using Design Expert software, as detailed in *Section 4.7.1* and *4.7.2*. Optimisation of the models allowed identification of the optimal spray parameters for each layer of the bi-layer coating. These spray conditions are summarised in *table 4.37*. Three coatings were sprayed for each of the optimised parameter settings. For the analysis of the coating layers, both Coating A and Coating B were sprayed directly on grit blasted titanium discs, prepared as per the standard procedure outlined in *Section 3.5*. Bi-layered coatings, coating Coating A as the base layer and Coating B as the top layer were also produced.

It can be seen from *table 4.37* that different parameter levels are required for each layer. The Current required for both layers is the same but each of the other parameters settings is different for the two layers. The response values predicted by the model for these two sets of parameters are given in *table 4.38*. These are

compared with the actual experimental response values, with the % error being given for each.

Table 4.37: Plasma Spray Parameters

	Current (A)	*Gas Flow Rate (B)*	*Powder Feed Rate (C)*	*Spray Distance (D)*	*Carrier Gas flow rate (E)*
	A	*SCFH*	*g/min*	*mm*	*SCFH*
Stable Base Layer (Coating A)	750	104.84	19.99	70.01	10
Active Surface Layer (Coating B)	750	90.01	10.2	100	20

Table 4.38: Response Values for Bi-Layered Coating

	Stable Base Layer			*Active Surface Layer*		
	Predicted	Actual	% Error	Predicted	Actual	% Error
Roughness (µm)	8.6	8.3	3.5	8.88	9.1	2.4
Crystallinity (%)	84.69	84.4	0.3	72.7	74.6	2.5
Purity (%)	98.53	98.1	0.4	95.67	96.1	0.4
Porosity (%)	6.31	8.9	29.1	53.01	47.3	10.8
Thickness (µm)	413.96	391.4	5.4	266.4	232.5	12.7

The % error is similar to that found for in the point prediction (*table 4.31*), with error being found to be lower for Roughness, Crystallinity and Purity, than for Porosity and Thickness.

The aim of the optimisation step was to produce two distinct layers with different properties depending on the optimisation criteria used. The stable base layer produced has high Roughness (8.3 µm) to allow good attachment of the surface layer. The Crystallinity and Purity are both high (84.4 % and 98.1 % respectively) to ensure in vivo stability high. The Porosity is low (8.9 %) to provide mechanical stability and the Thickness is high (391.4 µm). These measured response values meet the values required from the optimisation criteria.

The active surface layer has a high Roughness (9.1 μm) to allow good attachment of the surface layer. The Crystallinity and Purity are both low (72.7 % and 95.67 % respectively) to allow release of calcium and phosphate ions into the surrounding body fluid to increase biological response. The Porosity is high (47.3 %) to allow cell attachment and the Thickness is also high (232.5 μm). The measured responses for the active surface layer also meet the requirements set out in the optimisation criteria.

It can be concluded that the aims for the optimisation have been achieved and two differing HA layers with the required properties have been developed. It is hypothesis that the active surface coating layer produced in this work will allow an improved biological response *in vivo*, leading to more rapid formation of bone. In order to test this hypothesis a cell culture study was under taken. The results from this study are presented in the following section.

4.9 Cell Culture Experimental Work

4.9.1 Introduction

Rapid osseointegration is crucial in order for an implant to be successful *in vivo*. It is thus necessary to understand the biological response to an implant material. This is known to be dependent on a number of factors, such as the chemistry, surface energy and surface topography of the material. In this study, MG-63 osteoblast cells were cultured on the two HA coatings (A= Stable Base Layer; B= Active Surface Layer) developed from optimisation of the response models, as well as an uncoated titanium disk and on cell culture plastic as a control. The aspects of cell behaviour examined were cell proliferation, cell viability and gene expression levels. It is expected that two HA coatings should show earlier bone formation than the titanium and control surfaces. The results from this study are presented and discussed in this section.

4.9.2 Cell Proliferation and Viability

The proliferation of the MG-63 cells on each of the four surfaces at each time point is displayed in *figure 4.64*. Data for the control at day 7 is missing as this data was not recorded at the time. Initially, cells were seeded at a density of 10,000 cell per well, as described in *Section 3.11*. It can be seen from *figure 4.64* that cells numbers on all surfaces have at least doubled on each surface at day 7. This indicates that the MG-63 cells were able to attach and grow on all four surfaces. Cell numbers were found to continue to increase at each of the following time points. The cell number increases observed were typical of the kinetics expected for MG-63 proliferation. Similar proliferation rates for MG-63 cells have been observed by Richard et al. [155].

The difference in proliferation rates was found to be significant for each surface at each time point ($p < 0.05$). Comparing cell proliferation on each of the surface it can be seen that proliferation rates were lowest on the HA coatings, Coating A and Coating B. Proliferation was greater on Coating A (Stable Base Layer) than Coating B (Active Surface Layer) up to 14 days and proliferation was greater on Coating B than Coating A at day 21. At day 28 proliferation was again seen to be greater on Coating A than Coating B. Proliferation was seen to be greater on the titanium surface than on both HA coatings and the rate of proliferation was greatest on the cell culture plastic. This high rate of proliferation on cell culture plastic is expected as culture plates are specially designed to enhance cell growth [181]. Similar rapid osteoblast proliferation rates on cell culture plastic have been observed by Deligianni et al. [180], Chou et al. [153] and Wang et al. [154].

The large differences between cell numbers on the cell culture plastic and the other three coatings may also be partly due to difficulties detaching cells from the rougher surfaces before cell proliferation and viability was measured. Higher cell attachment on porous HA surfaces than on titanium has been reported previously in a study by Rouahi et al. [122] which reported a higher initial attachment of SaOS-2 cells on microporous HA than on dense HA and titanium.

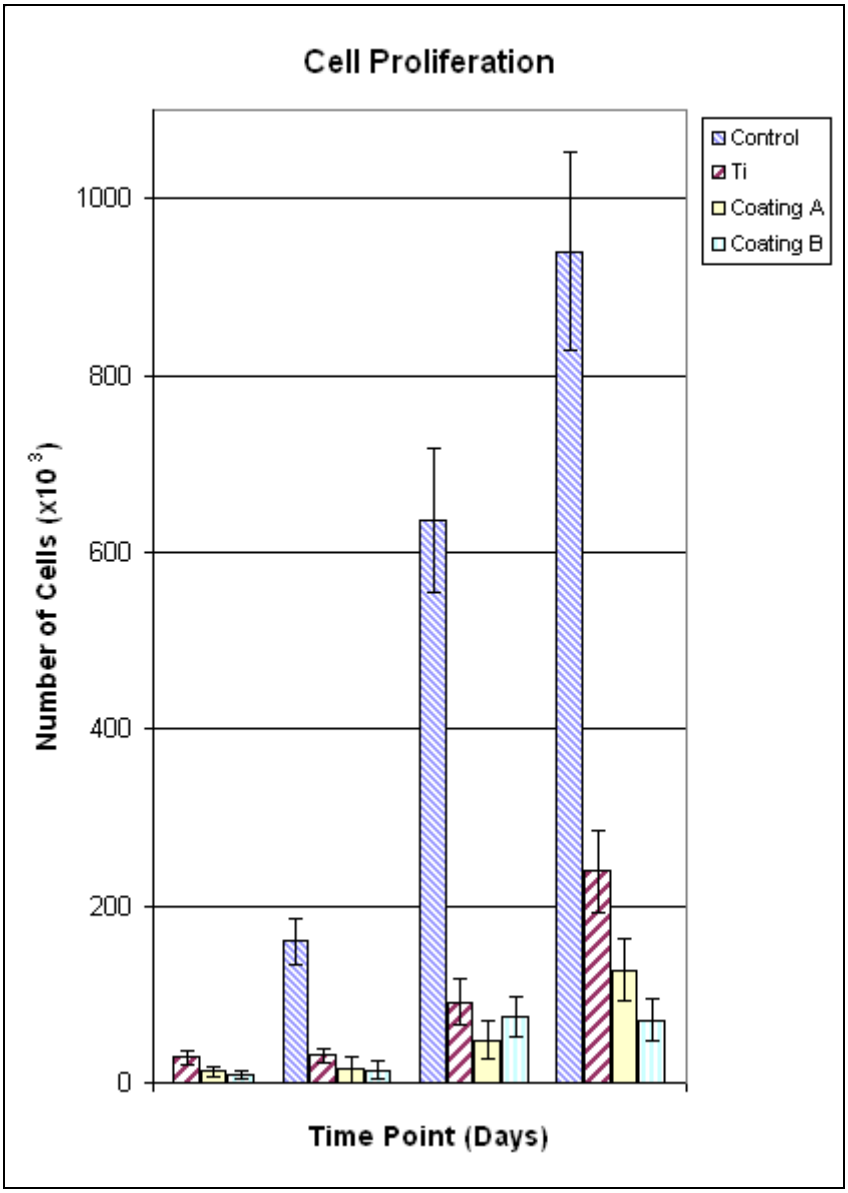

Figure 4.63: Proliferation of MG-63 cells from 7 to 28 days

Dead cells were counted following staining with Trypan Blue as described in *Section 3.11.3*. The percentage of viable cells present on each coating is displayed in *figure 4.65*.

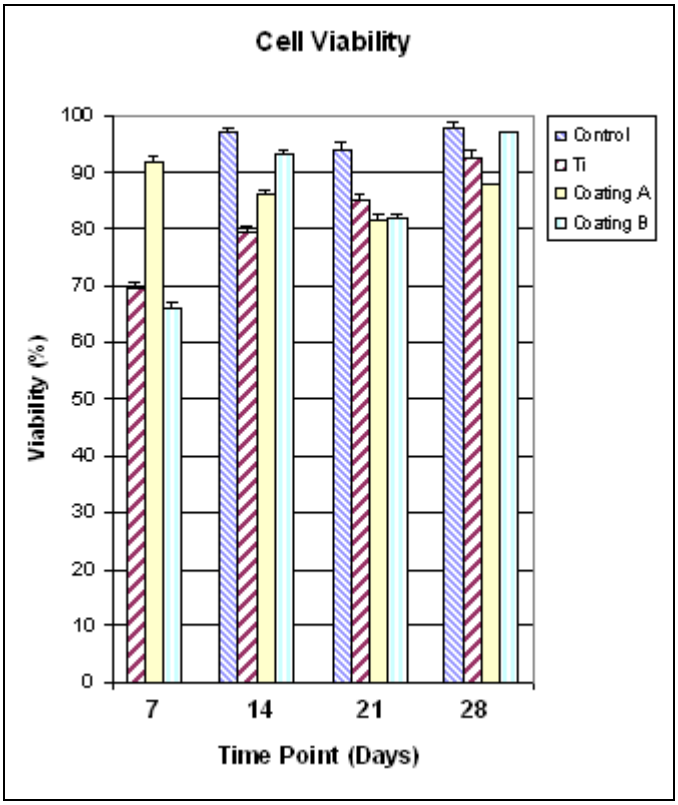

Figure 4.64: Viability of MG-63 cells from 7 to 28 days

The cell viability was found to be greater than 95% on cell culture plastic. Viability is less on titanium, Coating A and Coating B, with a large number of dead cells being observed. The viability of the MG-63 cells was less than 80% for Coating A and Coating B at day 7. After this, fewer dead cells were observed and the remaining viable cells were able to proliferate. A study by Chou et al. [153] also found that when culturing MC3T3-E1 preosteoblast cells on different calcium phosphate powders, cell death was high until day 14.

The cell proliferation and viability results indicate that MG-63 osteoblast cells were able to attach and grow on the titanium surface, on Coating A and on coating B. The slower proliferation rate on Coating A and Coating B may indicate the onset on cell differentiation on these surfaces. A similar slow down or cessation of osteoblast proliferation rates on calcium phosphate materials compared to culture plastic due to the onset of differentiation have been reported by Richard et al. [155] and Chou et al. [153].

4.9.3 Gene Expression Analysis

The expression of extracellular matrix mineralization markers Type 1 collagen (COL1A1), alkaline phosphatase (ALPL) and Osteocalcin (BGLAP) were determined using quantitative RT-PCR analysis as described in *Section 3.11.5*. In order to reduce sources of error and variability, day 7, 21 and 28 were placed in the same 96 well plate for quantitative RT-PCR. Each gene was analysed separately using GAPDH as the endogenous control. PCR for all genes at Day 14 was analysed in a separate plate. However, the results for did not fit with the other data, with all gene expression levels being seen to be unexpectedly high, and it was thus necessary to exclude them from the analysis. It is believed that errors were introduced in the incorrect measurement of the day 0 sample for this plate.

Type 1 collagen is the earliest marker of mineralization, being expressed in the cellular proliferation stage. The expression of Type 1 collagen (ColA1) is shown in *figure 4.66*. It can be seen that at day 7, the highest level of ColA1 expression is on the titanium surface. Expression of Type 1 collagen (ColA1) peaked at 21 days for all surfaces. At day 21, expression of ColA1 is highest on Coating A. Expression levels are higher on Ti, Coating A and Coating B than on the control plastic at day 21 and day 28.

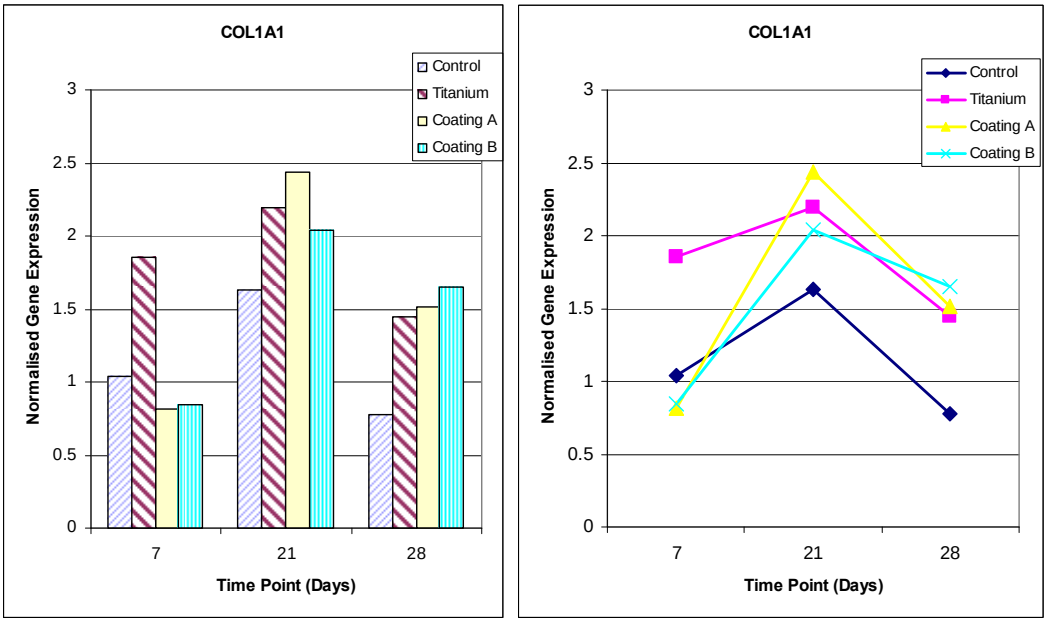

Figure 4.65: Type 1 Collagen (COL1A1) Expression Levels

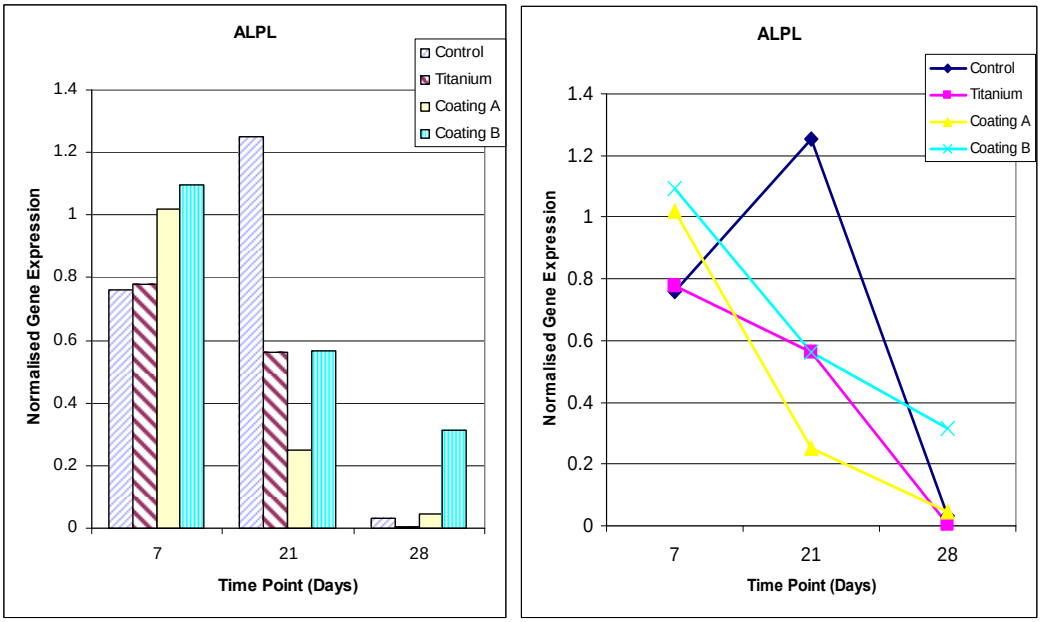

Figure 4.66: Alkaline Phosphatase (ALPL) Expression Levels

Alkaline phosphatase is expressed during in the osteoblast maturation stage. The expression of Alkaline phosphatase for each surface at each time point is shown in *figure 4.67*. Expression levels of Alkaline phosphatase were found to be low on all coatings. Upregulation of this gene was found for Coating A and Coating B at day 7. Upregulation of ALPL was also found for the control at day 21. At day 28 no expression of ALPL is recorded on the Control, titanium or Coating A, expression of ALPL can be detected for Coating B.

Osteocalcin is expressed latest, during the mineralisation stage. The level of expression of osteocalcin on each surface is shown in *figure 4.68*. Osteocalcin expression was found to be greatest on Coating B at all time points. Osteocalcin expression is seen on Coating B at 7 days and not on Coating A until day 21. This is an indication of early mineralization on Coating B.

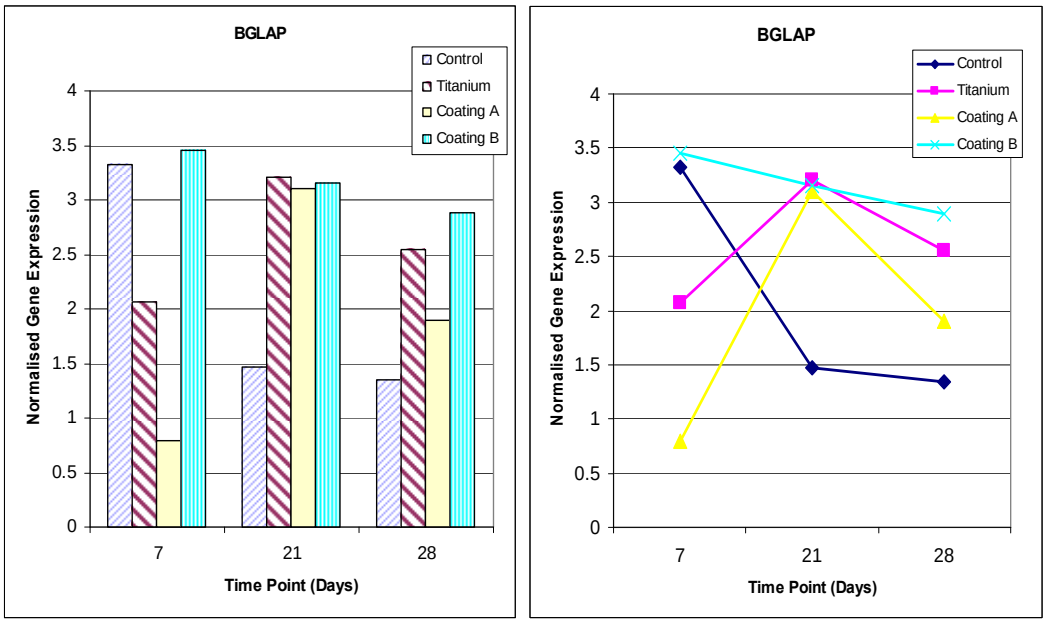

Figure 4.67: Osteocalcin (BGLAP) Expression Levels

4.9.4 Conclusions from Cell Culture Study

It was found in this study that proliferation of MG-63 cells was low initially on Ti, Coating A and Coating B. Initial cell viability was also found to be low on these surfaces. From gene expression analysis it can be seen that the surfaces influence gene synthesis at early time points. The results indicate that HA coating A and HA coating B promote human osteoblast differentiation, favouring extracellular matrix production. At day 28, the highest differential cell response for all gene expression studies was found on coating B. This is a tentative indication that Coating B provides the most favourable conditions for bone formation.

4.10 Summary

In this study, various aspects relating to hydroxyapatite coatings have been investigated. The use of a heat treatment process to investigate the recrystallisation potential of the amorphous component of HA coatings has been examined. The process-property-structure relationship for plasma spraying of hydroxyapatite coatings has been investigated using the Design of Experiment (DOE) technique. Process models have been developed that identify the process parameters that have the greatest effect on each response and relate these process

parameters to various responses. The developed models were then optimised based on two different optimisation criteria to produce two different coating layers that can be combined to produce a novel functionally improved bi-layer HA coating. An indication of the benefit of this coating design was shown through a cell culture study.

In the following section the main conclusions from this research work are outlined and the major contributions of the research work are summarised.

5 Conclusions and Major Contributions

5.1 Conclusions

The main conclusions from this work are outlined in this section.

5.1.1 Post Spray Heat Treatment Study

- The optimal conditions for post spray heat treatment of plasma sprayed HA coatings were found be 700 ºC for 1 hour. This allowed a ~ 7 % increase in crystallinity from the as-sprayed coating.

- The use of a post spray heat treatment induces cracks within the coating which are detrimental to coating stability and also causes an undesirable colour change. Production of a high crystallinity, high purity coating without the requirement for post spray heat treatment would be preferable.

5.1.2 Design of Experiment

- The Design of Experiment (DOE) technique enabled the HA coating responses to be modelled for both the Screening Design and Response Surface Methodology Design. Significant models were produced for each of the studied responses.

- Current and Gas Flow Rate both influence the coating roughness. Gas Flow Rate has a linear effect with highest roughness resulting at low Gas Flow Rates. Current has a quadratic effect, with highest roughness resulting at the central Current value.

- The Current * Spray Distance interaction has the greatest affect on Crystallinity, with the coating with the greatest % Crystallinity resulting at high Current and low Spray Distance.

- Coating Crystallinity increased with increasing coating Thickness due to recrystallisation of the coating at the lower cooling rate resulting from the lower thermal conductivity of HA compared to titanium.

- Purity was most affected by the Carrier Gas Flow Rate and Gas Flow Rate, being higher at low Carrier Gas Flow Rates and high Gas Flow Rate, due to reduced particle heating at these conditions.

- Porosity was affected most by the Gas Flow Rate, Powder Feed Rate and Gas Flow Rate * Spray Distance interaction, being highest at low Gas Flow Rate and Powder Feed Rate and at high Current and Spray Distance.

- Thickness was affected to the greatest extent by the Current, Gas Flow Rate, Powder Feed Rate and Spray Distance, being highest at high Current, low Gas Flow Rate, high Powder Feed Rate and low Spray Distance.

5.1.3 Bi-Layer Coating Development

- The spray parameters required in order to produce a bi-layer coating, consisting of a dense, highly crystalline stable base layer and a less crystalline, porous active surface layer, have been identified through optimisation of the developed response surface models.

- The optimal spray parameters for production of the stable base layer of the bi-layer coating are a Current of 750 A, Gas Flow Rate of 104.84 SCFH, Powder Feed Rate of 19.99 g/min, Spray Distance of 70.01 mm and Carrier Gas Flow Rate of 10 SCFH.

- The optimal spray parameters for production of the surface active layer of the bi-layer coating are a Current of 750 A, a Gas Flow Rate of 90.01 SCFH, Powder Feed Rate of 10.2 g/min, Spray Distance of 100 mm and Carrier Gas Flow Rate of 20 SCFH.

- The measured responses for the two coating layers were found to meet the values predicted by the models.

- The cell culture study showed that particles were able to adhere to and proliferate on all surfaces. There is a tentative indication that the active surface layer (Coating B) provides more favourable conditions for bone formation than the dense base layer (Coating A).

5.2 Major Contributions from this Work

Up to this point, the understanding, within the research community, of the relationships between properties of plasma sprayed hydroxyapatite coatings and the process parameters used during spraying, was limited. The literature contains many contradictions in relation to parameter effects, making selecting the parameter settings required to produce a coating with optimal properties difficult. The process models developed during the course of this research provide new clarity in relation to this. In-depth analysis of the models produced has led to the emergence of a clearer understanding of this complicated process.

The novel bi-layer coating produced though optimisation of the process models provides the second major contribution of this work to the research community. This novel coating combines the advantages of a dense, highly crystalline stable base layer with an active surface layer that meets the requirements for enhanced early osteoblast activity and thus early integration of the surrounding bone into the implant.

6 Recommendations for Future Work

The findings in this work have contributed greatly to the knowledge regarding plasma sprayed hydroxyapatite coatings. The models developed and understanding gained will prove valuable for future research carried out in this area. During the course of this work, further research and development steps that would contribute to this field have been identified. These recommendations are as follows:

1. Rig development

Changes to and development of the plasma spray rig would allow expansion of the functionally of the equipment.

a) Sample movement: Addition of a third axis to the sample mover would allow larger substrates to be sprayed. This third axis would also overcome problems relating to the uneven coating profile produced with the current set-up.

b) Spraying atmosphere: The spray booth could be developed to enclose the spray gun and substrate and allow the spraying atmosphere to be controlled. Sprayed could then to carried out in an environment containing water vapour. The presence of water vapour during post spray heat treatment has been shown by Chen et al. [131] to promote crystal growth and transformation of TCP and TTCP to HA.

2. The Spraying Process

Various aspects of the plasma spraying process present opportunities for further study and investigation.

a) Further process modelling: A similar DOE study to the one carried out in this work could be conducted in order to model the effects of other aspects of the spray process, such as the HA powders properties, on the resultant coating. This could include investigation of the spraying of nano HA particles to allow production of denser HA coatings [69].

b) Substrate preheating: The inclusion of a substrate pre-heating step into the process could be investigated. This would allow greater control over cooling rate and thus over coating recrystallisation and residual stress development.

3. Further analysis of developed bi-layer coating

The results and findings of the research work carried out as part of this thesis indicate the benefits of the bi-layer coating developed herein. Further analysis of this bi-layer coating would allow a greater understanding of how it would perform in the body, to be gained.

a) Further structure analysis: Investigation of the residual stress levels present within the bi-layer coatings and the mechanical properties of the bi-layer coatings would be useful in order to further characterise and optimise the bi-layered coating developed herein.

b) Further *in vitro* analysis: The *in vitro* cell culture study carried out here has shown promising results. To further optimise the two-layered coating developed in this work a more detailed *in vitro* study could be carried out in order to optimise the coating dissolution rates. The models developed in this thesis could be use to determine the spray parameters for production of the coatings of varying compositions.

c) In vivo analysis: Analysis of the bi-layered coating in an *in vivo* model would allow the benefits over traditional HA coatings to be determined.

4. Coating Design

There is potential for further research into the materials used in the design of HA coatings. These modifications could include the addition of bond layers, surface polymer layers and additions to the HA coating themselves.

a) Bond layer addition: The incorporation of a bond layer between the substrate and HA coating could be investigated. Some improvements

in coating adhesion strength have been found by Chou and Chang [182] and Kurzweg et al. [137] though the use of titania and zirconia bond layers respectively. Bond coating layers could be applied using the plasma spray equipment or using some of the other coating techniques available in the department, for example HVOF or Magnetron Sputtering.

b) Polymer layers: The addition of a polymer layer to the surface of HA coatings is suggested to be beneficial for initial cellular adhesion to the coating [183]. They also show potential for use as a drug eluting layer [183]. Layers added could be either natural polymers, such as collagen, or of a synthetic nature.

c) Addition of polymeric materials such as PCL Poly(e-caprolactone) to HA coatings, to produce thicker coatings/scaffolds for either the support and growth of biological cells or for grafting techniques.

Publications Arising From This Work

Books

T. J. Levingstone, Issue 1: Ceramics for Medical Applications, in L. Looney (ed.), Head Start: Graduate Level Resources in Materials Engineering, Dublin City University, 2008

T. J. Levingstone, J. Hingston, Issue 2: Guide to Hip Replacements for Engineers: Design, Material and Stress Issues, in L. Looney (ed.), Head Start: Graduate Level Resources in Materials Engineering, Dublin City University, 2008

Journal Papers

T. J. Levingstone, J. Stokes, L. Looney, Design of Experiment Analysis of the Factors Influencing the Plasma Spraying of Hydroxyapatite Coatings: Screening Results, Journal of Surface Coatings and Technology, In review, 2008

T. J. Levingstone, J. Stokes, L. Looney, Design of Experiment Analysis of the Factors Influencing the Plasma Spraying of Hydroxyapatite Coatings: Optimisation Results, Journal of Surface Coatings and Technology, In review, 2008

T. J. Levingstone, J. Stokes, L. Looney, Development of a Bi-layer Coating for Improved Cellular Response, 2008

Conference Papers

T. J. Levingstone, L. Looney, J. Stokes, “Plasma Thermal Spraying Influencing Parameters”, Proceedings of the International Conference on the Advanced Materials Processing Technology, Nov 2-5, 2008, Bahrain.

T. J. Levingstone, J. Stokes, L. Looney, “Investigation of Plasma Sprayed Hydroxyapatite Coatings”, Proceedings of the 2006 International Thermal Spray Conference, May 15 – 18, 2006, Seattle, Washington, USA.

T. J. Levingstone, J. Stokes, L. Looney, "Investigation of the Influence of Plasma Spray Process Parameters on Hydroxyapatite Coatings”; Proc. of Bioengineering in Ireland Conference, Clybaun Hotel, Galway, January 27-28, 2006.

T. J. Levingstone, J. Heaslip and L. Looney, “Effect of post spray heat treatment on plasma sprayed hydroxyapatite coatings”, in John Vickery, ed., Challenges facing manufacturing, Proceeding of the 22nd International Manufacturing Conference, 31st August to 2nd September 2005, Institute of Technology Tallaght, Dublin, pp. 583-589.

Conference Posters

T. J. Levingstone, J. Stokes, L. Looney, Optimisation of Plasma Sprayed Hydroxyapatite Coatings, ESB 2006, 20th European Conference on Biomaterials, 27 September - 1 October 2006 Cité des Congrès, Nantes, France.

T. J. Levingstone, J. Stokes, L. Looney, “The Influence of Plasma Spray Process Parameters on Hydroxyapatite Coatings”, International Conference on Biomaterials in Regenerative Medicine, October 22-25, 2006 Vienna, Austria.

Conference Presentations

T. J. Levingstone, J. Stokes, L. Looney, “Plasma spraying of Hydroxyapatite Biocoatings for Medical Applications”, 17th Annual Conference of the Irish Plasma and Beam Processing Group, National Centre for Plasma Science and Technology, Dublin City University, 13 – 14th June 2006.

T.J. Levingstone, J. Stokes, L. Looney, Plasma spraying of Hydroxyapatite Biocoatings for Medical Applications, Dublin City University, 22nd September 2006.

References

[1] T. J. Levingstone, *Issue 1: Ceramics for Medical Applications,* in Head Start: Graduate Level Resources Materials Engineering, Lisa Looney, ed., Dublin: Materials Processing Research Centre, Dublin City University, 2008

[2] T. J. Levingstone and J. Hingston, *Issue 2: Guide to Hip Replacements for Engineers: Design, Material and Stress Issues,* in Head Start: Graduate Level Resources Materials Engineering, Lisa Looney, ed., Dublin: Materials Processing Research Centre, Dublin City University, 2008

[3] Arthritis Foundation of Ireland, [online], http://www.arthritisireland.ie, (Accessed 25th May 2008)

[4] P. Grigoris, H. C. Amstutz and V. A. Fowble, "Precision-fit surface hemiarthroplasty for femoral head osteonecrosis", in *Hip Surgery: Materials and Developments,* L. Sedel and M. E. Cabanela, Eds. London: Mosby, 1998.

[5] Smith & Nephew Inc., [online], http://www.strongasanox.com/1300_oxhips.html, (Accessed May 25th 2008)

[6] D. N. Ghista, *Biomechanics of Medical Devices,* New York: Marcel Dekker Inc, 1981

[7] J. T. Scales, "Arthroplasty of the hip using foreign materials: A History", *Proceedings of the Institution of Mechanical Engineering,* vol. 181, pp. 63-84

[8] National Joint Registry (England and Wales) [online], www.njrcentre.org.uk, (Accessed 24th May 2008)

[9] J. R. Davis, *Handbook of Materials for Medical Devices,* Ohio: ASM International, 2003

[10] E. M. Ooms, J. G. C. Wolke, M. T. van de Heuvel, B. Jeschke and J. A. Jansen, "Histological evaluation of the bone response to calcium phosphate cement implanted in cortical bone", *Biomaterials,* vol. 24, pp. 989-1000, 3. 2003

[11] W. J. Maloney, "Polymethylmethacrylate", in *Hip Surgery: Materials and Developments* L. Sedel and M. E. Cabanela, Eds., London: Martin Dunitz Ltd, 1998, pp. 57-65

[12] K. Soballe and R. J. Friedman, "Calcium hydroxyapatite in total joint arthroplasty", in *Human Biomaterials Applications* D. L. Wise, D. J. Trantolo, D. E. Altobelli, M. Yaszemski and J. D. Gresser, Eds., Totowa, NJ: Humana Press, 1996, pp. 137-167

[13] J. B. Park, "Hip joint prosthesis fixation - problems and possible solutions", in *The Biomedical Engineering Handbook*, 2nd ed., vol. 1, J. D. Bronzino, Ed., Heidelberg; Boca Raton, FL: Springer, CRC Press, 2000, pp. 1-18

[14] L. L. Hench and J. Wilson, "Introduction", in *An Introduction to Bioceramics,* L. L. Hench and J. Wilson, Eds., Singapore: World Scientific, 1993, pp. 1-24

[15] L. L. Hench and O. Andersson, "Bioactive glasses", in *An Introduction to Bioceramics* L. L. Hench and J. Wilson, Eds., Singapore: World Scientific Publishing Co., 1993, pp. 41-62

[16] P. T. Scannell and P. J. Prendergast, "Simulation of changes in bone around hip replacement implants", *The Engineering Journal*, vol. 59, 6th July 2005

[17] B. D. Boyan, T. W. Hummert, D. D. Dean and Z. Schwartz, "Role of material surfaces in regulating bone and cartilage cell response", *Biomaterials,* vol. 17, pp. 137-146, 1. 1996

[18] P. Ducheyne, J. Beight, J. Cuckler, B. Evans and S. Radin, "Effect of calcium phosphate coating characteristics on early post-operative bone tissue ingrowth", *Biomaterials,* vol. 11, pp. 531-540, 10. 1990

[19] K. Soballe, "The role of H-A-C in ingrowth prostheses", in *Hydroxyapatite Ceramic, a Decade of Experience in Hip Arthroplasty, the Proceedings of a Two Day Symposium : Held at the Royal College of Surgeons of England on Thursday 2nd & Friday 3rd November 1995,* R. Furlong, Ed., London: Furlong Research Foundation, 1996, pp. 57-67

[20] R. Kettner, "The unique interface reaction of H-A-C", in *Hydroxyapatite Ceramic, a Decade of Experience in Hip Arthroplasty, the Proceedings of a Two Day Symposium : Held at the Royal College of Surgeons of England on Thursday 2nd & Friday 3rd November 1995,* R. Furlong, Ed., London: Furlong Research Foundation, 1996, pp. 41-55

[21] A. E. Porter, L. W. Hobbs, V. B. Rosen and M. Spector, "The ultrastructure of the plasma-sprayed hydroxyapatite-bone interface predisposing to bone bonding", *Biomaterials,* vol. 23, pp. 725-733, 2. 2002

[22] L. Sun, C. C. Berndt, K. A. Khor, K. A. Gross and H. N. Cheang, "Surface characteristics and dissolution behavior of plasma-sprayed hydroxyapatite coating", *J. Biomed. Mater. Res.,* vol. 62, pp. 228-236, 2002

[23] S. R. Sousa and M. A. Barbosa, "Effect of hydroxyapatite thickness on metal ion release from Ti6Al4V substrates", *Biomaterials,* vol. 17, pp. 397-404, 1996

[24] M. Nagano, T. Nakamura, T. Kokubo, M. Tanahashi and M. Ogawa, "Differences of bone bonding ability and degradation behaviour in vivo

between amorphous calcium phosphate and highly crystalline hydroxyapatite coating", *Biomaterials,* vol. 17, pp. 1771-1777, 9. 1996

[25] L. V. Carlsson, W. MacDonald, C. M. Jacobsson and T. Albrektsson, "Osseointegration principles in orthopedics: Basic research and clinical applications", in *Biomaterials in Orthopedics,* M. J. Yaszemski, D. J. Trantolo, K. Lewandrowski, V. Hasirci, D. E. Altobelli and D. L. Wise, Eds., New York: Marcel Dekker, 2004, pp. 223-239

[26] J. Currey, A. Unsworth and D. A. Hall, "Properties of bone, cartilage, and synovial fluid", in *An Introduction to the Bio-Mechanics of Joints and Joint Replacement,* D. Dowson and V. Wright, Eds., London: Mechanical Engineering Publications Ltd, 1981, pp. 103-119

[27] F. Fazan and P. M. Marguis, "Dissolution behaviour of plasma-sprayed hydroxyapatite coatings", *Journal of Materials Science: Materials in Medicine,* vol. 11, pp. 787-792, 2000

[28] J. Weng, Q. Liu, J. G. C. Wolke, X. Zhang and K. de Groot, "Formation and characteristics of the apatite layer on plasma-sprayed hydroxyapatite coatings in simulated body fluid", *Biomaterials,* vol. 18, pp. 1027-1035, 1997

[29] G. Scheller and L. Jani, "The cementless total hip arthroplasty," in *Pelvic Ring and Hip*, vol. 6, J. DuParc, Ed., Paris: Elsevier, 2003

[30] The Swedish National Hip Arthroplasty Register [online], http://www.jru.orthop.gu.se/, (Accessed 24th May 2008)

[31] H. Malchau, P. Herberts, G. Garellick, P. Soderman and T. Eisler, "Prognosis of total hip replacment: Update of results and risk ratio analysis for revision and re-revision from the Swedish National Hip Arthroplasty register 1979-2000", 2002

[32] Department of Orthopaedic Surgery Haukeland University Hospital, "The Norwegian Arthroplasty Register Report 2004", [online], http://www.haukeland.no/nrl/, (Accessed 25th May 2008)

[33] C. J. M. Oosterbos, A. I. A. Rahmy, A. J. Tonino and W. Witpeerd, "High survival rate of hydroxyapatite-coated hip prostheses 100 consecutive hips followed for 10 years", *Acta Orthopaedica Scandinavica,* vol. 75, pp. 127-133, 2004

[34] O. Reikeras and R.B Gunderson., "Excellent results of HA coating on a grit-blasted stem: 245 patients followed for 8-12 years", *Acta Orthop. Scand.,* vol. 74, pp. 140-145, 2003

[35] L. Sun, C. C. Berndt, K. A. Gross and A. Kucuk, "Material fundamentals and clinical performance of plasma-sprayed hydroxyapatite coatings: A review", *J. Biomed. Mater. Res.,* vol. 58, pp. 570-592, 2001

[36] S. J. Jr,Schneider, *Ceramics and Glasses,* vol. 4, Ohio: ASM International, 1991

[37] J. L. Lacout, "Calcium phosphates as bioceramics", in *Biomaterials- Hard Tissue Repair and Replacement,* D. Muster, Ed., North- Holland: Elsevier Science Publishers, 1992, pp. 81-95

[38] A. Ravaglioli and A. Krajewik, *Bioceramics- Materials, Properties, Applications,* London: Chapman and Hall, 1992

[39] Le Geros, Racquel Z. and Le Geros, John P., "Dense hydroxyapatite", in *An Introduction to Bioceramics,* L. L. Hench and J. Wilson, Eds., 1993, pp. 139-180

[40] C. A. Beevers and D. B. McIntyre, "The atomic structure of fluorapatite and its relation to that of tooth and bone material", *Min. Mag.,* vol. 27, pp. 254-257, 1946

[41] M. I. Kay, R. A. Young and A. S. Posner, "Crystal structure of hydroxyapatit", *Nature,* vol. 204, pp. 1050-1052, 12 December 1964

[42] K. Sudarsanan and R. A. Young, "Significant precision in crystal structural details: Holly Springs hydroxyapatite", *Acta Crystallographica, Section B (Structural Crystallography and Crystal Chemistry),* vol. b25, pp. 1534-43, 1969

[43] L. Calderín, M. J. Stott and A. Rubio, "Electronic and crystallographic structure of apatites", *Phys. Rev. B,* vol. 67, pp. 134106-134113, 2003

[44] A. T. Sanger and W. F. Khus, "Structural Disorder in Hydroxyapatite", *Zeitschrift Fur Kristallographie,* vol. 199, pp. 123-148, 1992

[45] J. C. Elliot, P. E. Mackie and R. A. Young, "Monoclinic Hydroxyapatite", *Science,* vol. 180, pp. 1055-1057, 1973

[46] D. Haverty, S. A. M. Tofail, K. T. Stanton and J. B. McMonagle, "Structure and stability of hydroxyapatite: Density functional calculation and Rietveld analysis", *Phys. Rev. B,* vol. 71, pp. 094103-094112, 2005

[47] J. W. Nicholson, *The Chemistry of Medical and Dental Materials,* Cambridge, UK.: Royal Society of Chemistry, 2002

[48] C. P. A. T. Klein, J. G. C. Wolke and K. de Groot, "Stability of calcium phosphate ceramics and plasma sprayed coating", in *An Introduction to Bioceramics,* L. L. Hench and J. Wilson, Eds., London: World Scientific, 1993, pp. 199-221

[49] P. Ducheyne and Q. Qiu, "Bioactive ceramics: the effect of surface reactivity on bone formation and bone cell function", *Biomaterials,* vol. 20, pp. 2287-2303, 12. 1999

[50] P. Buma, P. J. M. Van Loon, H. Versleyen, H. Weinans, T. J. J. H. Slooff, K. de Groot and R. Huiskes, "Histological and biomechanical analysis of bone and interface reactions around hydroxyapatite-coated intramedullary implants of different stiffness: a pilot study on the goat", *Biomaterials,* vol. 18, pp. 1251-1260, 9. 1997

[51] C. Ray, "Dissolution properties of calcium phosphates", 2nd Annual Biomaterials Workshop, Cranfield University, UK, 2004

[52] R. B. Heimann, "Thermal spraying of biomaterials", *Surface and Coatings Technology,* vol. 201, pp. 2012-2019, 2006

[53] K. Yamada, K. Imamura, H. Itoh, H. Iwata and S. Maruno, "Bone bonding behavior of the hydroxyapatite containing glass-titanium composite prepared by the Cullet method", *Biomaterials,* vol. 22, pp. 2207-2214, 8/15. 2001

[54] K. de Groot, "Calcium phosphate ceramics: Their current status," in *Contemporary Biomaterials- Material and Host Response, Clinical Applications, New Technology and Legal Aspects,* J. W. Boretos and M. Eden, Eds., New Jersey: Noyes Publications, 1984, pp. 477-492

[55] A. E. Porter, N. Patel, J. N. Skepper, S. M. Best and W. Bonfield, "Comparison of in vivo dissolution processes in hydroxyapatite and silicon-substituted hydroxyapatite bioceramics", *Biomaterials,* vol. 24, pp. 4609-4620, 11. 2003

[56] Sulzer Metco, [online], www.sulzermetco.com, (Accessed 25th May 2008)

[57] C. Liao, F. Lin, K. Chen and J. Sun, "Thermal decomposition and reconstitution of hydroxyapatite in air atmosphere", *Biomaterials,* vol. 20, pp. 1807-1813, 10, 1999

[58] T. M. Sridhar, U. Kamachi Mudali and M. Subbaiyan, "Sintering atmosphere and temperature effects on hydroxyapatite coated type 316L stainless steel", *Corros. Sci.,* vol. 45, pp. 2337-2359, 2003

[59] Y. Yang, K. Kim, C. M. Agrawal and J. L. Ong, "Interaction of hydroxyapatite-titanium at elevated temperature in vacuum environment", *Biomaterials,* vol. 25, pp. 2927-2932, 7. 2004

[60] S. Lazic, S. Zec, N. Miljevic and S. Milonjic, "The effect of temperature on the properties of hydroxyapatite precipitated from calcium hydroxide and phosphoric acid", *Thermochimica Acta,* vol. 374, pp. 13-22, 6/18. 2001

[61] R. Huiskes, "Mechanical failure in total hip arthroplasty with cement", *Current Orthopaedics,* vol. 7, pp. 239-247, 1993/10

[62] Y. Fang, D. K. Agrawal and D. M. Roy, "Thermal stability of synthetic hydroxyapatite", in *Hydroxyapatite and Related Materials,* P. W. Brown and B. Constantz, Eds., London: CRC Press, 1994

[63] E. Park, R. A. Condrate Sr., D. Lee, K. Kociba and P. K. Gallagher, "Characterization of hydroxyapatite: Before and after plasma spraying", *J. Mater. Sci. Mater. Med.,* vol. 13, pp. 211-218, 2002

[64] A. Tampieri, G. Celotti, S. Sprio and C. Mingazzini, "Characteristics of synthetic hydroxyapatites and attempts to improve their thermal stability", *Mater. Chem. Phys.,* vol. 64, pp. 54-61, 3/31. 2000

[65] V. Deram, C. Minichiello, R. -. Vannier, A. Le Maguer, L. Pawlowski and D. Murano, "Microstructural characterizations of plasma sprayed hydroxyapatite coatings", *Surface and Coatings Technology,* vol. 166, pp. 153-159, 3/24. 2003

[66] R. B. Heimann, *Plasma-Spray Coating: Principles and Applications,* Cambridge: VCH Publishers, 1996

[67] M. U. Schoop, "Improvements in or connected with the Coating of Surfaces with Metal, applicable also for Soldering or Uniting Metals and other Materials", GB 191,005,712, 1911-01-26

[68] M. U. Schoop, "An Improved Process of Applying Deposits of Metal or Metallic Compounds to Surfaces," GB 191121066 , 1912-09-23

[69] P. Fauchais, "Understanding plasma spraying", *Journal of Physics D: Applied Physics,* vol. 37, pp. R86, 2004

[70] H. C. Gledhill, I. G. Turner and C. Doyle, "In vitro fatigue behaviour of vacuum plasma and detonation gun sprayed hydroxyapatite coatings", *Biomaterials,* vol. 22, pp. 1233-1240, 6/1. 2001

[71] H. C. Gledhill, I. G. Turner and C. Doyle, "Direct morphological comparison of vacuum plasma sprayed and detonation gun sprayed hydroxyapatite coatings for orthopaedic applications", *Biomaterials,* vol. 20, pp. 315-322, 2, 1999

[72] J. D. Haman, L. C. Lucas and D. Crawmer, "Characterization of high velocity oxy-fuel combustion sprayed hydroxyapatite", *Biomaterials,* vol. 16, pp. 229-237, 1995

[73] K. A. Khor, H. Li, P. Cheang and S. Y. Boey, "In vitro behavior of HVOF sprayed calcium phosphate splats and coatings", *Biomaterials,* vol. 24, pp. 723-735, 2. 2003

[74] H. C. Gledhill, I. G. Turner and C. Doyle, "In vitro dissolution behaviour of two morphologically different thermally sprayed hydroxyapatite coatings", *Biomaterials,* vol. 22, pp. 695-700, 4. 2001

[75] L. Pawlowski, *The Science and Engineering of Thermal Spray Coatings.* New York: Wiley, 1995

[76] Gordon England, Thermal Spray Process," [online], http://www.gordonengland.co.uk/xhomepage.htm, (Accessed 25th May 2008)

[77] M. P. Taylor, "Assessment of plasma-sprayed hydroxyapatite coatings", PhD Thesis, University of Birmingham, Birmingham, 1994

[78] C. X. Wang, Z. Q. Chen, L. M. Guan, M. Wang, Z. Y. Liu and P. L. Wang, "Fabrication and characterization of graded calcium phosphate coatings produced by ion beam sputtering/mixing deposition", *Nuclear Instruments and Methods in Physics Research Section B: Beam Interactions with Materials and Atoms,* vol. 179, pp. 364-372, 8. 2001

[79] V. Nelea, C. Morosanu, M. Iliescu and I. N. Mihailescu, "Microstructure and mechanical properties of hydroxyapatite thin films grown by RF magnetron sputtering", *Surface and Coatings Technology,* vol. 173, pp. 315-322, 8/22. 2003

[80] T. N. Kim, Q. L. Feng, Z. S. Luo, F. Z. Cui and J. O. Kim, "Highly adhesive hydroxyapatite coatings on alumina substrates prepared by ion-beam assisted deposition", *Surface and Coatings Technology,* vol. 99, pp. 20-23, 2/5. 1998

[81] F. Fazan, "In vitro behaviour of plasma sprayed hydroxyapatite coatings", PhD Thesis, University of Birmingham, Birmingham, 2000

[82] W. R. Lacefield, "Hydroxylapatite coatings", in *An Introduction to Bioceramics,* L. L. Hench and J. Wilson, Eds., Singapore; River Edge, N.J.: World Scientific, 1993, pp. 223-238

[83] W. D. Kingery, H. K. Bowen and D. R. Uhlmann, *Introduction to Ceramics,* New York: John Wiley & Sons Ltd., 1976

[84] J. A. Darr, Z. X. Guo, V. Raman, M. Bououdina and I. U. Rehman, "Metal organic chemical vapour deposition (MOCVD) of bone mineral like carbonated hydroxyapatite coatings", *Chemical Communications,* pp. 696-697, Mar 21. 2004

[85] A. Stoch, A. Brozek, G. Kmita, J. Stoch, W. Jastrzebski and A. Rakowska, "Electrophoretic coating of hydroxyapatite on titanium implants", *J. Mol. Struct.,* vol. 596, pp. 191-200, 9/26. 2001

[86] C. Wang, J. Ma, W. Cheng and R. Zhang, "Thick hydroxyapatite coatings by electrophoretic deposition", *Mater Lett,* vol. 57, pp. 99-105, 11. 2002

[87] C. S. Yip, K. A. Khor, N. L. Loh and P. Cheang, "Thermal spraying of Ti-6Al-4V/hydroxyapatite composites coatings: powder processing and post-spray treatment", *J. Mater. Process. Technol.,* vol. 65, pp. 73-79, 3. 1997

[88] S. Amada and T. Hirose, "Influence of grit blasting pre-treatment on the adhesion strength of plasma sprayed coatings: fractal analysis of

roughness", *Surface and Coatings Technology,* vol. 102, pp. 132-137, 4/1. 1998

[89] B. J. Griffiths, D. T. Gawne and G. Dong, "The role of grit blasting in the production of high-adhesion plasma sprayed alumina coatings", *Proceedings of the Institution of Mechanical Engineers Part B Journal of Engineering Manufacture: Including Short Communications in Manufacture and Design,* vol. 211, pp. 1- 9, 1997

[90] Y. C. Tsui, C. Doyle and T. W. Clyne, "Plasma sprayed hydroxyapatite coatings on titanium substrates Part 1: Mechanical properties and residual stress levels", *Biomaterials,* vol. 19, pp. 2015-2029, 11. 1998

[91] S. J. Yankee, B. J. Pletka and R. L. Salsbury, "Quality control of hydroxyapatite coatings: The surface preparation stage," in *Thermal Spray Coatings: Properties, Processes and Applications,* T. F. Bernecki,ed.,Fourth National Thermal Spray Conference, Pittsburg, Pennsylvania, 4^{th}- 10^{th} May, 1991

[92] Y. C. Yang and E. Chang, "The bonding of plasma-sprayed hydroxyapatite coatings to titanium: effect of processing, porosity and residual stress", *Thin Solid Films,* vol. 444, pp. 260-275, 11/1. 2003

[93] "Standard Specification for Composition of Ceramic Hydroxyapatite for Surgical Implants," ASTM F1185-03, ASTM International, 2003

[94] “Implants for surgery- hydroxyapatite. Part 1: Ceramic hydroxyapatite”, BS ISO 13779-1:2000, International Organisation for Standards, 2000

[95] P. Cheang and K. A. Khor, "Thermal spraying of hydroxyapatite (HA) coatings: Effects of powder feedstock", *J. Mater. Process. Technol.,* vol. 48, pp. 429-436, 1/15. 1995

[96] S. M. Rossnagel, J. J. Cuomo and W. D. Westwood, *Handbook of Plasma Processing Technology: Fundamentals, Etching, Deposition, and Surface Interactions,* Park Ridge, N.J: Noyes Publications, 1990

[97] V. E. Golant, A. P. Zhilinsky, I. E. Sakharov and S. C. Brown, *Fundamentals of Plasma Physics.* New York: J. Wiley, 1980

[98] K. Leung, J. Heberlein, E. Pfender, "Particle trajectory control with the use of different carrier gases," in *Thermal Spray Science and Technology,* C.C. Berndt, S. Sampath, ed., 8th National thermal Spray Conference, Houston, Texas, 11-15th, September 1995

[99] S. Dyshlovenko, B. Pateyron, L. Pawlowski and D. Murano, "Numerical simulation of hydroxyapatite powder behaviour in plasma jet", *Surface and Coatings Technology,* vol. 179, pp. 110-117, 2/2. 2004

[100] W. Tong, Z. Yang, X. Zhang, A. Yang, J. Feng, Y. Cao and J. Chen, "Studies on diffusion maximum in x-ray diffraction patterns of plasma-

sprayed hydroxyapatite coatings", *J. Biomed. Mater. Res.,* vol. 40, pp. 407-413, 1998

[101] S. Fantassi, M. Vardelle, P. Fauchais and C. Moreau, "Investigation of the splat formation versus different particulate temperatures and velocities prior to impact," in *Thermal Spray: International Advances in Coatings Technology,* C.C. Berndt Orlando, 13th International Thermal Spray Conference, Florida, 28th May – 5th June 1992

[102] S. J. Yankee and B. J. Pletka, "An investigation of plasma sprayed hydroxylapatite splats", in *Thermal Spray Coatings: Properties, Processes and Applications, ,* T. F. Bernecki, ed., Fourth National Thermal Spray Conference, Pittsburg, Pennsylvania, 4^{th}- 10^{th} May, 1991

[103] S. J. Yankee and B. J. Pletka, "Microstructural analysis of impacted hydroxyapatite droplets," in *Thermal Spray: International Advances in Coatings Technology,* C.C. Berndt, ed., 13th International Thermal Spray Conference, Orlando, Florida, 28th May – 5th June 1992

[104] T. J. Steeper, Varacalle, D. J. JR., G. C. Wilson, W. L. Riggs, A. J. Rotolico and J. E. Nerz, "Optimizing plasma spraying alumina-titania coatings using statistical methods," in *Thermal Spray Coatings: Research, Design and Applications,* C.C. Berndt, T.F. Bernecki, ed., 5th National Thermal Spray Conference, Anaheim, California, 7 – 11th June, 1993

[105] Y. Cao, J. Weng, J. Chen, J. Feng, Z. Yang and X. Zhang, "Water vapour-treated hydroxyapatite coatings after plasma spraying and their characteristics", Biomaterials, vol. 17, pp. 419-424, 2. 1996

[106] C. H. Quek, K. A. Khor and P. Cheang, "Influence of processing parameters in the plasma spraying of hydroxyapatite/Ti-6Al-4V composite coatings", J. Mater. Process. Technol., vol. 89-90, pp. 550-555, 5/19. 1999

[107] J. Cizek, K. A. Khor and Z. Prochazka, "Influence of spraying conditions on thermal and velocity properties of plasma sprayed hydroxyapatite," Materials Science and Engineering: C, vol. 27, Issue 2, March 2007, pp. 340-344

[108] S. Guessasma, G. Montavon and C. Coddet, "Velocity and temperature distributions of alumina–titania in-flight particles in the atmospheric plasma spray process", *Surface and Coatings Technology,* vol. 192, pp. 70-76, 3/1. 2005

[109] L. Sun, C. C. Berndt and C. P. Grey, "Phase, structural and microstructural investigations of plasma sprayed hydroxyapatite coatings", *Materials Science and Engineering A,* vol. 360, pp. 70-84, 11/15. 2003

[110] C. Y. Yang, B. C. Wang, E. Chang and J. D. Wu, "The influences of plasma spraying parameters on the characteristics of hydroxyapatite coatings: a quantitative study", *J. Mater. Sci. Mater. Med.,* vol. 6, pp. 249-257, 05/01. 1995

[111] S. W. K. Kweh, K. A. Khor and P. Cheang, "Plasma-sprayed hydroxyapatite (HA) coatings with flame-spheroidized feedstock: microstructure and mechanical properties", *Biomaterials,* vol. 21, pp. 1223-1234, 6. 2000

[112] E. C. Shors and R. E. Holmes, "Porous hydroxyapatite", in *An Introduction to Bioceramics* L. L. Hench and J. Wilson, Eds., London: World Scientific, 1993, pp. 181-198

[113] J. R. Mawdsley, Y. J. Su, K. T. Faber and T. F. Bernecki, "Optimization of small-particle plasma-sprayed alumina coatings using designed experiments," *Materials Science and Engineering A,* vol. 308, pp. 189-199, 6/30. 2001.

[114] Y. P. Lu, S. T. Li, R. F. Zhu and M. S. Li, "Further studies on the effect of stand-off distance on characteristics of plasma sprayed hydroxyapatite coating," *Surface and Coatings Technology,* vol. 157, pp. 221-225, 8/22. 2002.

[115] Y. C. Tsui, C. Doyle and T. W. Clyne, "Plasma sprayed hydroxyapatite coatings on titanium substrates Part 2: optimisation of coating properties," *Biomaterials,* vol. 19, pp. 2031-2043, 11. 1998.

[116] "Implants for Surgery- Hydroxyapatite. Part 2: Coatings of Hydroxyapatite", International Organisation for Standards, *BS ISO 13779-2:2000,* 2000.

[117] W. Tong, J. Chen and Xingdong Zhang, "Amorphorization and recrystallization during plasma spraying of hydroxyapatite," *Biomaterials,* vol. 16, pp. 829-832, 7. 1995.

[118] K. A. Gross, C. C. Berndt and H. Herman, "Amorphous phase formation in plasma-sprayed hydroxyapatite coatings," *J. Biomed. Mater. Res.,* vol. 39, pp. 407-414, 1998.

[119] J. Weng, X. Liu, X. Li and X. Zhang, "Intrinsic factors of apatite influencing its amorphization during plasma-spray coating," *Biomaterials,* vol. 16, pp. 39-44, 1995.

[120] J. E. Dalton and S. D. Cook, "*In vivo* mechanical and histological characteristics of HA-coated implants vary with coating vendor," *J. Biomed. Mater. Res.,* vol. 29, pp. 239-245, 1995.

[121] Y. C. Yang, E. Chang and S. Y. Lee, "Mechanical properties and Young's modulus of plasma-sprayed hydroxyapatite coating on Ti substrate in simulated body fluid," *Journal of Biomedical Materials Research - Part A,* vol. 67, pp. 886-899, 2003.

[122] M. Rouahi, E. Champion, P. Hardouin and K. Anselme, "Quantitative kinetic analysis of gene expression during human osteoblastic adhesion on orthopaedic materials," *Biomaterials,* vol. 27, pp. 2829-2844, 2006/5.

[123] Y. Yang and E. Chang, "Measurements of residual stresses in plasma-sprayed hydroxyapatite coatings on titanium alloy," *Surface and Coatings Technology,* vol. 190, pp. 122-131, 1/3. 2005.

[124] J. Stokes, "Production of coated and free-standing engineering components using the HVOF (High Velocity Oxy-Fuel) process", PhD Thesis, Dublin City University, 2003.

[125] C. C. Berndt and K. A. Gross, "Characteristics of hydroxyapatite bio-coatings " in *Thermal Spray: International Advances in Coatings Technology,* C.C. Berndt Orlando, 13th International Thermal Spray Conference, Florida, 28th May – 5th June 1992

[126] K. A. Gross and M. Babovic, "Influence of abrasion on the surface characteristics of thermally sprayed hydroxyapatite coatings," *Biomaterials,* vol. 23, pp. 4731-4737, 12. 2002.

[127] A. Boyde, A. Corsi, R. Quarto, R. Cancedda and P. Bianco, "Osteoconduction in large macroporous hydroxyapatite ceramic implants: evidence for a complementary integration and disintegration mechanism", *Bone,* vol. 24, pp. 579-589, 6. 1999

[128] C. Chang, J. Huang, J. Xia and C. Ding, "Study on crystallization kinetics of plasma sprayed hydroxyapatite coating", *Ceram. Int.,* vol. 25, pp. 479-483, 7. 1999

[129] M. Espanol, V. Guipont., K. A. Khor., M. Jeandin and N. Llorca-Isern, "Effect of heat treatment on high pressure plasma sprayed hydroxyapatite coatings", *Surface Engineering,* vol. 18, pp. 213-218, 2002

[130] Y. Lu, Y. Song, R. Zhu, M. Li and T. Lei, "Factors influencing phase compositions and structure of plasma sprayed hydroxyapatite coatings during heat treatment", *Applied Surface Science,* vol. 206, pp. 345-354, 2/15. 2003

[131] J. Chen, W. Tong, Y. Cao, J. Feng and X. Zhang, "Effect of atmosphere on phase transformation in plasma-sprayed hydroxyapatite coatings during heat treatment", *J. Biomed. Mater. Res.,* vol. 34, pp. 15-20, 1997

[132] P. Cheang, K. A. Khor, L. L. Teoh and S. C. Tam, "Pulsed laser treatment of plasma-sprayed hydroxyapatite coatings", *Biomaterials,* vol. 17, pp. 1901-1904, 10. 1996

[133] K. A. Khor, A. Vreeling, Z. L. Dong and P. Cheang, "Laser treatment of plasma sprayed HA coatings", *Materials Science and Engineering A,* vol. 266, pp. 1-7, 6/30. 1999

[134] K. A. Khor, C. S. Yip and P. Cheang, "Post-spray hot isostatic pressing of plasma sprayed Ti---6Al---4V/hydroxyapatite composite coatings", *J. Mater. Process. Technol.,* vol. 71, pp. 280-287, 11/15. 1997

[135] S. W. K. Kweh, K. A. Khor and P. Cheang, "An in vitro investigation of plasma sprayed hydroxyapatite (HA) coatings produced with flame-spheroidized feedstock", *Biomaterials,* vol. 23, pp. 775-785, 2. 2002

[136] H. Kim, Y. Koh, L. Li, S. Lee and H. Kim, "Hydroxyapatite coating on titanium substrate with titania buffer layer processed by sol-gel method", *Biomaterials,* vol. 25, pp. 2533-2538, 6. 2004

[137] H. Kurzweg, R. B. Heimann, T. Troczynski and M. L. Wayman, "Development of plasma-sprayed bioceramic coatings with bond coats based on titania and zirconia", *Biomaterials,* vol. 19, pp. 1507-1511, 8. 1998

[138] B. Chou and E. Chang, "Plasma-sprayed hydroxyapatite coating on titanium alloy with ZrO2 second phase and ZrO2 intermediate layer", *Surface and Coatings Technology,* vol. 153, pp. 84-92, 4/1. 2002

[139] L. Fu, K. Aik Khor and J. Peng Lim, "The evaluation of powder processing on microstructure and mechanical properties of hydroxyapatite (HA)/yttria stabilized zirconia (YSZ) composite coatings", *Surface and Coatings Technology,* vol. 140, pp. 263-268, 6/1. 2001

[140] K. A. Khor, Y. W. Gu, C. H. Quek and P. Cheang, "Plasma spraying of functionally graded hydroxyapatite/Ti–6Al–4V coatings", vol. 168, pp. 195-201, 5/22. 2003

[141] C. Chu, J. Zhu, Z. Yin and P. Lin, "Optimal design and fabrication of hydroxyapatite-Ti asymmetrical functionally graded biomaterial", *Materials Science and Engineering A,* vol. 348, pp. 244-250, 5/15. 2003

[142] L. H. Wong, B. Tio and X. Miao, "Functionally graded tricalcium phosphate/fluoroapatite composites", vol. 20, pp. 111-115, 5/31. 2002

[143] M. Ogiso, M. Yamamura, P. T. Kuo, D. Borgese and T. Matsumoto, "Comparative push-out test of dense HA implants and HA-coated implants: Findings in a canine study", *J. Biomed. Mater. Res.,* vol. 39, pp. 364-372, 1998

[144] V. C. A. Martins, G. Goissis, A. C. Ribeiro, E. Marcantonio Jr and M. R. Bet, "The Controlled Release of Antibiotic by Hydroxyapatite: Anionic Collagen Composites", *Artif. Organs,* vol. 22, pp. 215-221, 1998

[145] The Materials Information Society, ASM *Handbook. - Vol.10 : Materials Characterization,* Ohio: American Society for Metals, 1992

[146] Callister, William D. Jr., *Materials Science and Engineering: An Introduction*, 4th ed., New York: John Wiley & Sons, 1997

[147] M. F. Morks and A. Kobayashi, "Effect of gun current on the microstructure and crystallinity of plasma sprayed hydroxyapatite coatings", Applied Surface Science, vol 253, Issue 17, 30 June 2007, pp. 7136-7142

[148] J. C. Knowles, K. Gross, C. C. Berndt and W. Bonfield, "Structural changes of thermally sprayed hydroxyapatite investigated by Rietveld analysis", *Biomaterials,* vol. 17, pp. 639-645, 3. 1996

[149] K. D. Rogers, S. E. Etok and R. Scott, "Structural characterisation of apatite coatings", *J. Mater. Sci.,* vol. 39, pp. 5747-5754, 2004

[150] British Standards Institute, "Advanced technical ceramics-Methods of test for ceramic coatings: Part 5: Determination of porosity", DD ENV 1071-5:1995, 1995

[151] Y. Lee, C. Wang, T. Huang, C. Chen, C. Kao and S. Ding, "In vitro characterization of postheat-treated plasma-sprayed hydroxyapatite coatings", *Surface and Coatings Technology,* vol. 197, pp. 367-374, 7/22. 2005

[152] Y. Yang, J. Tian, L. Deng and J. L. Ong, "Morphological behavior of osteoblast-like cells on surface-modified titanium in vitro", *Biomaterials,* vol. 23, pp. 1383-1389, 2002/3

[153] Y. Chou, W. Huang, J. C. Y. Dunn, T. A. Miller and B. M. Wu, "The effect of biomimetic apatite structure on osteoblast viability, proliferation, and gene expression", *Biomaterials,* vol. 26, pp. 285-295, 2005/1

[154] C. Wang, Y. Duan, B. Markovic, J. Barbara, C. R. Howlett, X. Zhang and H. Zreiqat, "Phenotypic expression of bone-related genes in osteoblasts grown on calcium phosphate ceramics with different phase compositions", *Biomaterials,* vol. 25, pp. 2507-2514, 2004/6

[155] D. Richard, N. Dumelie´, H. Benhayoune, S. Bouthors, C. Guillaume, N. Lalun, G. Balossier and D. Laurent-Maquin, "Behavior of Human Osteoblast-Like Cells in Contact With Electrodeposited Calcium Phosphate Coatings", *J Biomed Mater Res B Appl Biomater,* vol. 79, pp. 108-115, Oct. 2006

[156] C. Knabe, G. Berger, R. Gildenhaar, F. Klar and H. Zreiqat, "The modulation of osteogenesis in vitro by calcium titanium phosphate coatings", *Biomaterials,* vol. 25, pp. 4911-4919, 9. 2004

[157] J. Rossert and B. de Crombrugghe, "Type 1 collagen: Structure, synthesis and regulation", in *Principles of Bone Biology*, 2nd ed., vol. 1, J. P. Bilezikian, L. G. Raisz and G. A. Rodan, Eds., London: Academic Press, 2002

[158] M. J. Seibel, "Biochemical markers of bone metabolism", in *Principles of Bone Biology*, 2nd ed., vol. 2, J. P. Bilezikian, L. G. Raisz and G. A. Rodan, Eds., London: Academic Press, 2002

[159] D. A. Towler and R. St. Arnaud, "Use of cultured osteoblastic cells to identify and characterize transcriptional regulatory complexes", in *Principles of Bone Biology*, 2nd ed., vol. 2, J. P. Bilezikian, L. G. Raisz and G. A. Rodan, Eds., London: Academic Press, 2002

[160] B. Lin, M. Jean and J. Chou, "Using response surface methodology for optimizing deposited partially stabilized zirconia in plasma spraying" *Applied Surface Science*, vol. Volume 253, Issue 6, 15 January 2007, pp. 3254-3262

[161] J. F. Li, H. Liao, B. Normand, C. Cordier, G. Maurin, J. Foct and C. Coddet, "Uniform design method for optimization of process parameters of plasma sprayed TiN coatings," *Surface and Coatings Technology,* vol. 176, pp. 1-13, 2003/0.

[162] T. J. Steeper, Varacalle, D. J. JR., G. C. Wilson, W. L. Riggs, A. J. Rotolico and J. E. Nerz, "A taguchi design of experiment study of plasma sprayed alumina coatings", in *Thermal Spray Coatings: Research, Design and Applications,* 1993

[163] D. F. Gibbons and K. A. Buran, "Microscopic analysis of retrieved polymethylmethacrylate (PMMA) bone cement, implant retrieval: Material and biological analysis, National Bureau of Standards Special Publication 601", National Bureau of Standards, Washington DC, 1981

[164] T. J. Steeper, Varacalle, D. J., JR., G. C. Wilson, W. L. Riggs, A. J. Rotolico and J. E. Nerz, "A design of experiment study of plasma sprayed alumina -titania coatings," in *Thermal Spray: International Advances in Coatings Technology,*C.C. Berndt, ed., Orlando, 13th International Thermal Spray Conference, Florida, 28th May – 5th June 1992

[165] S. Dyshlovenko, C. Pierlot, L. Pawlowski, R. Tomaszek and P. Chagnon, "Experimental design of plasma spraying and laser treatment of hydroxyapatite coatings", *Surface and Coatings Technology,* vol. 201, pp. 2054-2060, 2006/10/25

[166] S. Dyshlovenko, L. Pawlowski, P. Roussel, D. Murano and A. Le Maguer, "Relationship between plasma spray operational parameters and microstructure of hydroxyapatite coatings and powder particles sprayed into water," *Surface and Coatings Technology,* vol. 200, Issues 12-13, 31 March 2006, pp. 3845-3855

[167] R. Roy, *Design of Experiments using the Taguchi Approach: 16 Steps to Product and Process Improvement,* New York: John Wiley & Sons Ltd., 2001

[168] "*ASM Handbook Vol 8 Mechanical Testing"*, ASM International, 1992 pp. 639-652.

[169] D. C. Montgomery, G. C. Runger and N. R. Hubble, *Engineering Statistics,* 2nd edition, New York: John Wiley & Sons, 2001

[170] C. Pierlot, L. Pawlowski, M. Bigan and P. Chagnon, "Design of experiments in thermal spraying: A review," *Surface and Coatings Technology,* vol. 202, Issue 18, 15 June 2008, pp. 4483-4490

[171] NIST/SEMATECH, "*e-Handbook of Statistical Methods*," [online] http://www.itl.nist.gov/div898/handbook, (Accessed 25th May 2008)

[172] P. L. Silva, J. D. Santos, F. J. Monteiro and J. C. Knowles, "Adhesion and microstructural characterization of plasma-sprayed hydroxyapatite/glass ceramic coatings onto Ti-6A1-4V substrates", *Surface and Coatings Technology,* vol. 102, pp. 191-196, 4/21. 1998

[173] ASTM International, "Standard Practice for X-ray determination of phase content of plasma-sprayed hydroxyapatite coatings", ASTM F 2024-00, 2000

[174] British Standard Institution, "BS ISO 14887:2000 - sample preparation-dispersing procedures for powders in liquids," 2000.

[175] British Standard Institution, "Particle size analysis- laser diffraction methods- Part 1: General principles," BS ISO 13320-1:1999, 1999

[176] Sharon Kehoe, "Investigation into the powder production and application of hydroxyapatite powder used in femoral implants", PhD Thesis, Dublin City University, Dublin, 2008

[177] G. Daculsi, O. Laboux and R. Le Geros, "Outcome and perspectives in bioactive coatings: What's new, what's coming", *ITBM-RBM,* vol. 23, pp. 317-325, 12. 2002

[178] M. F. Bahbou, P. Nylen and J. Wigren, "Effect of grit blasting and spraying angle on the adhesion strength of a plasma-sprayed coating", *J. Therm. Spray Technol.,* vol. 13, pp. 508-514, 2004

[179] L. Yan, Y. Leng and L. Weng, "Characterization of chemical inhomogeneity in plasma-sprayed hydroxyapatite coatings", *Biomaterials,* vol. 24, pp. 2585-2592, 7. 2003

[180] D. D. Deligianni, N. D. Katsala, P. G. Koutsoukos and Y. F. Missirlis, "Effect of surface roughness of hydroxyapatite on human bone marrow cell adhesion, proliferation, differentiation and detachment strength", *Biomaterials,* vol. 22, pp. 87-96, 1. 2001

[181] R. I. Freshney, *Culture of Animal Cells - A Manual of Basic Technique,* 5th Edition, London, John Wiley & Sons, 2005

[182] B. Chou and E. Chang, "Microstructural characterization of plasma-sprayed hydroxyapatite-10 wt% ZrO2 composite coating on titanium", *Biomaterials,* vol. 20, pp. 1823-1832, 10. 1999

[183] J. Lee, S. Nam, S. Im, Y. Park, Y. Lee, Y. Seol, C. Chung and S. Lee, "Enhanced bone formation by controlled growth factor delivery from chitosan-based biomaterials", *Journal of Controlled Release,* vol. 78, pp. 187-197, 2002/1/17

Appendix A – Statistical Measures

R^2

The R^2 value indicates the degree of the relationship of the response variable to the combined linear predictor variables. It is an estimate of the overall variation in the data accounted for by the model. The R^2 value is calculated as follows:

$$R^2 = \frac{(SS - SSresid)}{SS}$$

The R^2 value is a number between 0 and +1. The closer the value is to one the better the model is.

Adjusted R^2

The Adjusted R^2 value is an estimate of the fraction of the overall variation in the data accounted for by the model. It is the R^2 value adjusted for the terms in the model relative to the number of points in the design.

$$R_{adj}^{\ 2} = \frac{(MS - MSresid)}{MS}$$

$MS = SS/(n-1)$

$MS_{resid} = SS_{resid}/(n-p)$

n = number of experimental runs

p = number of terms in the model, including the constant

Predicted R^2

The Predicted R^2 value measures the amount of variation in new data explained by the model.

$$Predicted\ R^2 = \frac{1 - SSPRESS}{(SStotal - SSblocks)}$$

For an adequate model the Predicted R^2 and Adjusted R^2 values should be within 0.2 of each other.

Adequate Precision

The adequate precision is a measure of the range in predicted response relative to its associated error, in other words the signal to noise ratio. It should be greater than 4.

Appendix B – Substrate Holder

Sample Holder Movement

An x-y sample holder based on a pneumatic cylinder was designed for use in this work. The pneumatic system controlling the sample mover is shown in *figure A2*.

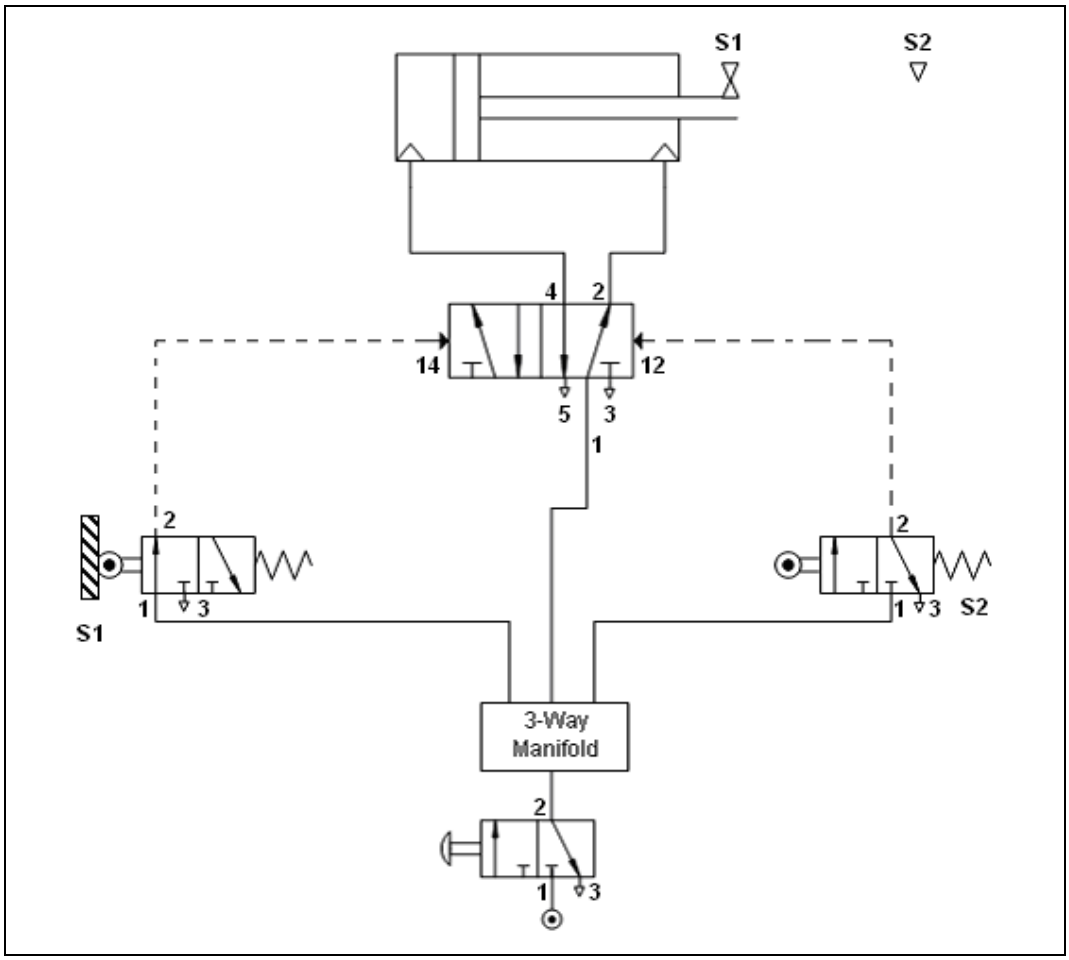

Figure A.1: Sample Movement Pneumatic Diagram

When the compressed air supply is switched on, air enters a 3-way manifold. Air flows from here to a 5/2 way valve and two spring return 3/2 way valves. The 5/2 way valve allows air to flow into one side of the pneumatic cylinder. The cylinder moves until it hits the roller switch (S2). The cylinder then moves back in the opposite direction until it hits the roller switch at the other end (S1). The speed at which the cylinder travels is controlled by valves that adjust the flow of air at each side of the cylinder.

Appendix C - Plasma Equipment Operating Instructions

Start-up

1. Ensure that both water valves are open at the wall. These supply water to cool the plasma gun and can be left open at all times unless maintenance work is being carried out.
2. Open the compressed air and argon gas valves, located on the wall behind the powder feeder at the wall. Argon is used as the primary gas. The primary gas pressure on the gauge on the control unit should be set to 75 psi.
3. Argon is also used as the powder carrying gas. The pressure for this gas also needs to be set at 75 psi. This can be checked on the gauge on the powder feeder unit.
4. The secondary gas pressure should be 50 psi. Although a secondary gas is not currently being used, there still needs to be sufficient secondary gas pressure in order for the system to operate. Argon is currently been used to supply this secondary gas pressure.
5. To switch on the control unit, turn the red and yellow 'Main Power' knob clockwise.
6. Initially the control unit will display:

VENTILATION FAULT

7. This message will disappear once the pressure in the electrical component box has built-up enough.
8. The control unit will then display:

E-STOP/ GASES ON

9. The powder feeder unit will display:

EMERGENCY STOP

10. Press the white 'System On' button in the automatic gun operation panel on the control unit.
11. The control unit will then display:

9MC SYSTEM READY

12. The cooling water flow rate can now been seen displayed on the junction box. This is usually 11.9 l/min. If the flow rate drops too low an alarm will sound and it won't be possible to run the spray equipment.

Extraction System

1. The extraction unit should be switched on when spraying, setting up gas flow rates and setting up powder feed rates. It should be left on for a few minutes after spraying to ensure that all gases and powders are properly removed from the spray room. Ear protection should be worn when the extraction system is on.
2. To switch on the extraction system press the green start button on the side of the extraction system.
3. The extraction system light can also be turned on at the side of the extraction system.

Gas Flow Rate Set-Up

1. To set the Gas Flow Rate press the white 'Purge' button on the test panel on the control panel. Hold in this button until the following steps have been completed.
2. The control panel display will now read:

SYSTEM PURGING

3. While purging, check around the gun for any water leaks. Check the nozzle and also the hoses and hose connection points. If there are leaks stop the system and check all o-rings and connections.
4. If everything is ok, check the primary gas pressure once again to ensure it is at 75 psi; adjust if necessary.
5. Set the primary gas flow rate to the required level by turning the black dial below the primary gas flow rate gauge.
6. The carrier gas flow rate can be set by turning the black dial above the carrier gas pressure gauge on the powder feeder to the required value.
7. The secondary gas flow valve should not be opened unless a secondary gas is being used.

Current

1. The current can be changed by turning the current dial. Lock the current at this value by pushing the knob on the dial.

Powder Hopper

1. Put powder into the hopper. There must be enough powder in the hopper to cover the powder pick up shaft. The weight of powder in the hopper is shown on the display.
2. To ensure that the powder does not run out during spraying, put enough powder in the hopper to cover the pick up shaft and then set the weight to zero.
3. Push the 'Set Points' button to set the powder flow rate required.
4. Enter the value required and press 'Enter'.

Powder Feeder Auto set-up

1. An auto-set-up should be run every time powder is added to the hopper, the powder feed rate is changed or the carried gas flow rate is changed. This determines the pressure required in the hopper to feed the powder at the set rate.
2. Remove the powder injector from the plasma gun and place into the powder collection pot.
3. Push the shift button on the powder feeder and then press local to set the hopper to be controlled locally.
4. Press the 'Auto Set-Up' button.
5. The display will say: WAITING FOR SIGNAL
6. Switch the black knob on the automatic gun operation panel on the control unit from preheat to spray and switch the powder feed knob on the test panel from feed off to feed on.
7. The powder feeder will run until the feed rate stabilises at the correct value. If it does not stabilise in time the auto set-up will fail and need to be run again.
8. Once auto-set-up is complete, set the powder feeder back to remote operation by pushing shift and then 'Remote'.
9. A number of alarms can be set on the powder feeder, for example an alarm can be set to come on if the spray rate drifts excessively.

Sample Mover

1. Set the spray distance to the required value by moving the sample holder in the y-direction along the sliding rails.
2. Mount the sample in the sample holder, ensuring that it is tightly clamped in place.
3. Turn on the second compressor by switching on the power at the wall and ensuring that the key is open at the back of the compressor.
4. Once the pressure has built up and the compressor cuts out, open the valve on the compressor to release any water vapour in the system.
5. Allow the pressure to build up again and turn on the sample mover by turning the red valve on the side of the extraction equipment.
6. Turn off the sample mover and ensure that it stops at one end of its stroke.

Spraying

1. Ensure that all personal protection equipment is being worn.
2. Before igniting the plasma gun, gas must be purged though the gas lines to get rid of any air, contamination or moisture that may be present.
3. Press the white 'Purge' button on the test panel on the control unit. Hold this button for 5 – 10 seconds.
4. The control panel display will now read: SYSTEM PURGING
5. Next press the 'Ignition' button on the test panel of the control unit to test for a spark. The control unit panel will read:

   IGNITION TEST/ COOL DOWN
6. Hold this button for about 10 seconds, until the display reads:

   9MC SYSTEM READY
7. To start spraying, press the green 'Start' button in the automatic gun operation panel on the control unit.
8. The system will try three times to ignite the plasma flame. If ignition is unsuccessful the display: IGNITION FAILURE

9. If this occurs, press the emergency stop on the control unit and allow the system to cool down for about a minute. Switch on the control unit again and re-run the steps in this section.
10. When ignition occurs the current will ramp up to the set value.
11. When the current reaches the correct value the powder feed can be turned on by turning the knob from 'Preheat' to 'Spray' and turn the feed from 'Feed Off' to 'Feed On'.
12. Turn on the sample mover. Start the stop watch and spray for the required time.
13. Stop spraying by pressing the black 'Stop' button in the automatic gun operation panel on the control unit.
14. Turn off the spray and powder feed.
15. Stop the sample mover and allow the sample to cool completely before removing from the sample holder.

Turning off the equipment

1. Turn off the argon and compressed air. If hydrogen is being used the compressed air must remain on to maintain a positive pressure in the control unit and prevent hydrogen coming in contact with the electrical components
2. Turn off the control unit by turning the red 'Main Power' knob and also press the emergency stop button.
3. The powder feeder can be left on.
4. Turn off the extraction system.
5. Turn off the second compressor.

Emptying the Hopper

1. Open the powder feeder and slide the hopper out along its rails.
2. Open the catch on the lid and open the lid.
3. Place a container underneath the hopper and open the catch at the bottom of the hopper. Let the powder fall into the container.
4. Clean out the hopper with a brush and compressed air.

Appendix D – Quantitative RT PCR Plate Set-Up

Table A.1 shows the set-up of a 96 well plate for quantitative Real Time PCR. X refers to an empty well. NTC is the non template control, dd H_2O in this case. Number 1 relates to the Day 0 sample. Number 2 relates to the pooled sample for the control on Day 7 and Number 5 relates to the pooled sample for Ti on Day 7 etc.

Table A.1: Sample Quantitiative RT-PCR Plate set-up

	Day 0			Day 7			Day 21			Day 28			Gene
Ctrl	1	1	1	2	2	2	26	26	26	38	38	38	ALPL
Ti	X	X	X	5	5	5	29	29	29	41	41	41	
C1	X	X	X	8	8	8	32	32	32	44	44	44	
C2	NTC	NTC	NTC	11	11	11	35	35	35	47	47	47	
Ctrl	1	1	1	2	2	2	26	26	26	38	38	38	GADPH
Ti	X	X	X	5	5	5	29	29	29	41	41	41	
C1	X	X	X	8	8	8	32	32	32	44	44	44	
C2	NTC	NTC	NTC	11	11	11	35	35	35	47	47	47	